# APIS

## Autonomous Pollination & Imaging System

DSE Team S9

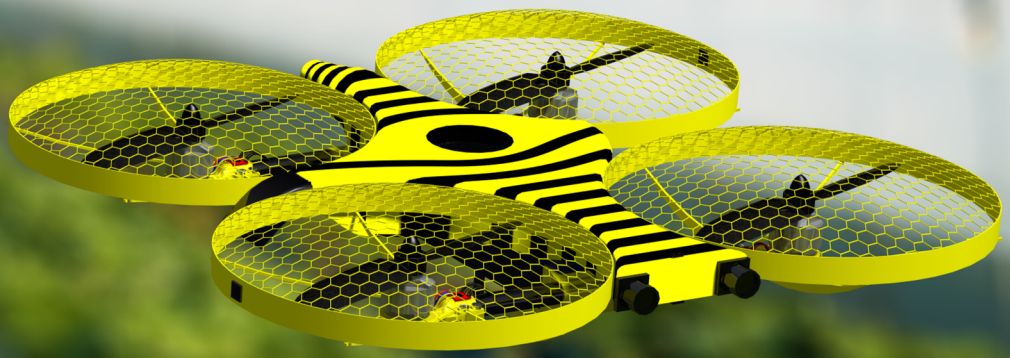

Delft University of Technology

TU Delft

# APIS

## Autonomous Pollination & Imaging System

by


DSE Team S9

| | |
|---|---|
| Bolton, T.K. | 4282752 |
| Commijs, T.J. | 4385853 |
| El-Hajj, I.Z. | 4304225 |
| Kapteijn, S. | 4301242 |
| Kuś, G.I. | 4354923 |
| Petrescu, V. | 4365119 |
| Petrov, A.P. | 4355474 |
| Quesada Mañas, J.M. | 4353889 |
| Van der Pluijm, A. | 4379497 |



| | |
|---|---|
| Project duration: | April 24, 2017 – July 6, 2017 |
| Tutor: | Christophe De Wagter |
| Coaches: | Alberto Rius |
| | Viswanath Dhanisetty |


TU Delft

# Preface

The number of calamities impinging upon mother nature are increasing. One unarguably worthy of tackling is the impending extinction of bees. This problem will propagate a direct influence on the ecosystem. Specifically, for horticulture, pollination of flowers will prove to be more and more challenging. Pollination is not only important for the reproduction of flowers but is also important in maintaining a clean environment. To ensure pollination is still properly done, drones can be used. The current report series will look into designing such a drone. This is the third report and will provide insights into the group's vision in the process of choosing the concept to be elaborated in the final phase of this project.

The team is composed of nine aerospace students who are all in the final year of their bachelor program. The biological and environmental aspects of the project, along with the opportunity to design a drone for a useful application, are the main motivations the group members share. The project started in April 2017 within the context of the course Design Synthesis Exercise at the Delft University of Technology. It is carried out under the supervision of ir. de Wagter.

The group would like to thank ir. C. de Wagter and the tutors A. Rius and V. Dhanisetty for their guidance, motivation and expertise during the design process. The group also wants to thank the DSE committee for making this project available. Furthermore, special thanks are extended to the MAV Lab, TU Delft, and in particular to ir. E. van der Horst for his help and shared experience on the micro air vehicles field. The team wants to express it deepest thanks to Wageningen University and to ing. J. Janse, for inviting the group to their research greenhouse facilities and for sharing knowledge about pollination. Besides, the group wants to extend its gratitude to Pieter Hermans from Jakajima, for inviting us to speak at the Smart Farming Conference, held on June 29, 2017 in Venlo. In addition, the group acknowledges the help provided by dr.ir. A. Dieleman and F. van Noort from Wageningen university, Mr. J. Van Marrewijk from van Marrewijk tomatoes and H. de Kroon from Vanilla BV. Moreover, the team appreciates the help received by PhD and Master students from the Delft University of Technology: PhD student M. Coutiño from the Center for Wireless Systems and Technology, for providing valuable insight in UWB technology and communication protocols, PhD student K. McGuire from the Aerospace Faculty, for her key advice on the navigation strategy, PhD student S. Lee, for his path planning expertise and Master student M. Ozo, for his experience with the Snapdragon Flight kit.

*DSE Team S9*
*Delft, July 2017*

# Executive overview

Pollination, the process where the pollen is transferred from the anther (male part) to the stigma (female part) of a flower, is the most important step in the production of seeds. Fruiting depends directly on how this fertilization process occurs as the yield, quality and size of the fruits are all affected. The transfer of pollen can be done in a variety of ways: through wind (anemophily), through insects or by manual methods. For fruits and vegetables, the main pollinators are bees. They are indeed directly responsible for 75% of all crops. In order for it to be done effectively, bees are being produced for greenhouses with the sole purpose of pollinating crops. Not all crops are however as interesting for the bees. Indeed, bees are attracted to scent and to flowers that are attractive on the outside. Planting cucumber next to tomatoes is therefore not an option as the bees would only visit the tomatoes. Furthermore, depending on the geographical location of the greenhouse, bees can be harder to purchase. In those cases, pollination can be done manually, but this process proves to be very time-consuming and expensive.

An autonomous system could therefore be envisaged for pollinating plants where their current methods are insufficient or ineffective. With the recent technical advances in domains such as precise vision based control, miniaturization and autonomous flight, an opportunity for an autonomous system of micro air vehicles presents itself. Indeed, drones such as the AscTec Firefly are capable of recreating an entire 3D map of an unfamiliar environment and others, such as the Aerix AERIUS, are 3 × 3 cm flight proven platforms. Autonomous flight has been achieved in projects such as the delftAcopter where a lost backpacker had to be found in the Australian outback. The main challenge remains in combining all these parameters into one flying vehicle. Projects such as the DelFly have shown autonomous flight is achievable on a 20 gram flapping wing system but the environment and goals for which it was tested, remain very different than the ones required in this project, namely a greenhouse. Therefore, the objective of this project was to make a proof-of-concept design of a swarm of fully autonomous pollinator micro air vehicles and its support systems, within 10 weeks' time and with a team of 9 students.

To do so, several key requirements regarding the drone itself but also the way the mission is to be performed were set. For example, the air vehicle was not to weigh more than 300 grams. It had to be able to visit at least 500 flowers a day and fly with multiple MAVs simultaneously in the same greenhouse. Furthermore, the flowers and plants were not to be damaged in any way. Communication with support systems should occur constantly and telemetry data was also to be tracked. Moreover, regarding the sustainability of the design, the minimum life cycle of the MAV was set at 8 months, the noise level was to be under 100 dB and no direct emissions were to be produced by the MAV. The budget for this project was set at €500,000. Finally, it was decided to target tomato flowers in particular. This selection was motivated by the extensive cultivated land of tomatoes in the Netherlands (1670 ha) but also by the fact that it is a self-pollinating flower. This means that vibrations have to be induced in the stem of the flower such that the pollen can fall into the stigma. This project therefore looks to provide a solid basis for the pollination of tomato plants that can in the future be expanded to other self-pollinating crops and to cross-pollinated crops, where the pollen need to be physically transported from the anther of one flower to the stigma of another.

The requirements listed in the previous paragraph were set in the first stages of the project. Specific technical and managerial tasks were given to each group member to ensure the predicted work would be equally split. A chairman was appointed to ensure managerial tasks were performed correctly and two system engineers were appointed to ensure the technical parts were detailed enough. A meticulous plan was furthermore set up in the form of a Gantt chart. This gave a first insight in the work that was to be done in the later stages of the project. In the next phase, the baseline phase, three concepts were generated that could solve the mission. The ground support and the ways the mission would be tackled were all tailored for each concept.

The first concept, named Flabbee, was inspired by the Delfly. It distinguished itself from the other concepts mainly by its propulsion system. Eight flapping wings are responsible to generate the thrust needed for the Flabbee to navigate in the greenhouse. Armed with a brushing tongue to pollinate the flowers, the Flabbee uses ultra wideband (UWB) transceivers for navigation and communication purposes. Power would come from a lithium-ion battery that would recharge when the Flabbee lands on a fixed ground station that contains a charging pad. It was moreover estimated it would weigh 32 g and would have a wing span of 14 cm. The main problem with this concept was however the accuracy needed to properly touch the flowers. Indeed, for it to be met, the size and mass of the Flabbee would have increased over the allowed limits. These limitations can be overcome with a quadrotor, which was explored in the second concept.

The second concept was called the Robuzz. Inspired by bees, the Robuzz also pollinates flowers by coming very close to them and vibrating at the right frequency. This is helped by the induced flow that is generated by the four rotors

it uses to propel itself. Just like the Flabbee, use is made of ultra wideband tags for navigation and communication. A big difference can however be found in the ground station. A mobile one on wheels would move along with the swarm of Robuzzes. Batteries would be swapped automatically to minimize the charging time and maximize the operational time. The Robuzz was expected to weigh around 77.3 g and have a size of 13 × 13 cm. The accuracy issues the Flabbee has were somewhat solved but at the expense of an increase in potential damage to the flower. This was coupled with another large problem. The smaller the design, the lower the life expectancy of the various components. Given that the design was to be sustainable, a scaled up version of the Robuzz was generated.

The third and final concept that was generated was named APIS. Both problems the Robuzz faced were solved. The flower safety issue was solved by introducing a blower on the drone. As such, the drone could pollinate flowers without directly coming into contact with them. The reliability issue was resolved directly as the component size increased. The extra weight added by the blower required more thrust to be generated. The motors were therefore selected based on the fact that the drone would weigh 250 grams. This allowed to bring additional mass on-board. As such, a powerful processor and a large battery were selected such that APIS could fly accurately over long distances. The next paragraphs will focus on the various subsystems that comprise the APIS.

The blower system was selected as damage to the flowers is reduced to a minimum once the optimal air speed is found. Through CFD simulations it was determined that at a distance of 50 cm from the flower, the exit velocity of the blower should be 10 m/s. The pointing accuracy that was found for such a jet was about 7 degrees. The blower was implemented in the drone such that it would have a dual usage. It indeed cools down the processor through ventilation and therefore expels warmer air towards the flower, something which improves the probability of successful pollination. The blower expels air from a nozzle that is at a 45 degree angle. This allows the MAV to blow air on the flower while flying above the plants.

For the power and propulsion sizing, a mission analysis was performed. A typical mission is divided into seven parts. Namely take-off, cruise, the detection phase, the pollinating phase, the turning back, the cruise back and the landing. A drone would need to cruise towards a row and start detecting flowers after leaving the ground station. The obstacle avoidance methods are on and the blower is also spinning during the pollination phase. The energy consumption was determined for each phase and the required capacity of the battery for a depth of discharge lower than 90% was determined. A Li-Po graphene battery with 2S1P was selected. It has a capacity of 1500 mAh and a lifetime of 385.35 h. The motors selected provide a maximum thrust of 130 g each, resulting in hovering at 48% throttle. This allows enough margin for agile acceleration and even extra payload mass of 10 g.

The microcontroller forms the base of the electronics system. It is comprised of a CPU for the logic operations, a GPU to process the arithmetics, a DSP to process signal inputs, a flash memory to store data from the flight sensor, a static random access memory, a read-only memory where the instructions are stored, I/O pins to attach more sensors and analog to digital converters. Communication is done through two DecaWave 1000 modules, that also provide localization and attitude information. Furthermore, additional sensors are brought on board. An IMU to measure the orientation of the quadrotor, a barometer sensor and a humidity temperature sensor are all added. For vision, as will be discussed later, a stereo camera and a monoscopic one are added. To accommodate all these sensors, the customized Snapdragon Flight board is used and optimized by removing several unused modules (such as GPS or WiFi).

As mentioned above, in order for the drone to localize itself, use will be made of ultra wideband (UWB) navigation. Two tags will be placed on the drone such that it can also determine its heading. UWB was selected as location precision up to 10 cm can be achieved. UWB also serves as the main way of communication with the ground station. With its position and heading known, the drone can fly towards its target, the flowers. To do so safely, obstacles must be detected and avoided. The stereo cameras located at the front of the drone do so by generating a first place disparity map. Those maps allow the MAV to perceive depth. If an obstacle is detected, a combination of the $D^*$ algorithm and probabilistic road maps for local path planning is considered. The code can be adjusted to detect objects that have a small resolution. This proves to be useful if the wires, connected to the tomato plants, have to be detected. Flowers are on the other hand not be detected by the stereopair but rather by the monoscopic fisheye lens located on the right side of the MAV. It is placed at an angle such that the drone can safely fly over the row and still detect flowers. The flowers are detected by an algorithm that is tailored to the colour of the tomato flowers, bright yellow. To confirm that pollination has been done, mean shift tracking is done to ensure the flower has indeed moved.

A slightly less traditional configuration was selected for the quadcopter structure: an H-configuration. This was to accommodate for the size of the battery. The material of the arms and the payload box is carbon fibre. The arms are hollow tubes that have been sized to the vibrational frequency of the motors. The battery is furthermore put on small latex foam cubes to damp those vibrations. The processing board is put on top of the battery, allowing the measurements to also be unaffected by the vibrations.

Control and stability methods were also selected for the drone. A static analysis when the blower is on, shows that the drone will be flying at an angle of 1 degree when flying in the rows. The dynamics of the quadcopter were not

simulated, as data about the motors is needed. However, once the missing data regarding the motors is found, the effect of the blower can best be modelled by making the latter an external disturbance in the body frame of the MAV. The control technique selected to damp out the effect of the blower was a PID controller. This was because of its simplicity and its capabilities to stabilize the attitude of the drone. The gains will be tuned at a later stage through either the Ziegler Nicols or the Tyreus-Luyben method.

Finally, the ground segment and ground stations were also considered. It must be first and foremost said that their name is misleading as they will actually be hanging from the roof structure of the greenhouse. This was decided such that it would not be in the way of the daily ground operations. Every greenhouse is equipped with hydraulic trolleys which makes their maintenance easy. Each ground station will have eight landing pads that will recharge the drones. Guiding cones and visual cues will guide the pin located on the drone towards one of several neighboring sockets. As such, the drone must land on a designated area, instead of one specific socket, a feat achievable with the UWB navigation and the visual cues. The ground stations are furthermore the link in between the drones and the central server. The server stores the images that the drones pass to the ground station when recharging. The health of each drone can furthermore be monitored on the main server. Connection between the main server and the ground station is done through standard LAN cables.

The final mass of the APIS is 250 ± 20 g and is designed in a modular way to accommodate different payloads for different pollination methods. The cost of one APIS drone is €394 ± 54. The weight of the ground station is expected to be around 13 ± 0.7 kg and the cost is expected to be €389.13 ± 73. The hub is expected to cost around €60 ± 30 and the server around €1500 ± 500. These do not include transportation, maintenance nor installation costs.

The typical greenhouse was defined to have a size of 200 × 200 m greenhouse. The greenhouse will first have a main corridor that splits it into an upper part and lower part, each 100 × 200 m in size. A ground station will be placed along the corridor approximately every 20 m such that the 8 ground stations have equal dedicated section. The ground stations will all be equipped with the maximum number of drones. Once the entire system is set up, the ground station starts sending the drones to the locations in the greenhouse that need to be pollinated. It does so by ensuring there is at all times a maximum of one drone in each half row and in each corridor. The drones are then sent one by one and start to pollinate and take images of the flowers. They do so by entering the row, turning the blower on and detecting the flowers. When the battery life reaches approximately 50%, the drones start flying back and start to pollinate the other side of the row. This entire process runs for 12 h a day unless stated differently on the user interface. This is because the vision system performs poorly in the dark and because the flowers have more difficulty getting pollinated in the dark. Finally, the material system cost for such a greenhouse amounts to €29,998 ± 4,570. This does not include transportation, maintenance nor installation costs.

The reliability, availability, safety and maintainability of the system were also considered. The system is made in a reliable way because the system should be effective in case of unexpected failure. Spare drones are for one included. 58 drones are needed to pollinate a 200x200 m greenhouse but 64 will be used such that all the charging pads are filled up. This ensures that if a drone fails, the task can still be accomplished within 3 days. The system is furthermore available during working hours as the maintenance plans that have been designed should be executed outside of operating hours. Moreover, regarding safety, an emergency system has been designed. A red button will be placed in a strategic location in the greenhouse and when pressed, the drones drop to the ground in a controlled manner. Safety has also been considered in the design of the drone. Propeller guards prevent them to damage plants and reduce injury risks. The electronics are sealed and coated to prevent short circuits and risks of fire. The battery is also enclosed in a casing such that it can not be punctured. Finally, the system was also made to be easily maintainable as access to the parts that most likely need to be replaced, such as the battery and the motors, is easily feasible.

The design of the system was done such that it also meets sustainability requirements. The power consumption of the drone is marginal compared to the typical electricity consumption of a greenhouse. The latter is expected to increase by 0.02% if the system is implemented. Noise levels were also considered. They were kept below 80 dB, a number which is also below the maximum noise levels allowed in a working environment in the Netherlands. Moreover, at the end of the pollination season, the batteries are collected and are to be recycled. Finally, the system contributes to sustainability on a social, environmental and economical level. Indeed, pollination services are provided to plants where the current methods are inefficient or ineffective. Economic value is also created as the drone market would be stimulated.

Finally, several recommendations are made and post DSE activities are considered. First a CFD analysis has only been made for the blower and testing on an actual tomato plant flower would help to determine the optimal exhaust velocity. Another recommendation that is made it to analyze the charging method further. The pin is currently "sticking" out of the drone and could reduce its aerodynamic capacities. Post DSE activities that have been listed include a marketing plan and the long term vision of the project. This includes building the prototype and testing it and also the expected future developments of drone pollinator technology.

# Contents

Cover photo: `http://www.onlinembatoday.com/mba-specializations/`

# Nomenclature

## Abbreviations

| | |
|---|---|
| $\dot{w}_{x,y,z}$ | Angular accelerations in x, y and z-direction |
| ADC | Analog to Digital Converter |
| AOA | Angle Of Arrival |
| API | Application Programming Interface |
| APIS | Autonomous Pollination & Imaging System |
| APM | Advanced Power Module |
| AWG | American Wire Gauge |
| BOM | Bill Of Materials |
| CAGR | Compounded Annual Growth Rate |
| CBS | Cost Breakdown Structure |
| CDMA | Code-Division Multiple Access |
| CEO | Chief Executive Officer |
| CER | Cost estimation relationship |
| CFD | Computational Fluid Dynamics |
| COO | Chief Operations Officer |
| CPU | Central Processing Unit |
| CRFP | Carbon Fibre Reinforced Plastic |
| CTO | Chief Technical Officer |
| DAC | Digital to Analog Converter |
| DC | Direct Current |
| DOD | Depth of discharge |
| DOF | Depth Of Field |
| DSE | Design Synthesis Exercise |
| DSP | Digital Signal Processor |
| EEPROM | Electronically Erasable Programmable Read-Only Memory |
| ESC | Electronic Speed Controller |
| EV | Economic Value |
| EV | Economic Value |
| FBS | Functional Breakdown Structure |
| FEM | Finite Element Model |
| FFD | Functional Flow Diagram |
| FOV | Field Of View |
| GFRP | Glass-Fiber Reinforced Plastic |
| GNSS | Global Navigation Satellite System |
| GPIO | General Purpose Input-Output |
| GPS | Global Positioning System |
| GPU | Graphical Processing Unit |
| H | Humidity |
| HR | Human Resources |
| HSV | Hue, Saturation, and Value |
| IC | Integrated Circuit |
| IMU | Inertial Measurement Unit |
| IPEV | Insect Pollination Economic Value |
| IPEV | Insect Pollination Economic Value |
| IPO | Initial Public Offering |
| LAN | Local Area Network |
| LiDS | Lifecycle Design Strategies |
| LTE | Long Term Evolution |
| MAV | Micro Aerial Vechicle |
| MISO | Master Input Slave Output |
| MOSI | Master Output Slave Input |
| MP | Mitigated Probability |
| MS | Mitigated Severity |
| NFC | Near Field Communications |
| P | Probability |
| PCB | Printed Circuit Board |
| PID | Proportional Integral Derivative (controller) |
| PIX | Pixel |
| R&D | Research and Development |
| RAM | Random Access Memory |
| RMS | Root Mean Square |
| ROI | Return on investment |
| ROM | Read Only Memory |
| RPM | Revolutions Per Minute |
| RRT | Rapid exploring Random Tree |
| RSS | Received Signal Strength |
| S | Severity |
| SCLK | Serial Clock |
| SD | Secure Digital |
| SLAM | Simultaneous Localization And Mapping |
| SoC | System on Chip |
| SPI | Serial Peripheral Interface |
| SPL | Sound Pressure Level |
| SS | Select Slave |
| SWOT | Strength, Weaknesses, Opportunities, Threats |
| SWOT | Strengths, Weaknesses, Opportunities and Threats |
| TCZ | Terminal Control Zone |
| TDOA | Time Difference Of Arrival |
| TOA | Time Of Arrival |
| UART | Universal Asynchronous Receiver Transmitter |
| UAV | Unmanned Aerial Vehicle |
| USB | Universal Serial Bus |
| UWB | Ultra Wide Band |
| VM | Von Misses stress |
| VP | Vice President |
| WBS | Work Breakdown Structure |
| WLAN | Wireless Local Area Network |
| WUR | Wageningen University of Research |

## Greek symbols

| | | |
|---|---|---|
| $\alpha$ | Angle camera makes with the horizontal or vertical axis | [rad] |
| $\alpha$ | Angle of attack | [deg] |
| $\alpha_b, \alpha_w$ | Coefficients for bearing and winding failures | [s] |
| $\alpha_e$ | Heading estimation error | deg |
| $\alpha_{loc}$ | Local angle attack of the propeller | [deg] |
| $\beta$ | Angle camera makes with the optical axis | [rad] |
| $\beta$ | Roll angle made when blower is on | deg |
| $\delta$ | Beam deflection | [mm] |
| $\delta_d$ | Depth error | [m] |
| $\delta_z$ | Pixel error | [pixel] |
| $\eta$ | Line lift coefficient with angle of attack | [-] |
| $\lambda_P$ | Rate of failure | [1/s] |
| $\lambda_{c/s}$ | Half chord sweep angle | [deg] |
| $\mu$ | Dynamic viscosity | [kg/m·s] |
| $\mu$ | Mean of the normal distribution | [-] |
| $\nu$ | Kinematic viscosity | [$m^2$/s] |
| $\omega$ | Angular velocity | rad/s |
| $\omega_f$ | Forced frequency | Hz |
| $\omega_n$ | Natural frequency | Hz |
| $\omega_{ss}$ | Steady state RPM | [RPM] |
| $\phi$ | Angle between axial and tangential flow velocities | [deg] |
| $\phi$ | Azimuth angle in spherical coordinates | [deg] |
| $\psi$ | Flow velocity potential | [-] |
| $\rho$ | Air density | kg/m$^3$ |
| $\rho_a$ | Ground-truth value of the range | |
| $\rho_r^b$ | Observation range between the beacon and the drone | |
| $\sigma_x$ | Bending stress | Pa |
| $\sigma_{yield}$ | Yield stress of the material | MPa |
| $\tau$ | External torques | Nm |
| $\tau_{zx}$ | Shear stress in the zx-plane | Pa |
| $\theta$ | Pitch angle | $[deg]$ |
| $\theta$ | Polar angle in spherical coordinates | [deg] |
| $\zeta$ | Damping ratio | - |

## Roman symbols

| | | |
|---|---|---|
| $\ddot{x}$ | Acceleration component | m/s$^2$ |
| $\Delta$ P | Pressure losses | [Pa] |
| $\Delta_{pix}$ | Variation in pixel pitch | $[pixel]$ |
| $\dot{y}, \dot{x}$ | Velocity components | m/s |

| | | |
|---|---|---|
| $\hat{R}_d, \hat{G}_d, \hat{B}_d$ | Color values | [-] |
| $\hat{x_r}$ & $x^b$ | Positions of the receiver (the drone) and the beacon, respectively | |
| $\hat{x_r}, \hat{x}^b$ | Tag and beacon position | [m] |
| $\overline{c}$ | Chord length | [m] |
| $\overline{z}$ | Distance to neutral axis | m |
| $A$ | Cross section area of the duct | $[m^2]$ |
| $a$ | Acceleration | [m/s$^2$] |
| $a$ | Parameter in the Squire jet solution | [-] |
| $A_e$ | Exhaust cross sectional area | [m$^2$] |
| $A_{i,j}$ | Matrix where each row corresponds to the measurement of a tag | [-] |
| $a_x$ | Acceleration in x direction | [m/s$^2$] |
| $a_y$ | Acceleration in y direction | [m/s$^2$] |
| $AR$ | Aspect ratio | [-] |
| $B$ | Number of propeller blades | [-] |
| $b$ | Baseline | m |
| $b$ | Distance to the half-velocity point | [m] |
| $C$ | Transformation matrix | - |
| $c$ | Circle of confusion | [m] |
| $c$ | Damping coefficient | kg/s |
| $C_D$ | Drag coefficient | [−] |
| $C_d$ | Local drag coefficient | [-] |
| $C_L$ | Lift coefficient | [−] |
| $C_l$ | Local lift coefficient | [-] |
| $C_T, C_Q$ | Thrust, Torque coefficient | [-] |
| $C_{L_\alpha}$ | Lift slope | [1/deg] |
| $D$ | Diagonal measure of a camera format, film, sensor, or print | [m] |
| $d$ | Characteristic length | [m] |
| $d$ | Distance between the lens and the object | - |
| $d$ | Nozzle outlet diameter | [m] |
| $D_h$ | Hydraulic diameter | [mm] |
| $D_N, D_f$ | Distance from the camera to the near/far limit of DOF | [m] |
| $E$ | Young's modulus | Pa |
| $F$ | External forces | N |
| $F$ | Jet force in the origin | [N] |
| $f$ | Focal length | m |
| $f$ | Vortex shedding frequency | [Hz] |
| $F_z$ | Resultant force in the Z direction | N |
| $F_x$ | Sum of the forces in x direction | [N] |
| $F_y$ | Sum of the forces in y direction | [N] |
| $g$ | Gravitational constant | m/s$^2$ |
| $I$ | Inertia matrix | m$^4$ |
| $I_x$ | Object dimension | $[pixels]$ |
| $I_{xx}$ | Area moment of inertia about x | m$^4$ |
| $I_{yy}$ | Area moment of inertia about y | m$^4$ |
| $I_{zz}$ | Area moment of inertia about z | m$^4$ |
| $J_m$ | Moment of inertia | m$^4$ |
| $k$ | Stiffness of the material | nm/rad |
| $K_c, K_p, K_{cr}$ | Gain values | [-] |
| $L$ | Beam length | [m] |
| $L$ | Distance between the lens | [m] |
| $L_d$ | Lumninance | $[cd/m^2]$ |
| $L_p$ | Sound pressure level | dB |
| $L_0$ | Distance from object to lens | [m] |
| $L_{beam}$ | Length of the beam | mm |
| $m$ | Magnification factor | [-] |
| $m$ | Mass of the drone | $[kg]$ |
| $m_{battery}$ | Mass of the battery | kg |
| $m_{motor}$ | Mass of the motor | kg |
| $M_y$ | Moment around the y-axis | Nm |
| $N$ | F-stop | [-] |
| $p$ | Wetted perimeter | $[m]$ |
| $P, Q, R$ | Roll, Pitch, Yaw rate | [rad/s] |
| $P, Q, R$ | Aerodynamic forces | N |
| $p_0$ | Reference, Ambient sound pressure | Pa |
| $P_{cr}$ | Period of critical sin wave | [1/s] |
| $Q$ | Second moment of area | mm$^3$ |
| $r$ | Radius in spherical coordinates | [m] |
| $r_{1/2}$ | Effective jet radius | m |
| $Re$ | Reynolds number | [-] |
| $S$ | Jet spread | [-] |
| $S$ | Surface area | [m$^2$] |
| $s$ | Disparity | m |
| $s$ | Distance covered | [m] |
| $St$ | Strouhal number | [-] |
| $T$ | Temperature | [° |
| $T$ | Thrust | N |
| $t$ | Total trip time | [s] |
| $T_{1,2,3,4}$ | Torques | Nm |
| $t_{acc}$ | Time of acceleration | [s] |
| $T_{cr}$ | Period of critical sin wave [] | |
| $u$ | Flow velocity in x-direction | [m/s] |
| $U, V, W$ | Velocity components | m/s |
| $u_0$ | Jet outlet velocity | [m/s] |
| $V$ | Air speed | [m/s] |
| $V$ | Velocity | [m/s] |
| $v$ | Flow velocity in y-direction | [m/s] |
| $V_0$ | Initial velocity | [m/s] |
| $V_c$ | Cruise speed | [m/s] |
| $V_e$ | Nozzle exit velocity | [m/s] |
| $V_i$ | Induced velocity below the propeller | [m/s] |
| $V_z$ | Shear force | N |
| $W$ | Weight | N |
| $w$ | Distributed load | [N/m] |
| $x, y, z$ | Position components | m |
| $z$ | Depth | m |
| | Volumetric mass flow | [m$^3$/s] |
| D | Drag | [N] |

# 1 Introduction

Pollination is the process of reproduction in plants, which allows plants to bear fruits and vegetables. In this light, the process of pollination has received much attention in the field of agricultural studies. A number of problems loom over modern horticulture. The most important of which is a shrinking bee population. This is a current and ever-growing problem. It has necessitated the search for alternatives to the natural process of bee pollination, such as manual pollination and mechanical pollination by a device. The effectiveness of natural pollination is further decreased in greenhouses. Although the greenhouse serves as a means of protection against adverse conditions, greenhouses are also a structural barrier that means the natural process of pollination is hampered.

For the purposes of mass production, manual pollination is not cost effective. As a result, the industry has been looking for engineering solutions that would take the place of human effort. One such possibility is the use of aerial vehicles, in particular micro air vehicles, to pollinate flowers. Thanks to their relatively small size, agility and the possibility for complete autonomy, they could keep the need for human intervention at a bare minimum.

The aim of this design synthesis exercise is to propose such a solution. Therefore the mission need statement is: "A micro air vehicle is needed to ensure that the pollination process is performed for the plant species where the natural mechanisms are insufficient, endangered or ineffective." During the design phase a planning, a preliminary investigation of technical aspects and several design options for different subsystems are treated. Furthermore a proposal for three concepts was made, which were investigated separately. Finally a trade-off was performed which resulted in a choice for one concept, which is elaborated in detail in this report.

The structure of the report is as follows. First, the market analysis is deliberated in Chapter 2, after which the mission overview is presented in Chapter 3. The services associated with the design, operations and logistics are shown in Chapter 4. Hereafter, the subsystem design ensues. Literature on the pollination process has been examined and is used to design the payload which is done in Chapter 5, the payload implementation is discussed in Section 5.3. This is followed by the design of the propulsion and power subsystem, the electronics, the navigation subsystem, the structure and the control and stability subsystem are presented in Chapter 6, Chapter 7,Chapter 8, Chapter 9 and Chapter 10, respectively. The technical diagrams including the software and hardware diagrams are presented in Chapter 12. With all the aspects of the design of the drone itself explained, the final configuration of the design is summarized in Chapter 13. Upon doing that, the reliability, availability, maintainability and safety are presented in Chapter 14. This is followed by a chapter on the details of manufacturing, assembly, and integration plan shown in Chapter 15. A risk assessment and mitigation plan is then described in Chapter 16. The sustainability of the design and the facilities is examined in Chapter 17. A sensitivity analysis is conducted in Chapter 18. Finally, the aspects of the project management involved in the project are delved into in Chapter 19.

# 2

# Market analysis

Before launching any new product, a market analysis should be performed to investigate whether or not the market is ready for such a product. General trends of important factors will be provided and analyzed. From this, it will be determined whether or not there is actually a need for the product. Moreover, the competition will be briefly looked into and the ideal customer will be depicted. A SWOT analysis is a market analysis tool that will also be used.

## 2.1. SWOT analysis

A SWOT analysis regarding the product-market combination has been made and applied to the pollinator drone company. The SWOT analysis helps the team with identifying beneficial circumstances and opportunities than can be utilized. At the same time, the SWOT analysis is a useful tool for discovering potential threats and risks well in advance such that precautions can be taken. The SWOT analysis can be seen in Figure 2.1.

## 2.2. General trends

The general development trends of the apiculture (beekeeping) and pollination market drivers will be addressed in the current section.

### 2.2.1. Apiculture

The global apiculture market is expected to grow at a compounded annual growth rate (CAGR) of 2.7% from 2015 to 2022 [1]. Some of the drivers behind this growth are the demand for more healthy food as well as the increase in demand for more sustainable living. Environmental issues are also a major driver. However, it must be noted that this growth is restrained by the maintenance and protection costs of bees. In the long run, a drone system could therefore contribute to a further increase in the CAGR of the global apiculture market.

In greenhouses, pollination is typically performed by bumblebees. In 1985 is was found that this species is capable of efficiently pollinating greenhouse crops [1]. Since then, the market has grown explosively. Today, the "Bombis Terrestris" is used in almost all tomato greenhouses. It is estimated that in 2004 around one million colonies were sold. For this reason, this market is a billion dollar market [2]. If pollination through bumblebees would become insufficient or ineffective, the pollinator drone could step in the void. Bumblebee development is found to be rather high-tech. Certain species are bred and specialized guiding systems for bees are developed. In Section 2.3.1, an overview of the biggest bumblebee producers is given.

### 2.2.2. Pollinators

Pollination is done by a variety of insects. The main one insect remains the bee. They are extremely important when it comes to the maintenance of wild plant communities and agricultural productivity. The honey bee has been capable of increasing yields up to 96% in animal pollinated crops. However, 60% of the colonies have been lost in America between 1947-2005 and 25% has been lost in Europe between 1985-2005. In 2013 it was reported that 1 out of 3 hives did not survive the winter [3]. It is clear there is a decline in the amount of hives. Moreover, Insect pollination is directly required for 75% of all crops humans use for food. These are mostly fruit crops, as rice and wheat are usually pollinated through wind [4].

[1] http://www.einpresswire.com/article/352458218/apiculture-market-to-grow-at-a-2-7-cagr-forecast-to-2022?ref=rss&code=qlGkSB28TKD5u8mX [Cited 1 June 2017]

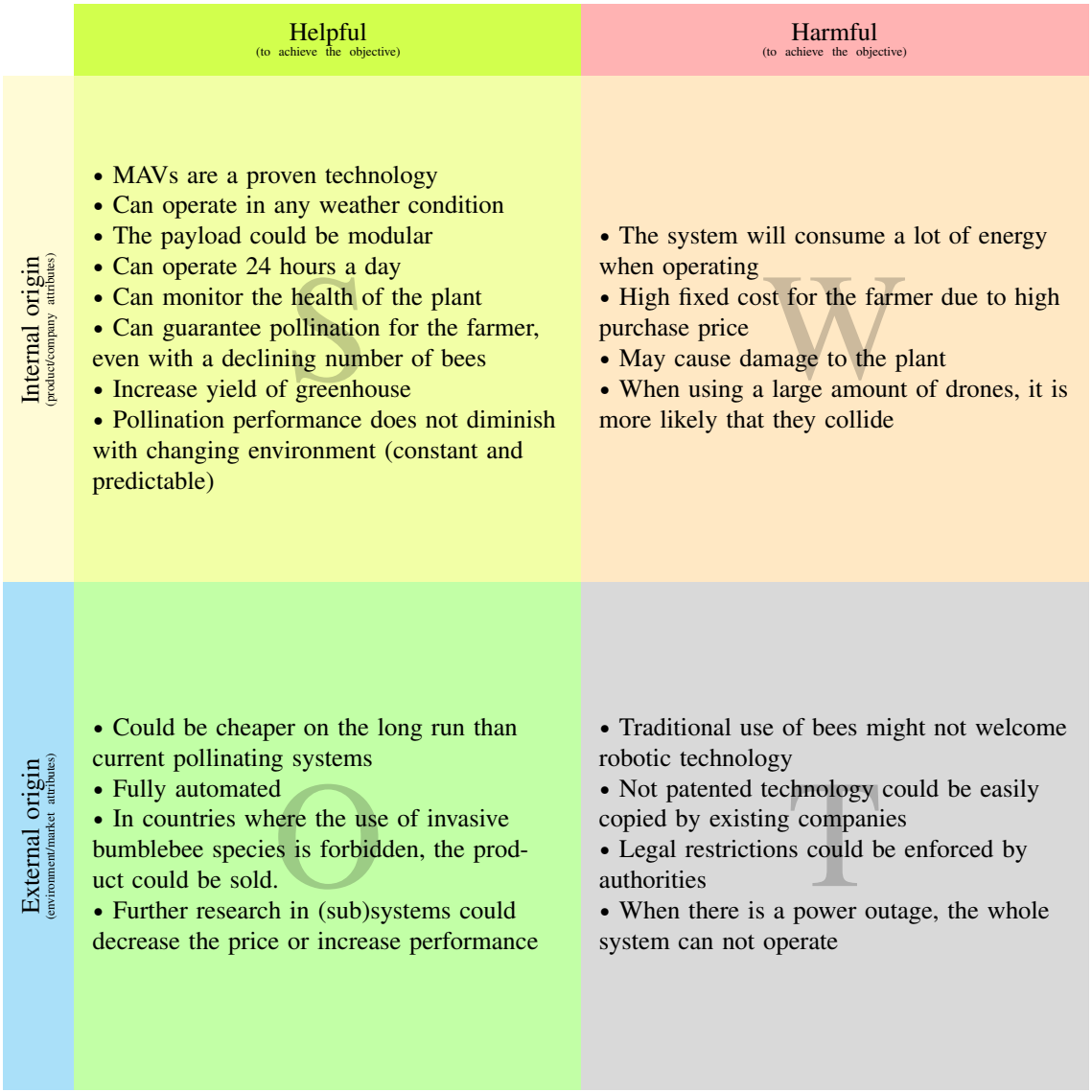


Figure 2.1: SWOT analysis

Pollinator dependant crops have increased since 1961. Their average yield increase over time is as high as non-pollinator-dependant crops. This is mostly due to the use of commercial pollinators (mostly bees) and the use of hand pollinators. The amount of pollinator-dependant crops has and is however increasing [4]. This means that the declining amount of pollinators will pose to be a problem in the future [5]. More commercial solutions will need to be found making a drone system interesting for the future.

### 2.2.3. Economic value

According to [1], a total of 40,000 hectares of tomato greenhouses use bumblebee pollination. The total value of these tomato crops is estimated to be 1,2 billion euros per year. The total world economic value of insect pollination was estimated at €153 billion in 2005 (approx 9.5% of total agricultural economic value). If insect pollination was to completely vanish a consumer surplus loss is estimated between €190 and €310 billion[2]. This negative effect would also translate differently on each crop type. According to a recent report [6], the total percentage loss, or as it is called in that report, vulnerability (ratio of insect pollination economic value (IPEV) to total economic value (EV)) was 23% for fruits, 12% for vegetables, 31% for nuts, 16% for edible oil plants and 39% for stimulants. Other crops such as cereals and spices would not really suffer with the disappearance of insect pollination. The loss of pollinators would therefore be fatal and alternatives such as the pollinator drone are needed to ensure pollination does not fully vanish,

[2] https://www.sciencedaily.com/releases/2008/09/080915122725.htm [Cited 1 June 2017]

if bees do. Furthermore, the economic value of pollination is dependant of the geographical location considered. The insect pollination economic value per region can be found in Table 2.1 [6].

Table 2.1: Insect pollination economic value (IPEV) per geographical region and vulnerability of the considered region [6]

| Geographical region | IPEV ($\cdot 10^9$ €) | Region vulnerability (%) |
|---|---|---|
| Africa | 11.9 | 8 |
| Asia | 89.4 | 10 |
| Europe | 22.0 | 11 |
| North America | 14.4 | 11 |
| South and Central America | 15.1 | 6 |

This data suggests that some regions are more dependent on insect pollination methods than other. This includes Asia, and Europe. Some regions are also vulnerable to the disappearance of insects. The regions that will be mostly affected are Europe and North America with each 11%. They might therefore be more interested in future solutions and alternatives such as the pollinator drone.

## 2.3. Competitor analysis

There are three key players on the pollination market that need to be considered. The dominant ones are companies that provide pollinators for greenhouses. As stated earlier, the bee-pollination is the most common pollination method used in agriculture. The second alternative is manual pollination. This method is rather uncommon, as it is relatively expensive and laborious. For some crops, however, it is the only available method. The last alternative is the drone pollination. There is a number of companies specializing in drone design that potentially would be capable of developing competitive pollinating drone once the business case proven to be profitable. Although it is not in industrial use yet the drone companies should be considered as key competitors as well.

### 2.3.1. Bee pollination

Global pollination market estimated to 153 billion euro worth [6]. Bee pollination is a serious competitor for the drone business case. The market is rather large and mature. Three big companies cover the most of the market share. Biobest is the first commercial producer and vendor of bumblebee colonies for agriculture. Koppert Biological Systems and Agrobio are two other big companies. The market of bumblebee pollinators is very competitive. No patents can be assigned to a natural species of bees. For this reason, companies compete on price, which decreases market prices.

Table 2.2: List of bumblebee producers

| Company | Country | Revenue [€] | # workers |
|---|---|---|---|
| Koppert Biological Systems | Netherlands | 180,000,000 [a] | 1,200 |
| Biobest | Belgium | 36,600,000 [b] | 440 |
| Agrobio | Spain | | |

[a] https://fd.nl/ondernemen/1150230/koppert-gaat-met-beestjes-en-microben-de-strijd-aan-met-chemiereuzen [Cited 1 June 2017]

[b] http://www.biobestgroup.com/nl/nieuws/biobest-genomineerd-voor-leeuw-van-de-export-2014 [Cited 1 June 2017]

### 2.3.2. Drone companies

Due to insufficient technology readiness, drones are not involved in pollination market yet. It is expected however that once the pollination with MAVs is proven possible and profitable, the drone companies might follow the trend and develop similar products relatively quickly.

A sample of drone manufacturers present on the market is made - small size, medium size and larger size companies are researched. The companies specializing only in drones like Prox Dynamics or Prioria Robotics are usually medium sized enterprises employing around 100 people. The revenues of this class of companies are in order of tens of millions euros. The main interest of those companies are solutions for the military sector. They often work in small projects for defence on government contracts. There are also few larger companies like Parrot SA. Their products are mainly

commercially oriented. That is why it is expected that the interest of such companies in industrial projects might be rather limited. Large global concerns like Lockheed Martin are also involved in UAVs development. Those companies however, are interested mainly in large scale projects contracted with governments. They are not expected to get involved into pollination business, and are therefore not considered as a direct competitor.

The players present on market are certainly capable of following and developing their own pollinating drone. Their interest however is in totally different branches. Naturally, companies that specialize in the greenhouse and agriculture business could also be interested in developing a drone. Their expertise in this field could be combined with the expertise of aerospace companies to develop a competitive and reliable vehicle on an industrial scale. Also, because of its early level of development, the emerging of new companies specializing in pollination drones could also be expected.

### 2.3.3. Manual pollination

Manual pollination is also used in several crops. Usually crops are hand-pollinated in case there is no other option. This is the case in south west of China in apple and pear orchards, where due to intensive use of pesticides bees do not pollinate. The drone pollination is not an option for these crops however, as the drone will be designed to operate in greenhouse. Another crop commonly pollinated by hand is vanilla. This process is very complicated and very labor intensive. On the other hand, vanilla prices are very high [3] (400 $ per kg). Currently, a large portion of vanilla cultivation happens in Madagascar. Pollination requires a lot of labor hours and the right climate conditions. In Madagascar labor is cheap and the climate is right. Research is performed to try to pollinate vanilla in greenhouses in other countries. Large scale development is hampered by high labor prices and large price fluctuations. A mechanical device could be a good solution for this problem. The challenge however lies in the state of the technology. In the past, greenhouse tomatoes were also manually pollinated by a vibrating device. Equivalent to this, a new automatic vibrating system was developed by Metazet/Formflex [4]. This system can be used in countries where insect pollination is not allowed or where it is too warm for insects to fly. The costs for this system are estimated to be between 1 and 1.50 euro per square meter. For a greenhouse of 1 hectare, the costs are between 10,000 and 15,000 euros.

## 2.4. Product competitiveness

In this section a preliminary estimation of the drone price will be made. This is needed in order to see whether the maximum of €500 per drone in only production costs is feasible. The drone system will be compared with bees and with manual pollination systems.

### 2.4.1. A comparison with bees

When looking at companies that sell bees, Planet Natural[5] was taken as a representative. They give the following guidelines: "Each hive consists of 45 to 60 workers and has an expected life span of 4-5 weeks. Covers up to 5,000 square feet". This means that 21 boxes are needed per hectare per 5 weeks. After talking with the company Jan van Marrewijk Tomatoes [6] , it was discovered that the pollination season lasts at least 35 weeks, which was verified at the greenhouse visit. 147 boxes are therefore needed per hectare per season. The price of a box is €145. The typical size of a greenhouse is 4 hectares. Using these values, the amount paid per season for pollination is around €85,260. Naturally, these numbers are not set in stone. The assumptions of lifespan and coverage can be subject to change. For example, on the website of Koppert [7], a lifetime of 8 weeks is mentioned. Also, the 5,000 square feet is dependent on the type of crop and the layout of the greenhouse. Finally, buying these boxes in bulk will decrease the price. For these reasons, the €85,260 can be considered as an upper limit. Once the total system price is determined, a return on investment analysis can be done. This is presented in Section 19.5.

### 2.4.2. A comparison with manual pollination methods

Costs of manual pollination are mainly the costs committed for the workers salaries. It is difficult to estimate how much time a worker needs to pollinate a single flower. Data on this issue is also scarce. Therefore, the costs are calculated for 3 different rates: 2, 5, and 10 seconds per flower. For those rates the number of flowers pollinated by a single worker in one day can be calculated. It is assumed that the work day lasts 8 hours. Next the number of workers needed to pollinate one hectare in one day can be obtained. Lastly, the total cost of workers for one 35 week long season are calculated. The

[3] http://rodellekitchen.com/img/site_specific/uploads/Rodelle_Vanilla_Market_Update_2017_web.pdf [Cited 1 June 2017]

[4] http://www.tomatennet.nl/tomaten/nieuws/nieuw-trilsysteem-wekt-veel-interesse/ [Cited 1 June 2017]

[5] https://www.planetnatural.com/product/bumble-bees-natupol/ [Cited 1 June 2017]

[6] http://janvanmarrewijk.com/overons.html [Cited 3 May 2017]

[7] https://www.natupol.com/why-natupol/our-best-bumblebees/longevity/ [Cited 1 June 2017]

salary is estimated from the statistics to be around 9.20 €/h[8].

Additionally the greenhouse owner needs to invest in electric pollinators. Prices of such a device vary from 30€to 300€[9]. Those costs however are 2 orders of magnitude lower comparing with labour costs, and therefore are not included in the estimates

In the most optimistic case - assuming it takes only 2 seconds for the worker to pollinate a flower the total costs of manual pollination for 1 season are about €16,100 per hectare. It is however more realistic that the costs will oscillate between values that are higher. Those costs need to be committed every season, and therefore the manual pollination is economically unfeasible.

Table 2.3: Estimated costs of manual pollination

| **Time to pollinate single flower [s]** | **Plants pollinated in 1 working day** | **Number of workers needed per hectare** | | **Cost of labour per season (35 weeks) per hectare** [€] | |
|---|---|---|---|---|---|
| | | **Lower bound: 3,000 plants/ha** | **Upper bound: 6,000 plants/ha** | **Lower bound: 3,000 plants/ha** | **Upper bound: 6,000 plants/ha** |
| 2 | 2,400 | 1.3 | 2.5 | 16,100 | 32,200 |
| 5 | 960 | 3.1 | 6.3 | 40,250 | 80,500 |
| 10 | 480 | 6.3 | 12.5 | 80,500 | 161,000 |

## 2.5. Customer

From the data found above, an attempt will be made to depict the ideal target customer. It is clear that the pollinator drone will be most interesting for farmers who own greenhouses. They are the ones who are currently buying or renting bees. With the increase in price of bees over the last years, some farmers might be interested in adopting a revolutionary technology as long as the price remains competitive. Other farmers who do not have access to bees will also be interested in this technology.

Preliminary estimations of the price show that the target customer should have a large amount of flowers in his fields. Indeed, if the drone is expected to pollinate a minimum of 500 flowers a day, the farmer should own a large field. Large commercial greenhouse farmers are therefore expected to be interested in the product, as opposed to local greenhouse farmers.

The crops that are most cultivated in the Netherlands are determined and listed in Table 2.4. This was done using the research done by Rabobank [7] which focuses on the importance of crops in The Netherlands. It showed that the most cultivated crops in greenhouses are:

Table 2.4: Most cultivated crops in the Netherlands with their current price in the supermarket

| **Vegetable** | **Quantity cultivated in 2016 [ha]** | **Current price** |
|---|---|---|
| Tomatoes | 1670 | 2.78 €/kg |
| Peppers | 1220 | 2.99 €/kg |
| Cucumber | 510 | 0.75 pp (approx 2.4 €/kg if weight of one piece is 0.312kg) |
| Strawberry | 320 | 5.73 €/kg |
| Eggplant | 120 | 3.16 €/kg |

In order to determine the most interesting crop to pollinate, the supermarket price of these vegetables and fruits has to be looked into. Using data provided by Albert Heijn, Table 2.4 can further be completed. The most interesting crop in the Netherlands is therefore the one that is the most cultivated and that is sold at the highest price. This is according to the provided data, the tomato.

[8] https://www.salaryexpert.com/salary/job/greenhouse-worker/netherlands [Cited 1 June 2017]

[9] https://www.gardenamerica.com/store/VegiBee-Garden-Pollinator-battery-powered-model.html [Cited 1 June 2017]

# 3

# Mission overview

This chapter gives a description of the objectives of the system. This includes the mission, the functional flow diagrams and the functional break down structure. It concludes with system sizing: estimating the number of drones and ground stations needed for pollinating a given greenhouse.

**Mission need statement** A micro air vehicle is needed to ensure that the pollination process is performed for the plant species where the natural mechanisms are insufficient, endangered or ineffective.
**Project Objective Statement** Make a proof-of-concept design of a fully autonomous pollinator micro air vehicle and its support systems, within 10 weeks' time and with a team of 9 students.

## 3.1. Mission description

As stated in Section 2.5, the plants that will be pollinated by the MAVs are tomato plants. A visit was paid to the Wageningen University & Research greenhouse in Bleiswijk, where some critical information about greenhouses was obtained. Tomato plants grow vertically within the greenhouse, supported by wires, with the flowers on top. This means that the MAVs should be able to pollinate from above. A greenhouse is typically 4 hectares and needs to be pollinated every 3 days. This means a swarm of drones is required in order to take care of the pollination of the whole greenhouse. Since the drones have a limited flying time, require guidance through the greenhouse and make use of autonomous charging, ground stations will be included as part of the system.

## 3.2. System sizing

The goal of this project is to pollinate all the flowers in a greenhouse every three days[1]. For calculating the number of drones that are needed for achieving this goal, parameters of a standard greenhouse should be known. These are the area of a green house, the numbers of plants per $m^2$ and the number of flowers per plant. The values for these parameters have been obtained by consulting the staff of the greenhouse of the Wageningen University during the group's visit there and can be seen in Table 3.1.

By knowing these parameters, the plants per greenhouse, row and meter could be calculated. On the same lines, the times assigned to each task also impact the number of drones. An overview of these can be found under Table 3.2. Coming from the navigation subsystem, the detection time and the time to go from one flower cluster to the next one could be estimated. The speed in which APIS will scout in the row is currently set to 0.5 m/s. This speed follows from a requirement of at least 5 frames for each flower cluster. A more comprehensive discussion can be found in Chapter 6. Taking an estimated distance between clusters of 42 cm, a travel time between clusters of around 0.9 s was found. Closely related to this, is the detection time, which is the time allocated to detect the flower once the location of the cluster has been reached. It has been estimated to be 1 second, which translates to 15 frames at the current examination rate of 15 fps, a more in depth discussion can be found in Chapter 8. With a combined input from the payload and navigation subsystems, the time assigned for blowing on the plant and for drone positioning was determined. Nonetheless, the performance times are not the only variables stipulating the number of drones. In fact, the duration of the mission or the time spent on charging also prove to be key when sizing the swarm. A more elaborate discussion can be found in Chapter 6. The current time allocated for the mission cannot exceed 10 min and 30 s for battery capacity and lifetime issues. For this, the battery is designed to charge for 15 min.

[1] Contact with expert: Anja Dieleman, Wageningen University & Research

Table 3.1: Greenhouse parameters

| Parameter | Value |
|---|---|
| Width of corridor | 1.6 m |
| Width of greenhouse | 200 m |
| Length of greenhouse | 200 m |
| Plants/$m^2$ | 3 |
| Flowers/plant | 6 |

Table 3.2: Time parameters for the mission with direct impact on the number of drones

| Parameter | Value [s] |
|---|---|
| Detection | 1 |
| Positioning | 4 |
| Flower blowing | 6 |
| In-between cluster travelling | 0.84 |
| Total flight time | 630 |
| Charging time | 900 |

On a higher mission level, when APIS enters the half-row it has to pollinate, it will start pollinating the right side of the half-row as the camera for flower detection is located at the right side of APIS as will be seen later. When almost half of the battery is depleted, APIS will turn around to now pollinate the flowers on the other side of the half-row while simultaneously returning to the ground station. Since one drone will not be enough to pollinate an entire row, it will communicate to the ground station how far it has made it, to ensure that the next drone will not pollinate the same flowers. The next drone will first fly to the location that was communicated to the ground station by the previous drone and will then start pollinating from that location onward. This process will be repeated until the specific row has been completely pollinated. Important to note is that several rows will be pollinated at the same time through this process.

Taking all of the above into account, it was determined that the number of drones which are strictly needed to pollinate the entire greenhouse is 58. Nonetheless, as it will be subsequently argued, the required number of ground stations with capacity of 8 drones has to be an integer number, so at least 8 ground stations are needed. These will be filled up, adding up to 64 drones. The margin of 6 extra MAVs will help bypass the inherent risks of being unable to fulfill the mission due to a malfunction of one or several drones.

## 3.3. Functional flow diagram (FFD)

In the functional flow diagram, the functions that need to be performed by the system are displayed in a chronological order. The most general system description is called the top level of the FFD and contains setting up the system, turning the drone on/off, operating the drone, checking the performance of the drone and performing maintenance to the drone. In the second level of the FFD, the operation of the drone is elaborated. Roughly, it is split into the take-off from the docking station, movement to the flowers, searching and approaching of the flowers, pollination and imaging of the flowers and checking the health of the drone. Finally in the third level, flying to starting position, searching the flower, detecting the flower, approaching the flower, and pollinating the flower are even further elaborated. Flying to the starting position involves a sequence of tasks starting with take-off determining the attitude, adjusting the attitude, and processing the video for obstacle avoidance. In case of obstacle detection, the drone will alter its path. Otherwise, the drone keeps on flying. Searching for a flower entails running the vision algorithm and checking for a stable detection. If a detection is obtained, then the flower can be approached. Otherwise, the process is repeated. A visual representation of this can be found in Figure 3.1.

## 3.4. Functional breakdown structure (FBS)

To group and further elaborate the functions found in the functional flow diagram a functional breakdown structure is created. Not only the behaviour of the drones during operation will be explained but also the the maintenance process will be discussed. All the drones should be checked after a certain time to make sure that the drones still have a sufficient performance. The aspects that will be checked during scheduled performance check are: the structure, the sensor calibration, the communication system, the propulsion system and if the drone is still operating (otherwise it might be stuck somewhere). If a subsystem is broken or not working well, the drone will be repaired by the user using maintenance instruction manuals or by a technician as will be explained in Chapter 4. The work breakdown structure of all the functions can be seen in Figure 3.2.

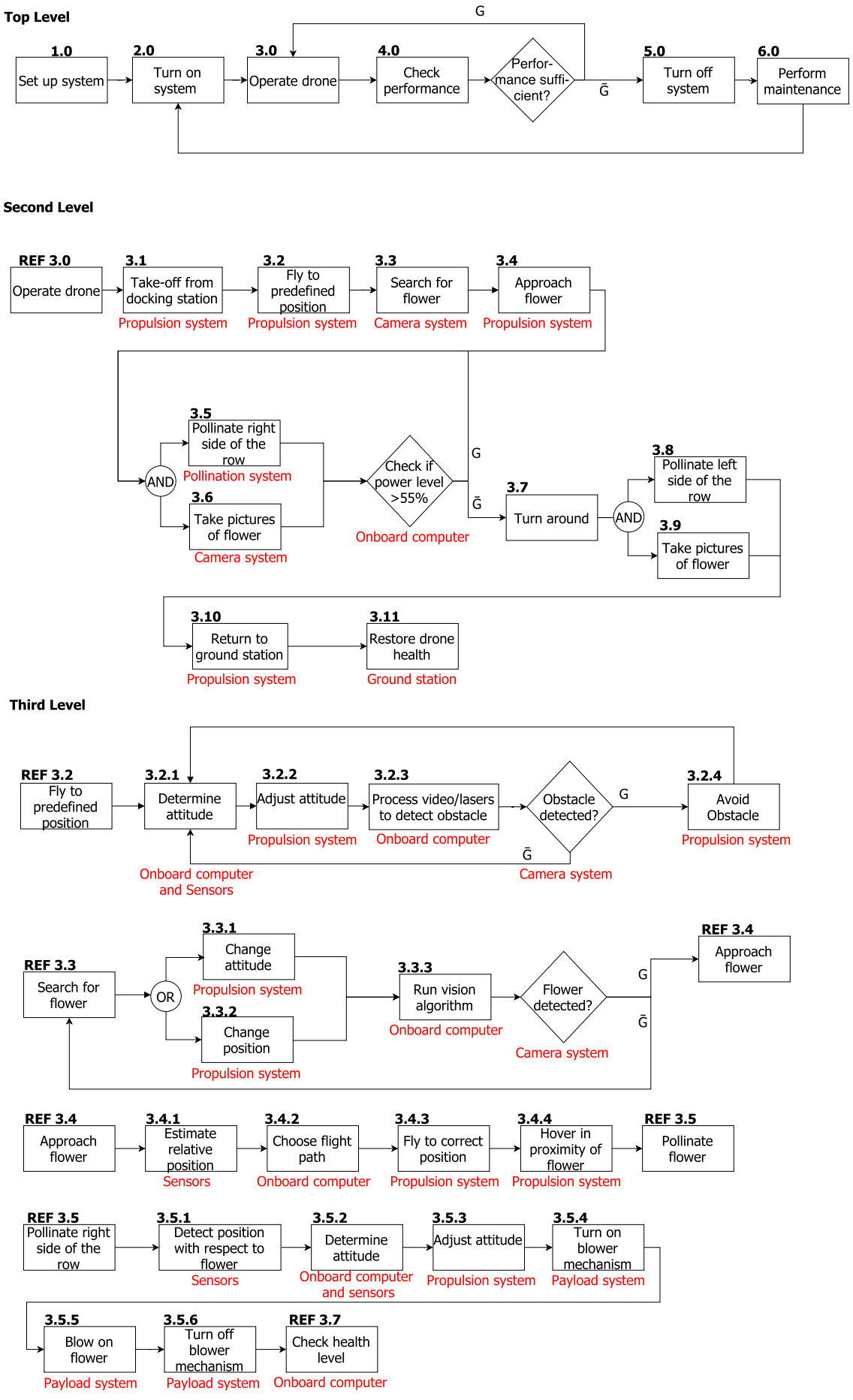


Figure 3.1: Functional flow diagram of operating the drone

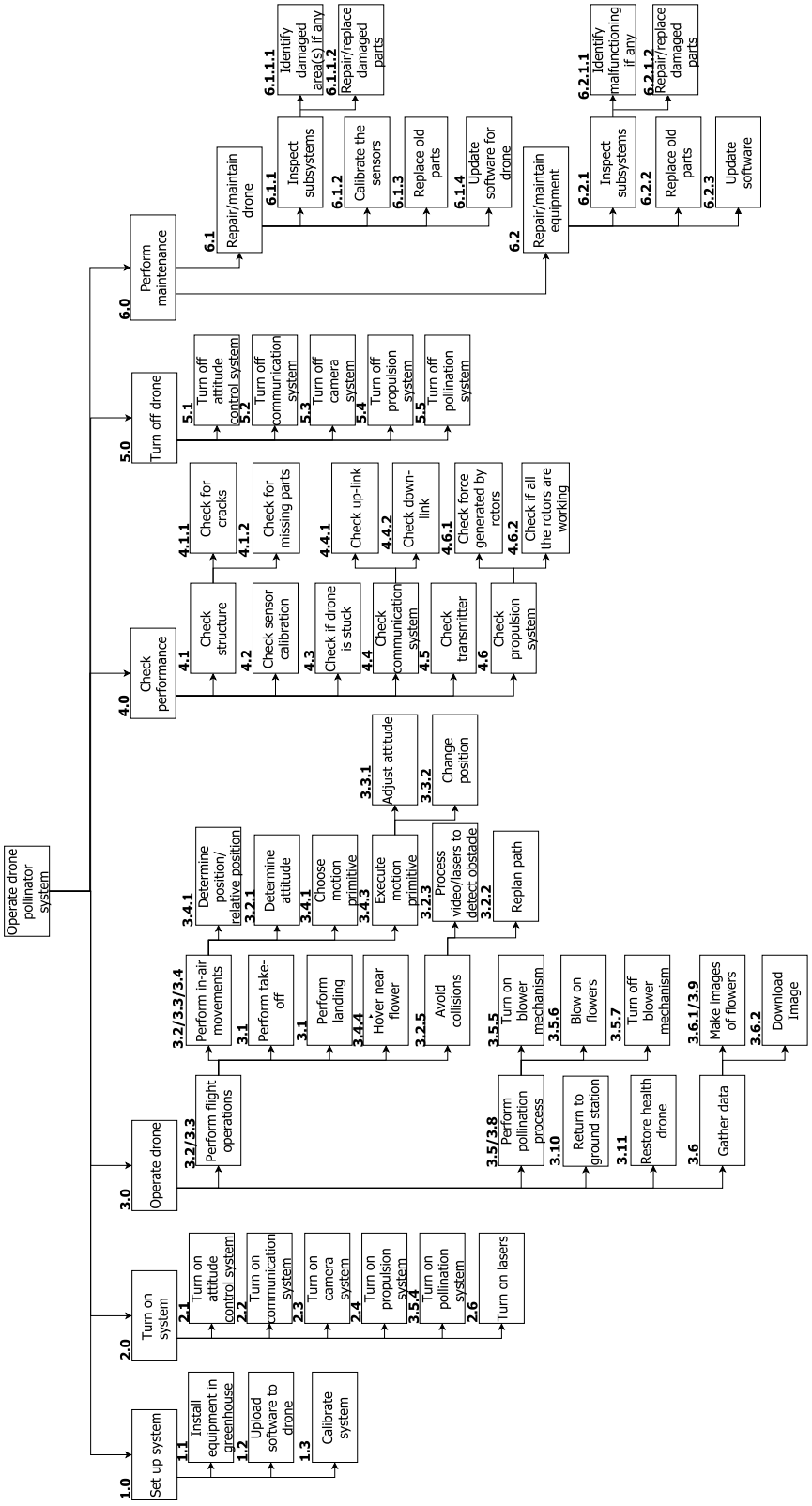


Figure 3.2: Functional breakdown system of the complete system

# 4

# Operations and logistics

In this chapter, first, the documentation that will come with the system will be explained. After that, the transportation of the system to the greenhouses will be addressed. Finally, the operations of the system will be elaborated upon.

## 4.1. Documentation

Each MAV and each ground station will come with a documentation that contains the parts and the owners guide. The latter will explain how to set up the product and how to use it.

**Part list**

The ground station and the drones will be packaged individually. The ground station package will contain the landing pads (8), the main strut (1), the bolts to attach the landing pads (16), the attachment pin to the structure (1), the cables needed (1 power cable + any other cables ordered) and a black box (1). The drone package will contain the drone, the payload and the batteries (12) that are needed to go through an entire season. A special case (1) will also be provided where the empty batteries can be stored in. A final package that contains the emergency system will also be shipped separately.

**Owner's guide**

An owner's guide will be included with each product that is shipped. It will contain the safety instructions, assembly instructions, installation instructions, instructions on how to use the product once installed, maintenance instructions, service locations, a regulatory code of compliance, the technical specifications of the product and finally the warranty.

The safety instructions will provide information on how to safely operate the system. Even though the MAV will be capable obstacle avoidance, the owner should be aware that the drone must be operated in certain conditions. The drone is indeed only limited to indoor usage and more specifically, greenhouse usage. The amount of open windows should be limited in order to minimize air currents that could disturb the drone. Additionally, the user should not be in proximity of the MAV when it is pollinating a flower as the airflow generated by the wake or at the nozzle could result in possible eye injuries. Infants and children under the age of 5 should not use this product nor be close to it.

The assembly instructions will explain how to assemble the various parts. If the product is purchased for the first time, a technician will come to help install the entire setup.

The installation instructions will cover how to get started once the owner is in possession of a least one MAV and one ground station. The installation of the ground station to the rest of the greenhouse will be explained. More information regarding the contents in this part can be found in Section 4.3. The instructions on the use of the MAV are also covered in this section. The maintenance of the drone is covered in Section 4.4.

Finally the warranty will also be provided. This document contains the assurance that repairs or replacements will be made free of charge. The warranty period lasts for 1 year, which is the equivalent to one pollination season. After that the user can decide whether he wants to purchase additional 1 or 2 year warranty packages.

## 4.2. Transport

Transportation of the entire system must be considered given that some greenhouses are located in remote locations. This will be arranged for the ground stations and for the drones.

Each ground station is composed of eight landing pads that are 40x40x5cm and of a main strut that is 4x4x100cm. 16 screws will also be included to attach the landing pads to the main strut. The electronics box has dimensions of 10x15x5cm and weighs 300grams. This means that a minimum volume of 0.0663 $m^3$ is needed per ground station

package. With additional protective wrappers such as foam, the package dimensions of one ground station mount up to approximately 0.072 $m^3$. The mass of the package will be pproximately 13.5kg. This includes the 13kg of the ground station, the 110g of foam, the cardboard box and a power cable. The box will have a length of 105cm, a width of 45cm and a height of 15cm.

The drones have a dimension of 28.4x29x7.62cm and weigh 250 grams. Each drone will have its own box. The drone will be shipped along with the batteries it needs to operate for the full season. This means 12 batteries that weigh 100g will also be provided. They will be placed in a special case where after usage they should be replaced back in. The total package will weigh 2kg. Foam will be used as protection. The box will have dimensions of 60x30x20cm.

The drones and the ground stations will be shipped individually by standard UPS mail unless an entire setup is bought for the first time. In that event, the amount of groundstations needed and the amount of corresponding drones will be shipped by truck to the greenhouse. A technician that knows how to set up the system will also be present. He will be responsible to calibrate the entire system for the first time, attaching the ground station to the structure, and initializing the rest of the system. A ModiForce [1] van will be used to ship the parts. The vans can be customized to fully accommodate the installation procedure that will be followed.

## 4.3. Operations (set up)

This section will describe how to set up the systems, the user interface and what to do in emergency situations.

**Setting up the system**

The first step of the application of the pollinator drone design in a greenhouse is the installation of the support system, consisting of the charging stations and anchors that will be placed at the beginning of the operation. For the final system, a certain number of ground stations is needed.

For the design case, 8 grounds stations are needed for a 200x200m greenhouse when a corridor runs through the middle separating each row in two. The ground stations will be placed at regular intervals in the corridor. Before placing them in the corridors however, they have to be assembled. The landing pads have to be screwed onto the main strut by using the screws provided. The power cables that connect each pad are then passed through the strut. When this is done, the ground station can be attached to the structure of the greenhouse. A special device will be used that varies depending on the beam geometry of the roofing of the greenhouse. Once the ground station has been securely attached, the cables can be connected to the electronics box that will rest on top of the beams of the structure.

With the ground station now secured to the structure of the greenhouse, the drones can be placed on the docking station. Attention must be paid to properly position the drones on the charging pad. The front part should point towards the main strut and the blower should point towards the side marker.

The system has to now be set up. Into the user interface, data regarding the greenhouse has to be manually inputted. Information about the relevant parameters is presented in the next subsection. All these details will, however, be performed by the technician who comes to set up the system. Only in case a separate ground station is bought, the procedure should be carried out by the client. He can be guided through the steps by visual and audio support or can ask a technician to come. The latter will come at a cost.

Once the software is set-up the emergency button has to be placed in the greenhouse as well. Together with the greenhouse owner, this location will be chosen as it should be easily accessible yet should not be in the way of the daily operations. A final aspect that should be adjusted before usage is the place of the visual marker hanging from the ground station. It should be adjusted to the row height of the plants. Every time this row height changes, the height of the visual marker should also be adjusted. The system is now ready for use. Unless specified otherwise, the default operational time is set to 12h. This can, however, also be changed in the user interface.

**The user interface**

The user interface will be where the main setup of the system will take place. It will also display health data of the drone, and the flower images that have been taken by the drones and transferred to the ground station, can also be accessed through it. More information about the data gathered can be found in Section 11.5. Here, the focus will be more on the parameters that affect the performance of the entire system.

Firstly, as explained above, data about the greenhouse has to be inputted. This is because the sections that a drone has visited will be registered and in order to direct the drone to a new section of the greenhouse, the ground station must know where that section is. Therefore, the 3D coordinates of the ground stations, the position in the x-y plane of each row, the maximum height of the greenhouse and the length of the rows should be provided. The width of the rows and of the corridors should also be provided. Data regarding the performance of the system can also be set. This includes

[1] `http://www.modiforce.com/en/mo` [Cited 26 June 2017]

for example adjusting the operational time.

**Emergency situations**
Emergency situations can arise with any system due to predictable or unpredictable circumstances. The predictable risks have been identified and mitigation plans are set up in Chapter 16. Not all are however completely gone. It is therefore important to have an emergency system. Two types of emergency systems are available.

The first is an emergency system integrated in the web interface. It is an emergency system that should only be used when needed. All the drones will attempt to go back safely to the ground station and land on the charging pad. They will not be damaged. The time to perform this entire operation can take a couple of minutes as air traffic around the ground station will still be respected in order to not damage any components.

If a faster emergency system is needed, a physical red button that is placed at a strategic place in the greenhouse can be pressed. The ground stations would stop communication with the drones and they all fall to the ground in a controlled manner. More information about these safety procedures can be found in Section 14.4.

## 4.4. Inspection and maintenance

Three types of maintenance will be considered: reactive, preventive and predictive maintenance. A description of each type will be provided, and the reasons as to why one was selected over another will be given.

Reactive maintenance, also called breakdown maintenance, is the repair of the system once it is broken down. It focuses on restoring parts back to its original state [8]. Maintenance plans that rely on this method usually cost more as it is usually not known when the system will breakdown. The life expectancy of the system is also lower. Reactive maintenance plans do however require lower initial costs as repairs are only done at the end. No time is spent on planning the repairs as these happen in an unpredictable way. The life cycle of the system being very important - partly also for sustainability - was the major factor that led to not using a reactive maintenance plan. A more proactive maintenance plan is needed.

A preventive maintenance plan is already a lot more interesting. The system is inspected on a periodic basis and repairs are carried out at fixed time intervals. The life expectancy of the system is increased and research has also shown that it can be up to 18% cheaper than a reactive plan [2].

Another type of plans that is more proactive are the predictive maintenance plans. In this type, attempts are made to predict failure before they happen. This is done by looking at some measurements taken by the drone. Catastrophic failures are reduced through this method. The life cycle of the system is also increased but the initial investment cost is larger as the necessary tools must be set up properly.

A preventive maintenance plan was created for the batteries and should be meticulously followed by the user. Predictive plans are also set up for the motors. A calibration procedure for the IMU is also done. Finally a preventive plan is also set up for the ground station.

**Battery replacement procedure**
***Goal*:** This procedure will guide the user on how to replace the batteries of the drone. The batteries are 1500 mAh 2S1P and can sustain 900 cycles of 27 mins (12 mins flying and 15 mins charging). Bearing in mind that APIS will pollinate for 12 h a day, this adds up to a maximum of 32 days without replacement, however 1 month seems a more suitable time span to replace them. A predictive maintenance plan is provided that explains how to properly and safely replace the batteries. The old batteries will be placed in the storage kit that will be sent back at the end of the season to the supplier such that they can properly be recycled.
***Timeline*:** Perform this operation every 1 month for every drone.
***Tools needed*:** 1 new fully-charged Li-Po graphene 1.5 Ah 2S1P battery, the storage kit.
***Instructions*:**

1. Identify the drone that needs its battery replaced. This can be done by looking at the interface as data about the drone health is collected there.
2. Once the entire system is at rest, take the drone from the charging pad. Bring the drone to ground level such that the operation can be performed in a safe manner.
3. Take the main casing off the drone. This can be done by squeezing it off.
4. Remove carefully the blower. The battery should be visible inside the case underneath.
5. Unplug the battery and place the old battery in the storage kit where the used batteries should be placed.
6. Before placing the new battery, a check for dead cells with a voltmeter has to be done. The indicated voltage should be at 7.4. If the voltage shown is 3.7, one of the cells is defect and the battery should not be used.

[2] `http://www.uesystems.com/mechanical-inspection/the-4-basic-maintenance-modes` [Cited 25 June 2017]

7. Connect the new battery and place the casing back around it. Place the blower back on top as well as the main casing. A clicking sound must be heard to ensure the casing is properly attached.
8. Place the drone back onto the charging pad in the right direction: the front side should be facing the main beam of the ground station and the side with the blower should be facing the visual marker on the right side of the charging pad.

**Motor health procedure**
***Goal*:** This procedure will guide the user on how to get the largest life cycle out of the motors of the drone. The motors are DYS BX1306 and have a lifecycle of 35,000 h. The motors are on for 296.5 mins during a 12 h day which means that they should be replaced every 19.5 years. This is, of course, only if they are properly maintained.
***Timeline*:** Perform this operation every 1 month for every drone.
***Tools needed*:** WD-40 spray, result sheets on thrust vs current needed.
***Instructions*:**

1. Gather the sheets that show the current needed for take-off.
2. If an increase in current consumption larger than 5% with respect to the initial value is noted, investigate the drone in question. Given that an increase in 5% would already result in an increase of DoD of the battery to 83.3%, heavily damaging battery lifetime.
3. Once the entire system is at rest, take the drone from the charging pad. Bring the drone to ground level such that the operation can be performed in a safe manner.
4. Take the WD-40 spray and apply in small quantity to the four motors.
5. Place the drone back onto the charging pad in the right direction: the front side should be facing the main beam of the ground station and the side with the blower should be facing the visual marker on the right side of the charging pad.

**Motor replacement procedure**
***Goal*:** This procedure will guide the user on how to replace a motor of a drone. The motors are DYS BX1306 and should only be replaced in case of physical damage as the expected life cycle is 18 years. If replacement is needed, the old motor will be placed in the storage kit that will be sent back at the end of the season to the supplier such that it can properly be recycled.
***Timeline*:** Perform this operation when the motor is broken or when the current consumption is larger than 25% of the initial value. As this would mean an increase to 97% DoD of the battery, which would affect the battery lifetime and puts into serious risk the mission accomplishment, as with this DoD no agile maneuvers can be performed anymore, given the small battery capacity left (barely 1.2 kJ out of the total 40 kJ of the full battery).
***Tools needed*:** 1 new DYS BX1306 motor, the storage kit, an imbus for 3 mm screws.
***Instructions*:**

1. Identify the drone that needs the motor replaced.
2. Once the entire system is at rest, take the drone from the charging pad. Bring the drone to ground level such that the operation can be performed in a safe manner.
3. Remove the protective covers.
4. With the imbus, carefully remove the screws that attach the motor to the structure.
5. Place the new motor on the structure and put screws back in. Make sure the screws are tightly secured.
6. Place the drone back onto the charging pad in the right direction: the front side should be facing the main beam of the ground station and the side with the blower should be facing the visual marker on the right side of the charging pad.

**IMU calibration procedure**
***Goal*:** This procedure will guide the user on how to calibrate the IMU of the drone. This should be done to reduce errors or inaccurate measurements.
***Timeline*:** Perform this operation when using the product for the first time, in case of any software/hardware upgrades or if alert has been given by main computer.
***Tools needed*:** N.A.
***Instructions*:**

1. Before starting calibration, remove the battery. Make sure the battery it has cooled down, before placing it back again.
2. Make sure drone is on but not flying.
3. Put the drone on a flat surface and follow instructions on the main screen of the user interface.

4. Place the drone back onto the charging pad in the right direction: the front side should be facing the main beam of the ground station and the side with the blower should be facing the visual marker on the right side of the charging pad.

**Ground station procedure**
***Goal*:** This procedure is needed to ensure that the ground station is fully functioning.
***Timeline*:** Perform this operation every 6 month for every ground station.
***Tools needed*:** WD-40 spray, cotton swabs
***Instructions*:**
1. Perform visual inspection of bolts and screws that keep the ground station attached to the structure of the greenhouse.
2. Get dust off the markers that the drone needs for landing purposes.
3. Apply WD-40 spray on the main landing pads of the ground station.
4. Turn the power off such that the dock where the pin of the drone is inserted can be properly cleaned. Insert the cotton swabs into the holes. A gentle rub on the sides is enough. Turn power back on.

## 4.5. Customer support

Customer support is nowadays very important as it plays a key role in customer satisfaction. A dedicated platform will be implemented. Customer support will be done by phone, email, and the use of social media such as a dedicated Facebook page could be considered at a later stage. Any questions can be addressed to the customer service of the manufacturing company. Moreover, technicians can be available for performing the repairs, within the warranty time or at an extra cost beyond this period. Customer support will also focus on providing the owners with any software updates. With big improvements, the owners will be contacted such that modifications that will boost the performance can be implement right away. Furthermore, the customers will have the option of subscribing to a newsletter of new products. This will of course only be considered at a later stage as the current one is only at the proof of concept phase.

# 5

# Pollination payload

Plant pollination is performed using a dedicated payload, a blower. The design process of this blower is explained in this chapter. Section 5.1 gives an introduction to the general process. Section 5.2 provides an extensive analysis about the flow analysis performed. The implementation and sizing details are presented in Section 5.3.

## 5.1. General pollination process

The mission of the drone system is to ensure pollination process of greenhouse crops where natural mechanisms are insufficient, endangered or ineffective. In the last phase of the project, it was chosen that this process is performed using a dedicated payload on the drone [9]. As the tomato plant benefits from wind pollination [10], the dedicated payload is a blower that can target the airflow at the stem of the flower. When the project group visited the research greenhouse of the Wageningen University, the idea was discussed with expert Jan Janse. He indicated that shaking the flower only slightly will be enough to ensure pollination. The targeted airflow will shake the flower enough to release pollen and ensure pollination. Before explaining the process of designing the payload, some remarks about this pollination mechanism should be made.

As discussed in Chapter 2, the conventional way of pollinating tomato flowers in a greenhouse is via bumblebees. The farmer usually buys a box of bees, places it in the greenhouse and pollination is ensured for a couple of weeks. In the past, pollination was performed by a vibrating stick, or even rarer, by a wind blower [10, 11]. This way of pollinating tomatoes gives less yield. However, both articles use a large scale blower that does not have a high accuracy. If the group achieves getting a higher accuracy in the blower, this effect could be reduced. Furthermore, Jan Janse indicated that one of the reasons tomatoes grow in greenhouses is the lack of wind in there. If there is less wind, tomato growth and fruit yield is promoted. For this reason, the blower should be designed in an accurate way precisely not to promote this effect. Some other practical points were also learned during the visit of the greenhouse. First, the flowers always appear on the top of a plant, and one plant only has one group of flowers at the top. For the bigger tomato species, each group of flowers is cut down to six flowers to get the well-known truss of six tomatoes. Smaller tomato species have more flowers per stem. Pollination tends to happen around three times per week and cannot happen all day long. Humidity should not be too high (usually in the afternoon), as the pollen tends to get too sticky and at night pollination is also difficult. In Figure 5.1, a flower of a tomato can be seen, with already pollinated flowers hanging below it. This truss could be targeted by the payload at the place where the hand is.

## 5.2. Flow analysis

This section introduces an analytical model for the flow analysis. After that a numerical model will be presented and explained. Then, verification and validation will be done and in the end system outputs will be given.

### 5.2.1. Analytical model

Facilitating basic estimations and fast exploration of the governing parameters was deemed possible only with an analytical model. In order to keep the model simple enough such that an analytical solutions exists, it was decided to recast it as a free axisymmetric submerged jet. The results of the model were then compared with experimental data in order to evaluate the effect of the assumptions made.

The problem of a free axisymmetric submerged jet was first introduced in 1933 by Schlichting [12]. He gave predictions about the variations in center-line velocity and jet width with the distance from the outlet. Four years later, in 1937, Bickley solved it for the case of the eponymous planar jet [13]. The solution for an axis-symmetric jet for given total jet momentum was developed by Landau [14], while Squire determined an exact solution for a laminar jet with a

Figure 5.1: Flower of tomato plant. The blower will target the stem of the flower, approximately at the location of the fingers.

point source of momentum [15]. Similar approach is also suggested by White [16]. The Squire solution, however, is the one used for the current treatment thanks to it being the most mathematically tractable.

This approach assumes a point source of momentum, neglecting the particular outlet dimensions and flow velocity. Furthermore, it presupposes potential laminar flow. The phenomena occurring in the shear layer between the jet and the ambient air are also ignored.

The equations of motion are expressed in spherical coordinates $(r, \theta, \phi)$ with $\theta$ measured from the axis of the jet. The velocity components are $(u, v, 0)$ measured in the same respective directions. Due to the problem being axis-symmetric, it does not depend on $\phi$. The streamlines are given by

$$\psi(r,\theta) = \nu r f(\theta), \tag{5.1}$$

$$f(\theta) = \frac{2\sin^2\theta}{a+1-\cos\theta}. \tag{5.2}$$

where $\nu$ is the kinematic viscosity of air. From Equation (5.1) and Equation (5.2) it becomes apparent that the flow behavior is solely dependent on the parameter $a$. This value of $a$ depends only on the momentum applied at the origin and this is expressed by the implicit relation

$$\frac{F}{2\pi\rho\nu^2} = \frac{32(a+1)}{3a(a+2)} + 8(1+a) - 4(1+a)^2 \log\left(\frac{a+2}{a}\right), \tag{5.3}$$

where $\rho$ is the air density and $F$ is the force applied at the origin. In the case of a round outlet with diameter $d$ and uniform outlet velocity $u_0$, this force equals

$$F = \frac{1}{4}\pi\rho u_0^2 d^2. \tag{5.4}$$

Finally, the velocity component in the flow are given as:

$$u = \frac{1}{r^2\sin\theta}\frac{\partial\psi}{\partial\theta} \qquad \text{and} \qquad v = -\frac{1}{r\sin\theta}\frac{\partial\psi}{\partial r}. \tag{5.5}$$

Equations (5.1) to (5.5) are sufficient to analyze the flow behaviour. An example of the flow streamlines can be seen in Figure 5.2. The jet boundary corresponds to the points where the streamlines are closest to the jet axis, as from this point the free flow expands together with the jet. This is referred to as *throat* precisely because of the minimum cross-sectional area of the streamtubes there. It is illustrated by a thick black line in Figure 5.2.

From Figure 5.2, it can be observed that 30 cm away from the outlet the jet size is 0.3 mm. That results in a spread ratio (cone radius increase per unit distance from the nozzle) of $S = 0.01$. However, this is an order of magnitude less than the expected $S = 0.1$ obtained from empirical studies [17]. This discrepancy is believed to be due to the Squire solution being limited to laminar jets and ignoring the shear layer between the jet and the ambient air. Figure 5.3 shows the expansion angle superimposed on a close-up from the numerical model of free jet injection into steady ambient air (details about the model can be seen in Section 5.2.2). To account for the point momentum source assumption in the Squire solution, the analytical expansion angle is located at the top end of the inlet. It can be concluded from Figure 5.3 that the expansion ratio found coincides with the expansion of the interface between the edge of the jet core (the region with the same velocity as the outlet).

Another issue observed with the analytical model is the unrealistically high jet centerline velocities for the first few meters from the outlet. This is illustrated in Figure 5.4. Figure 5.5 is a plot of the velocity profile of the jet 30 cm away

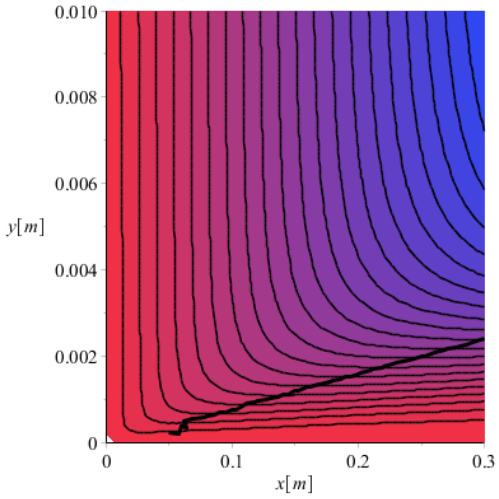


Figure 5.2: Contour plot of the Squire analytical solution for $d = 0.02$ m and $u_0 = 1$ m/s ($a = 0.00032$. The $x$ axis coincides with the jet axis. The outlet is assumed to be a point source of momentum located at the origin. The thick black line denotes the throat of the streamtubes

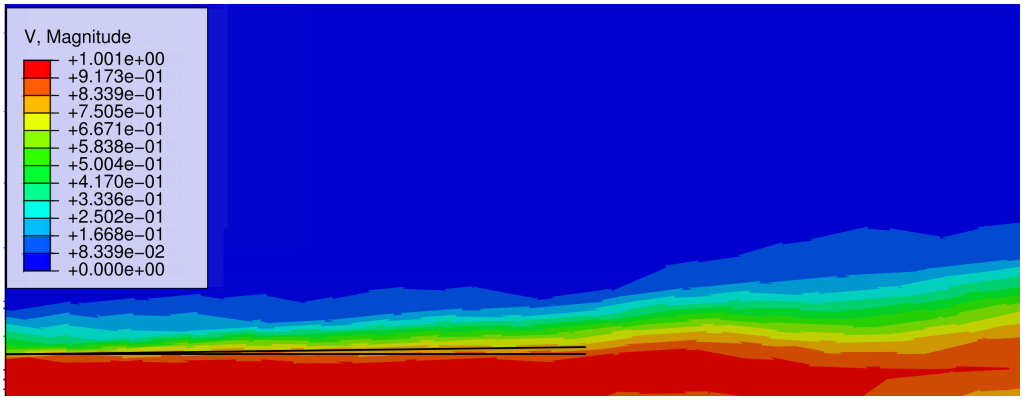


Figure 5.3: A close-up of the numerical solution of free jet injection with 1 m/s into steady ambient air with the expansion ratio $S = 0.01$ (the black lines) as found by the Squire solution superimposed on the top end of the inlet

from the outlet. Both figures show velocities larger than the outlet velocity $u_0 = 1$ m/s, which is physically impossible. Nevertheless, this result was expected due to the assumption that all the momentum of the outlet is concentrated at the origin. The analytical model used does not differentiate between a small outlet area with large velocity and a big outlet area with low velocity, as long as the products of velocity and area are the same. In fact, the Squire model assumes infinitesimal outlet area and infinite velocity. This is also illustrated by the asymptotic behavior close to the vertical axis in Figure 5.4.

The Squire analytical model was considered too simplified to be of practical value for accurately estimating the jet velocity profile at a distance from the outlet. The potential flow analysis cannot match perfectly the real behavior. One of the main reasons for the poor approximation is considered to be the premise of a point source of momentum for the outlet. This affects both the jet cone size, as in the physical case it has a radius at least the radius of the outlet, and the velocity profile along the jet axis. The presupposition of laminar jet with no shear layer and mixing with the ambient air is also suspected to affect the model results significantly. For example, this is believed to be the cause of the small expansion ratio of 0.01 in contrast with the expected 0.1.

If further research in analytical solutions is to be performed it is advised to look into approaches that levy these issues. For example, the treatment suggested by Abramovich [18] is deemed particularly applicable for the problem at hand. Nevertheless, it requires an empirical constant that can only be obtained in an experimental set-up. For this reason, it could not be applied at this stage of the development.

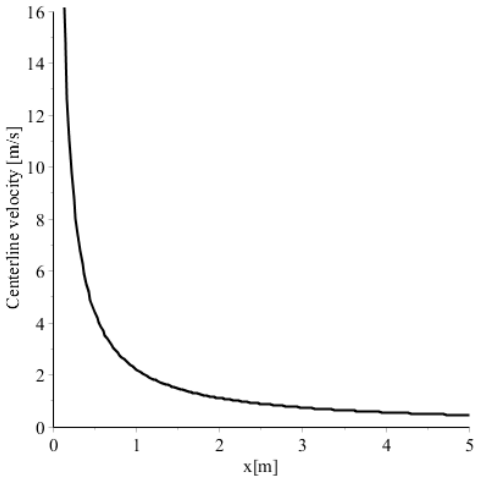


Figure 5.4: Centerline velocity of the Squire analytical solution for $d = 0.02$ m and $u_0 = 1$ m/s ($a = 0.00032$). The $x$ axis coincides with the jet axis. The outlet is assumed to be a point source of momentum located at the origin

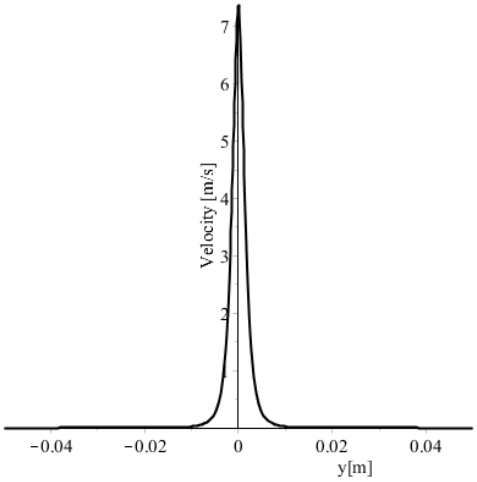


Figure 5.5: Velocity profile of the Squire analytical solution 30 cm from the for $d = 0.02$ m and $u_0 = 1$ m/s ($a = 0.00032$). The $y$ axis is perpendicular to the jet axis

## 5.2.2. Numerical model

Two numerical models of the blower jet were developed to predict the effectiveness of the blower. The first model is a free jet injection into steady ambient air. This model allowed to accurately estimate spread of the jet and decrease of the velocity along the distance and an effective range in which the jet is relatively coherent. The second model is the jet injection toward a cylinder in ambient steady air. The cylinder is considered representative of a tomato flowers branch stem. The model allows to estimate the flow interaction with the plant and the pressure distribution over the cylinder which yields forces acting on the plant. Estimated forces can be used to evaluate the jet effectiveness and to size the blower. Both simulations are done for idealized cases and the results are used only for the first order estimations.

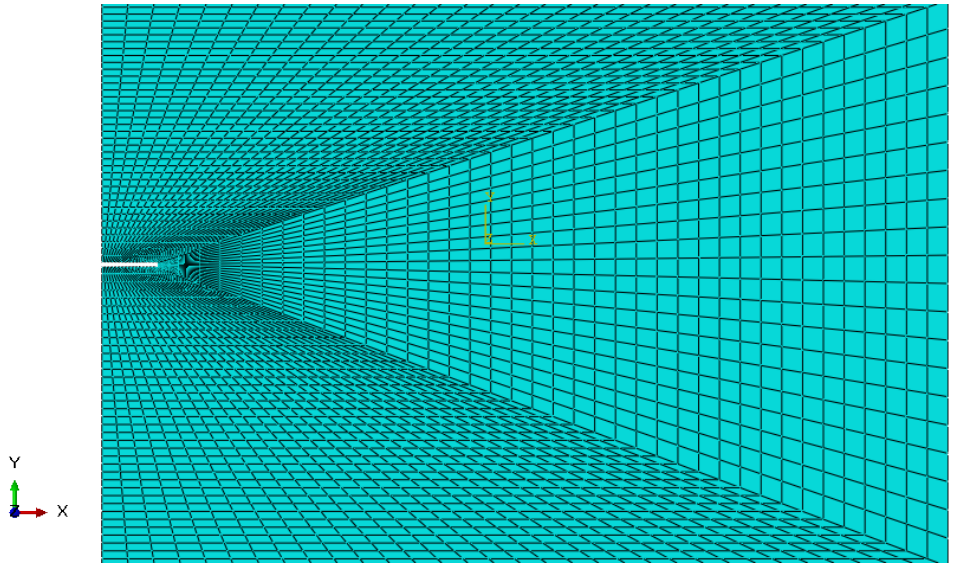


Figure 5.6: Meshed domain of the numerical model

The domain of the first model is a rectangle 2 m high and 3 m long which is equivalent to 100 and 150 nozzle diameters respectively. An elongated channel on the left side as shown on Figure 5.6 imitates the blower exhaust. The channel length is 30 cm and the exhaust diameter is 2 cm. Such an approach was taken to account for the jet sucking in the air from the surroundings, which might result in strong vortices. The walls of the channel are set with the wall boundary condition which imposes no slip condition (null velocity). All the other edges of the domain are set with the outlet boundary condition with null relative pressure.

The mesh for the model is shown in Figure 5.6. It consists of 4,560 hexahedron elements. The mesh is refined near the inlet to account for developing shear layer around the jet core. The smallest elements have length of about 2 mm. The closer the outlet the coarser the mesh becomes. The elements at the right boundary have length up to 10 cm. This approach allowed to optimize number of elements and the computation time. In the future the mesh could be better optimized by making it coarser close to the upper - right and bottom right corners.

The simulation was run for 30 s, with time increment of 0.01 s. This was enough to obtain the steady solution. The Courant–Friedrichs–Lewy condition coefficient is set to 0.45. The convergence was achieved and verified by plotting root mean square (RMS) of residual values. The plot is shown on Figure 5.7.

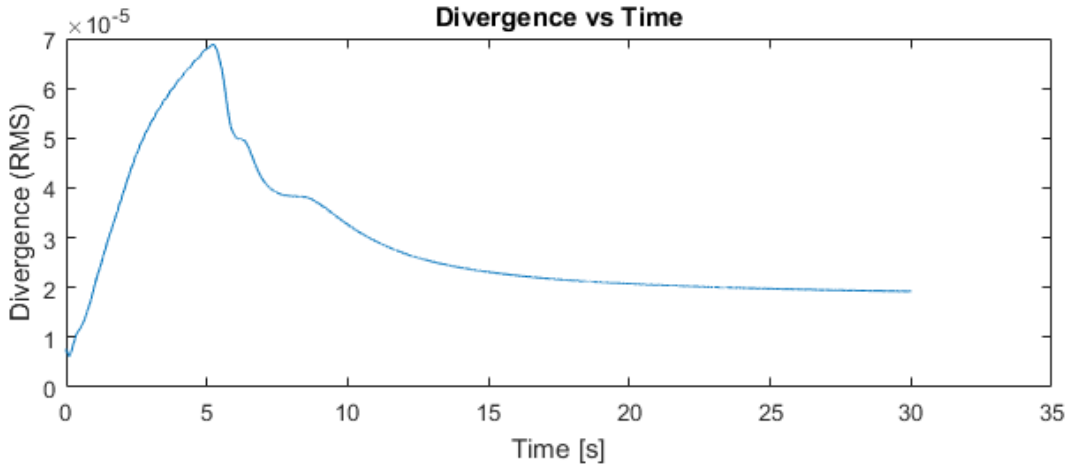


Figure 5.7: Root square mean of residual errors vs time for steady flow CFD simulation without turbulence

The results of the simulation are shown on Figure 5.8. From the results, a velocity decay with distance is determined and plotted on Figure 5.12. The results are compared wit analytic model, and discussed in more details in Section 5.2.3.

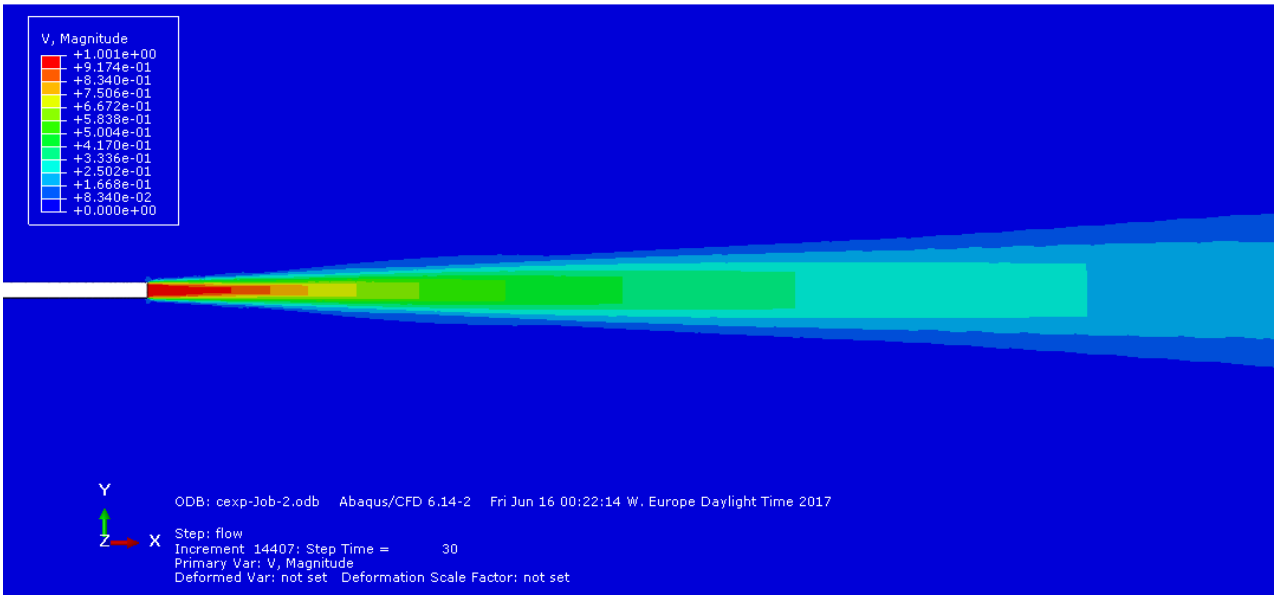


Figure 5.8: Results of a CFD simulation: close up on fully developed steady state jet flow for the exhaust velocity of 1 m/s

Next, the turbulence was implemented to determine how much of an influence it has on the flow. The k-epsilon model was used. For the coefficients, default values were used and the mesh was more refined near the inlet to enable better convergence.

The results of this simulation are shown in Figure 5.9. The conical divergent part of the jet close to the exhaust is due to insufficiently refined mesh. The geometry of the jet is not much different than the one obtained with the steady solution without turbulence model in Figure 5.8. One difference, however, is a slightly wider, more dissipated shear

layer between the ambient air and the jet, which is caused precisely by the turbulence.

Further downstream some mild fluctuations are visible. Those fluctuations are initiated by the transient part of the solution. In general, two regions can be distinguished in the jet flow: a stable one, where the jet is relatively coherent, and an unstable one, where the jet is dissipated and the flow forms large eddies, shedding in random directions. The simulation focuses on the stable region, and thus does not include the region with instabilities. It is aimed to utilize this region of the jet to pollinate the flowers. The main advantage is that the coherent jet flow can be effectively concentrated on the target, and the flow is fully utilized, which increases efficiency of the system. In comparison, vortices in the unstable region are much more dissipated, and their velocity is reduced. In this case the transition zone (which lays about 50 cm from the exhaust) imposes the limitation on the maximum distance from the nozzle. In order to catch all the instabilities and vortices the domain should be extended further in the flow direction, and a Large Eddies Simulation should be implemented. This approach however is not feasible as the computational cost of such a simulation (due to complexity of the problem, and time) is disproportionate to added value. The simulation would result in much larger precision, however it would not necessarily model the reality more accurately. It needs to be emphasized that the model is idealized, and does not account for interactions with environment (like downwash from propellers or interaction with the plant).

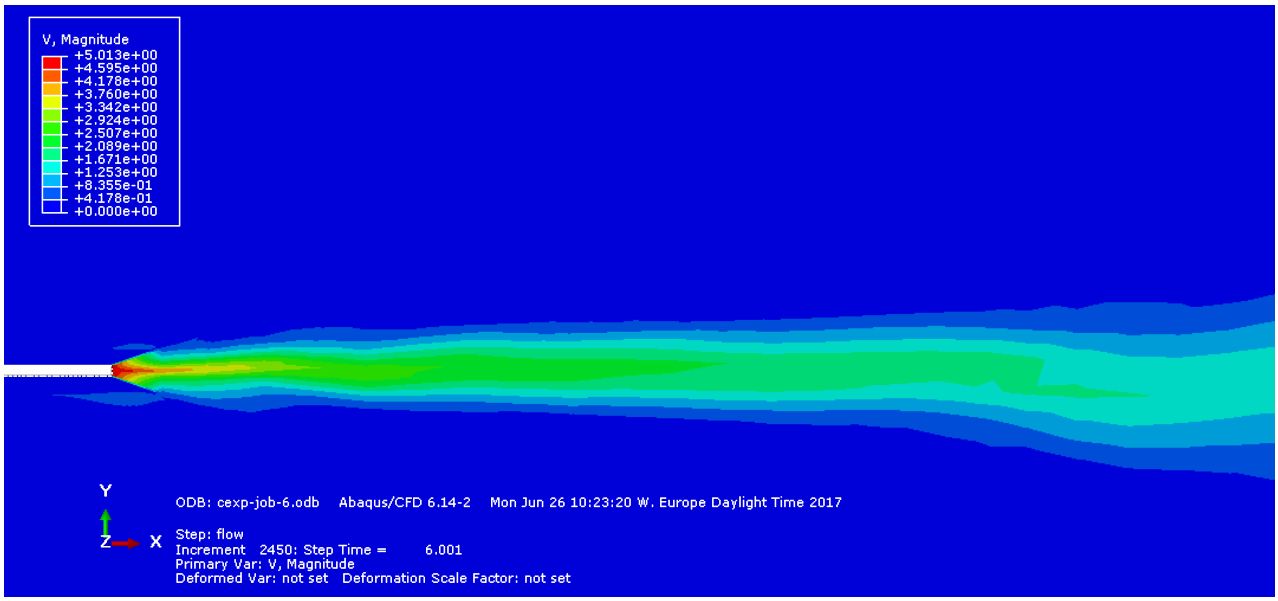


Figure 5.9: Results of a CFD simulation with exhaust velocity of 5m/s and k-epsilon turbulence model

The second model is the exhaust flow pointed toward the cylinder. The objective of this simulation was to investigate the influence that the cylinder (that imitates the plant stem) has on the jet. The goal was to determine the order of magnitude of the aerodynamic forces acting on the stem, to later determine whether those forces are sufficient to shake the flower. Flow around a cylinder in a free-stream is a relatively well understood problem. In case of the flow from the blower, where the mass flow is relatively small, the free-stream conditions do not apply any more. This results in strong interaction between the jet and the cylinder.

The model is set up on a 2 m high, and 1.5 m long rectangular domain (equivalent to 100 and 75 nozzle diameters) with 1 slab width shown in Figure 5.10. The inlet is a 2 cm high patch on the left boundary, as in the first model. The boundary conditions are also the same: all the edges have an outlet condition imposed, with pressure set to 0. The cylinder is placed 30 cm from the exhaust. It has 5 mm diameter which corresponds to estimated size of the tomato stem.

The mesh is split into several partitions to enable structured layout. It consists of 6,392 hexahedral elements. The mesh is refined near the cylinder and near the inlet as shown on the Figure 5.10. This approach is chosen to account for relatively small size of the features, and prevent large numerical errors.

The results of the simulation are shown on Figure 5.11. Only the transient part was caught, because the solution was diverging due to software limitations. Despite these issues the treatment was considered sufficient considering the time and resource constraints of the project. Moreover, the results from these simulations are used only for order of magnitude estimations and sufficient margins were applied to account for these issues.

Some conclusions can be drawn. Due to minor instabilities, the flow splits on the cylinder asymmetrically. This

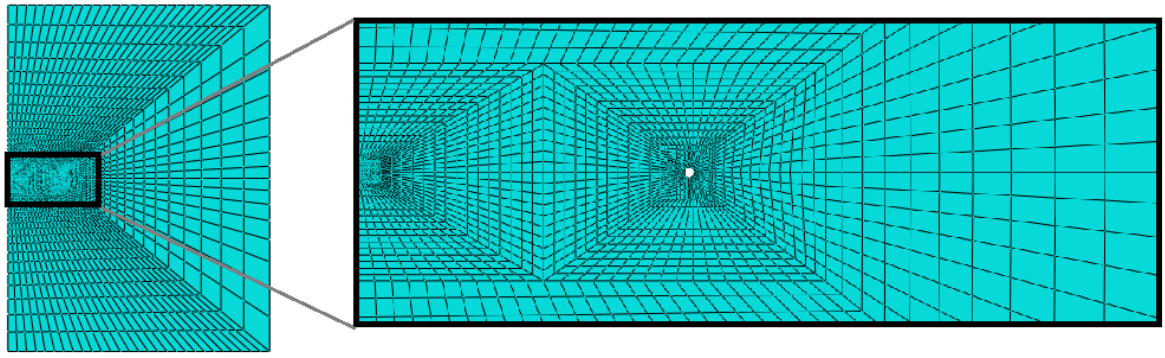

Figure 5.10: Mesh of the model of the jet flow on cylinder

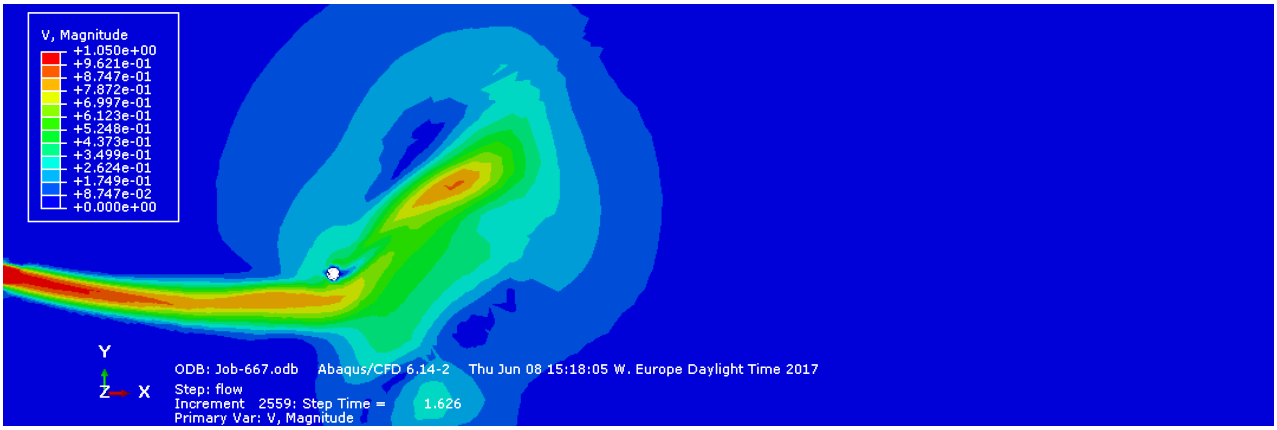


Figure 5.11: Flow on the cylinder: large eddy roll-up

results in a vortex rolling up on one of the sides of the cylinder, as shown on Figure 5.11. This asymmetric vortex induces a velocity field that tends to deflect the jet even more away from the cylinder.

The simulation also allowed to estimate forces acting on the cylinder. The force in $x$ and $y$ direction was calculated by integrating the pressure acting on the surface. The forces per unit length calculated for 5 mm diameter cylinder in 1 m/s flow are 1.15 mN/m in $x$ direction and 0.44 mN/m in $y$ direction. These results are validated in Section 5.2.3.

In reality the stem subjected to asymmetric forces will deflect, and therefore will influence the jet in slightly different way than shown by the simulation. To account for this effect more accurately, a flow-structure interaction should be set up. Even then the uncertainty of the results will be relatively poor. The main reason is that the plant is idealized, in fact the stem has multiple branches that will interact with the flow as well. The stiffness of different plants might vary which will result in various deflections and different effects. That is why the focus of this analysis was simply to estimate the order of magnitude of the forces and to obtain a general overview of extent up to which the plant affects the flow.

### 5.2.3. Verification and validation

The numerical results are compared and validated with the experimental results reported by Pope [17]. The core velocity change with distance is plotted in Figure 5.12. The red line corresponds to measurements of the core velocity from the CFD results. The measurements were done for five different time frames with a 5 s step for fully developed flow. This approach was taken to measure averaged velocity and account for vorticity and oscillations downstream.

The yellow line corresponding to experimental model is plotted starting from a distance of $6d$ (where $d$ is the nozzle diameter). As mentioned by Pope [17], the experimental model is not valid close to the nozzle, and for smaller distances this model can not be applied (it diverges due to singularity). The numerical results predict slightly higher velocities than estimated by the Pope's model. The most likely reason is that the flow in this region becomes unstable with large vortices present, which is not accounted for in the experimental model.

The turbulent and steady state model correspond relatively closely. Comparing with the steady state solution the core velocity of the turbulent jet is slightly lower at the beginning (until $x/d = 25$). This is most likely caused by a higher rate

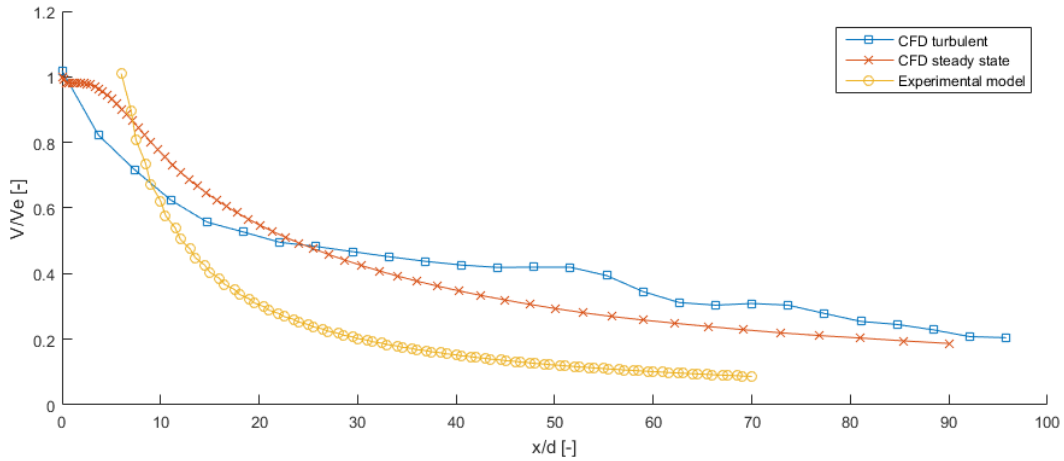


Figure 5.12: The jet core velocity in respect to the distance from the exhaust in dimensionless form. On the vertical axis ratio between core velocity V and the exhaust velocity Ve, on the horizontal axis distance expressed in nozzle diameters. Comparison between CFD steady flow simulation, CFD simulation with turbulent model implemented and experimental model [17]

of dissipation due to the turbulence. For larger distances however the velocity is slightly higher. Another remarkable feature is that the line is not perfectly smooth, i.e. it has some local peaks. This is caused by instabilities in the flow caused by the turbulence and high vorticity.

Concluding, the numerical model gives reasonable results. The discrepancies between the lines stem from the assumptions and idealization of the experimental model. Taking a conservative approach, it is preferred to use the experimental model for the sizing of the blower, as it gives some safety margins for velocities.

The drag force acting on the cylinder obtained from the second CFD model was compared with analytically derived drag force per unit length (Equation (5.6)) obtained for the same conditions.

$$D = C_D \frac{1}{2} \rho V^2 d = 1.2 \cdot \frac{1}{2} \cdot 1.225 \cdot 0.55^2 \cdot 0.005 = 1.11 \text{mN/m} \tag{5.6}$$

The cylinder diameter $d$ is 5 mm and the effective velocity is 0.55 m/s (as it drops on the distance from the exhaust). The drag coefficient for cylinder in applicable range of Reynolds number is 1.2 [19]. The result is 1.11 mN/m.

The difference between the analytic solution, and the drag obtained with CFD is in the order of 3%. The discrepancies stem most likely from different assumptions - in CFD the flow is non-uniform, and some instabilities occur.

It is assumed that the size of the nozzle is sufficient to provide enough flow velocity to pollinate the flower. The effectiveness could be improved more by increasing its size. However, this would result in a bigger motor and propeller needed, which would require more power and add weight. Additionally, the force produced would increase, which would have negative consequences on the control system. Smaller mass flow on the other hand would decrease the efficiency of the pollination. The interaction between the flower and the jet would be more pronounced (as observed on Figure 5.11), and could result in lower effectiveness of the pollination.

Internal experiments were performed in the laboratories of TU Delft to validate the performance of the blower. However the accuracy of the setup and the results are much lower than Pope´s and it is recommended to run the experiments again in the future. It was found that a flow of 2.4 and 5.8 m/s was recorded at a distance of 50 and 25 cm respectively, for a nozzle diameter of 14 mm and 10 m/s exit velocity.

### 5.2.4. System output determination

As mentioned before in Section 5.1, only a slight shaking of a flower is enough to pollinate it. Nevertheless, in order to ensure proper pollination, it was decided that the flowers have to be shaken at the frequency of about 200 Hz, similar to bees [20]. The shaking arises thanks to the induced vibrations of the von Karman vortex street. The frequency of the lift variation is the same as the vortex shedding frequency while the one of drag variation is twice as much [21]. In order to reduce the energy necessary to be put in the flow, the analysis is performed for shaking due to variation in drag. Therefore, the blower system has to produce a von Karman street at the flower with vortex shedding frequency of 100 Hz.

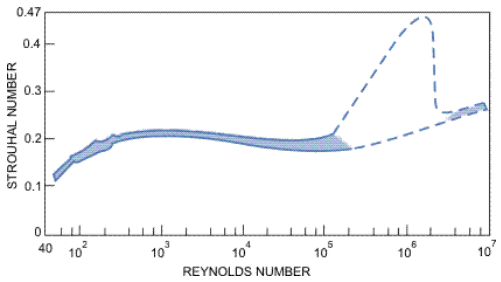


Figure 5.13: Dependence of the Strouhal number on the Reynolds number for a cylinder [22]

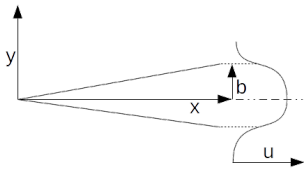


Figure 5.14: Illustration of a jet and its velocity profile. The nozzle outlet is located at the origin. The distance $b$ is measured from the jet axis $x$ to the circle of the cross-section that observes half the centerline velocity

The non-dimensional parameter describing the vortex shedding frequency is the Strouhal number, defined as

$$\mathrm{St} = \frac{f d}{u}, \tag{5.7}$$

where $f$ is vortex shedding frequency, $d$ is a characteristic length and $u$ is the flow velocity. The characteristic length $d$ is taken to be the diameter of the branch stem (modelled as a cylinder), which is estimated to be 5 mm from measurements made during the greenhouse visit. The velocity $u$ that the flower stem must be subjected to is the unknown that needs to be solved for. To do this, the value of the Strouhal number must be fixed. Both St and Re vary with changes in the diameter of the cylinder and the free-stream velocity it sees, assuming fixed properties of air. Therefore, a relation between the two can be made. Such a relation for flow impinging on cylinders can be seen in Figure 5.13. The same characteristic length of 5 mm was used together with standard atmospheric properties (density $\rho = 1.225$ kg/m$^3$ and dynamic viscosity $\mu = 1.81 \times 10^{-5}$ kg/(m s)) and expected range of velocities from 3 to 10 m/s. In this fashion the Reynolds number was found to be in the range from 1,020 to 3,400. From Figure 5.13 it can be concluded that St is relatively constant in this range of Re values, therefore the average value of 0.2 will be considered in the rest of the exposition in this section. Following from Equation (5.7), a Strouhal number of 0.2 and a frequency of 100 Hz for a cylinder with diameter of 5 mm are achieved for a free-stream flow velocity of about 1.25 m/s.

With the target velocity that is to be achieved at the flower, the required velocity at the outlet of nozzle can be obtained. Moreover, the required pointing accuracy of the drone can be established. In order to ensure that the flower experiences flow with velocity of at least 1.25 m/s, given some pointing uncertainty, it was decided that this should be the velocity at the jet edge (defined as the surface where the velocity is half of the velocity on the jet axis). Therefore, the velocity of the jet axis at the flower has to be 2.5 m/s.

In next step, it was found what nozzle exhaust velocity is needed to achieve 2.5 m/s at given distance. For this purpose the relationship between the core velocity and the distance was used (Figure 5.12). Furthermore the velocity profile from the experimental model developed by Pope [17]. In this case the jet spread can be approximated with Equation (5.8), where $r_{1/2}$ is the effective jet radius, $x$ is the distance from the exhaust, and $S$ is an experimentally found constant, equal to 0.096. With this relationship the width of the effective jet could be estimated for a given distance as illustrated on Figure 5.14.

$$r_{1/2} = Sx \tag{5.8}$$

The maximum pollination range that is considered is stipulated by the flow phenomena observed in the results of the numerical model. It was noted that regardless of the nozzle outlet velocity, the jet becomes unstable at a distance of about 50 cm. This instability is mainly expressed in large deflections of the jet due to the forming of vorticity. These instabilities were more pronounced at higher velocities. Therefore, to ensure that the airflow hits the flower and is not deflected instead, the maximum pollination distance was fixed at 50 cm. For this distance the maximum exit velocity found with the model (Figure 5.12) is 10 m/s.

Having the distance and the jet width the pointing accuracy needed could be estimated. The accuracy is defined as the angle between the nozzle axis and extension to the furthermost point with sufficient velocity. As the exhaust is not an infinitesimally small point as shown on the Figure 5.14, but it has finite diamater, the pointing angle is slightly smaller than the jet angle. The variation with distance in considered range however is in order of 1 degree, as the dimensions of the nozzle are relatively small. Taking conservative approach the most critical case is taken, which is the pointing accuracy of ±7deg. for distance of 50 cm.

To estimate whether the force acting on the flower is able to deflect it sufficiently for pollination, a simple first order estimations are done. The deflection can be estimated using the beam bending formula (Equation (5.9)). The elasticity of

the tomato stem is assumed to be 600 MPa, basing on [23]. The moment of inertia is calculated assuming that the cross-section is circular, with diameter of 5 mm. The distributed load $w$ is estimated with the drag formula (Equation (5.6)), where the velocity taken is 2.5 m/s (for effective pollination), and $C_D$ is 2 to account for roughness of the stem. With length of the stem assumed to be 25 cm the maximum deflection is 1 mm.

$$\delta = \frac{wL^4}{8EI} \tag{5.9}$$

The approach however is very conservative, as it accounts only for drag of the main stem. In reality the drag will be 1 up to 2 orders of magnitude higher, as the stem has multiple branches with flowers, which significantly contribute to the surface area, and increase the drag. This will result in deflection in range of few cm. The first order estimates suggest that the design is feasible. Due to complexity of the problem and multiple uncertainties the performance will need to be verified in a series of tests in a greenhouse.

Finally the time of pollination is estimated. To allow the flow to develop a 1 s is taken. This estimate is base on CFD simulation. Then for the actual pollination in nominal flow conditions 5 s period is assumed. During this period ideally the flower will oscillate 1,000 times. The value however accounts for possible pointing jitter of the drone. Even in case that the drone floats away slightly due to disturbances, there will be enough time for the control system for corrections. In total, a 6 second period should be considered as time for pollination of 1 flower.

## 5.3. Payload implementation

Given the pollination task, it was concluded that the blower should have an exhaust velocity of at least 10 m/s. With this driver requirement, the payload on board of the APIS drones can be sized. The problem will be approached while keeping in mind a modular configuration, making the drone flexible for a variety of payloads with different pollination methods. Therefore, a certain mass and power budget is reserved for this subsystem, which will be discussed below. First, the functionality will be discussed, followed by the design of the payload and the results of the analysis.

### 5.3.1. Functionality

Generating a flow to shake the flower can be combined with cooling the electronics on board. This is implemented by placing a heat sink in the duct. The heat sink is placed on top of the CPU to absorb the generated heat. The fins of the heat sink are inserted into the flow through the rectangular cut out on the bottom of the duct. The duct flow passing along the heat sink fins provides active means of cooling.

As the heat is transferred from the heat sink to the flow, the temperature of the air in the duct increases slightly. This decreases relative humidity of the air. This effect is beneficial for effectiveness of pollination - too high humidity of the air makes the pollen more sticky and hinders its motion.

### 5.3.2. Design

The blower consists of a fan and duct ending with a nozzle bent 45° downward. Additionally there is a heat sink inside the duct that cools the electronics. A cut view of the blower is shown in Figure 5.15.

The main reason for the choice of fan is that it could be placed in a horizontal position, which makes the whole drone assembly more compact. Another driving factor is the availability and variety of fans offered on market. The parts come with accurate performance data provided by the manufacturer, which allows to choose a fan tailored for the design, as the performance uncertainties were minimized.

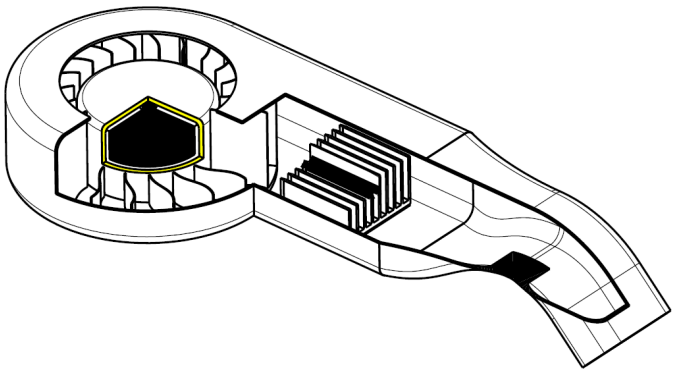

Figure 5.15: Isometric cut view of the blower

Table 5.1: Estimations of the jet deflection due to propeller wake

| | **Critical resultant V [m/s]** | **Angle with horizontal [deg]** | **Deflection from the nozzle axis [deg]** |
|---|---|---|---|
| Ve = 2.5 m/s | 5.08 | 69 | 24 |
| Ve = 15 m/s | 17.25 | 52 | 7 |

The fan is placed in the middle of the main structure box of the drone, very close to the center of gravity. The reason for this is to optimize control and stability characteristics, but also the available space. The length of the channel from the exit of the fan to exit of the nozzle is about 80 mm. The duct has a rectangular cross-section with rounded corners, such a shape has been chosen mainly due to space limitations and to make the duct flat and compact.

The first section of the duct, starting from the fan has a constant cross-section of 30 mm length and inner dimensions of 24.8×17.8 mm. The length of the section was chosen to accommodate the heat sink. The next section of the duct has variable cross-section and is smoothly profiled to accelerate the air to the exhaust velocity. The last section of the duct is an elbow bent under 45 deg and ending with the nozzle. The air inlet of the blower is placed on top of the fan, which is protected by a grill in order to prevent the sucking of particles and leafs in. The speed of the fan (and therefore speed of the exhaust) can be controlled via an Electronic Speed Controller (ESC). Sizing of the blower, and especially the exit cross-section stems from the analysis of the subsystem, which is explained in Section 5.3.3.

### 5.3.3. Analysis

The aerodynamic analysis of the pollination payload has been done to determine the interactions of the system with the surroundings and other subsystems. First, the flow conditions are analyzed to evaluate effectiveness of the blower. In this way it can be verified whether the system provides sufficient performance necessary for the effective pollination. The analysis includes influence of the external conditions - namely the interaction of the propeller wake as well as internal conditions which focuses on the pressure losses. Furthermore, the force due to blowing is estimated, this force will be the main disturbance exerted on the drone during the pollination and it has significant influence on the design of the control and stability system. Last but not least the results of the analysis are used to size the blower, and especially the exhaust nozzle.

**Rotors interaction**

When the drone is pollinating (while hovering), the estimated exit velocity just below the propeller is on average 3 m/s, and in the most critical locations, at the propeller tips, up to 6 m/s. This has been found by using the blade element theory, which will be described in Section 6.5. To estimate the jet deflection, the average induced velocity of 3 m/s is used. The resultant jet velocity and deflection is calculated using vector addition of different velocity components. The results for two most critical cases - the slowest and the fastest jet exhaust velocities are listed in Table 5.1. The deflection for higher velocities decreases, for the maximum exhaust velocity of 15 m/s it is about 7 deg. It should be stressed that the estimations do not account for effects such as swirl, turbulence and vorticity of the rotor wake, which might slightly change the flow field. In order to predict those phenomena, a thorough aerodynamic analysis needs to be done, which is however out of scope for this stage of the design.

The propeller wake contains two major vortex systems - tip vortex initiated at the tip of the blade and the vortex sheet shedding along the length of the blade. The overview of the phenomena is presented on Figure 5.16a.

As shown in Figure 5.16b the tip vortex moves towards the central axis of the rotor - the radial coordinate decreases and the vortex approaches 0.8 of the blade radius. This indicates that the wake below propeller contracts. Analyzing the axial component of the tip vortex gives an indication of the induced velocity of the flow in the wake. For the azimuth angles between 0 and 180 deg the coordinate varies linearly with angle, which indicates a constant velocity. The slope of the curve changes suddenly at an angle of 180 deg which indicates that the flow accelerates, which is caused by the passage of the second blade. The velocity remains constant until an azimuth angle of around 500 degrees, where it starts to decay and approaches zero. Analyzing results of CFD simulation of the quadcopter wake reported in [24], it can be concluded that just below the propeller the wake is indeed relatively concentrated, as found by Landgrebe [25].

In order to minimize the influence of the wake, the nozzle exhaust should be placed sufficiently far away from the propellers. Basing on the Landgrebe's results it can be concluded that this can be achieved by placing the nozzle outlet just outside of the perimeter of the propeller. Considering the fact that the jet is going away from the propeller wake due to 45 deg nozzle inclination and that further downstream the wake contracts, it is concluded that the interaction is significant close to the exhaust (where the jet is the closest to the propeller).

The disadvantage of this solution is that a longer duct is needed, which adds weight and contributes to pressure

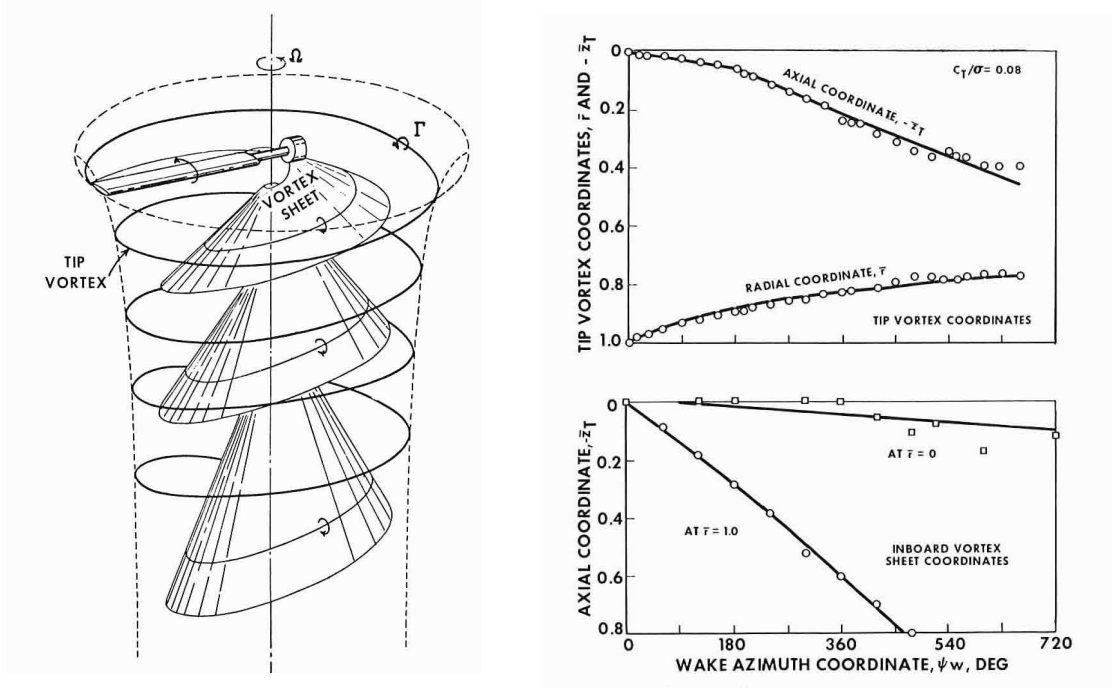


(a) Overview on propeller wake geometry. Both vortex sheet shedding from the propeller blade, and the tip vortex trajectory are shown. [25]

(b) Measurements of the rotor wake shedding from double blade rotor [25]

Figure 5.16: Overview on the results of Landgrebe's research [25]

losses. Furthermore, as the exhaust is placed further from the center of gravity of the drone, the disturbance moment due to the blowing force will be larger.

**Pressure losses**

The pressure losses are estimated between the fan and the exhaust of the nozzle to ensure that the fan provides sufficient performance and that the required exhaust velocity can be reached. The losses considered, are only due to friction - as the flow is assumed to be incompressible (valid for M = 0.04) the losses due to compressibility can be neglected. Along the duct, there are three main contributors - friction due to heat sink, friction with the pipe walls and friction due to the elbow.

To calculate the losses in the duct a standard approach is used and the calculations are done using the Darcy–Weisbach equation[1]:

$$\Delta P = f \frac{L}{D_h} \frac{1}{2} \rho V^2. \tag{5.10}$$

The length of the duct is 116 mm, the flow velocity at the exit of the fan is estimated using mass flow rate equation, where the mass flow and the cross-section area are given by the fan producer. The velocity estimated for unobstructed flow is 7.95 m/s. The f is the friction factor and the $D_h$ is the hydraulic diameter.

The Reynolds number for flow in the duct is estimated to be around 62,760. For this regime the flow is turbulent, and the friction factor can be read from the Moody diagram shown in Figure 5.17[1]. The friction factor for the flow is around 0.018. Finally the hydraulic diameter is calculated. For non-circular cross-sections this is done using Equation (5.11) where $A$ is the cross-section area, and $p$ is the wetted perimeter.

$$D_h = \frac{4A}{p} = \frac{4 \cdot 0.0238 \cdot 0.0168}{2 \cdot 0.0238 + 2 \cdot 0.0168} = 0.0197 \text{ m} \tag{5.11}$$

With these values the pressure loss for the straight section of the duct is calculated, which can be seen in Equation (5.12).

[1] https://neutrium.net/fluid_flow/pressure-loss-in-pipe [Cited 20 June 2017]

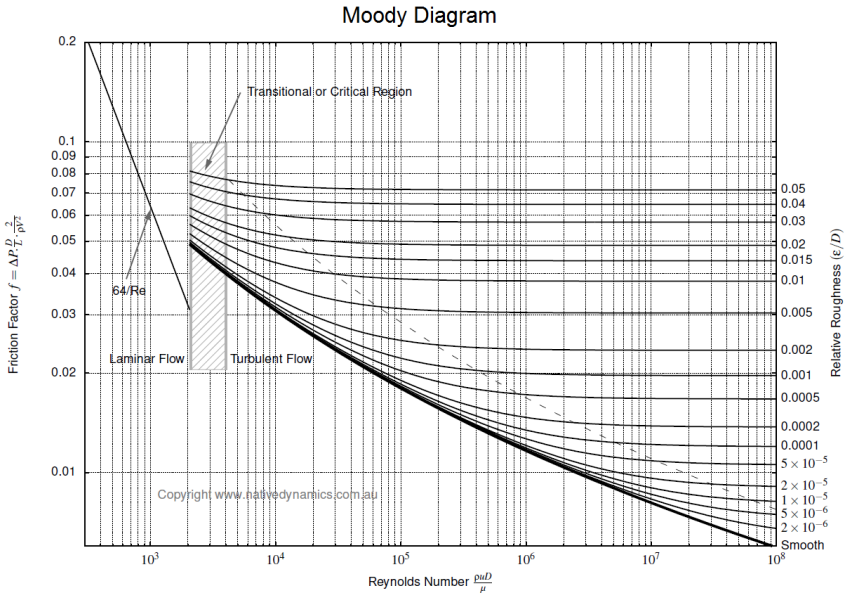


Figure 5.17: Moody diagram

$$\Delta P = 0.018 \frac{0.116}{0.0197} \frac{1}{2} 1.225 \cdot 7.95^2 = 4.1 \text{ Pa} \tag{5.12}$$

To calculate the effect of an elbow, the equivalent pipe length method is used. The method assumes that the pressure loss over the fitting is equivalent to pressure loss over a straight pipe of a certain length. Those equivalent lengths were experimentally determined for different elbow geometries and listed in standard fitting tables[2]. For an elbow of 45 deg that is used in this design the equivalent length is equal to $16d$, where $d$ is the pipe diameter. The pressure loss due to elbow is then calculated by using Equation (5.13).

$$\Delta P = 0.018 \cdot 16 \frac{1}{2} 1.225 \cdot 7.95^2 = 11.1 \text{ Pa} \tag{5.13}$$

The pressure loss across the heat sink is calculated using adapted Darcy–Weisbach method. Taking a conservative approach, it is assumed that the flow is fully ducted i.e. that the whole mass flow passes only through the heat sink. With this assumption the relative velocity $U$ is calculated. The value found is 23 m/s. This will result in overestimation of the friction, however this accumulated margin will account for the other not considered losses. Furthermore, taking a heat sink length of 16 mm, and assuming that the flow velocity is 7.95 m/s, the Reynolds number is calculated to be around 8,650. The friction factor corresponding to this value is 0.035, as can be read from Figure 5.17. Eventually, the hydraulic diameter $D_h$ is calculated for single channel in between the heat sink fins. The pressure loss is then calculated as shown in Equation (5.14).

$$\Delta P = f \frac{L}{D_h} \frac{1}{2} \rho U^2 = 0.035 \frac{0.016}{0.0197} \frac{1}{2} 1.225 \cdot 23^2 = 9.2 \text{ Pa} \tag{5.14}$$

The total pressure loss over the blower between the fan and the exhaust is the sum of all the three losses and is equal to 24.4 Pa. The estimated pressure losses can be considered as a resistance for the fan that must be overcome. This resistance will result in a decreased mass flow, because part of the fan power will be lost to overcome the friction. The decrease in the mass flow can be estimated using the mass flow - pressure relationship provided by the fan producer. The relationship has been determined through experiments and the results are plotted in Figure 5.18. The pressure in the vertical axis is the static pressure relative to atmospheric pressure, which can be considered as a resistance acting against the fan. For instance when the exhaust is completely blocked by a plate the mass flow is 0, and the relative static air pressure exerted on the plate is 18.5 mm $H_2O$. On the other hand when there is no resistance - the relative static pressure is 0 mm $H_2O$ the maximum mass flow of 0.19 $m^3$/min can be achieved.

[2] `https://neutrium.net/fluid_flow/pressure-loss-from-fittings-equivalent-length-method/` [Cited 20 June 2017]

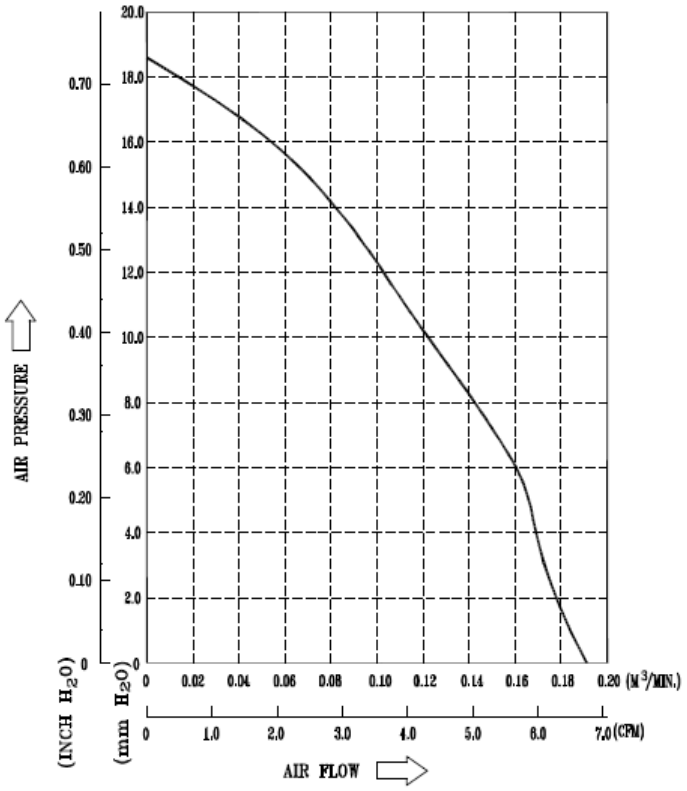


Figure 5.18: Pressure vs mass flow relationship for the blowing fan [26]

In this way, knowing the resistance pressure (calculated pressure losses) the maximum mass flow can be calculated. For 24.4 Pa (equivalent to 2.5 mm $H_2O$) it can be read that the maximum volumetric mass flow is 0.175 $m^3$/min (0.002917 $m^3$/s).

Knowing the maximum achievable mass flow and and the required exhaust velocity, the mass conservation equation can be used to size the exhaust nozzle. The required area is calculated by using Equation (5.15).

$$A_e = \frac{\dot{v}}{V_e} = \frac{0.002917}{15} = 194.4 \text{ mm}^2 \tag{5.15}$$

The width of the duct is fixed due to the fan outlet geometry and is equal to 17 mm. Assuming a square cross-section the height of the exhaust becomes 11.4 mm.

All the estimated pressure losses are slightly overestimated, this has been done in order to have an extra margin. As the friction decreases the mass flow from the blower, it slightly decreases the velocity as well. The velocity however is used is used in the model for all three considered friction contributors. Lower velocity results in smaller losses and so on. The right approach to accurately solve this relationship would be to iterate the calculations. This has not been done in order to leave a margin for unexpected phenomena. In case the more accurate analysis is needed, a CFD simulation should be considered.

**The thrust force**

The force exerted by the blower is calculated by using the principle of conservation of momentum, which can be seen in Equation (5.16). Taking conservative approach it is assumed that the flow is accelerated from stationary and therefore the initial velocity is 0. The maximum achievable exhaust velocity is 15 m/s. The effective mass flow generated by the blower is taken for idealized case neglecting the pressure losses. This approach is taken to add a margin in case that the losses are lower than estimated (as the estimations resulted in rather conservative values).

$$F = \dot{m} \cdot (V_e - V_0) = 0.003879 \cdot 15 = 0.058 \text{ N} \tag{5.16}$$

# 6

# Propulsion and power

In this chapter the power consumed during the mission will be discussed in more depth with the ultimate aim to size the battery. Starting with, in Section 6.1, a simple, yet representative, model will be created to account for the main aerodynamic forces to realistically find the required thrust forces. Later, the thrust required will be translated into power consumption in Section 6.2. Following, the nominal mission will be split into different phases for which an elaborate power drainage will be given in Section 6.3. The final battery requirements and selection is made in Section 6.4. Lastly, an analysis required for the rotor-blower interaction will be looked into in Section 6.5.

## 6.1. Aerodynamics

In order to accurately size the required thrust for the travelling phases of the mission, an aerodynamic model which incorporates aerodynamic forces and angles was created. It will be hereby explained. The solely goal of this model is to output the required thrust at a given part of the mission for a horizontal or vertical trip. It is a coarse and conservative model which will play an important role in sizing the energy consumption. The model was implemented in Python 2.7.

**Assumptions**

- Symmetric flight: the blower is not connected during the flight, or the flight controller has counteracted it.
- The aerodynamic reference frame coincides with the body fixed reference frame.
- The drone can be modelled as a flat plate for the payload part, but the rotors do not contribute to this surface area.
- Both lift and drag are present, are dependent on the pitch angle and act at the center of gravity which coincides with the center or pressure of the plate.
- The pitching moment is neglected.
- The thrust force is equally distributed along the four rotors and is fixed perpendicular to APIS' surface.
- Pitch is defined positive downwards, as it will promote positive velocity and will make APIS advance.
- Humidity contributes to a negligible increase in density at the temperatures of the greenhouse. (Up to 40 ° C in the worst case)[1].

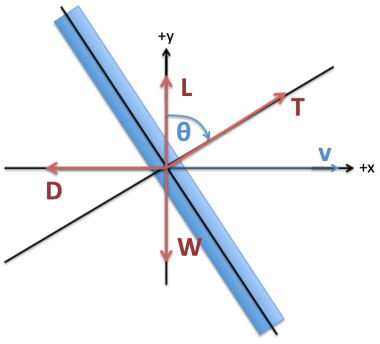


Figure 6.1: Free body diagram of APIS

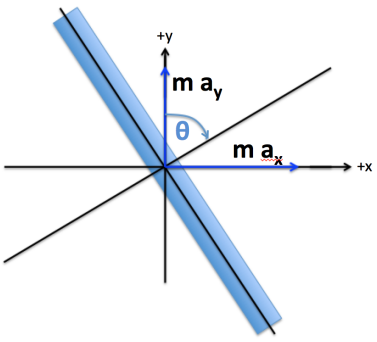


Figure 6.2: Kinetic diagram of APIS

[1] http://www.engineeringtoolbox.com/density-air-d_680.html [Cited 23 June 2017]

**Free-body, kinetic diagrams and equations of motion** From the free body diagram and kinetic diagram on Figure 6.1 and Figure 6.2, the following equations of motion can be derived:

$$\sum F_x = m \cdot a_x = T \cdot sin(\theta) - D = T \cdot sin(\theta) - \frac{1}{2}\rho V^2 S C_D \tag{6.1a}$$

$$\sum F_y = m \cdot a_y = L + T \cdot cos(\theta) - W = \frac{1}{2}\rho V^2 S C_L + T \cdot cos(\theta) - m \cdot g \tag{6.1b}$$

Where, $F_x$ and $F_y$ are the forces in the x and y axis in N, respectively, m is the mass in kg, a are the accelerations in x and y axis in m/s$^2$, T is the thrust in N, $\theta$ is the pitch angle in deg, $\rho$ is the density in kg/m$^3$, V is the forward velocity in m/s, S is the surface area and $C_D$ and $C_L$ are the drag and lift coefficients. The latter two will be discussed in more depth in the subsequent paragraph.

**Lift and drag coefficients** For what concerns the lift and drag, APIS is modelled as a flat plat with dimensions 87x139 mm$^2$, which would yield an aspect ratio of around 1.6. Nonetheless, the coefficients are not constant values as they depend on the pitch angle. To model these variations, the lift coefficient has been calculated following the Lowry and Polhamus lift coefficient dependence on the angle of attack empirical formula, Equation (6.2). This empirical relation was found to be acceptable for aspect ratios below 2, [27]. Based on experiments, the drag coefficient was found to behave linear for the aspect ratio of 1.6 in the range of 0 to 50 degrees of angle of attack, for which the limits of the $C_D$ were shown to be 0.061 and 0.781 [28]. Consequently, the $C_D$ was modelled through interpolation of these two limits as shown in Equation (6.3), where $\theta$ is the pitch angle at a given moment in degrees and is not expected to be more than 50 degrees in any traveling phase.

$$C_{L_\alpha} = \left(\frac{1}{57.3}\right) \frac{2\pi AR}{2 + \sqrt{\left(\frac{AR^2}{\eta^2}\right)(1 + tan^2(\lambda_{c/2}) + 4}} \tag{6.2}$$

Where $C_{L_\alpha}$ is the variation of the lift coefficient with the angle of attack in 1/deg, AR is the aspect ratio as an unit-less parameter, $\eta$ is the line lift coefficient derivative with the angle of attack ($C_{l_\alpha}$) over $2\pi$ and $\lambda_{c/2}$ is the half-chord sweep angle. For $C_{l_\alpha}$, a value of 5.3743 (1/rad) was found to be a recurrent nominal value for flat plates.

$$C_D = 0.061 + \frac{0.781 - 0.061}{50 - 0} \cdot \theta \tag{6.3}$$

**Kinematics and dynamics** In order to find the required thrust, any trip is always split into three phases, acceleration, cruise and deceleration to null velocity. Both acceleration and deceleration have been set to 10% of the total required time for the trip. For any trip, the following kinematics hold:

$$t_{acc} = t \cdot 0.1 \tag{6.4}$$

$$V_c = \frac{s}{t - t_{acc}} \tag{6.5}$$

$$a = \frac{V_c}{t_{acc}} \tag{6.6}$$

Where $t_{acc}$ is the time of acceleration in s, t is the total trip time in s, $V_c$ is the cruise speed in m/s, s is the space to cover in m and a is the acceleration required to accomplish it in m/s$^2$.

Also a distinction has to be made between horizontal and vertical travel. For vertical trips, the x-axis acceleration and $\theta$ is set to 0, making the y-axis the only axis to look into. In this case, only the y-axis equation of motion is of relevance, but with the difference that there will be drag but no lift. A value of 1.28 for the $C_D$ was used for this case[2]. The equation to solve becomes:

$$m \cdot a_y = T - m \cdot g - \frac{1}{2}\rho V^2 C_D \tag{6.7}$$

For the case of the horizontal, the acceleration in the y-axis can be set to 0, but a system of two non-linear equations and two unknowns (T and $\theta$) remains to be solved, namely Equation (6.1). It is worth pointing out that lift will usually point in the negative direction, this will increase the required thrust level.

[2] `https://www.grc.nasa.gov/www/k-12/airplane/shaped.html`[Cited 23 June 2017]

**Inputs, outputs and variables** The model takes as solely inputs the distance to be covered and the time needed. As variables, the greenhouse temperature can be changed in Kelvin, as it impacts the air density. Also, the mass in g and surface area in $mm^2$ of APIS are variables. On the modelling side, the timestep can also be varied. The model outputs:

- Cruise velocity in m/s
- Thrust required during the trip in N
- The $\theta$ at which to fly during the trip in degrees.

As previously stated, the sole goal of this model was to get a more accurate result for the required energy consumption of the motors to size the battery. In fact, now that the thrust required is known, the power can be derived from Section 6.2. Once the power is known, the energy follows from the time required per phase. Another advantage of this model is the output of the intensity required in any point for the trip which can provide insight on more accurate required C-rates.

**Verification and validation** Bearing in mind that the current model only played a role on the battery model, the verification and validation will be as in depth as it feels sensible. In fact, for the case of the validation of the model, almost no applicable literature can be used. When it comes to the verification of the model, several unit tests can be performed for which a clear output is expected, these can be found under Table 6.1. In order of appearance, the top test aims at showing how by decreasing the acceleration time, the distance and time which remains for the cruise phase leads to an unaccelerated travel for which the cruise speed approaches the distance to cover over the input time. Subsequently, on the $C_L$-$C_D$ calculator module, if $\theta$ is set to zero, the lift coefficient is expected to be 0, while the drag coefficient can only be the zero-lift coefficient. Following with, a simple test to check for internal coherence is setting the distance to cover to 0 meters, this has to translate into hovering thrust and zero pitch angle. Next is checking the environment, if the temperature is set to sea-level temperature, the density must match the sea-level temperature. Lastly, a last sanity check on the thrust level for the cruise phase is that the thrust must always be at least slightly higher than the weight.

Table 6.1: Verification tests for modules in the propulsion energy calculation

| Test | Input | Expected output | Output | Checks? |
|---|---|---|---|---|
| **Horizontal case:** Set acceleration time to small value, cruise velocity should approach s/t | s = 50 m<br>t = 10 s<br>$t_{acc}$/t = 0.01 | vc = 5 m/s | vc = 5.05 m/s | Ok, approaches vc as expected |
| **CLCD unit calculator:** Set theta to 0 | $\theta$ = 0 rad | CL = 0<br>CD = CD0 = 0.067 | CL = 0<br>CD = 0.067 | Ok |
| **Horizontal and vertical case:** Set distance to cover to 0 meters | s = 0 m | T = m·g<br>$\theta$ = 0 deg | T = m·g<br>$\theta$ = -3.12E-12 | Ok |
| **Environment module:** Set temperature to 15 C (287.15K) and ignore humidity | T = 15 C | $\rho$ = 1.225 kg/m^3 | $\rho$ = 1.225 kg/m^3 | Ok |
| **Horizontal and vertical case:** If s>0, the minimum thrust must be higher than the weight. | s = 100 m<br>t = 50 s | T >m*g = 2.4525 | Hor: T = 2.4598 N<br>Ver: T = 2.4972 N | Ok |

On the other hand, validation proves to be a more challenging matter, given the inherent uniqueness of any MAV and especially the choice of code implementation. Nonetheless, some modules can be validated, and such is case for the $C_L$-$C_D$ calculator. Using the values from [28], it can be shown how the $C_L$ does agree with the proposed approach in Equation (6.2). Needless to say, the $C_D$ also matches to a high accuracy level. The only remaining module which can be validated is the environment module, for which the only input was temperature. The densities match for the given temperatures[3]. Unfortunately, the thrust level cannot be directly compared to any available literature, thus cannot be validated in the same manner it was done for the $C_L$-$C_D$ calculator and environment module.

## 6.2. Propulsion and power

With the final goal of accurately sizing the battery, the power consumed by the propulsion system is required. For that, a first order thrust estimate is needed. Iterations were performed in order to come up with a total weight of the drone. The final result was 249.5 ±23.3 g and because the DP-MAV-14 requires the drone to hover at 50% of the maximum thrust, the latter can be found from the equilibrium state to be 500 g of thrust. With this value being fixed, the motors can now be chosen.

DYS 1306 motors[4] with 2,300KV were suited for the current mission, leaving even room for extra payload and safety

[3] `https://en.wikipedia.org/wiki/Density_of_air` [Cited 20 June 2017]
[4] `http://www.dys.hk/ProductShow.asp?ID=115` [Cited 15 June 2017]

margins with a maximum thrust of 130 g each. At this value, a maximum power consumption of 18.5W was registered by the manufacturer´s tests. At 80 g of thrust 11.8 W were consumed and at 40 g of thrust 4.4W were drawn by the motor. These three data points on the thrust vs. required power graph do not lie on the same line and were used for interpolating the points in between. For example if a mission stage requires the drone to hover, it would mean that 249.5 g of thrust are to be provided. This translates to 62.4 g of thrust per motor. With a linear interpolation in between the two data points (40 g and 80 g) 11 W are found to be required by each motor.

All the information about the motors was taken from the experiments that were performed with the DYS 1306 in combination with a 5x3 propeller (5" diameter and 3" pitch). This was found to be the best match for this motor as 5" propellers have usually a low efficiency (because of the small diameter). At maximum thrust, the efficiency of this combo can be expressed by the thrust over power ratio, which in this case is 7 g/W.

## 6.3. Power consumption

In order to find an accurate power consumption, the mission will be divided into seven main stages. For each stage, two main parameters are assigned: the time duration and the subsystems that are needed. The mission is divided into the following phases: take-off, cruise, detecting, pollination, turning, cruise back, landing. For the case of the subsystems, all the subsystems will be grouped into 5 main groups: the fish eye camera, the stereo-avoidance system (stereo cameras), the blower, the propulsion and the electronics which gather the IMU, processing unit with storage, GPU and CPU, laser-avoidance rangers, UWB, multi-function barometer and ESC. In fact, the latter will always be on for all the mission phases. The final flight mission time is found to be optimal at 10.5 min, consequently it will from now on be used as the mission duration. In order to assign the respective times for each phase, the phases of take-off, turning and landing will be assigned fixed times, given that they do not change, are well defined and there is no clear benefit in assigning variable times to them. Then, the phases of cruise and cruise back are variable depending on the stage of the pollination in the greenhouse. But for the nominal mission, they will be assigned average values of distance and time. On the other hand, the phases of pollination and detection are where the maximum time is to be invested and also when the maximum power is required, partly because of the blower drainage. Consequently, the time allocated for them is the remaining time from the flight time minus the other phases. It is assumed that the phases occur subsequent to each other, with the exception of the pollination and detection phases, which occur simultaneously, and turning, which happens at half the time duration of the pollination plus detection phases. More graphically, APIS will pollinate plus detect on one side of the row and when the battery level is at half, it will turn and pollinate the opposite side in the same direction from where it took off. In order to accomplish this, the remaining time of the mission minus the time-fixed phases, is fully dedicated to pollination plus detection. This approach allowed to fiddle with and iterate on the mission time, which will ultimately size the battery capacity needed.

**Take-off** The first phase of the nominal mission is the take-off. In this phase, APIS takes-off from the hanging ground station and sets itself to the height of the top of the crops, from where the navigation to the target commences. For this phase, a height decrease of around 0.5 m has to be covered. This height is the difference between the hanging ground station and the top of the crop. Moreover, a time of 3 s is allocated. When it comes to the subsystems, the electronics must always be on. Also, the stereo cameras will be on for object avoidance, especially for other drones approaching the ground station to charge. Lastly, the propulsion must be on to provide necessary lift to cover -0.5 m in 3 seconds. According to the model previously explained, the power will have to be set to 61.9% of the maximum the motor can consume.

**Cruise** The second phase is cruising to the required location. Given that the distance to travel will depend on what has and has not been pollinated, an average between the best and worst scenario is taken. The best case is that the row to pollinate is right in front of the ground station, so practically speaking, this is a 0 meter distance. On the other hand, the worst case would be having to start from the very end of the row, so a travelling of 100 meter. Consequently, for a nominal mission a distance of 50 meter is taken, for which a duration of 50 seconds is assigned, leading to a speed of around 1.01 meter per second. For the case of the subsystems, electronics will again be on. Similarly, the stereo-avoidance will be on for object avoidance, again focused on other APIS suddenly appearing. The propulsion will have to be powered at a 59.7% of the maximum power to get this done.

**Detection** The phases of detection and pollination happen interleaved. During the detection phase, APIS focuses on flower detection in order to go from one bunch of flowers to the next one. According to the input from ing. Jan Janse, there are around 4.5 plants per meter square, each has one cluster of 6 flowers and there are 63 rows in the greenhouse. Bearing in mind that the blower can pollinate the entire cluster in one go, the distance in between the plants will size

the time for this phase. Considering a greenhouse of 200x200 meters, a total of 180,000 plants are raised inside, which means that there are around 2,857 plants per column. With a length of 100 meters per row, the distance in between plants is of about 0.28 meters. Given that in this phase detection is key, the proposed speed to improve detection is 0.5 meters per second. Assuming from Section 8.6 that 15 frames per second are scanned, then at the given speed each image is 3.3 cm apart. Further including the fact that flowers are in clusters of 15 cm across, the cluster will appear is around 5 frames in the worst case scenario, which seems reasonable to ensure detection. This phase requires the electronics to work together with the stereo avoidance system for obstacle avoidance with special attention to both: APIS and hanging wires. Also, given the soft-start properties of brushless motors and control implications, the blower will be continuously on during the detection and pollination phases, rather than switching in between on and off. The propulsion model outputs a require 59.7% of the maximum power to fly at required speed.

**Pollination** The pollination phase is the heart of the mission. In this phase, three main sub-phases take place: flower detection confirmation, positioning and blowing. For these three, the assigned times are 1 s for confirmation of detection, 4 s for positioning and 6 s for blowing and making sure the flowers are shaken. The times come from conservative analysis on different subsystems, 1 s for confirmation feeds from Section 8.6 and the 6 s for pollination was found to be a conservative value from Section 5.2.4. Lastly, the 4 s for positioning and pointing of the blower was assigned on a conservative basis. As aforementioned, this phase is the core of the mission and for this reason the time for it is adaptable to the level of battery left on board. This being the case, this phase will consume the most energy when compared to the other phases. The subsystems which will work during this phase are the same as for the detection phase, with the main difference of the propulsion thrust. Assuming that this phase will mainly be done in hovering mode, the power output from the model is 59.6% of the maximum achievable.

**Turning** When the battery levels are at half, APIS will initiate the other-side mode, for which a change of heading will be necessary. The assigned time for this task is 2 s. It is assumed that the maneuver can be accomplished by hovering and shifting the rpm of counter-rotating propellers to allow the variation in angular momentum to change the heading. For this, the electronics and stereo avoidance system will be on. To accomplish this, the power setting output is the same as for when hovering in the pollination phase: 59.6% of the maximum power.

**Cruise back** This phase is similar to the second phase, with the fundamental difference that now APIS returns to the hive from its mission accomplished. Nonetheless, when looking at the practical aspect, the distance and time assigned is also set to 50 m in 50 s. As previously discussed, these values are dependent on the stage of pollination of the greenhouse, but for battery sizing purposes a mean value was chosen. The same subsystems that were connected for the cruise phase are functioning here and the same 59.7% of propulsion power is used.

**Landing** The very last phase of the mission is returning home safely to ensure a proper landing to pin charge the battery. Similar to the take-off, APIS has to climb for around 0.5 m to arrive tot he hanging ground station from the top of the crops. Nonetheless, given the added difficulty of the pin charge, extra time is budgeted for this phase, being 10 s. The subsystems used for this phase coincide with the take-off phase with the exception for the propulsion subsystem. The latter is modelled to require a 59.8% of maximum power.

**Power profile and energy consumption overview** At the end of the day, each phase contributes to the final energy with its own power consumption. The final values for these are tabulated on Section 6.3.

From Section 6.3 it can be seen how the phase with the highest power drainage is detection, in fact, after some examination it also turned out to be the mission with the highest required nominal intensity, being 8,716 mA.

However, for the battery it is also important that the ability to deliver sudden short bursts of intensity to allow quick maneuvering. For this purpose, a conservative limit has been chosen for the propulsion subsystem. Assuming that the propulsion will work at a 100% thrust for a quick maneuvering, the intensity it would require to power APIS at the pollinating phase would add to 12,677 mA. These values will be used to size the battery subsequently.

Graphically, the energy consumption can be visualized into a percentile distribution per phase, as it can be seen in Figure 6.3. In this figure, it can be seen how the most energy costly phase is the pollination with up to 77% of the total consumption. This is mainly driven by its lengthily duration. Then, the phases of detection and cruises each consume 6% and 8% of the total energy, respectively. Lastly, for the case of the phases of take-off, turning and landing, their contributions are hardly visible, mainly because they extend shortly in time when compared to the other phases.

Table 6.2: Energy consumption breakdown and power consumed per phase

| Phase | Max power [W] | Energy [J] | Duration [s] |
|---|---|---|---|
| Take-off | 49.376 | 143.1 | 3 |
| Cruise | 49.276 | 2,388.2 | 50 |
| Detection | 50.231 | 1,809.4 | 36.5 |
| Pollination | 49.499 | 24,058.9 | 478.5 |
| Turning | 47.7 | 95.4 | 2 |
| Cruise back | 49.276 | 2,388.2 | 50 |
| Landing | 47.856 | 477.9 | 10 |
| **Total** | **50.231** | **31,361.1** | **630** |

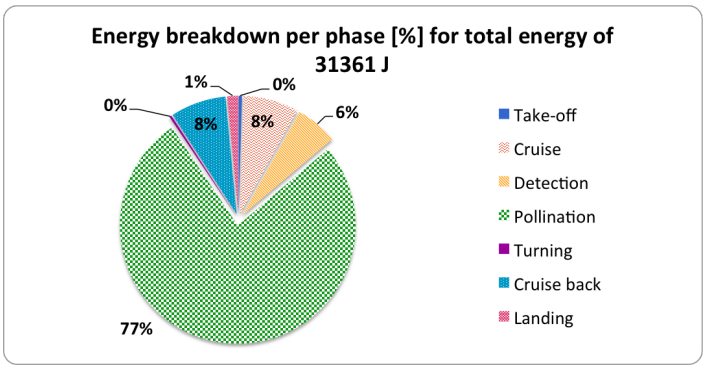


Figure 6.3: Energy consumption per phase during the mission

## 6.4. Battery selection

The battery plays a key role in the mission development. To start with, the capacity sizes the endurance of the mission, the maximum intensity it can deliver constraints the connected subsystems, the maximum intensity at which it can be charged affects the size of the batch of drones in the greenhouse, the voltage has an impact on the number of voltage regulators on board and the choice of motors and, last but not least, the number of cycles the battery can cope without important degradation also has to be taken into account. These properties have to be traded-off with mechanical characteristics like weight and volume.

To start the selection procedure, the voltage required for APIS subsystems was the first design stage. As previously stated, the sized motors for APIS's weight were found to run on 7.4 V. Considering that lithium polymer is the technology found to best fit APIS needs [9], the cell-voltage is 3.7 V, consequently, the battery was already constraint to have a 2S structure. The next step is finding what capacity the battery needs. Following from the mission breakdown and energy consumption, the required watt-hours can be found converting the Joules, from where the capacity follows from the well-known power, intensity and voltage equation. In the end, the energy needed was 31,361.1 J, which meant 1,177 mAh. Also fed from the mission breakdown, the intensity required for both nominal and short sudden bursts must be taken into account to find the C-rate required from the battery. When it came to charging, the shorter the charging time the better at the expense of reduced lifecycles. The approach taken was based on manufacturers' information on the charging capabilities of the pack and if the charging C-rate was pushed more than what was recommended, the lifecycles were lowered for that battery pack.

In the end, the decided approach was looking into currently available solutions at the worldwide supplier HobbyKing[5]. Also following from the requirements (DP-MAV-3-POW-3) to maintain a good battery health, the depth of discharge (DoD) was set to be less than 90%, which means a battery capacity of at least 1,307 mAh. The DoD has been implemented as an extra layer of security for the battery lifetime, given that the manufacturer already designs its batteries with mechanisms to increase it. After a lengthily investigation targeting batteries with more than 1,307 mAh, the main candidates can be found in Table 6.3. Furthermore, a final overview of the required capacities can be found in Table 6.4.

[5] `https://www.hobbyking.com` [Cited 15 June 2017]

Table 6.3: Options for batteries.

| Option | Brand-Family | Capacity [mAh] | Config. | C-rate (Nom, burst, charge) | Mass [g] | Cycles [-] | Price [€] | Comments |
|---|---|---|---|---|---|---|---|---|
| 1 | Turnigy-Lipoly[a] | 1500 | 2S1P | (25C, 35C, 5C) | 84 | 160+ | 8.92 | - |
| 2 | Turnigy-Nanotech[b] | 1500 | 2S1P | (20C, 40C, 5C) | 75 | 250+ | 8.78 | - |
| 3 | Turnigy-A spec G2[c] | 850 [1700] | 3S1P [2S2P] | (60C, 90C, 15C) | 84 [112] | <320 | 11.51 [23.02] | [Customized: buy 2, get rid of 1 cell in each and place them in parallel.] |
| 4 | Zippy-Compact[d] | 1500 | 2S1P | (40C, 50C, 5C) | 99 | 100+ | 10.81 | - |
| 5 | Turnigy-Graphene[e] | 1500 [1500] | 4S1P [2S1P] | (45C, 90C, 15C) | 201 [100.5g] | 900+ | 14.62 | [Customized: get rid of 2 cells to end with right voltage and modify dimensions to be 139x27x15 $mm^3$] |

[a] https://hobbyking.com/en_us/turnigy-1500mah-2s-25c-lipoly-battery.html [Cited 23 June 2017]
[b] https://hobbyking.com/en_us/turnigy-nano-tech-1500mah-2s1p-20-40c-lipo-receiver-pack.html [Cited 23 June 2017]
[c] https://hobbyking.com/en_us/turnigy-nano-tech-a-spec-g2-850mah-3s-60-90c-lipo-pack.html [Cited 23 June 2017][Cited 23 June 2017]
[d] https://hobbyking.com/en_us/zippy-compact-1500mah-2s-40c-lipo-pack.html [Cited 23 June 2017]
[e] https://hobbyking.com/en_us/graphene-1500mah-4s-45c-w-xt60.html [Cited 23 June 2017]

Each of the above batteries are the best suited from their technology family or available brand. However, only one can be chosen for APIS.

Table 6.4: Overview of capacities for battery selection

| | DoD [%] | Capacity [mAh] |
|---|---|---|
| Nominal mission | 100 | 1177 |
| From requirement | 90 | 1307 |
| Chosen battery | 78.5 | 1500 |

Considering a self-posed margin of around 105 g and €50 for the battery, almost all the above options fit, except for number 3, which is heavier due to its overdesigned capacity, so it will be discarded. As it can be directly seen, option 1 has no added value when compared to number 2, consequently it can be directly discarded. Now that the remaining options (2,4,5) adapt to the energy and intensity consumption, a check on the charging capabilities followed. Lithium polymer technologies bears the ability to be charged at an intensity higher than for lithium-ion, in fact manufacturers will always provide the maximum charging rate that can be used without incurring into overheating problems. From experience, the lower the C-rate used the less the lifecycles get affected [6]. This is especially the case if the recommended C-rate is further above the charging C-rate, however there does not seem to be enough literature on this matter and relying on hobbyist proves to be one of the few available sources. For the chosen battery and the given consumed energy, the time for charging results from the Equation (6.8):

$$\text{Charging Time} = \frac{\text{Energy Consumed [mAh]}}{\text{Nominal Intensity [mA]} \cdot \text{C} - \text{rate}} \cdot 3600 = \frac{1177}{1500 \cdot \text{C} - \text{rate}} \cdot 3600[s] \tag{6.8}$$

Consequently, when looking at the options provided in Table 6.3, the best options would be either option 3 or 5, but given that 3 is discarded, option 5 would be the most suitable for this aspect. However, charging at such a high C-rate might still have detrimental effects on the battery lifecycle [7], consequently, a more conservative value is chosen for the charging C-rate. Aiming to have a charging time of 15 min, in order to result in a total number of 58 drones and at least 7.25 ground stations, from the drone sizing model calculation, the final C-rate required is of 3.1C. A key check is that the required intensity can be met by the battery. For this, the discharge C-rate is looked into. Knowing that the mission entitles a nominal intensity of 8,716 mA and a maximum sudden burst of 12,677 mA, the options must at least have 5.8 nominal and 8.45 burst C-rate. Given that all the options check out, this is not a driving design requirement. Another important factor is the cycles of life. According to HobbyKing [8], Zippy batteries make around 100 lifecycles, Turnigy Lipoly around 160 and Turnigy nano-tech makes it all the way to 250 lifecycles. On the other hand, the new technology of graphene anodes allows for a longer cycle life at the expense of some extra weight. Ultimately, the lifetime of the

[6] Private conversation with Erik van der Horst, MAV lab, TU Delft
[7] https://www.rcgroups.com/forums/showthread.php?2748131-Does-charging-at-more-than-1C-reduce-battery-life [Cited 23 June 2017]
[8] http://www.hobbyking.com/hobbyking/store/ebasic.asp [Cited 23 June 2017]

battery was considered to be a key parameter. Not only it heavily impacts sustainability, but it also forces the farmer to perform battery replacements more frequently, which is always undesired. Thus, considering the lifetime, for a mission that takes 10.5 min and charges for 15 min for 12 hours during every 3 days, a battery of a 100 cycles will have to be replaced every 3.6 days. For the case of option 5, the graphene-anode battery, the lifetime could be stretched up to around 4.6 weeks of battery up to a 80% degradation. Considering that the battery is currently with a DoD of 78.5%, the limit of usable life of the battery will lay around these 900 cycles. Having weighted all of the above, the battery which seems to best suit APIS is option 5, the customized state-of-the-art graphene electrode battery. Lastly, concerning size, the size of the battery will be adapted to the drone sizes, however the volume will be kept constant. Using an initial size of 107x35x28 $mm^3$, this has to be halved following the cut in the number of cells, and then the final dimensions will be 139x27x15 $mm^3$, which matches the needed volume. As a last advantage of the graphene technology, the internal resistance (IR) is usually smaller than for conventional Li-Po batteries. In fact, according to the manufacturer, an IR of only 1.2 miliOhm is present. Conservatively speaking, using the maximum intensity found along the mission, 8,716 mA during detection, and taking it for the entire 10.5 min of the mission, only 57 J or 0.1% of the total energy consumed is loss in this resistance. Internal resistance has thus not being considered for the battery sizing. The final battery properties can be found in Table 6.5.

Table 6.5: Final battery implications for customized Turnigy graphene 2S1P 45C to 90C

| **Mass [g]** | **Capacity [mAh]** | **Charging time [min]** | **DoD [%]** | **Lifetime [h]** | **Change every [Days]** | **Dimensions [mmXmmXmm]** |
|---|---|---|---|---|---|---|
| 100.5 | 1500 | 15.2 | 78.5 | 385.35 | 32.11 | 139x27x15 |

## 6.5. Blade element momentum theory

To validate the thrust that is produced and to find the induced velocity, a blade element momentum analysis is made. The rotor is divided in a number of elements. At each element, a set of non-linear equations is set up, based on force and momentum balance. This set of equations can be solved and the overall thrust of the rotor can be found[9]. First, the elemental thrust of a blade element $dr$ can be found using Equation (6.9), where V denotes the section local flow velocity, B the number of blades, $\overline{c}$ the local chord length, $C_l$ and $C_d$ denote the local lift and drag coefficients respectively and $\phi$ is the local angle between the axial and tangential flow velocities. The section local flow velocity can be found by summing the axial and tangential velocities $V_0$ and $V_2$, as described in Equation (6.10).

$$dT = \frac{1}{2}\rho V^2 B\overline{c}(C_l\cos\phi - C_d\sin\phi)dr \quad (6.9) \qquad V = \sqrt{V_0^2 + V_2^2} \quad (6.10)$$

The tangential velocity $V_2$ is assumed to be equal to the rotational speed of the propeller times the distance. The axial velocity $V_0$ can be assumed to be equal to the induced velocity below the motor $V_i$. and is more difficult to calculate. As it is dependent on the local thrust at the several blade elements, an iterative process should be performed to converge to the induced velocity. The local thrust from Equation (6.9) can be integrated over the radius of the propeller to find the total thrust that is required. Further inputs that are required, are the local lift and drag coefficients, the shape of the propeller and the number of rotations per minute. The coefficients are assumed from simple linear lift behavior ($C_l = 2\pi\alpha_{loc}$). The propeller is assumed to have a constant chord length over the radius of 1 cm and a constant blade pitch of 16 degrees. Another assumption is that no tip loss is calculated and that all the thrust is produced between $0.2\overline{c} < \overline{c} < 0.95\overline{c}$. Running this model over 16 blade elements and 7,500 rotations per minute gives an induced velocity profile. The total thrust of four motors at this condition is 246.7 grams. In Figure 6.4, the induced velocity is plotted.

[9] `http://s6.aeromech.usyd.edu.au/aerodynamics/index.php/sample-page/propulsion/blade-element-rotor-theory/` [Cited 7 June 2017]

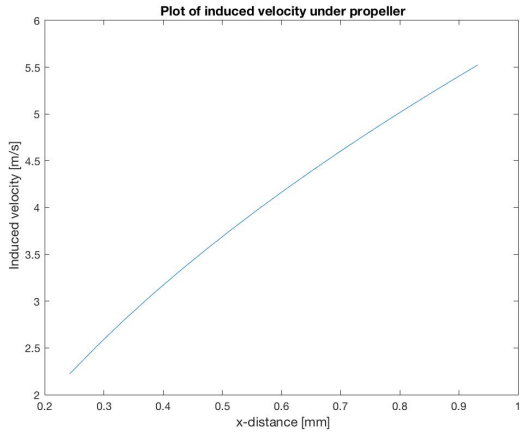


Figure 6.4: Induced velocity over length of the rotor

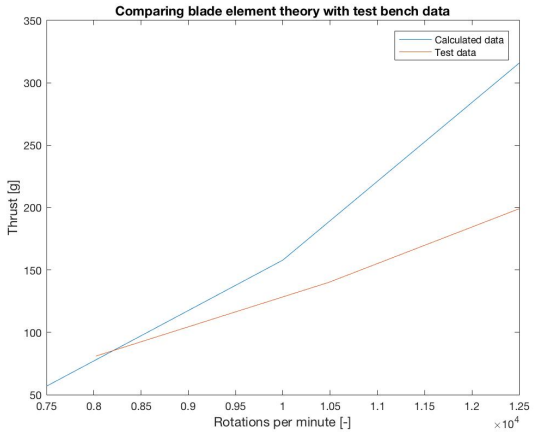


Figure 6.5: Comparing test data with blade element theory calculations

The model is verified using the limit cases. For example, zero RPM should yield zero thrust, in the model, this is the case. Also, the results of the model are compared with a tool from internet [9]. Finally, the model is validated comparing the results to actual test data from an article [29]. Comparing with this data gives no large discrepancies. Finally, to validate the model, it is useful to compare the test data of the actual propeller of the APIS with the blade element model. A test was performed [10], where thrust force is tabulated together with the rotational speed, using the 5030 propeller. This comparison is shown in Figure 6.5.

For the lower magnitude of revolutions per second, the total thrust seems to match quite well. At a higher number of rotations per minute, the thrust quickly diverges. This can be explained by the assumption of linear lift behavior and the constant angle of attack. In reality, at higher speeds, flow separation of stall phenomena occur, while this is not modeled in the analysis.

[10] `http://www.myrcmart.com/rcx-h1306-3100kv-micro-outrunner-brushless-motor-efficiency-racing-p-7937.html` [Cited 21 June 2017]

# 7

# Electronics

This chapter will show the process used for establishing the final electronic system of the quadcopter. First, the components that are needed will be described, which are the microcontroller Section 7.1, the communication system Section 7.2 and the sensors Section 7.3. After that the electrical design process will be described and the block diagram will be provided, Section 7.4. Also a mass and power estimation will be given, Section 7.4.3. Finally, a insightful description about wiring will be given in Section 7.5

## 7.1. Microcontroller

As in many of the nowadays smartphones, the microcontroller forms the base of an electronic system. It basically consists of a small computer known as system on a chip (SoC) or integrated circuit (IC). This is composed of central processor units (CPU), memory (ROM, RAM or flash) and pins for input/output peripherals. The microcontroller often also include a graphics processor unit (GPU), a digital signal processor (DSP) and support for camera, display, location of connectivity (LTE/Wi-Fi/BT).

The microcontroller should come pre-loaded with a bootloader in order to make it possible to be program the controller through USB (an example could be DFU Bootloader). The peripherals, or in this case the sensors, can be connected through different interfaces, the most common ones being the SPI (Serial Peripheral Interface), UART (Universal Synchronous/Asynchronous Receiver Transmitter) or I2C (Inter-Integrated Circuit). SPI is faster and it requires 4 lines: SCLK, MOSI, MISO, SS; I2C requires only 2 lines: SDA bidirectional data and SCL, same as UART with Tx and Rx lines (one transmitting to the receiver and the other one revceiving form the transmitter). To conclude, if there are plenty of IO lines, SPI is better because it´s up to 2-3 times faster.

The number of bits of a microcontroller refers to the size of the data bus. In general, heavier computations can be performed on a larger data bus. Hobbyists usually opt for 8 or 16 bit with less than 128kB of flash ICs for a simple drone because it is sufficient for the level of computations required and it is easier to solder (less pins). The components of the SoC are hereby discussed.

**CPU** The Central Processing Unit is the chip in charge of handling the arithmetic, logic and pin operations required by the software. This part of the microcontroller can be chosen on the basis of three main characteristics: clock rate, instructions per clock and, their product, Instructions Per Second (IPS). Nonetheless, this information is rarely used due to the difficulty of coupling it with the requirements from the desired algorithm.

**GPU** As for the Graphical Processing Unit, it allows to process lots of arithmetic threads by using multiple small cores; however, not all microcontrollers for MAV are equipped with it. In fact, it is only considered here due to the demand from the optical flow and stereo matching.

**DSP** The Digital Signal Processor is a chip whose sole function is to process digital inputs, which can come from a ADC or from the communication subsystem. Modern microcontrollers take care that the DSP matches the CPU and GPU processing capabilities.

**Flash memory** The flash memory is the storage capacity of the microcontroller. Here the data is stored from the in-flight sensor measurements. It has to be sized to handle the monitoring images for the entire flying time. The downloading capacity also plays a role here.

**(S)RAM** The (Static) Random Access Memory is the memory space where calculations take place. The higher the amount of RAM, the more information "readily available". The RAM requirement comes from the chosen algorithm and it is also limited by the amount of bits the microcontroller runs at.

**(EEP)ROM** The Electronically Erasable Programmable Read-Only Memory is the location where the instructions are stored. The MAV reactions to external stimuli are based on the code found in this location. The memory size of the code is the main input to size it.

**I/O pins** The number of available Input/Output pins basically allows to attach more or less external sensors. The protocol on which they run also has a major effect on the final required number of pins. The microcontroller must have enough pins to connect all the required sensors.

**ADC/DAC** The Analog to Digital or Digital to Analog Converters, are usually coupled to the pin capabilities and they transform the analog to digital signal and viceversa. These are rarely a variable when choosing a microcontroller, as they come together with the pin choice.

## 7.2. Communication

The choice of communication was previously discussed to be the DecaWave Module 1000[1]. However, in order to integrate the DWM1000, the microcontroller must have at least one SPI port open. This means that 4 pins on SPI protocol must be available, namely, one for chip select, Master Output Slave Input (MOSI), Master Input Slave Output (MISO) and clock. Lastly, this module requires a 3.3V input, a ground output and a reset input. The module will take an area of 13±0.2 x 23±0.21 $mm^2$ on the board.

## 7.3. Sensors

Similar to insects, the pollinator drone also needs sensors to monitor and fly around in its environment. In the greenhouse, environmental conditions are challenging. The temperature range is between 28 and 35 degrees Celsius and average humidity is around 70%, with maxima lying at 95%, minima lying around 40%[2]. Moreover, there is a need for having a mobile sensory system on board a flying vehicle. Therefore, it is investigated if such a sensor can also be incorporated in the electronics. These sensors can gather data all around the greenhouse and allow for more accurate climate control and failure detection [30]. Temperature and humidity models in greenhouses are well researched and implemented. A Mini-UAV based sensory system for greenhouses has been designed and used [31]. In this study, the DHT-22 temperature/humidity sensor from Table 7.1 is used, combined with a luminosity and $CO_2$ sensor. Challenges lie in accurately choosing the position of the sensor and defining the influence of the airflow on the sensor. Errors for the measurements are around 4%. Therefore, it can be stated that all the sensors listed in Table 7.1 can measure temperature and humidity accurately enough for control and monitoring for the farmer.

Table 7.1: Humidity and temperature sensors. The T and the H in the accuracy column are the temperature and humidity, respectively

| Sensor | Voltage [V] | Current [mA] | Accuracy |
|---|---|---|---|
| **DHT-22** | 3.3 - 3.6 | 1.5 | T: ±0.5 °C<br>H: ±2% |
| **DHT-11** | 3.0 - 5.5 | 2.5 | T: ±2°C<br>H: ±5% |
| **BME280** | 1.7 - 3.6 | 0.0036 | T:± 0.1 °C<br>H ±3% |
| **HTS221** | 1.7 - 3.6 | 0.002 | T: ±0.5 °C<br>H ±3.5% |

Generally, most small aerial vehicles have a barometer to accurately measure the height at which it is flying. In Table 7.2, a list of barometers is presented. Looking at the table, its relatively small size and low cost stand out. Attentive readers might have seen a commonality between the temperature/humidity and barometer table. The BME280 is an environmental sensor that can measure temperature, relative humidity and pressure.

[1] `https://www.decawave.com/products/dwm1000-module` [Cited 9 June 2017]
[2] Talk with greenhouse expert Jan Janse, 2 June 2017

Table 7.2: Barometer sensors. Note that all the barometer sensors have an accuracy of 8.33 cm/pa

| Sensor | Max Amps [$\mu$A] | Max Voltage [V] | Cost [$] | Size [mm] |
|---|---|---|---|---|
| **BME 280** | 3.6 | 1.2-3.6 | 7.5 | 2.5 x 2.5 x 0.93 |
| **BMP 280** | 2.7 | 3.6 | 3.87 | 2.0 x 2.5 x - |
| **BMP 380** | 2.0 | 3.6 | - | 2.0 x 2.0 x 0.75 |
| **SPT-B10W** | - | 1.8 | - | 1.4 x 1.0 x 0.6 |
| **MPL115A1** | 10 | 5.5 | 2.12 | 5.0 x 3.0 x 1.2 |
| **MS5607-02BA03** | 12.5 | 4.0 | 3.68 | 5.0 x 3.0 x 1.0 |

Another unit that is needed in order to control the quadcopter is the inertial measurement unit (IMU). This unit consists of accelerometers, gyroscopes and magnetometers and these are essential to know the orientation of the quadcopter. For choosing the IMU, the following aspects are considered: mass, power consumption, communication, cost and size. Table 7.3 shows the IMUs that are suitable for the mission, including their properties. Moreover, not only the aspects mentioned in the table have been considered, also the number of bits and pins have been investigated. These aspects are important in order to size the micro controller. Due to the fact that for the inertial measurement units these values are mostly the same, these columns have not been included in the table. The number of bits is 16 and the number of pins is 24. However, for the ones without a magnetometer the number of pins is less. For the BMI160 and the BMI055 the number of pins are 14 and 16, respectively.

Table 7.3: Inertial measurement units and their properties. Note the mass is not for the chip, but for the breakout (PCB included). The (no mag) after a IMU serial number is added if there are no magnetometers included

| Sensor | Mass [g] | Current [mA] | Voltage [V] | Communication | Cost [dollar] | Size [mm] |
|---|---|---|---|---|---|---|
| **MPU-9250** | 8.5 | 3.5 | 2.4 – 3.6 | $I^2C$ (400kHz)<br>SPI (1MHz) | 14.95 | 3.1 x 3.1 x 1.05 |
| **LSM9DS1** | - | 4.6 | 1.9 - 3.6 | $I^2C$ (100kHz<br>or 400kHz)<br>SPI (1MHz) | 24.95 | 3.5 x 3.0 x 1.0 |
| **MPU-6050** | 85 | 0.50 | 2.3 - 3.4 | $I^2C$ (400kHz)<br>SPI (1MHz) | 39.95 | 25.5 x 15.2 x 2.48 |
| **BMI160 (no mag)** | - | 0.95 | 1.2 - 3.6 | SPI, $I^2C$,<br>4x digital | - | 2.5 x 3.0 x 0.8 |
| **BMI055 (no mag)** | - | 5.15 | 1.2 - 3.6 | SPI, $I^2C$,<br>4x digital | - | 3.0 x 4.5 x 0.95 |
| **FIS1100 IC,** | .146 | 0.990 | 2.4 - 3.0 | SPI, $I^2C$ | 9.36 | 3.3 x 3.3 x 1.0 |
| **IMU-3000** | 0.091 | 6.1 | 2.1 - 3.6 | $I^2C$ | 9.82 euros | 4.1 x 4.1 x 0.95 |
| **LSM303C** | 8.5 | 4.90 | 1.9 - 3.6 | $I^2C$ (100kHz<br>or 400kHz)<br>SPI (1MHz) | 14.95 | 2.0 x 2.0 x 1.0 |

## 7.4. Electrical design

In this section, the final design of the electronics on board the drone will be presented. The interaction between the peripherals and the main controller are explained and illustrated in a block diagram (Figure 12.5). Although the main focus is on the interfaces between the components needed, a full schematic of the printed circuit board (PCB) will not be provided in this report, due to the copyrights of Qualcomm. After the choice of the microcontroller needed, a general explanation of the Snapdragon flight kit is provided on Section 7.4.1. Once the kit is presented, the steps to optimize it will be discussed on Section 7.4.2. Lastly, the positive consequences of this optimization are given on Section 7.4.3

### 7.4.1. Snapdragon Flight kit

The Snapdragon Flight kit provides with the state-of-the-art most basic elements to program the controller for the drone. This kit allows the buyer to code the brain of the drone from scratch, making it a really attractive option for developers. In a nutshell, these type of System on a Chip (SoC) are equivalent to a small, yet powerful, on-board computer and they come with their own power feeder and data bus. This computer is initially required to stabilize the drone, but with the recent advances on computer technology, more applications can be done on-board, such as image recognition or autonomous flight.

In order to accomplish these, a powerful CPU, GPU and DSP come installed on the microcontroller i.e. Snapdragon 801 (illustration in Figure 7.1[3]). In fact, the computing power on-board allows to not only analyze data from the sensors, but also to transmit it. The development board can also communicate wirelessly through all the current technologies, such as Bluetooth, LTE or Wi-Fi, apart from modern Near Field Communications (NFC). As an example, the development board can extract velocity out of optic flow and record high resolution video, while enabling a wireless communication, running a heavy-duty algorithm and balancing the drone all at the same time a GPS location is looked for. Furthermore, the board comes with the possibility to connect more external sensors for other activities, which allows for even more design space.

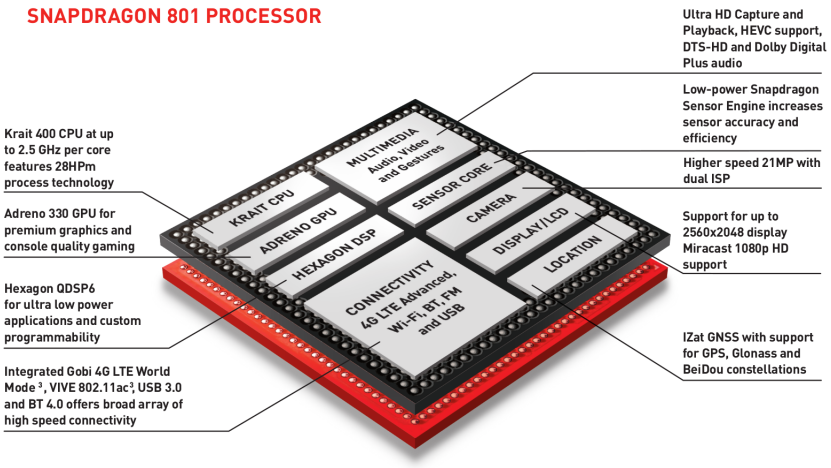


Figure 7.1: Snapdragon 801 microcontroller features

More exhaustively, the Snapdragon Flight kit comes with the development board, a 4K and an optic flow camera, a power adapter and a serial connector. It features a Qualcomm Snapdragon 801 microcontroller with 2GB of RAM and 32GB of flash. On the board itself an IMU (MPU-9250) and a barometer (BMP-280) are installed as well as modules for GPS, WLAN and Bluetooth. External connectors for GPS and WLAN antennas are implemented together with and SD card slot, an ESC connector on I2C, a USB 3.0 connection and other external ports for sensors on I2C or UART interfaces. A diagram of the board can be seen in Figure 7.2[4][3] and the corresponding pin-outs and external connectivity options are summarized in Table 7.4[5][3].

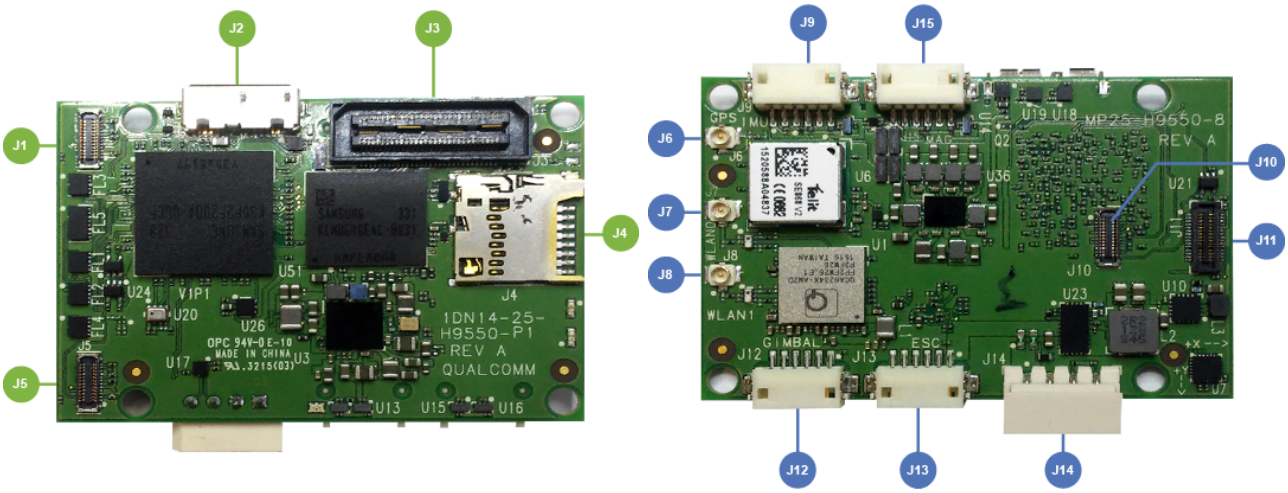


(a) Front side

(b) Back side

Figure 7.2: Illustration of the Snapdragon Flight PCB. The connectors J1 to J15 are described in Table 7.4

[3] https://www.intrinsyc.com/vertical-development-platforms/qualcomm-snapdragon-flight/ [Cited 12 June 2017]

Table 7.4: The external connections of the Snapdragon Flight

| Connector | Function |
|---|---|
| J1 | Stereo camera (Right) |
| J2 | USB 3.0 (KMMX-AB10) max. 2A |
| J3 | Debugging expansion B2B, 60 pins available |
| J4 | Micro-SD slot |
| J5 | Stereo camera (Left) |
| J6 | GPS passive antenna configuration |
| J7 | WLAN0: Wi-Fi MIMO Channel 0 |
| J8 | WLAN1: Wi-Fi MIMO Channel 1, Bluetooth 4.0 |
| J9 | BLSP2: External IMU or GPS (on UART or I2C interface) |
| J10 | Optic flow camera (640×480px) |
| J11 | High resolution camera (4K) |
| J12 | BLSP8: External gimbal or sensor (on UART interface) |
| J13 | BLSP6: External ESC (on UART interface) |
| J14 | 5V DC IN (max. 2A) with I2C interface for Advanced Power Management (APM) |
| J15 | BLSP9: External magnetometer/radio receiver/sensors (on UART or I2C interface) |

### 7.4.2. Flight board optimization

Fortunately, the spectrum of features the Snapdragon can accomplish is too broad for this mission. Consequently, in order to save on both power and mass, several modules will be disabled or completely removed. These changes will adapt the electronic system to the exact mission requirements and enhance the final performance, especially on the battery side. In this subsection, the customization process will be shown and explained, including the required additions to the board and the modules which were eliminated. An overview can be found in Table 7.5.

Table 7.5: Modifications on Snapdragon 801

| Removed | | Add-on |
|---|---|---|
| *Module* | *Jumper* | Ultra wide band [DWM1000] |
| Barometer [BMP280] | (U20) | Barometer, thermometer & humidity [BME280] |
| Bluetooth/WLAN [QCA6234] | J7, J8 | Power module [LTC2960] |
| GPS [SE868V2] | J6 | ATmega 328 |
| Micro SD | J4 | |
| USB 3.0 | J2 | |
| Optical flow camera | J10 | |
| External sensors [BLSP (2,8,9)] | J12, J13, J15 | |

**Barometer** Bosch has recently released a new version of the BMP280 barometer which incorporates more functions than just measuring the pressure. The new chip is BME280 and in addition to the pressure, it also measures the temperature and humidity. With only an extra 25% in surface (from 2x2.5 mm to 2.5x2.5 mm) and extra 30% in power consumption (from 2.8 $\mu$A to 3.6 $\mu$A) the new sensor is relatively small and consumes an insignificant amount of power compared to the entire electronic system. The added value (i.e. getting more data) can be used as an extra feature in monitoring the plants better, possibly generating heat and humidity maps of the greenhouse. This is not a requirement, but in the future a software update can be released to incorporate extra functionality. It is noted that the electronic schematic does not require any modifications for implementing the new chip. It has the same number of pins (8) and it works on the same interface (I2C).

**GPS, WLAN & UWB** The module SE868V2 used for GPS signal reception is interesting for autonomous MAVs, but in closed environments the signal acquisitions deteriorates. In order to fix this, a different positioning technique was chosen, namely the ultra wide band module provided by decaWave, DWM1000. Furthermore, DWM1000 allows to also transmit data wirelessly at different rates (110kbps, 850kbps or 6.8Mbps). Provided that the mission is to be performed autonomously, that the images will be downloaded during the 15 min of charging and that only location data is to be shared at all moments, the data rates are good enough for the mission. Consequently, the dedicated module

for communications, QCA6234, based on Bluetooth and WiFi is no longer needed. By implementing these changes, a save on power of 52% can be achieved; the SVE868V2 and the QCA6234 consume 45 and 260 mA respectively, while the DWM1000 only consumes 160 mA. Moreover, DWM1000 is a mere 17% of the surface area of QCA6234 plus SVE868V2.

The UWB module requires 4 lines of communication with the main controller i.e. the Sanpdragon 801 via the SPI interface. The data sheet of the Snapdragon Flight board provides information about additional I2C and UART interfaces as being available[6], but it does not mention anything on SPI. The serial peripheral interface is the only bus supported by the decaWave DWM1000. Given that the IMU on board the flight controller is already connected on SPI and that it is assumed there are no more slaves supported by the Snapdragon 801, it was decided that the IMU (MPU-9250) will be connected on the I2C interface as it supports both SPI and I2C. With the main advantage being that the UWB module could be now implemented, the cost paid is on the clock speed. As mentioned in the beginning of this chapter, the I2C is two times slower than the SPI, lowering the IMU data to 400 kHz. However, this is not a big problem, since the closed feedback loop between the IMU and the motors was originally on 400 kHz, as the interface for electronic speed controllers (ESCs) is on UART not SPI.

**SD & USB** Transmitting data to the Snapdragon 801 can be accomplished in several ways: through the USB 3.0, the micro SD and the debug connector. In order to reduce surface, power and mass, only one of these three is required to load the code for the mission. Given that this will be done once in every long time, a high data rate is not of utter importance. This can rule the USB 3.0 out, plus this connector requires of 9 connections points while the debug connector is based on a USB 2.0 with only 4 connectors. The main advantage of the SD slot is the increase on flash memory, however given the 32 GB of flash on the Snapdragon, it is not that advantageous. Consequently, given that the debug connector can also accomplish data transfer, the USB 3.0 and SD slot have been removed. At the end of the day, this change means saving 62% on surface area (from 396.9 $mm^2$ to 149.8 $mm^2$) and 35% on power (from 4.3 W to 2.8 W) was accomplished by this change.

**External connectors** One of the many positive aspects of the Snapdragon 801 is the amount of available external ports, Table 7.4. Nonetheless, for this specific application, three of them will be removed for the sake of power and surface area reduction. In fact, the jumpers 9, 12 and 15 will be disabled and dismounted. Jumper 9 was there to allow for an external IMU or GPS, but an IMU is already on board and, as previously reasoned, a GPS is not useful in a closed environment. For the case of Jumper 12, a gimbal is not required for this particular MAV, thus this port is not required. Lastly, the jumper 15 is meant for an external magnetometer or a radio receiver, which for this application do not add extra value. These removals will ultimately reduce the mass of the board. Plus, each jumper requires of its own voltage regulator before attaching to the main board, thus the power consumption will be also benefited.

**ESC** The ESCs (one for each motor) will also be added on the main PCB. Such a speed controller consists of several MOSFETs which work on PWM (pulse width modulation). A low level signal is sent from the main controller to control the gates that feed in high current to the motors. Because there is no information on the Snapdragon being able to send PWM signals, an additional controller ATmega328 will be added as an interface between Snapdragon 801 and the actual MOSFETs. Therefore connector J13 from Table 7.4 will be used to send UART signals to the ATmega328 which would be able to send further PWM signals to the MOSFETs. Five ESCs will be considered for APIS. Four for the main rotors and one for the fan blower.

**APM** In order to allow for a proper battery-board communication, an Advanced Power Module (APM) is required. For this purpose, a wide range APM (LTC2946) is chosen to monitor the battery current, power, voltage, charge and energy at any moment. The benefit of this module on board is that battery charging monitoring can be done on-board, thus the charging process can also be done autonomously. According to its datasheet, implementing this module on-board would cost 10 mW (1.3 mA at the battery 7.4 V).

### 7.4.3. Mass and power estimation

Now that all the components are known, the mass and the power consumption can be determined. Due to the fact that the mass of most of the components are unknown, a different approach should be used in order to get a mass estimation. Since the mass and volume of the Snapdragon Flight are known, these can be used in order to calculate the mass of all the components. The first step is to find the volumes of the components. After this, the volume of the components that will not be used are subtracted of the total volume of the Snapdragon Flight and the volumes of the components that are

[6] `https://www.intrinsyc.com/vertical-development-platforms/qualcomm-snapdragon-flight/` [Cited 12 June 2017]

not provided by the Snapdragon Flight will be added. Now, by using the relation between the mass and the volume, the mass of the electrical system can be calculated. This method will be verified by checking if the area and volume of all the components is the same as the area and volume of the Snapdragon Flight.

First the area will be investigated. This is done by estimating the size of the PCB that is needed to combine all the components. In order to estimate the size of the PCB it is assumed that the PCB should have an area which is the same as the areas of the components combined. When using this method the area of the PCB is 1493.3 $mm^2$, the the area of the Snapdragon Flight is 2320 $mm^2$ (58 x 40 mm)[7]. This gives a difference 35 %, which can be explained by the fact that the components do not lie exactly next to each other, there should be extra space for circuits. This can be seen in Figure 7.2. Now by using a typical PCB thickness of 1.6 mm [8], the volume can be verified. By adding all the volumes of the components a total volume of 4953.2 $mm^3$ is determined. The volume of the Snapdragon Flight is estimated to be 5336 $mm^3$. This gives a difference of 7.2%. Lastly, the mass of the Snapdragon Flight board is estimated. A prototype of the board was obtained and weighed by people from the MAVlab. A weight of around 30 grams was found, including plastic attachments and the camera. The weight for the board only was estimated to be 18 grams. Some online sources state even lower values[9], but their numbers are not verified.

Now that the area and the volume are estimated, it is possible to remove and add the components that are needed for this project. The list of components used with their volumes can be seen in Table 7.7. The total volume of all the components is 3443.2 $mm^3$. By using the relation between the mass and the volume of the Snapdragon Flight a density of 3.37 $g/cm^3$ is obtained. Using this density gives a mass of 11.6 grams, which is 35.4% lower than the Snapdragon Flight.

In order to find the total power of the electrical system, the power consumption of the components should be known. This can be done by looking at the data sheets provided by companies. The power consumption will be provided in terms of current, because this is directly related to power. The power consumption can be seen in Table 7.7. What can be seen in the table is that the total power consumption is 2039.3 mA of the modified Snapdragon Flight. For the Snapdragon Flight the total power consumption is 2292.5 mA. This means that the power consumption of the new system uses 11.0 % less power than the Snapdragon Flight.

## 7.5. Wiring

To provide power to the motors and to transmit data between the motor and the processor, wires need to be installed between these two systems. Wires are usually represented by the American Wire Gauge (AWG). A higher AWG number means a lower diameter wire that can carry less current. Two wires, one positive and one negative, provide the power to the motors. These need to be able to sustain a current of 3 A. These cables are 26 AWG ones [10], with an outer diameter of 1.5 mm, can sustain 3.5 A maximum and weigh 3.5 grams per meter [11]. Moreover, from each motor, three wires need to transmit data with a current of at most 0.05 A. Therefore, the smallest wire available at Hobbyking [12], the 36 AWG wire is chosen. These wires have an outer diameter 0.3 mm and an estimated weight of around 0.2 gram per meter. The distance from the motor to the battery is 150 mm. From these values, Table 7.6 can be made. Having eight AWG26 wires gives a wire mass of 4.2 grams. The twelve data wires have a total mass of 0.36 gram. This gives a total wire weight of around 4.6 grams.

Table 7.6: Overview of wire length, wire type and mass

| Type | # of wires per motor | Type and max. current | Length [mm] | Weight [g] |
|---|---|---|---|---|
| **Power** | 2 | AWG26 - 3.5 A | 1200 | 4.2 |
| **Data** | 3 | AWG36 - 0.05 A | 1800 | 0.36 |

[7] https://www.intrinsyc.com/vertical-development-platforms/qualcomm-snapdragon-flight/ [Cited 12 June 2017]
[8] http://blog.7pcb.com/pcb-thickness-options/ [Cited 12 June 2017]
[9] https://finance.yahoo.com/news/intrinsyc-distribute-qualcomm-r-snapdragon-130000236.html [Cited 12 June 2017]
[10] https://hobbyking.com/en_us/catalog/category/view/s/26awg/id/6905 [Cited 23 June 2017]
[11] https://hobbyking.com/media/file/480129157X285439X54.jpg [Cited 23 June 2017]
[12] https://hobbyking.com/en_us/catalog/category/view/s/36awg/id/6849 [Cited 23 June 2017]

Table 7.7: Components used in the electrical system with their current and volume. Note that the volumes of the cameras are not taken into account for the total volume, this is because the mass of the cameras are known

| **Component** | **Serial number** | **Current [mA]** | **Volume [mm$^3$]** |
|---|---|---|---|
| Ultra wide band x 2 | DW1000[a] | 320 | 57.6 |
| Temperature, humidity and barometer | BME280[b] | 0.0036 | 5.8 |
| Flight controller | ATmega328[c] | 0.3 | 85.6 |
| Charging system | SMBC PM8941[d] | 900.0 | 8.0 |
| IMU | MPU9250[e] | 3.7 | 10.1 |
| Voltage regulator | TPS62130RGTT[f] | 10.0 | 11.6 |
| Storage | EMMC flash 32 GB (KLMBG4GEAC-B031)[g] | 180.0 | 149.5 |
| Debug interface | J3 connector[h] | 2000.0 | 456.9 |
| Processor | Snapdragon 801 (APQ8074)[i] | 50.0 | 236.6 |
| Charge and Energy Monitor | LTC2946[j] | 1.3 | 9.0 |
| Mosfetdigital power conversionmicrocontrollers | PM8841[k] | 940.0 | 7.7 |
| Cameras | Stereo pair plus fish eye camera [Chapter 8] | 325 | - |
| Lasers x 2 | VL53L0S | 19 | 21.12 |
| Connectors | J1 to J11 connectors | - | 451.4 |
| PCB | - | - | 1450.8 |
| **Total** | | **2039.3** | **3443.2** |

[a] https://www.decawave.com/sites/default/files/resources/DW1000-Datasheet-V2.12.pdf [Cited 12 June 2017]
[b] https://ae-bst.resource.bosch.com/media/_tech/media/datasheets/BST-BME280_DS001-11.pdf [Cited 12 June 2017]
[c] http://www.microchip.com/wwwproducts/en/ATmega328 [Cited 12 June 2017]
[d] http://www.ebay.com/itm/1PCS-Samsung-Galaxy-S4-I9500-Power-Supply-Chip-PM8941-IC-for-Motherboard-Repair-/400875210727?hash=item5d560647e7:g:5xgAAOSwh2xX~xH- [Cited 12 June 2017]
[e] https://www.invensense.com/wp-content/uploads/2015/02/PS-MPU-9250A-01-v1.1.pdf [Cited 12 June 2017]
[f] http://www.ti.com/product/tps62130 [Cited 12 June 2017]
[g] http://www.samsung.com/global/business/semiconductor/file/media/Samsung_eMMC_2013_Final_HR-0.pdf [Cited 12 June 2017]
[h] hhttp://suddendocs.samtec.com/catalog_english/qsh.pdf [Cited 12 June 2017]
[i] https://www.usenix.org/legacy/event/atc10/tech/full_papers/Carroll.pdf [Cited 12 June 2017]
[j] http://cds.linear.com/docs/en/datasheet/2946fa.pdf [Cited 12 June 2017]
[k] http://www.st.com/content/ccc/resource/technical/document/datasheet/group3/73/70/c1/17/c8/92/4a/8c/DM00141527/files/DM00141527.pdf/jcr:content/translations/en.DM00141527.pdf [Cited 12 June 2017]

# 8

# Navigation

In this chapter, the navigation and communication between the drones and ground stations in the greenhouse are addressed. First, the overall navigation of the APIS will be discussed on a detailed level. Next, the positioning system used, which relies on UWB, will be elaborated by first discussing the protocol used and then the method for ranging adopted. After that, the method for determining the attitude based on using two UWB tags is explained. The way the drone navigates safely through the greenhouse will then be considered. This entails an overview of obstacle detection and obstacle avoidance methods used. This is followed by a discussion on the flower detection module and the way it confirms that pollination has been done. The choice of cameras and the rationale behind the choice made is made clear in the section that follows. Finally, verification and validation methods pertaining to this segment are briefly discussed in the last section of this chapter.

## 8.1. Navigation strategy

For the MAVs to perform the pollination process they need to travel to and come close to the flowers. The process starts with the ground station determining the area that has to be pollinated by each MAV. The location of this area and the position the drone should fly result from the 2D-map of the greenhouse that the ground station will create and update during the mission. This is further explained in Chapter 11. This section will also explain the positioning of the ground stations in the greenhouse. The MAV, when taking off will go to the height of the rows where the tomato flower plants are located. It leaves the ground station and descends to a certain height that is specified by a visual marker. This visual marker has to be manually adjusted to the row height (approximately 10 cm higher). This allows the drone to enter the row and start pollination directly. The trajectory that has to be followed to reach it's destination will be computed by the ground station and communicated to the MAV.

For the MAV to follow the right trajectory, a high positioning accuracy is needed. GNSS (Global Navigation Satellite System), which is not very accurate [1], is therefore not possible. Camera based positioning was eliminated due to the fact that the MAVs are navigating in a cluttered environment and thus will be hard to track. Since an ultra wideband (UWB) system is known for its very good positioning accuracy [32], this system will be used to determine the MAVs current position compared to its destination. A great advantage of such a system is that it can also handle the sending and receiving of signals and data. Several algorithms are available to perform the position estimations for the UWB. The most interesting ones are the following: time of arrival (TOA), angle of arrival (AOA), received signal strength (RSS) and time difference of arrival (TDOA). According to Hatami and Pahlavan, RSS is the most suitable for narrowband systems instead of wideband systems, thus not suitable for the UWB system [33]. Although AOA has an interesting accuracy it is not practical for the design since AOA requires the MAVs to carry large antennas. Two time-based methods remain. Both have a high accuracy due to the fact that UWB has a high time resolution [34]. The pollinator drone system will use the TDOA algorithm since no clock synchronization is needed between the different components of the system. This algorithm measures the difference in time between the arrival of the signal sent by the MAVs to the multiple receivers placed in the greenhouse. To obtain global orientation information, a second UWB tag will also be put on drone.

To navigate the MAV to the desired location, its current one is used. The positioning accuracy is furthermore improved through the IMU and the on-board cameras that can also compute the MAVs location. These three location estimates can be combined by applying a form of sensor fusion such as Kalman filtering [35].

When the distance between the MAV and its destination is known, the MAV will move forward, the relative distance will be measured again and the attitude of the MAV will be adjusted accordingly. This process will continue until the MAV reaches the start of the row. The attitude of the MAV will now be adjusted to the location in the row where it needs

[1] `http://www.gps.gov/systems/gps/performance/accuracy/` [Cited 21 June 2017]

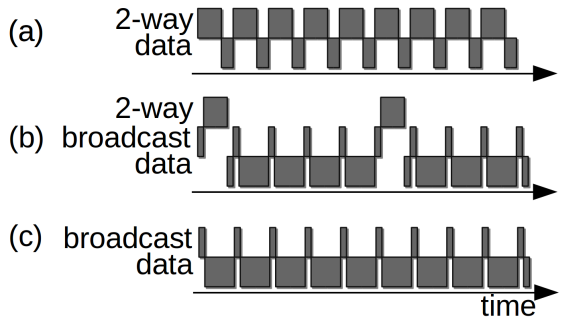


Figure 8.1: An illustration of three possible UWB protocols. (a) 2-way ranging; (b) combination of broadcasting and 2-way ranging; (c) broadcasting only ranging

to start pollinating. The MAV will fly to this location under the guidance of the fused location estimation and will start with the flower detection phase.

The altitude at which the MAV enters the row is stored and is used as reference altitude for the entire row. The MAV travels within the row using stereo-vision to detect obstacles (more inforation provided in Section 8.5). As will be explained in Section 8.6, a fisheye camera will be placed at the right side of the MAV at an angle of 45 degrees to detect the flowers. The drone would then be flying at a slight elevation above the top of the row at approximately 10cm. The wake of the MAV will also not distort the images taken by the fisheye as the camera is not directly pointing downwards.

## 8.2. UWB protocol

UWB radio technology uses low energy signals spread over a large portion of the spectrum for short-range, high-bandwidth communications. UWB is also relatively immune to multipath fading. UWB localization and communication is based on the the IEEE 802.15.4 [36], a standard for wireless personal area networks. They therefore only use frequencies allowed for general use and witness minimum interference as they represent a local small-scale network.

The biggest advantage of UWB is that the same technology and hardware are used for both localization and communication. Communication with throughput of up to 6.8 Mbps can be achieved with the module selected [2]. Doppler effects are considered in the protocol implementation. Nevertheless these are assumed to be negligible as the maximum velocity under nominal operating conditions of the APIS drones is about 1 m/s. Furthermore, the UWB communication system automatically tries to re-establish connection in case it is lost.

Localization of an UWB tag is achieved by finding the distance from it to a fixed beacon position. This distance can be found from the time of flight of a message (a frame) between the tags. The distance can then be computed and the location can be determined through a technique called trilateration.

One of the potential issues that might arise with high number of UWB modules trying to achieve ranging is the low update rates they observe. This is highly dependent on the underlying communication protocols and physical layer frame formats implemented. For example, if no two messages between UWB modules can be communicated at the same time and have to wait for each other, then the position update rate will decrease as the number of drones increases. After a consultation with a wireless communications expert[3], it was concluded that it is possible to greatly increase the ranging update rate by modifying the existing protocols. For example using code-division multiple (CDMA) channel access methods with orthogonal codes can allow for all the fixed UWB tags to broadcast time-stamped signals to all the drone tags at the same time.

However, in order to obtain the flight time, one needs to account for the clock differences between the drone tags and the fixed ones. For this, generally two-way communication is needed. This however, requires that each drone UWB tag sends a message to each fixed beacon, again leading to reduced update rate or decreased data throughout (Figure 8.1 (a)). The following protocol is however proposed: the fixed tags broadcast time-stamped signals with a predetermined high frequency and two-way ranging will happen infrequently in order to correct for drift errors in the clocks (Figure 8.1 (b)). This requires synchronization of the clocks of the fixed UWB tags, which is readily achievable as they are connected in a single wired system. Such a combination of broadcast and two-way signals can significantly increase the position update rate and the data throughput.

An alternative approach to look at the localization aspect is by applying techniques commonly used for localization

[2] `https://www.decawave.com/products/dw1000` [Accessed: 26 June 2017]

[3] Consultation with Mario Coutiño, PhD student, TU Delft Center for Wireless Systems and Technology

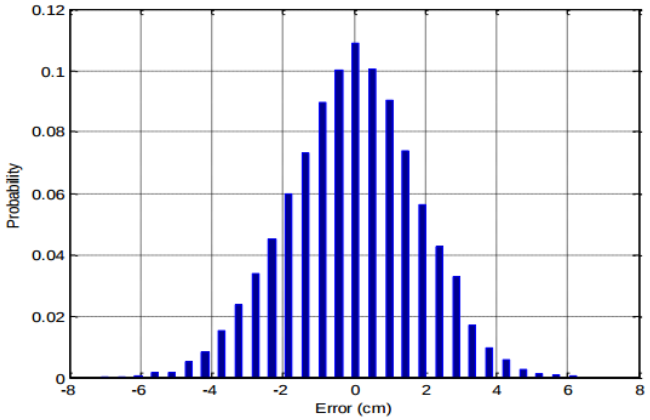


Figure 8.2: Typical probability distribution of line of sight 2-way ranging performance

with GNSS signals. These treat the clock correction of the drone tags as a fourth unknown (the other three being the Cartesian coordinates) in a system of four linearized equations. This method is similar to the method described in Section 8.3 with only the fourth unknown added. Details can be found in [37, 38]. In case four or more fixed beacons are present, using this technique allows positioning only with the fixed beacons broadcasting at fixed regular intervals. There is no need for the drone tags to reply, allowing for even more time for data communication (Figure 8.1(c)) compared to the methods presented before.

## 8.3. Indoor positioning system

To obtain the global position of the drone in the greenhouse, UWB is relied upon. It is important to know the precision of this positioning within the greenhouse as well as the effect that the number and the placement of the beacons have on the precision. A model has been created to estimate these numbers.

The observation equation which will be used to connect the estimated parameters with the range measurements is given by Equation (8.1):

$$\rho_r^b = \|\hat{x_r} - \hat{x}^b\| = \sqrt{(X_r - X^b)^2 + (Y_r - Y^b)^2 + (Z_r - Z^b)^2}, \tag{8.1}$$

where $\rho_r^b$ represents the range observation between the beacon and the drone, and $\hat{x_r}$ and $\hat{x^b}$ represent the positions of the receiver (the drone) and the beacon, respectively.
Linearizing Equation (8.1) about the ground-truth value of the range which is $\rho_a$, leads to the Equation (8.2).

$$\rho_r^b = \rho_a + \frac{(X_{ra} - X^b)}{\rho_a} \cdot \Delta X_r + \frac{(Y_{ra} - Y^b)}{\rho_a} \cdot \Delta Y r + \frac{(Z_{ra} - Z^b)}{\rho_a} \cdot \Delta Z_r \tag{8.2}$$

The parameters to estimate are then $\Delta X_r$, $\Delta Y_r$, and $\Delta Z_r$. In matrix notation this becomes : $A\hat{x} = \hat{y}$, where $\hat{y} = \rho_r^b - \rho_a$ and $\hat{x} = (\Delta X_r, \Delta Y_r, \Delta Z_r)^T$. The matrix A is composed of rows which will be filled as such. Each row will correspond to the measurement of a certain tag.

$$A_{i,1} = \frac{(X_{ra} - X^i)}{\rho_{a,i}} \tag{8.3}$$

$$A_{i,2} = \frac{(Y_{ra} - Y^i)}{\rho_{a,i}} \tag{8.4}$$

$$A_{i,3} = \frac{(Z_{ra} - Z^i)}{\rho_{a,i}} \tag{8.5}$$

The model makes use of the distribution of the error in the positioning of the chosen UWB tag. This is shown from Figure 8.2 [4].

From this distribution, its peak value was used to determine its standard deviation. This was done using Equation (8.6) while setting x equal to $\mu$.

$$P(X) = \frac{1}{\sigma \cdot \sqrt{2\pi}} e^{\frac{-1}{2}(\frac{x-\mu}{\sigma})^2} \tag{8.6}$$

[4] https://www.decawave.com/sites/default/files/resources/DW1000-Datasheet-V2.12.pdf [Cited 15 June 2017]

The value obtained for the standard deviation is 3.5 cm. This was then used in order to sample random errors for each observation using the function "normrnd" which takes as arguments the mean and the standard deviation of the normal distribution. The standard deviation was computed to be 3.5 cm and the mean is taken to be 0 cm.
Using the equations presented earlier and the values of $\mu$ and $\sigma$, it was possible to make a model in MATLAB. This model was used to study the effect of a number of factors:

- Height of the beacons
- Planform location of beacons
- Number of beacons

The effect of the height of the beacons is shown through Figure 8.3 and Figure 8.4. A similar analysis was performed for the planform location of the beacons from which it was also seen that the error was largest when closest to the tags. It was seen that an increase in the number of tags leads to a decrease in the maximum error obtained, while keeping the same discretization for the generation of the 3D grid map. A summary of the effect of making changes to these three aspects is presented in Table 8.1.

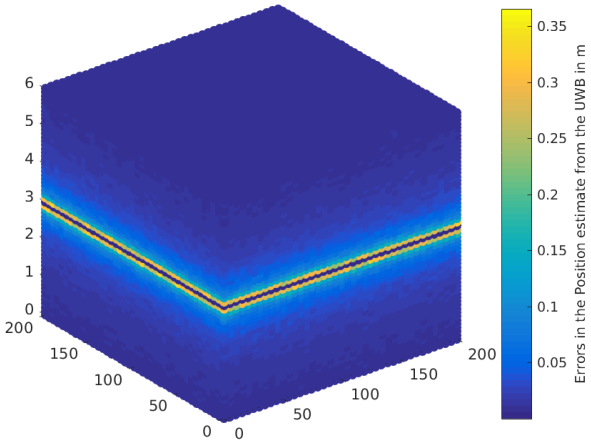


Figure 8.3: 3D plot of the accuracy of the UWB position estimates with tags placed at height of 3 m

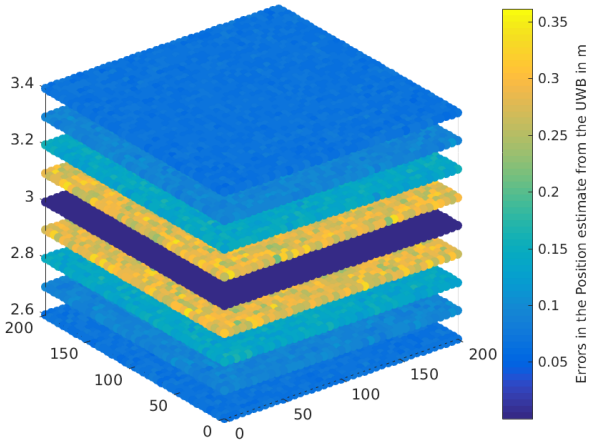


Figure 8.4: 3D plot of the accuracy of the UWB position estimates with tags placed at height of 3 m with zoom on the height close to height of the tags

Table 8.1: Summary of effect of changes

| **Change** | **Effect** |
|---|---|
| Number of tags | An increase in the number of tags leads to a reduction of the position error |
| Height of the tags | When the receiver is exactly at the height of the tags, the error is negligible. However, when there is a slight offset from the tag height, the error explodes, but it decreases with distance from the tag. |
| Planform location of the tags | Similar to the analysis for the height, the farther away from the tags, the better. |

## 8.4. Attitude determination

For the drone to navigate successfully in the greenhouse, position estimations alone are not sufficient. Attitude (orientation) information is also required. In case the drone has to orient itself in a given direction (for example to point its cameras towards flowers), it has to know where it is currently pointing at. Therefore, hardware that can facilitate attitude determination is also implemented in the drone design. Two different types of sensors will be used for that.

The magnetometers in the IMU module are used for crude local (in the drone frame of reference) attitude changes. They cannot be reliably used for global (in the greenhouse reference frame) absolute attitude determination. If that was the case, then a map of the orientation of the local magnetic field lines would have to be uploaded to the drones. Such

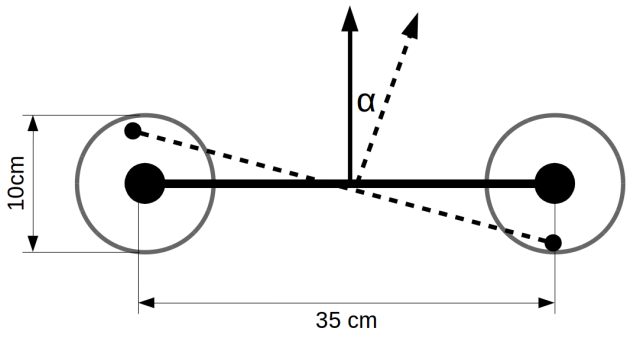


Figure 8.5: An illustration of the heading error estimation model. The big circles represent the actual UWB module locations while the smaller ones represent the position estimates. The spheres in which the positioning estimates can reside are also shown. The solid line is the true heading while the broken one is the estimated heading. The difference $\alpha_e$ is the heading error

maps are readily available in sufficient detail for an arbitrary location. Moreover, large-scale maps do not take into account local geological features like iron deposits. Additionally, the magnetic field of the Earth has a both short-term and long-term time dependency [39]. Solar wind is an example of such a short-term dependency, while the movement of Earth's northern magnetic pole is an example for a long-term one. Therefore the magnetometers on board can not be used for accurate global attitude determination. Nevertheless, IMU is sufficient for measuring the pitch and roll angles of the drone, as used in most drones already. Hence, the rest of the discussion in the current section will focus only on heading determination.

A pair of UWB modules will be used for global heading determination. By using the location estimates for the two modules and the knowledge of their position on the drone attitude determination can be achieved. The underlying principle of using location information about two points on a rigid body for heading determination is based on satellite attitude determination with two GNSS receivers [40].

The range values to the beacons obtained via UWB are noisy, which results in a level of uncertainty in the location estimates for the two on board receivers. Such a positioning error inadvertently results in heading errors. Therefore, in order to discover the heading determination accuracy of the system, a simple model of the propagation of the uncertainty in the receiver position can be made. Basing on Section 8.3, it is assumed that this position will be modeled as an uniform distribution on a sphere with radius 10 cm centered at the true receiver position. As will be shown later, the heading estimation error is inversely related to the distances between the two modules. Therefore, they are placed on the extremes of the drone structure, in particular on the outer side of two propeller protectors on the diagonal of the drone. This results in a separation distance of about 35 cm.

As mentioned before, the pitch and roll angles are of little importance for navigation and pollination and are constantly adjusted by the flight controller. Therefore, even though the error is considered in three dimensions (to ensure correspondence to the physical distribution), the analysis is performed only in the azimuth plane. An illustration of the heading error $\alpha_e$ can be seen in Figure 8.5. A simulation was performed in which 10,000 samples for the positions of the two UWB tags are selected from the above-mentioned spherical uniform distribution. The number of samples was selected with a convergence analysis, the results of which are presented in Figure 8.6. The angle between the normal and the line connecting the tags and the true heading (heading error $\alpha$ in Figure 8.5) is computed for each UWB module pair. A histogram of the calculated errors can be seen in Figure 8.7. From there it can be seen that the 95th percentile of the heading error is 20.15°.

It was observed that due to the random nature of the position estimate errors, the law of large numbers can be applied to the heading angle estimation. If multiple measurements are averaged in order to obtain a single position sample, then the mean of these measurements will converge to the true average. That also means that the variance will decrease with the decrease in the number of measurements taken per sample. Therefore, a study in the dependence of heading error on the number of measurements was performed.

The single measurement sample is compared with multiple measurements samples in Figure 8.8. It can be clearly seen that the effect of measurement averaging is strongly pronounced and that the heading error converges to about 3° as the number of measurements increases. However, as tempting as it may be to use such a high number of measurements per sample, there are hardware limitations to that. Namely, the UWB module can deliver position data with frequency of only about 90 Hz[5] (for 6.8 Mbps data link). If one uses 30 position measurements for a single attitude sample, then the heading information can be provided at a rate of only 3 Hz. Therefore, during the implementation phase, a trade-off must

[5]Estimated from `https://www.pozyx.io/Documentation/Datasheet/SystemPerformance#timing` [Cited 21 June 2017]

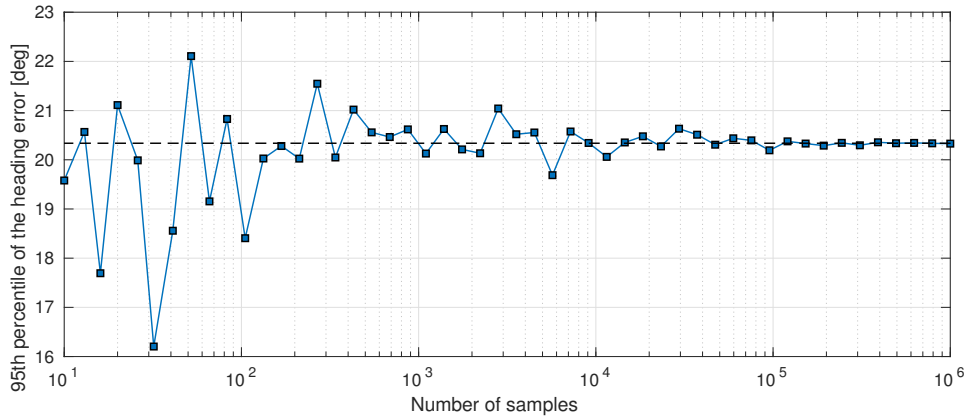


Figure 8.6: Convergence analysis of the 95th percentile of the heading error as affected by the number of samples taken in the simulation. It can be seen that for sample sizes in excess of 10,000 the error is less than a quarter of a degree away from the converging value

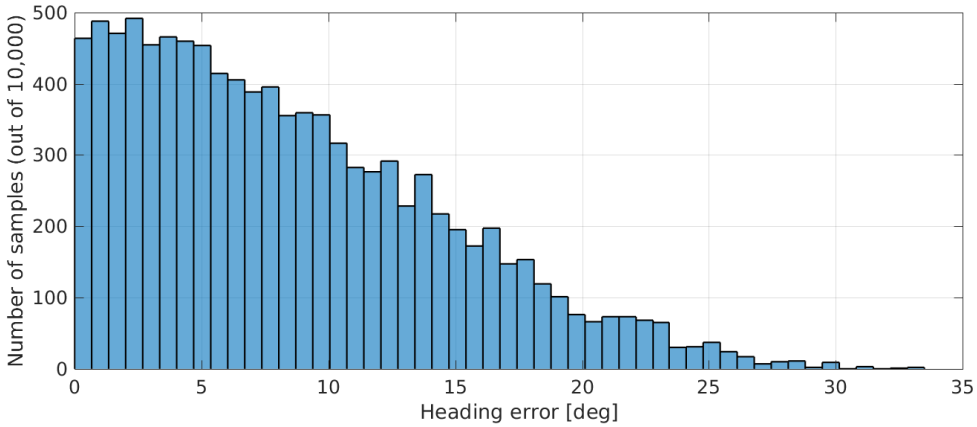


Figure 8.7: Histogram of the heading errors as observed from a simulation of 10,000 samples

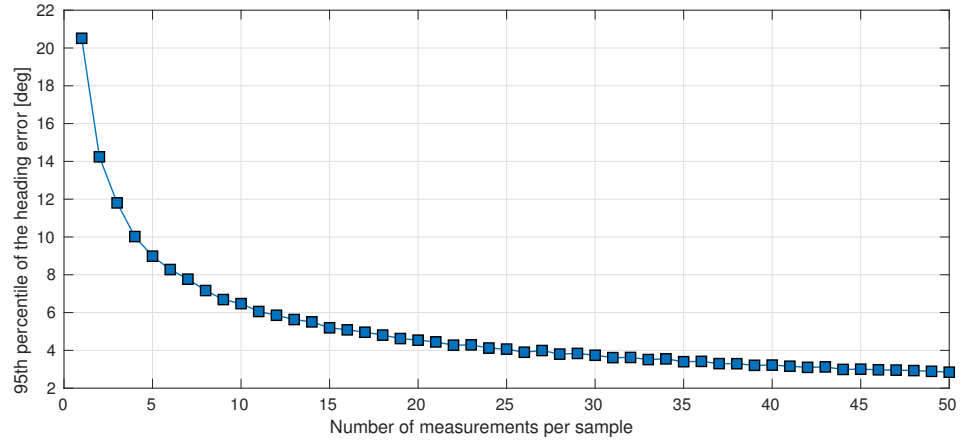


Figure 8.8: Dependence of the heading error on the number of measurements averaged to obtain each sample. Data generated with simulations of 10,000 samples

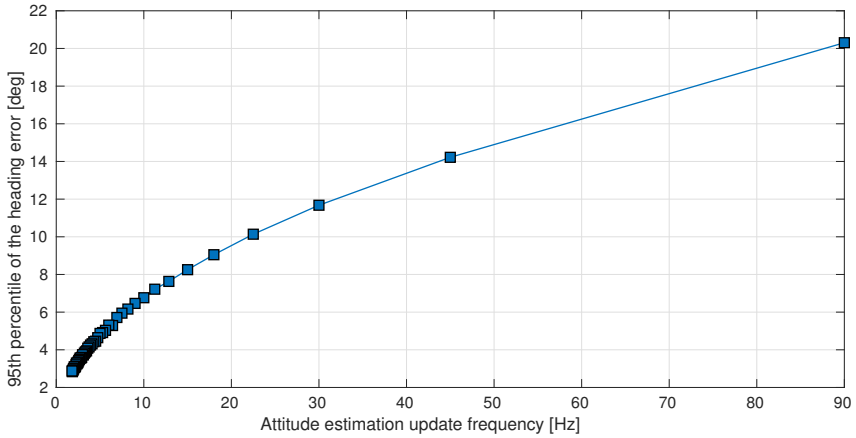


Figure 8.9: Relationship between heading estimation accuracy and update rate. Based on position estimation rate of 90 Hz. Data generated with simulations of 10,000 samples

be made between heading update rate and accuracy. The plot in Figure 8.9 illustrates the relationship found between the two.

The software tool developed for the analysis of the UWB attitude determination presented above was verified by manual calculation of several representative cases. As no empirical studies of using UWB positioning for such applications were found, validation can only be done after tests and experiments are performed. These are presented in Chapter 19.

## 8.5. Navigating safely through the greenhouse

Autonomous navigation is one of the big challenges for current MAVs. This is partially due to the obstacle avoidance challenge that they currently face. The on-board sensors should not weigh too much as the payload capacity of such an MAV is limited. The same goes for the power consumption as a too large one could have a detrimental effect on the available flying time.

Obstacle detection and avoidance are two very different aspects to consider. Even though they seem very similar, one aspect focuses on detecting an obstacle while the other looks into finding a way around the obstacle. In this section, the tools needed to detect an obstacle will be provided. The path planning method will then be discussed.

### 8.5.1. Obstacle detection

The first step in safely flying around the greenhouse is to detect obstacles. This can be done in several ways that will be presented below.

The first category considered makes use of on-board sensors. Two types of sensors were considered: active and passive. According to NASA[6], active sensors transmit energy to the environment and measure how much is reflected (or refracted - depending on the method considered) back to the sensor. Active sensors include lasers, radar instruments, sonars and any camera that uses flash.

Most of the active sensors were however not further considered for obstacle detection due to their significant weight and power consumption [41]. Additionally, the lenses required to focus some of these active sensors, such as lasers, make them quite large in size.

Passive sensors on the other hand gather data from the environment and process it to fly safely. Passive sensors include cameras without flash, heat, seismic and electric field sensors. Only cameras were however considered, as the other examples listed did not seem relevant for obstacle that need to be detected. Cameras take pictures of the environment and process them for obstacle avoidance. This can either be done through monocular vision or stereoscopic vision.

Monocular vision is interesting as it costs less and weighs less as only one camera is used. In 2016, Tae-Jae-Lee and his team [42] developed a monocular vision obstacle detection algorithm for autonomous robots. They use inverse perspective mapping and have achieved average distance estimation errors of 1.6cm with a segmentation precision of

[6] `https://www.nasa.gov/directorates/heo/scan/communications/outreach/funfacts/txt_passive_active.html` [Cited 8 June 2017]

81.4%. The algorithm is however limited to ground usage. Jaysinh Sagar and Arnoud Visser use a monocular camera by combining background subtraction, optical flow and proximity estimations [43]. They were able to detect obstacles and allows the MAV to navigate semi-autonomously in outdoor scenarios. The method relies entirely on corners and edges of the object. Monocular vision is also used to perform SLAM (Simultaneous localization and mapping). Achtelik [44] has demonstrated that by using one camera, that SLAM autonomous flight can be done in large unknown outdoor areas. The power consumption and the memory demand of SLAM is however quite significant [45] and vision fails under 20cm [44]. A more power friendly method of SLAM was also suggested by Serrata [46], fastSLAM. Using a low variance technique, they were able to recognize artificial landmarks in a real environment with a power consumption of about 1.14 W.

Stereoscopic vision leads to the generation of disparity maps. Using a definition found on Stackoverflow, disparity maps "refer to the apparent pixel difference or motion between a pair of stereo image." [7]. An example of how such a disparity map is created is shown in Figure 8.10. The image taken through the left side camera is combined with the one of the right side camera and after block matching is done, the disparity map is generated.

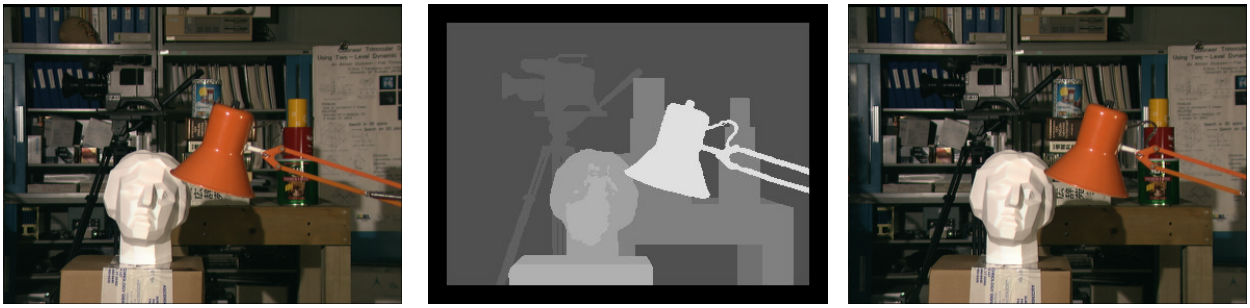

(a) Image taken by the left side camera (b) Disparity map (c) Image taken by the right side camera

Figure 8.10: Combination of the images of the stereo camera to create a disparity map [47]

Using stereoscopic vision for obstacle detection is therefore arguably more robust than a monoscopic cameras. In nature this is also the method that is used for depth perception. Monocular cameras were therefore disregarded for several reasons. One, they are poor in depth perception. Monocular vision is additionally notably poor at the focus of expansion. Stereo-vision also provides true scale estimates of distances to obstacles. These can be estimated at a same point in time. For these reasons, it was decided to arm the drone with a stereo camera for obstacle detection.

Finally, a laser on top and one on the bottom of the drone will be placed. Even though it was stated that active sensors would be disregarded, a laser was found that was extremely power efficient and lightweight. The power and weight budgets allowed to place them and it was therefore decided to do so. This will help the drone to detect if obstacles are located on top/bottom of it or not. The lasers selected are from ST Micro Electronics. The model is VL53L0X and it is known to be the world smallest time-of-flight ranging and gesture detection sensor. It is 4.4 x 2.4 x 1.0mm and can measure distances up to 2m.

In the next subsection, the way the drone will plan its path around the obstacles will be looked into. This includes the way the disparity maps are processed and what will be done with them.

### 8.5.2. Obstacle avoidance

When the obstacle is detected, the MAV has to navigate around it. This can again be done in several ways.

Putting cameras in the environment was the first option to be considered. They would follow the movements of the craft allowing it to avoid obstacles. This category was however not pursued as tracking drones within a greenhouse could prove to be very challenging. The abundance of plants in a given area and the height of the rows make it impossible to use external cameras to ensure object collision does not occur.

The second way is by using active sensors. Even though it was stated in the previous section that the power consumption was high, lower range lasers that consume less can be considered. If they are placed in a strategic manner around the drone, the MAV could navigate to its target by moving around as long as it stays far away from what the lasers detect. This however does require the presence of multiple lasers on the drone.

A third method that is more robust than the first two explained are to process the images taken by the stereo cameras. A first, more power efficient way, is to not produce 3D maps. Oleynikova [48] showed that a light-weight low power stereo vision system that uses an FPGA chip can successfully avoid obstacles in both out and indoor environments. This

[7] `https://stackoverflow.com/questions/7337323/definition-of-a-disparity-map` [Cited 8 June 2017]

reactive avoidance system makes use of U-map representations of the disparity maps. The power consumption is 5 Watt and the payload weighed 50g. The Delfy Explorer uses a "Droplet" strategy [45]. There is no need for previous images or maps and it is power and weight efficient. This method was however only tested on a flapping wing system. Given that they are passively stable, there is no need to compensate for drift. For quad-copters however, velocity estimations are necessary for stabilization of the MAV [49]. Finally an article regarding obstacle avoidance for autonomous pocket drones was found. McGuire has studied how obstacle avoidance can be done through stereo vision and efficient optic flow [49]. A 4g stereo-camera is used and edge distributions are used to calculate the depth and optical flow. The limitations of this method can be noted when the MAV approaches walls with a small angle. The field of view of the stereo-camera could not see it and the propellers touched the wall.

The other way that the stereo images can be used is by generating 3D point clouds. This helps to plan path around the obstacles. The first of the sort that was looked into is RRT (Rapidly-exploring random tree). This method is designed to tackle nonholonomic constraints and high degrees of freedom [50]. A* [51] is another path planning algorithm that can determine a way to move around an obstacle. It uses a heuristic constant that searches for cells in a map and calculates the best trajectory that can be made. It must however be noted that the a map must be made that contains the position of the obstacles. Hrabar [52] has used a variation of A*, namely D* in combination with probabilistic roadmaps for path planning in order to perform obstacle avoidance in an unknown environment. Finally, SLAM (Simultaneous Localization And Mapping) was considered as it allows to localize the MAV within the map it generates. This option requires however a lot of power and additional hardware such as lasers that scan the environment. Different SLAM algorithms were then looked into such as fastSLAM. These were however not pursued as the need to localize the MAV while performing the mission was not deemed necessary as UWB is used. Given that the environment changes every time the plants are lowered, an algorithm that has been tested in an unknown environment was preferred. The use of two UWB tags solved position and heading problems and algorithms that calculate those were therefore dropped. The total amount of hardware needed should also be at a minimum as the mass of the MAV cannot exceed 300g. SLAM was therefore not pursued. Finally, the processing capabilities of the processor did allow to use an algorithm that processes the images and converts them into point clouds.

In his paper, Hrabar's uses as previously mentioned D* in combination with probabilistic roadmaps for obstacle avoidance. This method will be implemented for obstacle avoidance and local path planning. He applies this method for a rotorcraft UAV that has to fly close to a power line. Obstacles are detected through the stereo camera and a 3D occupancy map is built. D* is then used to build a probabilistic roadmap for path planning. This is done by searching for the shortest collision free path. The roadmaps are updated with the information gathered from the occupancy grid maps. The next paragraph will give some more detail into how exactly the stereo based occupancy mapping works. As stated in the paper of Hrabar [52], the points generated by the stereopair camera are sub sampled and translated to the world coordinate system. Every $10^{th}$ point in the point cloud is taken to increase processing speed, but given the processing capacity of the APIS, an attempt can be made to use all the points. The point cloud is binned into voxels - arrays of elements that have a volume - and their size depends on the required resolution of the environment, value which can be found at the end of the chapter. Probabilities are given to each voxel that they are occupied and are updated after every observation. Thresholds are defined as to whether the voxel is free, occupied or if the state is unknown. Once obstacles are detected, the path around the obstacle can be planned. This can only be done once it was determined whether or not the voxel was free. If the voxel was free, the quadcopter can fly in a straight line towards the goal prescribed by the ground station. If an obstacle is detected, more information about it is gathered as the MAV gets closer. The path is adapted to ensure no collisions occur. Using the D* algorithm the path is planned around the obstacle. D* lite was selected as the algorithm that would plan the path. The reason for this is that this algorithm only plans this locally instead of globally such as algorithms like A*. A global path planner is indeed not needed as the rest of the path that should be followed is provided through the UWB.

## 8.6. Flower detection

The flowers of a tomato plant have a bright yellow color. This will be used to our advantage in the implementation of the flower detection algorithm which is based on [53]. The algorithm outlined in the paper consists of five main steps. The first step is to transform the RGB image to the HSV color space. The saturation in the HSV color space allowed to estimate the lighting condition. The median of the saturation and the skewness of the saturation values are used in order to make the distinction between the darker and the brighter images. This is followed by image segmentation using two threshold ranges, one for the images classified as brighter and another range for the darker images. Next, some noise is removed from the images using morphological operations: opening by reconstruction and closing by reconstruction. Finally, the regions are assessed, and the ones that are too small are discarded. The paper then classifies the regions that are left as tomato flowers. We have implemented the flower detection algorithm in MATLAB, and the implementation

was then tested on one of the images captured during the excursion to the greenhouse of Wageningen University & Research Centre. The results are presented in Figure 8.11 until Figure 8.18, showing the results of the intermediate steps followed in the implementation.

For the task of detecting flowers, a sideways camera will be used as mentioned earlier. For this camera, a fisheye lens will be used, which is an ultra wide-angle lens. Based on the routine described earlier, using a fisheye lens will allow for capturing more flowers in the images, which means that falling into the state of not seeing any flowers and not knowing where to fly to in order to detect the flowers is smaller. The fisheye lens demonstrates significant radial distortion. However, models and software exist for the correction of these effects. Examples of such models are Brown's distortion model and Conrady's model.

When a flower is detected, the drone will fly vertically and sideways and will be constraint to flying within the plane parallel to the rows of the plant (unless an obstacle is detected in which case the local planner allows for replanning and the replanning will not be subject to such a constraint), until the detected flower is in the center of the image. Knowing the camera and lens properties and the fact that the tomato flowers have a diameter of 1-2 cm, it is possible to estimate the distance to the flower. In order to ensure that the payload is able to perform proper pollination, the drone needs to be sufficiently close, at most 50 cm Chapter 5. Since the corridors are 1.6 m wide, the drone might have to approach the flower. Feature points are extracted and tracked from the detected flowers in order to determine the relative change in scale. This will be based on the method described by Sagar and Visser in [43]. Thus, the distance to the flower can be estimated and the approach can be performed. Although stereo is more effective for distance estimation, having two pairs of stereo cameras will lead to excessive mass and an overdesigned system. Moreover, the sideways distance estimate need not be as precise as in the case of forward vision because the distance estimate would be needed to make sure that the blower is at most 50 cm away from the flower.

**Robustness to variation in lighting**

Varying lighting conditions lead to changes in the irradiance of the object. The apparent color of the object as it appears in the image depends on properties of the incident light and the light source such as color intensity and location of the light source relative to the object. It also depends on the reflectance characteristics of the object, as well the properties of the camera taking the image of the object [54].

The camera is fixed, and if the properties of the flowers are more or less assumed to be fixed, the one aspect remaining which seems to affect the final detection is the variation in the lighting. In order to make the flower detection algorithm more robust to variations in lighting, a color correction method will be applied namely the HSV-based color correction method elaborated in [55].

The method involves using neural networks in order to learn a more robust parametrization that is robust to lighting changes. The architecture of the neural network employed is shown in Figure 8.19. The input to the network are the R G B values of a certain pixel. A bottleneck layer can be seen in the network, where parameters $\lambda$ and $\mu$ are obtained. Moreover, it is at the bottleneck that a desired luminance, $L_d$, is inserted to allow the inclusion of information about the illumination conditions for which the specific desired color values, $\hat{R}_d$, $\hat{G}_d$, and $\hat{B}_d$, need to be obtained.

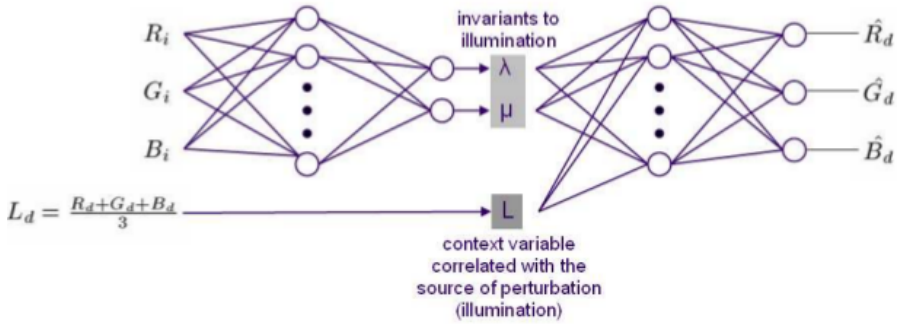


Figure 8.19: Neural network architecture for color parameterization [55]

# 8.7. Flower motion tracking

When the flower is shaking, it is important to know for how long the blower needs to keep blowing the flowers, or whether the drone has to approach the flowers even more for effective pollination. This can be done by tracking the detected flower to check whether it is moving or not.

In general, tracking and detection can be either performed separately or jointly. However, for this mission they will

be performed separately as first the flowers need to be detected to be approached. According to [56], there are three main categories of object tracking: point tracking, kernel tracking, and silhouette tracking. Moreover, a taxonomy of the tracking methods is also provided. From those, the kernel tracking methods seem to be most fit for the task. The reasoning for that is as follows. The category of point tracking methods is more suitable for tracking small objects. As the object becomes larger, more points need to be tracked which will require an extra step of clustering points. For the category of kernel tracking, the methods are good for estimating object motion as these involve parametric transformation and hence the estimation of object rotation as well as translation. The last category is suitable for tracking of the complete region of the object which would have been important for tracking an object whose different parts move differently.

In this category, the mean-shift tracking was deemed a good approach, especially when compared to the template-based matching approaches which require brute force in searching the image to find matches between two time frames and thus are computationally intensive. The mean-shift tracking procedure is an efficient algorithm which makes use of histograms to describe the appearance of the object to be tracked.

## 8.8. Camera selection

**Required camera sensor resolution**

The first step to make the choice of the camera was to determine the required resolution. This was based on the requirement for detecting the object in the greenhouse with the smallest dimension: the wires. In order to determine this resolution, three parameters needed to be decided upon. Those were the dimension of the smallest feature, the working distance, and the field of view, where the required field of view is the area under inspection that the camera needs to acquire at a certain working distance. These relate to the required resolution of the camera sensor as shown in Equation (8.7). With the required resolution estimate obtained, the choice for camera sensor can be made.

$$\text{Required resolution} = \frac{2 \cdot \tan\left(\frac{FOV}{2}\right)}{\text{smallest feature}} \cdot \text{wire thickness in pixels} \tag{8.7}$$

**Required focal length**

Upon making the choice of a camera sensor, the next step is to determine the required focal length, or the relation between the focal length and the working distance where there is flexibility in the working distance. In order to choose the right lens to still be able to have the wires in focus from a certain distance d, the following analysis is performed.
The magnification is given by the ratio of the object size in the image to the real size of the object. This leads to the following equation for magnification.

$$|m| = \frac{I_x}{L_x} \cdot \Delta\text{pix} \tag{8.8}$$

Here $\Delta$ pix denotes the pixel pitch, $I_x$ is the object dimension in pixel and $L_x$ is the actual object dimension. This is a characteristic of the camera sensor. Thus, for a chosen camera sensor, a certain required magnification factor can be computed. With the estimated required magnification factor, the required focal length for the lens to be chosen can be calculated. This is done through Equation (8.9).

$$m = \frac{f}{f - d} \tag{8.9}$$

It should be noted that this equation holds for cameras whose behaviour is close to that of the pinhole camera model - in other words, for which rectilinear lenses are used. However, it will be assumed that it is good for making initial approximations for the requirement on the focal length.
For the OV2680 camera sensor, for example, the $\Delta$ pix is 1.75 micrometers. Making the calculations for a wire which is estimated to have a width of 2mm, and to correspond to a width of 5 pixels in the image, this leads to a magnification magnitude of 0.004375. However, for real images, the magnification is negative. Thus, it is -0.004375. The required focal length is then obtained through a manipulation of Equation (8.9). This gives:

$$m = \frac{f}{f - d} \iff f = \frac{m \cdot d}{m - 1} \approx 0.00439 \cdot d \tag{8.10}$$

From this, it is clear that a good working distance for the stereo would require a focal length smaller than 15mm. As for the monocular camera, due to its much shorter working distance the focal length will be in the order 1-2mm.
The final step is to check the near and far limits of the depth of field of the camera. Based on the thin lens equations which relate the image distance, object distance, and focal length, the expression for the near and far limit of the depth of field can be derived.

$$D_N = \frac{d \cdot f^2}{f^2 + N \cdot c \cdot (d - f)} \quad (8.11) \qquad D_F = \frac{d \cdot f^2}{f^2 - N \cdot c \cdot (d - f)} \quad (8.12)$$

Here the circle of confusion, c, depends on the lens properties, the distance between the sensor and the lens, as well as the distance between the lens and the object. This is summarized in equation Equation (8.13). A desired circle of confusion can be computed with Zeiss formula. It involves D which is the diagonal of the image sensor format. Hence, it depends on the choice of the camera sensor.

$$c = \frac{2 \cdot (S - d_i) \cdot A}{d_i} \quad \text{where} \quad c = \frac{D}{1730} \quad (8.13)$$

The depth of field equation is the distance between the farthest and the nearest points at which the image is still in focus. Thus, the formula for depth of field is obtained by taking the difference between these limits, and the result is shown in Equation (8.14), where N is the F-stop

$$DOF = \frac{2 \cdot N \cdot c \cdot (m + 1)}{m^2 - \left(\frac{N \cdot c}{f}\right)^2} \quad \text{where} \quad N = \frac{f}{D} \quad (8.14)$$

**Chosen stereo camera sensor and lens**

As mentioned earlier, two cameras are needed for obstacle avoidance. Ideally, they should have a minimum resolution of 1K. This is based on equation Equation (8.7), and taking wire thickness in pixels to be around 5 pixels, and a FOV of around 90°, in order to detect the wire of thickness of 2 mm from around 1m distance. For this resolution, a suitable camera sensor was chosen. The chosen camera sensor for the stereo pair is the OV2680[8]. If the disparity range is estimated to be around a quarter of the width, and since the disparity range scales with the product of the width, depth, and height, then the estimated computation will be 0.597 billion computations for an image. The camera is running at 30 fps which amounts to 17.9 billion per second. This will be the worst case scenario when all the points on the images are used for stereo-matching.

After employing the equations presented above on several lenses, the results are presented in Table 8.2 and Table 8.3, corresponding to an object distance of 0.5m and 2 m. From that, it was deemed that the DSL235 lens would be most suitable for the stereo camera due to its having the largest DOF.

Table 8.2: Depth of field calculations for several lenses for the stereo camera and an object located at a distance of 0.5 m

| Lens | Focal length (f) [mm] | Aperture (N) [-] | $D_N$ [m] | $D_f$ [m] | DOF [m] |
|---|---|---|---|---|---|
| DSL235 | 3 | 3.2 | 0.37 | 0.77 | 0.4 |
| DSL355 | 4.2 | 2.8 | 0.43 | 0.59 | 0.16 |
| DSL944 | 7.5 | 2.8 | 0.48 | 0.53 | 0.05 |

**Chosen monocular camera sensor and lens**

For the monocular camera, a higher resolution camera was chosen in order not to compromise the robustness of the flower detection algorithm. A high resolution is also more so needed as the corrective models for distortion will lead to a loss of accuracy. The flower detection algorithm involves the use of filters applied to the image which means that the computational effort scales by the product of the width and height of the image. However, an increase in resolution for the stereopair would lead to graver consequences since the disparity range scales with the product of the width, depth, and height. The camera chosen for the monocular vision is the OS08A10[9]. The camera supports a resolution of 2592 x 1944 which means the 5.04 million computations will be needed for every filter applied in the flower detection algorithm

[8] `http://www.ovt.com/sensors/OV2680` [Cited 9 June 2017]

[9] `http://www.ovt.com/sensors/OV5675` [Cited on 9 June 2017]

Table 8.3: Depth of field calculations for several lenses for the stereo camera and an object located at a distance of 2 m

| Lens | Focal length (f) [mm] | Aperture (N) [-] | $D_N$ [m] | $D_f$ [m] | DOF [m] |
|---|---|---|---|---|---|
| DSL235 | 3 | 3.2 | 0.83 | $\infty$ | $\infty$ |
| DSL355 | 4.2 | 2.8 | 1.22 | 5.46 | 4.23 |
| DSL944 | 7.5 | 2.8 | 1.67 | 2.49 | 0.83 |

as well as for each of the morphological operations. This will lead to around $5 \cdot 5.04 \approx 25.2$ million computations for an image. Since the camera has a frame rate of 30, the total number of computations per second will be 756 million computations.
Similar to the analysis performed for the stereo camera, the equation for the depth of field was used to asses different lenses for the monocular camera and the results are presented in Table 8.4. From that, it was deemed that the DSL218 lens would be the most suitable lens.

**Estimated number of total computations**

For the hardware chosen, the main CPU has a clock speed of 2.4 GHz and an estimated 19.2 billion computations per second. As for the GPU onboard the snapdragon 801 chip, it is the Adreno 330 which can do 158.4 GFlops[10]. From, the estimated computations for the stereo matching and the flower detection, the estimated total number of computations per second is 17.9+0.756 which is 18.7 billion computations. Thus, the GPU will be able to accommodate for these computations.

Table 8.4: Depth of field calculations for several lenses for the monocular camera and an object located at a distance of 0.5 m

| Lens | Focal length (f) [mm] | Aperture (N) [-] | $D_N$ [m] | $D_f$ [m] | DOF [m] |
|---|---|---|---|---|---|
| DSL218 | 1.2 | 2 | 0.21 | $\infty$ | $\infty$ |
| DSL255 | 1.5 | 2 | 0.265 | 4.395 | 4.13 |
| DSL419 | 1.6 | 2 | 0.28 | 2.26 | 1.98 |
| DSL219 | 2 | 5.2 | 0.22 | $\infty$ | $\infty$ |

**Baseline and Mount Tolerance**

For the calculation of the required baseline, the equation relating the depth to the focal length, baseline, and disparity error shown in Equation (8.15) is used.

$$z = \frac{f \cdot b}{s} \tag{8.15}$$

Here f is the focal length, b is the baseline, d is the disparity, and z is the depth. In order to compute the required baseline, a minimum depth for which stereo matching will be possible has to be decided upon. Moreover, the maximum disparity error has to be considered. For the lens chosen for the stereo camera, the focal length is 3 mm. The maximum disparity, considering that the width of the images is 1612, is taken to be 350 pixels. Knowing that the pixel pitch is 1.75 $\mu$m, this converts to a disparity in meters of $6.125 \cdot 10^{-4}$ m. For a minimum depth of 0.2 m, the required baseline would be 4 cm.
For a sanity check, the baselines of reference drones have been referred to. For navigation in office-like environments, a baseline of 6-7 cm is typically used. That is because the distance between the eyes of a human adult is usually 6.5 cm.
A cluttered environment such as a greenhouse is more analogous to a dense forest environment, where smaller animals navigate more easily, and the distance between the eyes of these is around 4 cm. As a result, the choice of a baseline of 4 cm is deemed a reasonable choice.

The stereo cameras need to be physically connected. That is usually done using a rod. Because the camera mount is not perfectly rigid, vibrations will causes rotations that will ruin the calibration of the cameras. Rotations will occur about the horizontal axis as well as the optical axis. These rotations will lead to an offset in the epipolar line which risks the stereo matching algorithm searching at the wrong line for correspondence. This means the structure has to be sufficiently rigid. The vibrations could lead to misalignment about the horizontal axis, the vertical axis, and the optical axis. The rotation of camera about the horizontal axis or the vertical axis relative to the other is given by equation Equation (8.16). The rotations about the vertical axis will result from bending of the rod holding the camera, and the rotations about the horizontal axis will result from the torsion of the rod.

$$\alpha = \frac{\Delta pix}{f} \tag{8.16}$$

Here f is the focal length of the camera in pixels, and $\Delta pix$ is the pixel displacement that results in the image due to the rotations. The latter can be calculated with Equation (8.17), which demonstrates its relation to the focal length in meters [57].

$$f_{pixel} = \frac{f}{\text{sensor width}} \cdot \text{Image width in pixels} \tag{8.17}$$

[10] http://kyokojap.myweb.hinet.net/gpu_gflops/ [Cited 21 June 2017]

Moreover, some rotations will also occur about the optical axis which is the axis of symmetry for the stereo vision system.

$$\beta = \arctan\left(\frac{\Delta pix}{\frac{S_x}{2}}\right) \tag{8.18}$$

Here, $S_x$ is the image width in pixels, which based on the specifications of the camera OV2680 is 1616 pixels. Based on Equation (8.16) and Equation (8.18), the values corresponding to 1 pixel error are 0.0335° and 0.0709°, for $\alpha$ and $\beta$, respectively. Moreover, the pixel error can be related to the depth error with Equation (8.19), where $\delta d$ corresponds to the disparity error and is equated to the pixel error resultant from the rotations induced by the vibrations.

$$\delta z = \frac{z^2}{B \cdot f} \cdot \delta d \tag{8.19}$$

By combining Equation (8.16), Equation (8.18), and Equation (8.19), the plots for the depth error as a function of the rotation angles $\alpha$ and $\beta$ are shown in Figure 8.20 and Figure 8.21 for angles between 0 and 10°. As can be seen, the relations seem linear for both plots. That is expected for one corresponding to $\alpha$. For the plot of depth error against $\beta$, since the angles are quite small, $\tan\beta$ approximates to $\beta$ which leads to a straight line, approximately.

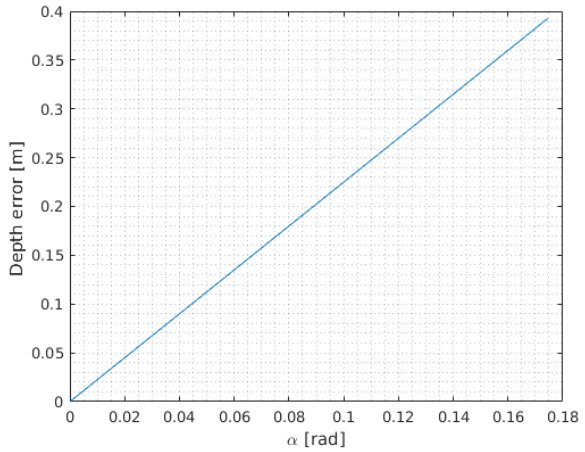


Figure 8.20: Plot of depth error vs. $\alpha$

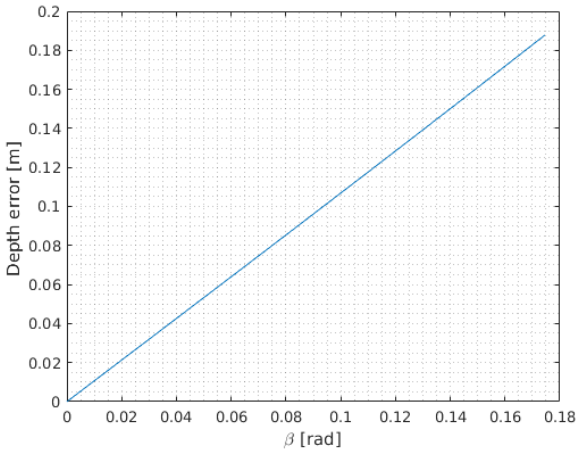


Figure 8.21: Plot of depth error vs. $\beta$

## 8.9. Verification and validation

In the following, a number of tests are proposed and performed to verify the flower detection algorithm. These comprise of two main groups: unit tests and an overall system test. First, the unit tests will be discussed, and then the overall system test along with its results will be presented.

**Unit tests**

The unit tests conducted are used to check whether each and every function that has been employed has executed its task properly. Due to the extensiveness of the tests, only a few examples will be delineated. For example, the first unit test employed was to check if the image has been loaded properly. This was done by simply displaying the image. Displaying intermediate results after applying the numerous filters was performed throughout. These intermediate results were then examined and were subject to a number of sanity checks. For example, the image obtained after applying opening by reconstruction was expected to have a reduced number of small patches of color.

**System test**

The system test would be to run the program and test it on actual images containing tomato flowers to check whether the program performs what it is supposed to do. The program was applied to a photo taken from the excursion to a tomato greenhouse. Indeed the program fulfills its intended purpose, and the result is presented in Figure 8.18.

**Validation**

As for validation, this will require comparison to the results of an existing and trusted implementation of the algorithm. However, to the knowledge of the authors this is not available.

Figure 8.11: Original Image

Figure 8.12: HSV image

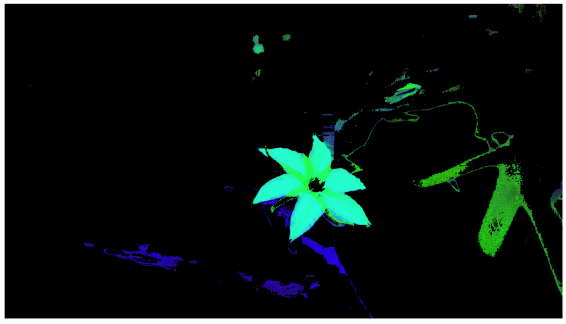

Figure 8.13: HSV image after hue filtering

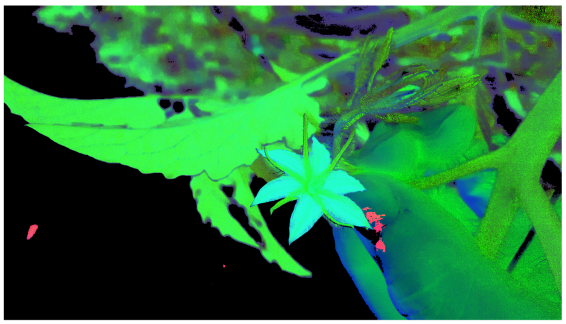

Figure 8.14: HSV image after saturation filtering

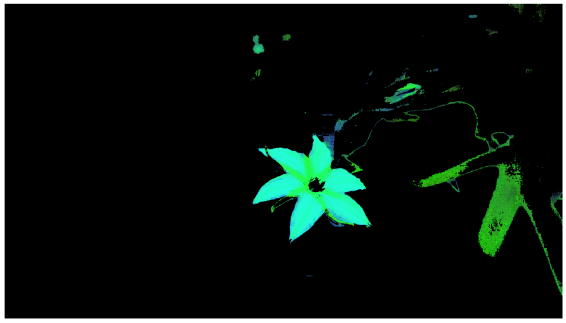

Figure 8.15: HSV image after applying AND operator between hue-filtered and saturation-filtered images

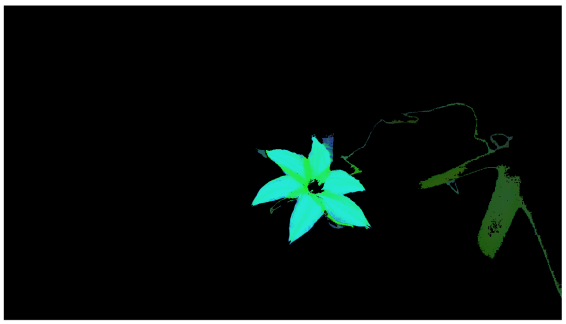

Figure 8.16: HSV image after performing opening by reconstruction

Figure 8.17: HSV image after performing closing by reconstruction

Figure 8.18: Final image showing flower detection result

# 9 Structure

This chapter will explain how the structure of the quadcopter is determined. The quadcopter consists of two main parts, the arms and a payload box in the middle. First the configuration of the quadcopter will be discussed. After that the material selection will be explained. Thirdly, an analysis will be done for the arms, followed by the sizing of the payload box. After that a FEM analysis for the whole quadcopter is done and in the end verification and validation will be discussed.

## 9.1. Choice of configuration

For the configuration of the quadcopter two configurations are considered, an X-frame and an H-frame. These are commonly used configurations and can be seen in Figure 9.1 [1]. What can be seen in the figure is that a H-frame has a payload box with a larger length than width, for the X-frame the payload box is a cube. Due to the fact that the battery has a large length and a small width, the H-frame has been chosen for the main frame of the quadcopter. This configuration can be more compact because smaller arms are used and therefore, less material is needed.

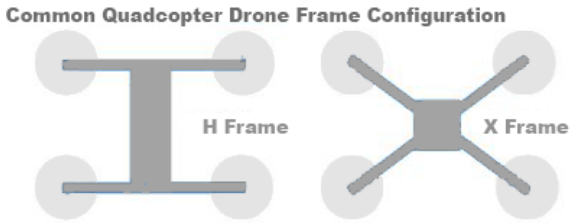


Figure 9.1: H-shape and X-shape configuration

## 9.2. Material selection

Five materials are considered for use in the structure of the drone. These materials are shown in Table 9.1, with their Young's modulus, yield stress, specific cost and density [2,3]. For selecting the material these aspects will be taken into account. The Young's modulus influences the frequency and displacement, this value should be as high as possible in order to have a high frequency and a small displacement. A high yield stress is preferred such that the cross-section can be as small as possible. Because of the fact that the natural frequency will be critical for this design, for the material of the motor arms a comparison has been made between aluminum and carbon fibre composites thanks to their high Young's Modulus. An aluminum arm has to be bigger in order to meet the requirement when comparing it with a carbon fibre composite arm. This means that the mass of the arm will be bigger due to the density and volume difference and therefore, carbon fibre is used. This is despite the fact that the specific costs are high. Due to the fact that the mass of the arms are expected to be small the costs will not be critical.

[1] https://skynexglobaldrones.com/skynex-blog/walkera-runner-250-pro-fpv-quad-drone-racer-review-everything-you-need-to-know/ [Cited 16 June 2017]
[2] http://www.goodfellow.com/E/Carbon-Epoxy-Composite.html [Cited 15 June 2017]
[3] http://web.mit.edu/course/3/3.11/www/modules/props.pdf [Cited 15 June 2017]

Table 9.1: Several materials and their properties

| Material | Young's modulus [GPa] | Yield strength [MPa] | Specific cost [$/kg] | Density [g/cm^3] |
|---|---|---|---|---|
| **Aluminum** | 69.0 | 500.0 | 1.8 | 2.7 |
| **Carbon fibre** | 100.0 | 200.0 | 110.0 | 1.6 |
| **GFRP Laminate (glass)** | 26.0 | 125.0 | 3.9 | 1.8 |
| **Spruce** | 9.0 | 48.0 | 1.0 | 0.6 |
| **Polypropyleen** | 3.2 | 35 | 1.1 | 1.2 |

## 9.3. Design of the arms

This section will explain how the arms will be sized. For this a common load case will be considered. First load case will be explained, followed by discussing the different cross-sections. After that the results for different cross-sections will be given.

### 9.3.1. Loads on the arms

The load case that will be considered for sizing the arms is the take-off condition, where there is maximum available thrust. This is because during this phase the force generated by the propellers will be maximum. Furthermore, the arms can be modeled as a rigid, cantilevered beams which are clamped at their base. At this place, there is a clamped connection to the payload box in the middle. At the end of the beams, the rotors are located. These rotors create a force going up, which is the thrust force. A moment around the z-axis is created by the propellers due to their aerodynamic drag. This moment is neglected in the stress analysis, as it is small compared to the larger thrust force. The motor also has a mass, which is taken into account. The mass of the arm itself will also be neglected because it will be distributed over the length of the arm and is also negligible compared to the thrust force. The free body diagram can be seen in Figure 9.2, where T is the thrust force of the motor, $W_{motor}$ is the mass of the motor, $F_z$ is the reaction force and $M_y$ is the reaction moment around the y-axis. The reaction force is equal to the thrust minus the mass of the motor and the reaction moment is equal to the resultant of the thrust and the mass of the motor times the length of the arm. Since all the forces and moments are known the shear diagram and the moment diagram can be created. Due to the fact that there is no distributed load the internal shear force over the arm will be constant and equal to the reaction force. The moment diagram will be linear and proportional to the length of the beam. These diagrams can be seen in Figure 9.3. These diagrams are valid for the situation when vehicle is hovering at level flight.

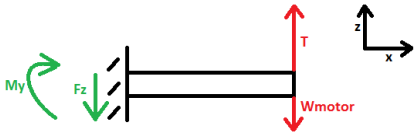


Figure 9.2: Free body diagram in the z-x plane

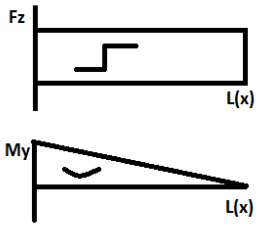


Figure 9.3: Shear force diagram above and the moment diagram below

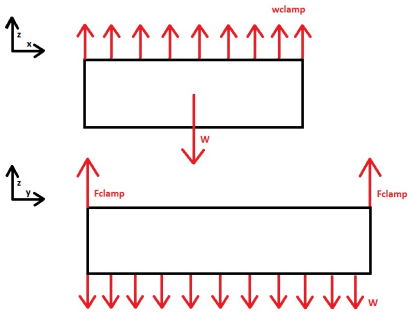


Figure 9.4: Free body diagrams of the payload box in the xz-plane and the zy-plan

### 9.3.2. Structural analysis

In Equation (9.1), the equation is presented for bending around one axis for symmetrical cross-sections. A moment $M$ is applied around the y-axis, with a distance $\overline{z}$ to the neutral axis and a moment of inertia $I_{yy}$ around the y-axis. In Equation (9.2), the equation for calculating the shear stress due to a shear force can be seen. This equation is valid if the shear force is applied goes through the shear center. For symmetrical closed cross-sections the shear center is located in the middle. The cross-sections that will be considered are closed symmetrical cross-sections, which means that the force of the propeller will go through the shear center and the equation can be used. In the equation the $V_z$ is the shear force applied along the z-axis, the Q is the second moment of area, the $I_{yy}$ is the moment of inertia around the y-axis and the t is the thickness of the cross-section.

$$\sigma_x = \frac{M_y \cdot \overline{z}}{I_{yy}} \quad (9.1) \qquad \tau_{zx} = \frac{V_z \cdot Q}{I_{yy} \cdot t} \quad (9.2)$$

The bending and shear stress can be compared with the yield stress of the material, using the Von Mises stress criterion. A simplified version of this criterion is presented in Equation (9.3), where the structure yields if the this is valid. The deflection at the tip of a cantilevered beam can be calculated by Equation (9.4), which is loaded with only a force at the tip $F_z$. $L_{beam}$, $E$ and $I_{yy}$ denote the properties of the beam.

$$\sqrt{\sigma_x^2 + \tau_{zx}^2} > \sigma_{yield} \quad (9.3) \qquad \delta = \frac{F_z L_{beam}^3}{3EI_{yy}} \quad (9.4)$$

Quadcopters are vehicles that can be very sensitive to induced vibrations. The inertial measurement unit needs to be excluded from external vibrations as much as possible. Also, resonance phenomena can occur in the structure itself. A first order frequency analysis is therefore performed to investigate these phenomena and try to mitigate these issues. The main source of external vibration is on the propellers [58]. These spin at a high frequency that could match the normal frequency of the arm. The maximum RPM of the motor used is 17100, which gives a frequency of 285 Hz.From basic vibration theory, it is known that the amplitude of an harmonically forced vibration is very high when the natural frequency is equal to the forced frequency ($\omega_n = \omega_f$). When the ratio $\frac{\omega_f}{\omega_n}$ increases or decreases, amplitude decreases. It is therefore assumed that the resonance can be avoided if $0.5 > \frac{\omega_f}{\omega_n} > 2$. This means that the natural frequency of the beam should at least be 570 Hz. Furthermore, it is assumed that the motor arm can be modeled as a clamped, massless beam with the mass of the motor lumped at the tip. The simplified equation for the resonance frequency in this case is presented in Equation (9.5), where $E$ is the Young's modulus and $I_{yy}$ is the moment of inertia around the y-axis of the beam, depending on the cross-section used. $m_{motor}$ and $L_{beam}$ are the mass of the motor and the length of the beam respectively.

$$\omega_n = \sqrt{\frac{3EI_{yy}}{m_{motor} L_{beam}^3}} \quad (9.5)$$

### 9.3.3. Cross-section selection

This subsection will first explain how the length of the arms are determined and after that the shape selection will be done. For the length of the arm the aerodynamic properties are important. This is because the flow of the propellers should not interfere with one another. The diameter of the propellers is 127 mm. This means that the arm should be at least as long as the radius of the propellers, which will be the starting point of the iteration process.

For the shape the dimensions are not determined yet. Five typical shapes of beams are considered for the arms: two hollow beams, a circular hollow and a rectangular hollow beam, one simple closed rectangular beam, an I-beam and a T-shaped beam. Their general structural properties are already known. Hollow closed beams perform well in shear and torsion and the 'letter'-shaped beams have better performance in bending. As mentioned above, the loading conditions elaborated is in level, hovering flight. When flying forward or blowing, the vehicle encounters other loading situations, with torsional and shear loads. Other considerations are the aerodynamics and the placement of the wires to the motors. In a hollow beam, the wires can be placed within the beams, while for the other shapes, they need to be placed on the outside. The aerodynamics of a closed beam are also preferable. From the deliberation above, two options arise: the rectangular or the circular hollow beam. These are further investigated in the next subsection.

### 9.3.4. Comparison and results

The analytical model developed in the previous section is solved for two options. A beam with rectangular and circular hollow cross-section is put in the model and the displacement due to a load, the natural frequency $\omega_n$, the mass, stress due to bending and the shear stress is found. A carbon fibre reinforced plastic (CFRP) beam with length of 62.5 mm, an E-modulus of 100 GPa and a thickness of 1 mm is taken. Typical carbon fibre tubes were investigated [4], and typical wall thickness is around 1 mm. At the tip of the beam, the mass of the motor (12 gram) and the maximum thrust of 1.275 N is applied. Finally, a safety factor of 1.5 is added to the load. In Table 9.2, the results for a circular hollow beam are presented for a varying diameter. Table 9.3 shows the different properties for a rectangular hollow beam with a width of 6 mm, where the height is varying.

From the results presented above, conclusions can be made. First of all, the natural frequencies at all considered diameters are sufficiently high to prevent resonance. For the circular beam a diameter of 4 mm is needed with a mass of 0.9 g in order to meet the frequency requirement. The rectangular beam needs a height of 3 mm with a mass of 1.4 g. Comparing the circular and rectangular hollow beam, the circular beam performs better when looking at the mass. For

[4] https://www.rockwestcomposites.com/round-tubing/round-carbon-fiber-tubing [Cited 19 June 2017]

Table 9.2: Mechanical properties of CFRP circular hollow beam with length of 62.5 mm

| Diameter [mm] | Displacement [mm] | $\omega_n$ [Hz] | Mass [g] | $\sigma_x$ [MPa] | $\tau_{zx}$ [MPa] | VM [MPa] |
|---|---|---|---|---|---|---|
| 3 | 0.434 | 553.7 | 0.6 | 47.67 | 0.78 | 47.69 |
| 4 | 0.145 | 959 | 0.9 | 21.19 | 0.52 | 21.21 |
| 5 | 0.064 | 1443.8 | 1.2 | 11.68 | 0.38 | 11.7 |
| 6 | 0.033 | 1996.3 | 1.6 | 7.33 | 0.3 | 7.35 |
| 7 | 0.02 | 2608.7 | 1.9 | 5.01 | 0.25 | 5.03 |
| 8 | 0.012 | 3275.6 | 2.2 | 3.63 | 0.21 | 3.65 |

Table 9.3: Mechanical properties of CFRP rectangular hollow beam with length of 62.5 mm and width of 6 mm

| Height [mm] | Displacement [mm] | $\omega_n$ [Hz] | Mass [g] | $\sigma_x$ [MPa] | $\tau_{zx}$ [MPa] | VM [MPa] |
|---|---|---|---|---|---|---|
| 3 | 0.103 | 738.1 | 1.4 | 16.5 | 1.7 | 16.8 |
| 4 | 0.046 | 1101.7 | 1.6 | 9.9 | 0.8 | 10 |
| 5 | 0.025 | 1487.8 | 1.8 | 6.8 | 0.4 | 6.8 |
| 6 | 0.016 | 1893.6 | 2 | 5.0 | 0.3 | 5.0 |
| 7 | 0.010 | 2317.7 | 2.2 | 3.9 | 0.2 | 3.9 |
| 8 | 0.007 | 2759.1 | 2.4 | 3.1 | 0.1 | 3.2 |

this reason the circular beam will be chosen. Because of the fact that five wires need to go through the arms, a bigger cross-section is needed. There are two big wires with a diameter of around 1.5 mm and three smaller wires that have a diameter of around 0.5 mm. This means that the inner diameter should at least be 5.5 mm, an extra 0.5 mm will be added to make sure all the wires fit. Therefore, the outer diameter of the circular hollow cross-section will be 8 mm.

## 9.4. Payload box design

This section will describe the process followed for the sizing of the payload box, which is the box in between the rotors were the battery, the electronics and the blower are located. The first step is to model the loads on the payload box and create the shear, normal force and moment diagrams. After that the stresses are calculated and the thickness of the payload box can be determined.

### 9.4.1. Loads on the payload box

When looking at the payload box different forces need to be taken into account, the weight of the payload and the force generated by the blower. However, the load of the blower is 0.04 N and the load of the payload is 1.472 N, which is 30 times bigger than the load of the blower and therefore, the force of the blower is neglected. The arms are connected to the payload box by a clamped connection, which will be placed along the width of the payload box. This will result in a distributed load exerted on the box by the clamp, which can be seen in the top image in Figure 9.4. The weight can be modelled as a distributed load as well. The free body diagram can be seen in Figure 9.4 in the xy-plane. Now that the loads are known the shear and moment diagrams can be made. These can be seen in the top figures shown in Figure 9.5. What can be seen is that the critical locations are located at the half of the length of the payload box.

### 9.4.2. Sizing of the payload box

The sizing of the payload box will be done by analyzing the stresses. The box will have an U-shape and will be carrying the battery. The length, width and height are already known because the size of the battery, electronic components and blower have been determined and can be fitted into the payload box together. By doing this, a length of 140 mm, a width of 28 mm and a height of 17 mm has been determined. This means that only the thickness is left to decide. By looking at the yielding stress of the material, the required thickness can be determined. However, when investigating typical carbon fibre sheets a thickness of 1 mm has been found as minimum thickness [5], therefore this value will be used as. The maximum stress that will occur in the material has been determined by using the Von Mises stress proposed in Section 9.3.2. For calculating the Von Mises stress, the stress due to bending and shear force have to be calculated. These equations have already been given in Section 9.3.2. In order to know the maximum stress the highest value from the loading diagrams Section 9.4.1 have been used. An safety factor of 1.5 has been added to the force applied. Since

[5] `http://www.carbonmods.co.uk/Departments/Carbon-Fibre-Sheet/Rigid-Sheet.aspx` [Cited on 20 June 2017]

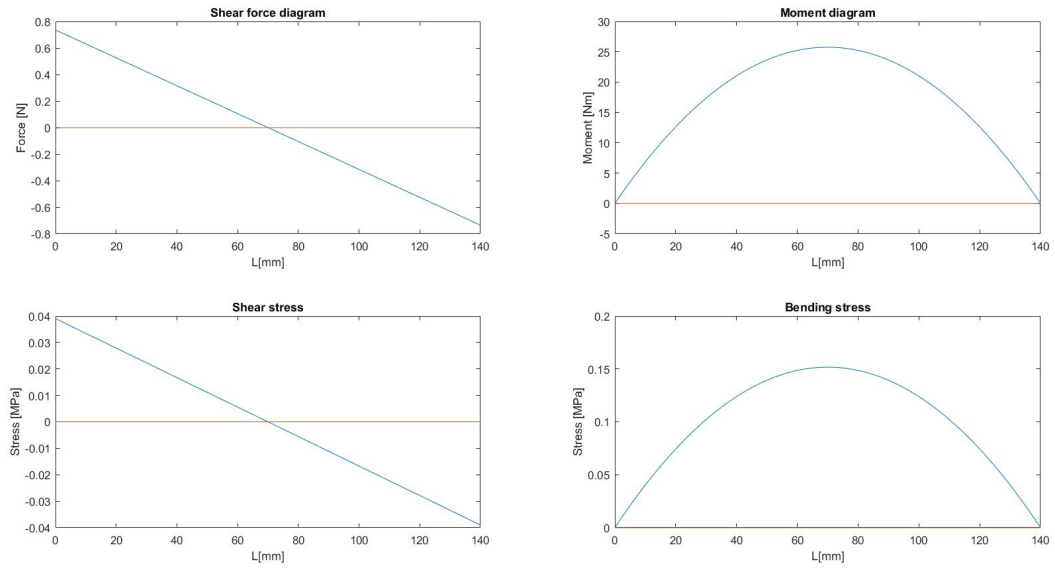


Figure 9.5: Shear force, moment, shear stress and bending stress diagrams for the payload box over the length of the box

it was clear that a thickness of 1 mm was enough to carry all the loads, this value will be used in the final design. In Figure 9.5 the values of the shear and bending stresses over the length can be seen. The maximum value for shear stress and bending stress are 0.15 MPa and 0.039 MPa, respectively. This gives a maximum von mises stress of 0.16 MPa.

### 9.4.3. Vibration in the payload box

In the payload box, induced vibrations by the motor should be mitigated as much as possible. The electric components are very sensitive to shaking, as their working frequency could correspond with the induced one. Placing the electric components on a heavy mass (like the battery), or dampening out these components with a dedicated damper can reduce this effect. A simplified model of the vibrating battery can be made. A payload with a mass 124 grams is placed on a vibrating base with stiffness k and damping ratio c, that is moving only in one degree of freedom.

The equation of motion of this model is shown in Equation (9.6). The motion of the base is given by $y(t)$ and the response of the mass by $x(t)$ over a time t. $y(t)$ has the form of $y(t) = Ysin(\omega_b t)$. $m$ represents the mass of material that needs to be damped in kg, c and k the damping coefficient and stiffness of the material, respectively. The simple equation of motion of this figure is shown in Equation (9.6). This can be rewritten to find the required parameters. [59]

$$m_{battery}\ddot{x} + c(\dot{x} - \dot{y}) + k(x - y) = 0 \tag{9.6}$$

The battery is put on small cubes of latex foam [6], that are placed on the corners of the battery. Equation (9.6) can be solved for the variables. The material properties are taken from online sources [60] [7]. The size of the damper is estimated to be 1 $cm^2$ and an initial length of 6 mm is taken. This results in a spring constant k of 6,000 $N/m$ for the four dampers and a damping ratio $\zeta$ of 0.4, where $\zeta = \frac{c}{2\sqrt{km_{battery}}}$. The mass of the battery and printed circuit board is estimated to be 124 grams. This results in a natural frequency of around 220 $rad/s$. The response is plotted for a unit base excitation magnitude of 1 at three different base frequencies. This response can be seen in Figure 9.6. Natural frequency $\omega_n$ and $\omega_b$ are also presented in the figure.

## 9.5. Cover

The quadcopter can harm the surroundings due to the high rotational speed of the propellers. However, the quadcopter will not fly directly through the rows, which means that the plants should never be close to the propeller, but when the navigation of detection system fails the quadcopter can come close to the plants. Therefore, a cover will be added which will be done by using a circular plastic ring around the propeller and a net structure on top. This casing has also been

[6] `https://hobbyking.com/en_us/anti-vibration-foam-orange-latex-190mm-x-140mm-x-6mm.html?___store=en_us` [Cited 16 June 2017]

[7] `http://www.engineeringtoolbox.com/young-modulus-d_417.html` [Cited 16 June 2017]

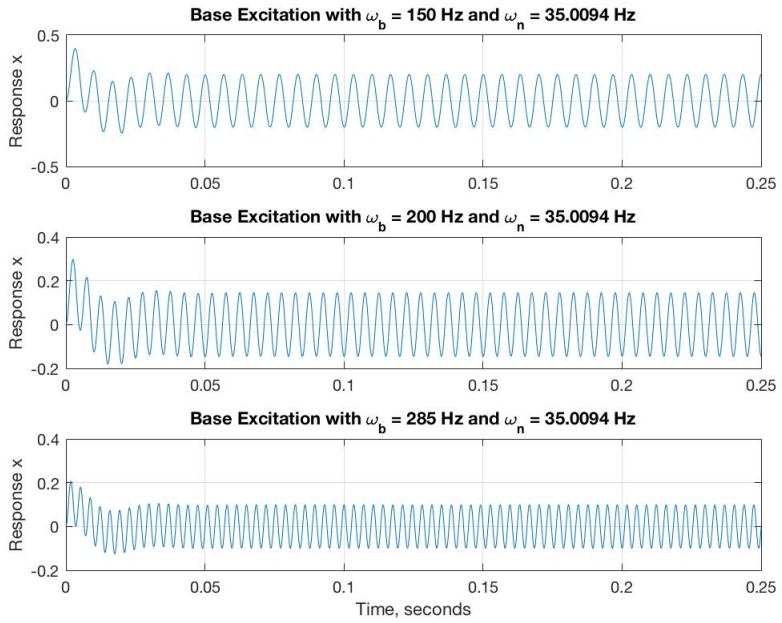


Figure 9.6: Response of base-excited system for three different base frequencies

added such that when falling on the arms, the casing will break first. Which means that the casing has to be replaced and the arms are still in tact. Furthermore, not only the propellers will be protected. A case is added to the payload box and blower, this has been added to protect the electronic components and the blower.

## 9.6. Verification and Validation

This section will describe the verification and validation processes performed. First the verification shall be completed, then the validation will be performed.

For the verification first unit tests are performed in the code. Unit testing is important to check and prove that the implementation of the code is correct even on the smallest building blocks of the code. It ensures that all the values have been used correctly and that the units are correct. For example, checking if values that should be inserted in mm are actually filled in as mm. Next to this it is also checked if the values are filled in at the correct place. For example, does the mass have the correct value of 250g. Not only the inputs of the program have to be checked but also the outputs of part of the system and the outputs of the total system. For example, it was tested if the moments of inertia calculated by the program coincide with manual calculations. Furthermore, the eigenfrequencies of the motor arms that were found have been verified by using a quadcopter sizing process proposed by [61].

For the validation of the stresses computed by the model, a finite element method (FEM) will be used. This numerical method is performed in the CATIA model of the design. The FEM model will divide the total CATIA model in smaller simpler parts called finite elements, will apply the equations to these elements and finally assemble all of this into one large system again. First the arms will be analyzed. These will be analyzed the take-off case. A point load is added at the tip of the structure and the clamp is situated at the other side of the structure. The point load has a value of 1.275 N. After the load case has been defined the stresses could be calculated. For the Von Mises stresses calculated by the FEM model a mesh size of 0.5 mm is used. The results that are found can be seen in Table 9.4. The stress distribution can be seen in Figure 9.7. For the Von Mises stress the deviation is 2.5 %, which means that the model has been validated.

Table 9.4: Comparison between Von Mises stresses of the analytical model and the FEM model for the arms during take-off at the critical location

| | **Analytical model including safety factor (MPa)** | **Analytical model excluding safety factor (MPa)** | **FEM model (MPa)** | **Percentage of deviation (%)** |
|---|---|---|---|---|
| Von Mises stress | 3.6 | 2.4 | 2.34 | 2.5 |

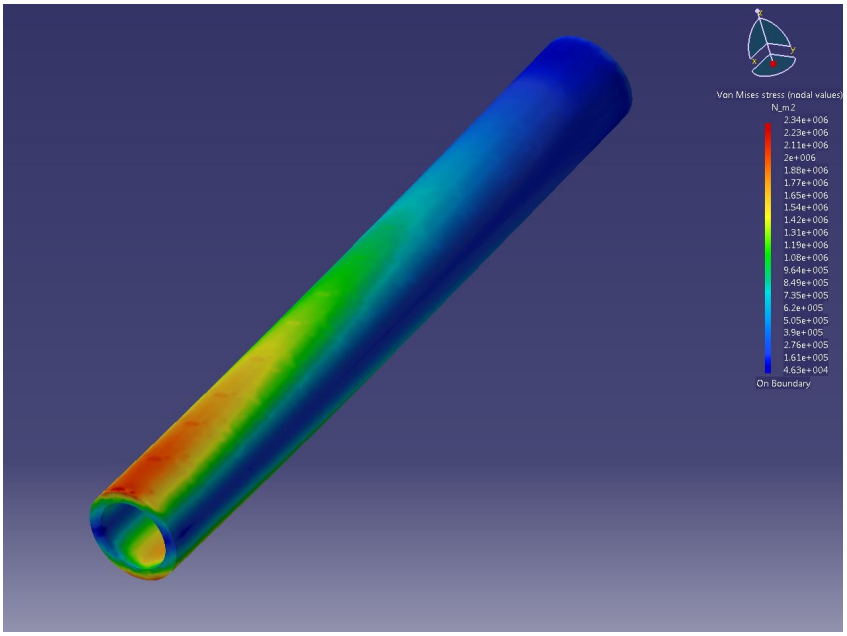


Figure 9.7: Von Mises stress on the arm computed by using the finite element method of CATIA

For validating the payload box the load case is assumed where the sides of the payload box are clamped. Furthermore, the weight of the payload box is applied as a distributed force over the length of the box, which is 1.472 N. The model proposed in Section 9.4.2 gives a maximum value for the Von Mises stress in the middle of the length of the payload box. However, in the FEM model the maximum Von Mises stress occurs close to the clamp, the stress distribution can be seen in Section 9.6. For the analytical method this has not been taken into because the equations used do not account for stress concentrations in corners of rectangular shapes. However, the maximum Von Mises stress computed by the FEM method is 3.03 MPa, which means that the box can easily take the load. To validate the model a fair comparison of the Von Mises stresses is required. Therefore the Von Mises in the middle of the box will be compared. When comparing the Von Mises stress in the middle of the payload box the value for the analytical method is 0.10 MPa, whereas the numerical method gives a value of 0.11 Mpa. This gives a deviation of 10 % . These values can also been seen in Table 9.5.

Table 9.5: Comparison between Von Mises stresses of the analytical model and the FEM model for the payload box in the middle of the length of the payload box

| | **Analytical model including safety factor (MPa)** | **Analytical model excluding safety factor (MPa)** | **FEM model (MPa)** | **Percentage of deviation (%)** |
|---|---|---|---|---|
| Von Mises stress | 0.15 | 0.10 | 0.11 | 10 |

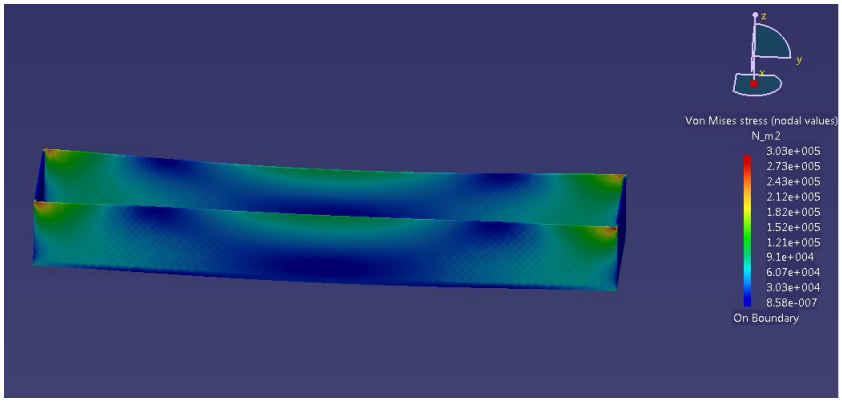


Figure 9.8: Von Mises stress on the payload box computed by using the finite element method of CATIA

# 10

# Stability and control

The aim of this chapter is to investigate the stability and control characteristics of the drone. First, disturbances, static stability and quad-rotor dynamics are researched in Section 10.1, Section 10.2 and Section 10.3, respectively. Hereafter, this information is used to determine control and stability characteristics, as shown in Section 10.4 and Section 10.5.

## 10.1. Disturbances

The main disturbance that will be modelled is the blower. The forces and torques it generates are all modelled in the body frame. The blower is located in the center of gravity on the x-y plane. The blower also propels air at an angle. A force in the positive z-direction and one in the positive x direction are therefore generated. A torque will also be modelled to simulate the gyroscopic procession of the motor and the moment the z component of the blowing force causes about the center of gravity. The forces of the blower are decomposed in components and can be visualized in Figure 10.1. From Section 5.3 it was determined that the magnitude of the force of the blower was 0.06 N and that the blower is at a 45 ° angle. Another force that can be modelled are the fans placed on the floor of the greenhouse. These will generate a force in the positive z direction. This force is however expected to be very small. The MAV will however not be affected by this as it flies on top of the row and those blowers are mainly used to keep insects away from the fruits that are at the bottom of the rows.

## 10.2. Static stability

A free body diagram of the forces acting on the drone can be made. Two reference systems will also be considered. It is shown in Figure 10.1. Two coordinate systems are furthermore selected. The first, which is also shown in Figure 10.1, is the body reference frame. It is a right handed orthogonal system that takes its reference at the center of gravity of the drone. When subjected to a perturbance, the reference frame remains fixed to the drone. The forces of the propellers and the blower will be modelled in this frame. The second frame that is considered is the inertial reference frame. It is Earth-centered and also uses the right-handed orthogonal axis system. Besides the blower, all the other external disturbances will be modelled in it.

The equations of motion when the blower is at full power can be set up. Taking the sum of the forces in x, z and the sum of the moments about the center of gravity yields Equation (10.1), Equation (10.2) and Equation (10.3).

$$\sum F_x = 0 = F_{x_{blower}} - W sin(\beta) \tag{10.1}$$

$$\sum F_z = 0 = T_1 + T_3 + T_2 + T_4 + F_{z,blower} - W cos(\beta) \tag{10.2}$$

$$\sum M_{y_{cg}} = 0 = F_{x_{blower}} 2.74 + F_{z_{blower}} 100 + (T_1 + T_3)77.8 - (T2 + T4)77.8 \tag{10.3}$$

Rearranging Equation (10.1) allows to find the angle at which the MAV will be when hovering with the blower on. It is shown in Equation (10.4).

$$\beta = sin^{-1}\left(\frac{F_{x_{blower}}}{W}\right) = sin^{-1}\left(\frac{0.06\cos(45)}{0.25 \cdot 9.81}\right) \approx 1^\circ \tag{10.4}$$

When the blower is on, the MAV will be tilted by 1 °. The x component of the mass will ensure that the x component of the blower force does not move in the x direction. Now the variation in thrust can be calculated. Assuming that motors 1 and 3 generate the same thrust and motors 2 and 4 do the same, Equation (10.2) and Equation (10.3) can be rearranged to yield Equation (10.5) and Equation (10.6).

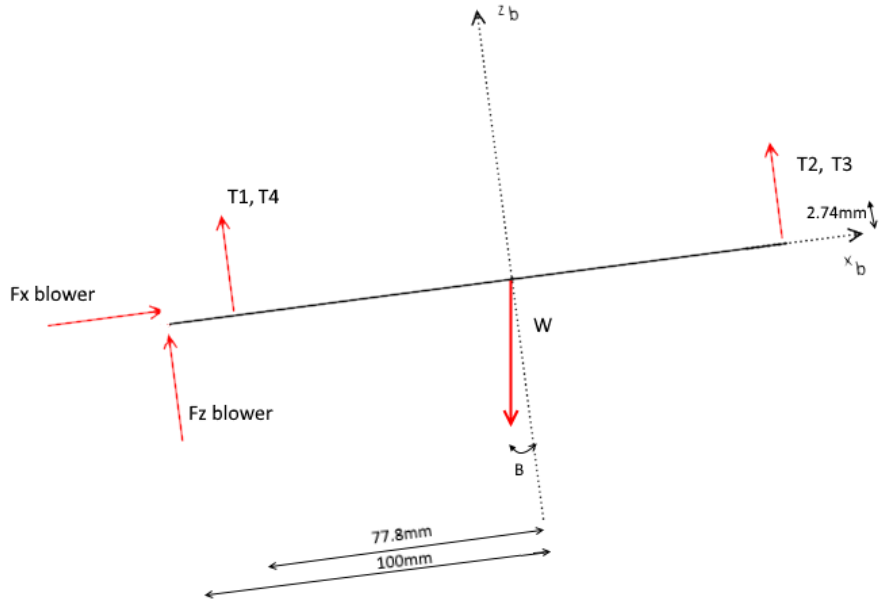


Figure 10.1: FBD of the MAV and the forces acting on it

$$\sum F_z = 0 = T_{13} + T_{24} + F_{z,blower} - W cos(1) \tag{10.5}$$

$$\sum M_{y_{cg}} = 0 = F_{x_{blower}} 2.74 + F_{z_{blower}} 100 + T_{13} 77.8 - T_{24} 77.8 \tag{10.6}$$

Substituting the force of the blower as well as the lateral angle $\beta$ that is generated when the blower is on, allows one to solve for $T_{13}$&$T_{24}$. The thrust that should be generated by motors 2 and 4 is in total 1.233N and the one that should be generated by 1 and 3 is in total 1.1768N. This is what one would expect as part of the force generated by the blower does indeed contribute towards lift on side of motors 1 and 3.

## 10.3. Quad-rotor dynamics

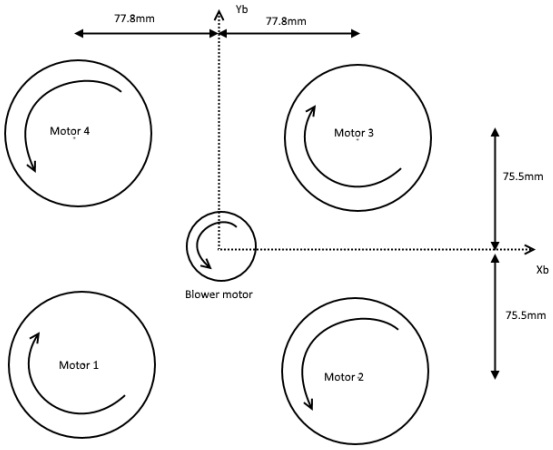


Figure 10.2: Top view of the MAV

This section will look into modelling the quadcopter dynamics. The forces will be grouped into a matrix. Before doing so, the thrust each motor/propeller delivers will be expressed in terms of the angular speed. In a simplified form thrust can be related to angular velocity as follows: $T = c_T \omega^2$. Summing the forces in each direction and grouping

them into a matrix yields Equation (10.7). It must be noted that additional aerodynamic forces such as frame drag are neglected. Indeed, the forces in the x-y plane are, as can be seen from the matrix, equal 0.

$$F^b_{A,T} = \begin{bmatrix} 0 \\ 0 \\ c_T(\omega_1^2+\omega_2^2+\omega_3^2+\omega_4^2) \end{bmatrix} \tag{10.7}$$

Next the moments about x, y, z can be calculated. The thrust forces generate moments about the body axes when multiplied by the distances that are shown in Figure 10.2. This figure also shows the spinning directions of the motors: clockwise for motors 1 and 3, counterclockwise for motors 2,4 and the blower. The rotors also spin and generate gyroscopic moments in the x and y planes. They are described by Equation (10.8) and Equation (10.9).

$$\tau_\phi = J_m Q\left(\frac{\pi}{30}\right)(\omega_1-\omega_2+\omega_3-\omega_4) \tag{10.8}$$

$$\tau_\theta = J_m P\left(\frac{\pi}{30}\right)(-\omega_1+\omega_2-\omega_3+\omega_4) \tag{10.9}$$

where P and Q are the rolling and pitching rates. The inertia ($J_m$) and the speed of the the motor/propeller are also considered to calculate those. The term $\frac{\pi}{30}$ converts RPM to radians.

Regrouping the aforementioned moments yields Equation (10.10).

$$M^b_{A,T} = \begin{bmatrix} \tau_\phi \\ \tau_\theta \\ \tau_\psi \end{bmatrix} = \begin{bmatrix} -dc_T\omega_1^2+dc_T\omega_2^2+dc_T\omega_3^2-dc_T\omega_4^2+J_mQ\left(\frac{\pi}{30}\right)(\omega_1-\omega_2+\omega_3-\omega_4) \\ -dc_T\omega_1^2-dc_T\omega_2^2+dc_T\omega_3^2+dc_T\omega_4^2+J_mP\left(\frac{\pi}{30}\right)(-\omega_1+\omega_2-\omega_3+\omega_4) \\ -c_Q\omega_1^2+c_Q\omega_2^2-c_Q\omega_3^2+c_Q\omega_4^2 \end{bmatrix} \tag{10.10}$$

The state equations used for the dynamic model are described below. The first defines the angular velocity and is based off the simple Euler equation shown in Equation (10.11). $\tau$ refers to all the external torques.

$$I\dot{\omega}+\omega\times(I\omega)=\tau \tag{10.11}$$

Rearranging for the angular acceleration, yields Equation (10.12). Use is made of $\omega^b_{b|i}$ which refers to the body's angular velocity.

$$\dot{\omega}^b = I^{b,-1}\left(\tau^b-\omega^b_{b|i}\times\left(I^b\omega^b_{b|i}\right)\right) \tag{10.12}$$

$$\begin{bmatrix} \dot{\omega_x} \\ \dot{\omega_y} \\ \dot{\omega_z} \end{bmatrix} = \begin{bmatrix} \tau_\phi I_{xx}^{-1}-\frac{I_{yy}-I_{zz}}{I_{xx}}\omega_y\omega_z \\ \tau_\theta I_{yy}^{-1}-\frac{I_{zz}-I_{xx}}{I_{yy}}\omega_x\omega_z \\ \tau_\psi I_{zz}^{-1}-\frac{I_{xx}-I_{yy}}{I_{zz}}\omega_x\omega_y \end{bmatrix} \tag{10.13}$$

The next state equation used is the velocity state equation. It is represented in Equation (10.14). It describes the linear acceleration of the center of mass in the body frame with respect to the inertial reference frame. The final state equation that is used in the model is the position state equation shown in Equation (10.15). It gives the velocity of the MAV in the inertial reference frame. In this equation, use is made of the transformation matrix $C_{i|b}$. This is the equivalent of a XYZ rotation transformation. Combining all these equations in MATLAB allows to model the dynamics of a quadrotor.

$$\dot{v}^b_{cm} = \begin{bmatrix} \dot{U} \\ \dot{V} \\ \dot{W} \end{bmatrix} = \frac{F^b}{m}+g^b-\omega^b_{b|i}\omega^b_{CM|i} \tag{10.14}$$

$$\dot{X}^i_{cm} = \begin{bmatrix} \dot{x} \\ \dot{y} \\ \dot{z} \end{bmatrix} = C_{i|b}v^b_{cm|i} \tag{10.15}$$

# 10.4. Control

Several techniques exist to control an autonomous quadrotor. The available linear and non-linear techniques are explored.

## 10.4.1. Linear control techniques

The linear techniques take the governing flight dynamics equations of motion of the quadrotor and simplify them. They are then used for the design of a linear controller. There are two main ways to do that. The first involves further simplifications by trying to further decouple the dynamics in order to make use of "successive loop closures". The other group does not perform this decoupling. This category makes use of state space control approaches and linear

feedback control. Examples that employ this method are PID (proportional–integral–derivative) and MIMO (multiple input, multiple output) controllers.

The PID controller stabilizes the attitude of the quadrotor by calculating the error between a measured value and a predefined set point. It adapts the actuators by calculating the proportional, integral and derivative responses of the outputs. The proportional part of the controller calculated an error term in between a set point and a variable. An increase in the proportional gain will increase the speed of the control system. Attention must be paid to not enter the oscillatory region of the variable. This occurs when gain values are too large. The integral response uses errors that were previously made to minimize the errors that will come. The derivative response reacts if too fast changes occur. It is proportional to the rate of change of the variable it is controlling and is very sensitive to noise. It could for this reason make the system control loop unstable if the gain is too large.

MIMO controllers are easier to use when more than one sensor and actuator are present. Full state feedback controllers use the inputs change the system dynamics. It does so by attempting the eigenvalues that are unstable to a more stable location. This can be done through a linear quadratic regulator (LQR) [62]. Hoffman has done this to control autonomously a rotorcraft [63]. Large stability margins to loop errors are obtained but this comes at the expense of needing a full state of the quadcopter [64].

Finally a last linear control method that will be explored is the H-infinity. They guarantee stabilization through optimization of a mathematical problem. A big advantage they have is that they are directly applicable to MIMO controllers. However, the mathematical level needed to apply them is too big and the full state of the quadcopter is needed. It was decided to not further explore these types of controllers for this project.

### 10.4.2. Non-linear control techniques

The non-linear control techniques depend vastly on the Lyapunov theory [64]. Various methods use this theory for control. Notable ones are gain scheduling, back stepping control and model predictive control.

The idea behind gain scheduling is to design several linear controllers, each with gains optimized for different trim conditions. During flight, the appropriate controller is chosen by the selector module basing on the state data. Implementing this method could optimize controllability of the drone, especially by designing control mode when the blower is on.

Backstepping uses nested loops to provide a powerful approach for stabilizing systems [64]. Raptis has used this type of controller for an autonomous helicopter [65]. Attitude dynamics were found to be exponentially stable and translational dynamics were asymptotically stable with this method. A drawback of this method however, is that full knowledge of the state of the vehicle is needed.

Finally, predictive control methods rely on a prediction model that often due to required accuracy, is expensive. The method in principle is based on iterative optimization of the cost function. This requires considerable computational power which hinders the implementation on a simple airborne embedded systems. Indeed, their performance is insufficient to provide a real time response.

### 10.4.3. The control method selected

The controller selected for the drone was the classic PID controller. The ease of implementation as well as its attitude stabilization performance were driving factors in this decision. Furthermore, given that there are only a few types of disturbances, that each do not produce a large force, there was no need for a more elaborate control method.

Two types of controllers are used: one for the position and one for the attitude of the drone. The attitude of the drone will be corrected by PID controllers whereas the position will be controlled by PD controllers. The PID controller used for the attitude is shown Figure 10.3. This figure illustrates the one that is used in the Matlab code to control the yaw motion of the rotorcraft.

The yawing rate (R) of the MAV is is differentiated to predict the future value of the yaw angle. The current yaw angle (Psi) and the wanted attitude command are subtracted and the error is found. This error is integrated and the accumulated offset is multiplied by the gain. The error is also passed in the proportional part of the PID controller and is multiplied by a gain.

The PD controller used for the position controllers is shown in Figure 10.4. The inertial frame velocity is the one that is controlled. It is then mapped to the desired theta attitude command.

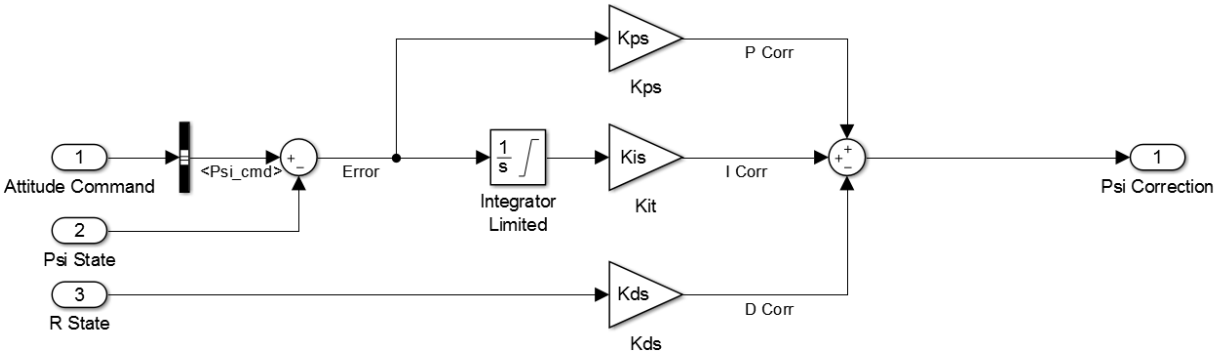


Figure 10.3: The PID controller used for yaw control [66]

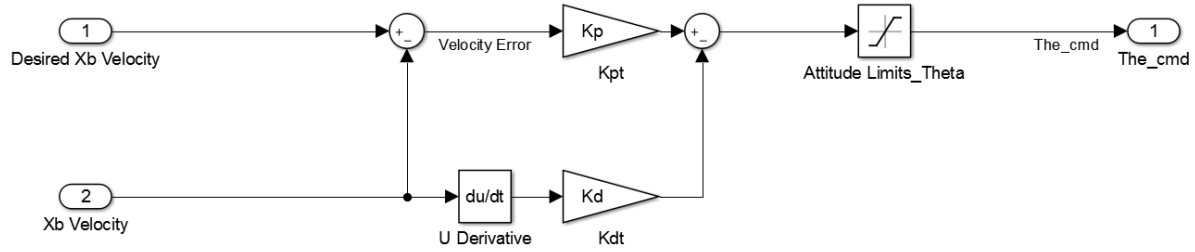


Figure 10.4: The PID controller used the x position of the MAV [66]

## 10.5. Stability

The model used to simulate the dynamic behaviour of the drone is the one created by MEM Senior Design Team 37 for Drexel University. It is rated 5 stars on the MathWorks official website and is open source [1]. The reason this model was used, is that it was too time consuming to make a new one.

In order to properly use this model however (or any model that gives accurate results), information about the motors is needed. Given that the motors were not tested, it was not possible to model the dynamic behaviour of the drone. This section will therefore focus more on explaining how the missing data can be obtained and how gain tuning can be done rather than showing how the drone reacts to disturbances. The coefficients that need to be determined are $C_T$, the thrust coefficient, $C_Q$, the torque coefficient and $C_r$ and b, which are constants that are obtained by passing a linear fit in between the throttle percentage and the RPMs of the motor.

The thrust coefficient, $C_T$ can be determined with Equation (10.16), where T is the thrust and $\omega$ represents the RPMs. $C_Q$ can also be determined in a similar fashion. Use of Equation (10.17) is made where Q is the torque created by the motor.

$$C_T = \frac{T}{\omega^2} \tag{10.16}$$

$$C_Q = \frac{Q}{\omega^2} \tag{10.17}$$

Finally, $C_R$ and b have to be determined. $C_R$ is the throttle % to RPM conversion coefficient. It can be determined through equation Equation (10.18). $\omega_{SS}$ is the steady state RPM of the motor and b is the y-intercept of the linear regression that relates the percentage to the RPMs.

$$\omega_{SS} = \text{Throttle\%} \cdot C_R + b \tag{10.18}$$

Once these values are determined, the blower can be modelled as a disturbance through functions in SIMULINK. The forces are listed below

1. $F_{x,blower} = 0.06 \cdot cos(45°) \approx 0.042N$
2. $F_{z,blower} = 0.06 \cdot cos(45°) \approx 0.042N$

[1] https://nl.mathworks.com/matlabcentral/fileexchange/48053-quad-sim [Cited 9 June 2017]

3. $M_{y,blower} = F_{z,blower} \cdot 0.1 \approx 0.0042Nm$
4. $\tau_{\theta,gyro} = J_m P \left(\frac{\pi}{30}\right) \omega$
5. $\tau_{\psi,gyro} = J_m R \left(\frac{\pi}{30}\right) \omega$

To calculate $\tau_{\theta,gyro}$, P and R have to be determined. This can be done by observing the model behaviour when the other forces and moments are applied on the MAV. Applying these forces, it was noted that the roll and yaw rates were very small and were therefore approximated to 0. The inputs are modelled through a ramp that takes 2 seconds and a step function. The time the ramp should be used for is the time the blower takes to spin at max RPM. This was found through the maximum RPM value of 5300 and the acceleration of 20g. The inputs used to simulate the blower should reassemble to the ones of Figure 10.5. The time the blower is on at max RPM was selected arbitrarily to 6s.

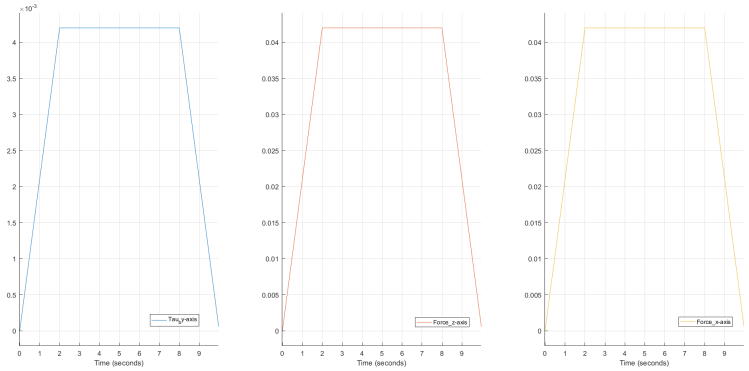


Figure 10.5: The inputs provided for the model of the MAV

Once the inputs are modelled, the gains of the controllers can be tuned. Gain tuning is important as it allows the drone to respond more accurately to disturbances. If done poorly, the system can behave in an unstable way by diverging or oscillating around the desired value. Two gain tuning methods will be looked at Ziegler–Nichols and Tyreus-Luyben. Both require some trial and error and both are relatively aggressive tuning methods. This means that it is easy for it to overshoot or become unstable.

The Ziegler–Nichols method tries to find the gain values when the system responds to a step input. At first a low $K_p$ value should be used. It should be increased until the system responds in a steady state oscillation. The value of $K_p$ for which this occurs is denoted as $K_{cr}$. $P_{cr}$ is the period of the sinusoidal wave. The gain parameters can now be tuned by following Table 10.1.

| **Controller** | **Kc** | $\tau_{int}$ | $\tau_{der}$ |
|---|---|---|---|
| **P** | $K_{cr}/2$ | | |
| **PI** | $K_{cr}/2.2$ | $P_{cr}/1.2$ | |
| **PID** | $K_{cr}/1.7$ | $P_{cr}/2$ | $P_{cr}/8$ |

Table 10.1: Gain tuning according to the Ziegler Nichols method

| **Controller** | **Kc** | $\tau_{int}$ | $\tau_{der}$ |
|---|---|---|---|
| **PI** | $K_{cr}/3.2$ | $P_{cr}$ 2.2 | |
| **PID** | $K_{cr}/2.2$ | $P_{cr}$ 2.2 | $P_{cr}/6.3$ |

Table 10.2: Gain tuning according to the Tyreus-Luyben method

The method proposed by Tyreus-Luyben follows the same method as Ziegler-Nicols but the coefficients used to determined the gains are slightly different. They are regrouped in Table 10.2. Reducing the oscillations is the main reason that these gains are different. Both methods can be tried out and the one that yields the most satisfactory results can be used.

# 11

# Ground segment

The APIS consists of the aerial segment (all the drones) and the ground segment (the supporting equipment). Most of the previous chapters have focused predominantly on the aerial segment. The current chapter, however, investigates the details about the ground segment.

The means for integrating the support equipment within the existing greenhouse environment are presented in Section 11.1. Then, the landing pads, fundamental for the autonomous recharging of the drones, are outlined in Section 11.2. Details about the electronics for the ground stations and the rest of the support equipment are given in Section 11.3. Following, an air traffic management strategy for making sure that the drones can fly and navigate safely in the greenhouse environment is suggested in Section 11.4. Section 11.5 sketches the user interface. Finally, the concluding Section 11.6 gives estimates for the weight and the cost of a ground station.

## 11.1. Greenhouse integration

One of the main aspects of designing the ground equipment for the pollination system is the integration with existing infrastructure. The aim is for it to require minimum additional equipment and to be not intrusive to the established greenhouse practises. In order to boost production level, the amount of land unused by the plants is minimized. Therefore, introducing additional facilities would hinder the usability of these areas. For example, rows and paths should have sufficient width to allow for transport carts to pass (see Figure 11.2). Therefore, there is limited space on the floor to locate the ground stations.

It was noted that the greenhouses typically have an elaborate roof structure featuring numerous truss structures that support the weight of the tomato plants. It was therefore concluded that this structure can be used to hold the ground stations in the air above the center corridor (see Figure 11.10). Located several meters above the path, they will not obstruct the path. Maintenance can still be facilitated as most greenhouses have moving hydraulic trolleys like the one in Figure 11.3[1]. Therefore, in case maintenance is needed, access can be readily obtained by using already existing equipment.

Pollination is also to be performed only at the very top of the plants, hence flying down to and up from ground level for charging is not efficient. By placing the charging stations at the height of the flowers, the energy required for the non-pollinating part of the flights is reduced. The truss structure of the greenhouse roof also can support the power and communication cables feeding to the ground stations. No redesign of the floor infrastructure would have to be made. In this way the pollination system's impact on the normal operations and equipment in the greenhouse is minimized.

The structure of the charging station will have a main vertical strut connected to the roof truss. The connection will be such that the charging system is rigid enough to not move upon drones landing. The charging pad will be arranged on two layers of four pads. If the height of the roof allows, additional layers can be added. A box holding the main electronic components of the ground station will be located close to the strut connection to the truss. An illustration of a ground station can be seen in Figure 11.1.

## 11.2. Landing pads

The charging pin on the drones is designed after the standard 6.3 mm phone connector like the one in Figure 11.4[2]. This pin design was selected due to the relative ease with which it can be plugged, even if not ideally aligned with the socket. A drawing of the socket designed for the landing pads can be seen in Figure 11.5[3]. The contact surfaces on the sides are

[1] Buitendijk-Slaman `http://www.buitendijk-slaman.nl/mpt.html` [Cited 16 June 2017]

[2] Image from `http://www.conrad-electronic.co.uk/ce/en/product/304313` [Cited 16 June 2017]

[3] Image from `https://www.thomann.de/gb/harley_benton_parts_mono_output_jack_socket.htm` [Cited 16 June 2017]

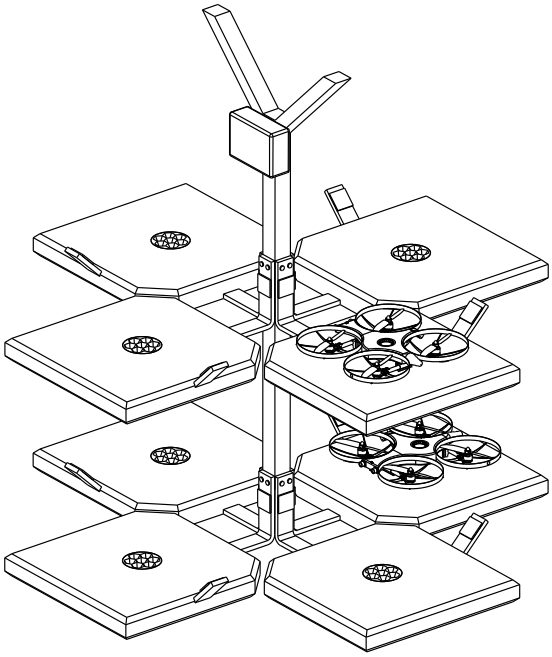

Figure 11.1: An illustration of the ground station configuration

Figure 11.2: Typical tomato picking procedure and equipment (transportation cart behind the man)

Figure 11.3: Hydraulic cultivation trolley

compressed upon jack insertion, and hence provided restorative force that ensures proper contact. Moreover, due to the shape of the tip of the jack, and the spring-like connection, accidental detaching is improbable.

A guiding cone is located above the socket in order to assist the plugging of the pin. It was deemed desirable for the guiding that, if misaligned, the bottom of the pin touches the cone walls with the side of the bottom-most part, instead of with the tip. The larger horizontal component of the reaction force, as well as the resulting moment acting on the drone due to the offset of the force application point, both contribute for more effective guiding. This puts limits on the maximum cone angle as can be seen in Figure 11.6. The cone angle cannot be more than 45° as that is the typical plug tip angle. With 1 cm cone depth, the resulting cone opening has a diameter of 1.8 cm.

Still, the accuracy necessary for the control system to land the drone while plugging such a jack in the cone of the respective socket is prohibitive. In order to allow landing with lower precision, multiple ports are used instead. They are arranged in a honeycomb pattern with ridge and cone structure guiding the pin to the closest socket. This socket array has a diameter of 5 cm. To assist the drone to align itself above the socket array, two markers are put in front of its forward-facing stereo and its side-facing mono camera. These markers are aligned with the center of the socket array. Therefore, by aligning the markers in the center of its field of vision, the drone can align itself above the center of the socket array as well. The charging pad design can be seen in Figure 11.7.

Figure 11.4: Standard 6.3 mm phone jack

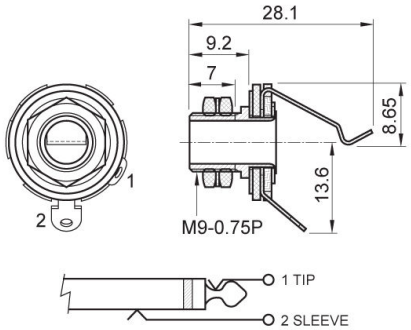


Figure 11.5: Standard 6.3 mm phone socket

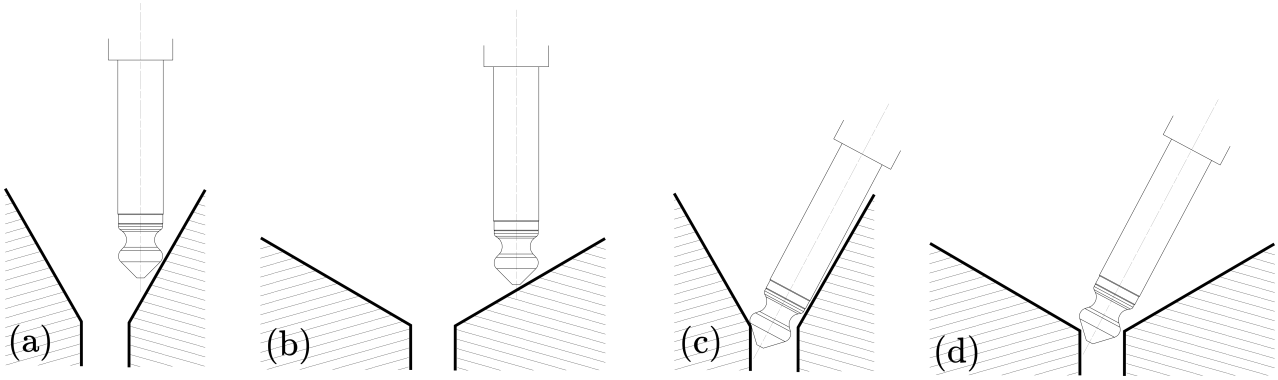


Figure 11.6: Effect of cone angle on guiding the plug into the socket. A cone angle of 30° is shown in (a) and (c), and a cone of 60° is shown in (b) and (d). Images (a) and (b) illustrate the case of vertical descend, while images (c) and (d) the case of tilted descend

## 11.3. Electronics and infrastructure

The ground stations have partial autonomy, receiving commands and reporting solely to a central server. This server can be located in any supporting facility outside the actual greenhouse. It stores the images taken by the drones, provides the user interface, communicates with the ground stations and monitors the status of every component, as well as the system as a whole. One or more emergency stop buttons are also connected to the server. When such a button is pressed, the server instructs the drones to slowly land wherever they are. This can result in serious system and greenhouse damage so is to be used only in a serious emergency. In case a ground station loses contact or malfunctions, it informs the user via the user interface and reassigns its drones to other ground stations. The server also holds records of the performance of every drone and measurements for the temperature and humidity levels as measured by them. It also performs calibration of location information of the UWB tags based on readings recorded during flight.

The server communicates with the ground stations via a Local Area Network (LAN) through a network switch. The connections between the central server, the switch and the ground stations are facilitated by a standard LAN cables with RJ45 connectors. In order to reduce the number of LAN cables that need to be placed in the greenhouse, the ground stations are given also network hub functionality. Every ground station also has extra four RJ45 ports that can be used as for connecting other stations. This effectively reduces the total cable length needed. Nevertheless, concatenating ground stations in this fashion runs the risk of loss of multiple stations in case the hub station fails. Therefore, the trade-off between total cable length and redundancy should be made separately for the specific greenhouse architecture and user preferences. The power lines follow the same philosophy with several ground stations connected to the same main line by using T-junction cable connectors. An illustration of the ground segment connections for a small greenhouse can be seen in Figure 11.9.

The ground station controller is to be based on a general purpose microcomputer. Raspberry Pi[4] and Beaglebone[5] were considered as a baseline. Beaglebone was eventually preferred because of the higher number of general purpose input-output (GPIO) it has (69 vs. 40). Sets of such GPIO pins can be used in order to allow concetivity following

[4] `http://www.raspberrypi.org/products/raspberry-pi-3-model-b/` [Cited 16 June 2017]
[5] `http://beagleboard.org/black` [Cited 16 June 2017]

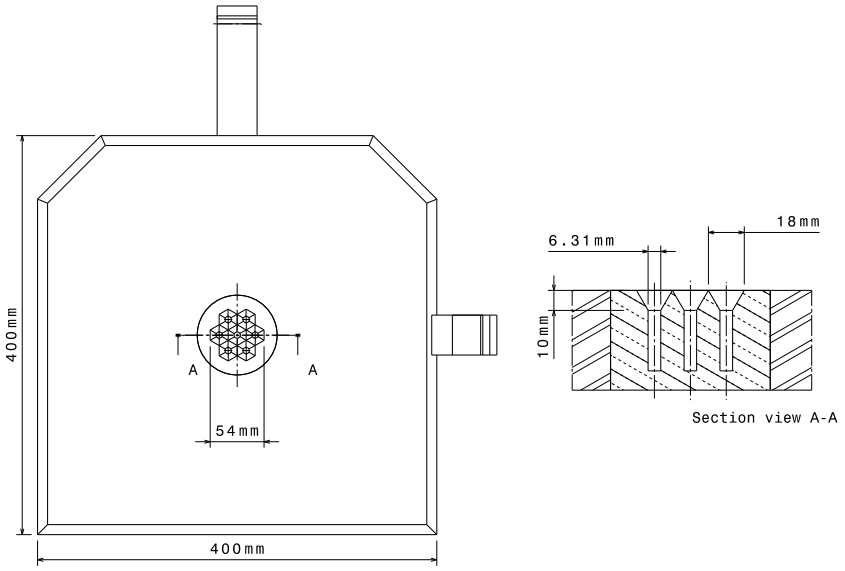


Figure 11.7: An illustration of the charging pad with a section view on the charging sockets

standards like SPI or RJ45. An illustration of the electronics diagram for the ground station can be seen in Figure 11.9.

One of the main functions of the ground station controller is to facilitate the charging of the drones via the charging pads. The PMM8920 power management module (as introduced in Chapter 7) on board of each drone can control the battery charging and balancing process. Its charging integrated circuit supports four charging techniques: trickle, constant current, constant voltage, and pulsed. It monitors the charging parameters and makes decisions to control the charging process automatically [67]. Therefore, the ground station only has to supply DC current to the PMM8920 module. Status about the charging and measures of the state of the battery do not need to be communicated to the ground station as all decisions regarding the charging process are made on the drone. As a result, having a charging pin with only two contacts is sufficient. A relay can be used to start and stop the current supply to the sockets. The relay controls the input from a voltage supply that supplies the required current. Controlling the 8 relays for the charging integrated circuits for each of the 8 charging pads requires 8 GPIO pin of the controller.

Each ground station is equipped with a single Decawave DWM1000[6] UWB module for drone communication and ranging. As for large greenhouses the coverage of this module might be insufficient, two ports for external UWB modules are also present. These modules can be located away from the ground station and connected to it via cables in order to improve the UWB localization. Each of the three UWB modules connects via SPI interface that requires 4 GPIO pins, resulting in a total of 12 pins.

The LAN hub function of the ground stations is facilitated by adding 4 additional RJ45 connectors to the controller board. Each such connector requires 8 GPIO pins

## 11.4. Air traffic management

With dozens of drones flying within the greenhouse, air traffic management strategy is of fundamental importance for ensuring safety and preventing collisions. Hereby, a basic strategy is outlined. During future developments it can be further optimized to increase the efficiency and capacity of the system.

Each row in the greenhouse will be accommodated with drones coming from a certain ground station. This reduces the risk of collision since only drones guided by the same ground station will be flying in certain areas. To eliminate the risk of collision in this scenario completely the drones are programmed to ask permission to the ground station when they need to land for recharging purposes. When the ground station confirms, the drone will land and the other drones requiring recharging will wait until they get confirmation from the ground station as well.

The risk of drones colliding inside the rows is successfully eliminated since almost all rows only have a single drone performing the pollination. The rows that are on the transition between two ground station areas do have two drones that perform the pollination. However, the risk of these two drones colliding is mitigated by the fact that one of the two

[6] `https://www.decawave.com/products/dwm1000-module` [Cited 16 June 2017]

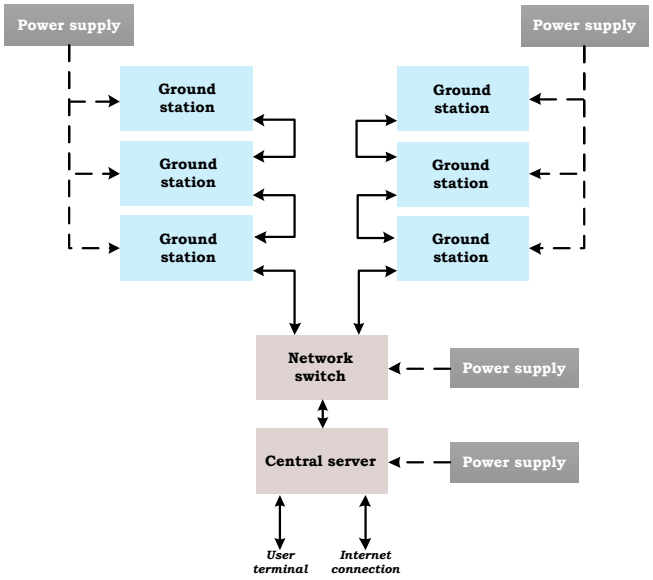


Figure 11.8: An example of the ground segment for a small greenhouse. The six ground stations are powered by two main lines. Only two of the ground stations are directly connected to the network switch, the other use the hub functionality. Solid lines represent signals and broken lines represent power connections

drones will start its mission in this row and the other drone operating in this row will end its mission here. This results in a huge time difference of presence of both drones in the row.

The airspace in the greenhouse is divided in segments. In each segment, there could be only a single flying drone at a time. Every half-row is a segment by itself. Additionally, along the corridor, every ground station has its own segment as well (called terminal control zone, or TCZ), dynamically corresponding to the space between the rows allocated to the given station. An illustration of the TCZs can be seen in Figure 11.10. As there might be two ground stations sharing the responsibility for a row, it is possible that their TCZs intersect. When a drone is in the intersection of two TCZs, then in neither of them can be another drone flying. A drone instructed to land has to wait at the border of the TCZ if there is another drone performing take-off or landing operations in the TCZ of the same ground station.

The main server allocates the rows in the greenhouse among the ground stations. This is done on the base of the performance statistics for each individual drone, as well as on the location of the ground stations. This allocation is updated dynamically as information about the pollinated quantities are dynamically reported by the ground stations. Each ground station autonomously makes the decision of which rows to assign to which drones. It would usually assign the drones closest to it first. In this way, if at that location the rate of pollination is lower than expected, the furthermost rows can be reassigned to the neighbouring stations without the need for drones crossing through the several TCZs.

The ground stations give high-level instructions to each drone. The instructions involved with typical operations are: take-off, navigate to the beginning of the row, go to a specified starting position, execute pollination procedure; and after the pollination procedure is completed, navigate to beginning of the row, if TCZ is free navigate to a specified landing pad, if not wait for the TCZ to become free. After each trip, the drones report how far in the row they have advanced and both the ground station and the main server store this information and use it for planning and task allocation.

## 11.5. User interface

The user interface is web-based. In this way, it is compatible with virtually any computing platform the user might want to use. Access is provided via cable or wireless LAN connection, or remotely if the network switch is connected to the internet. This will be the primary tool for the user to monitor, manage and control the drone swarm and the pollination process. The user interface is also the main way for the system to communicate warnings, malfunction reports or other messages.

It provides a gallery of all images taken by the drones together with a map of the greenhouse that shows where the images were taken. Additionally, maps of the temperature and humidity distribution in the greenhouse, measured at different times, are also included.

Pollination and performance statistics are also given either per drone, ground station or for the system as a whole.

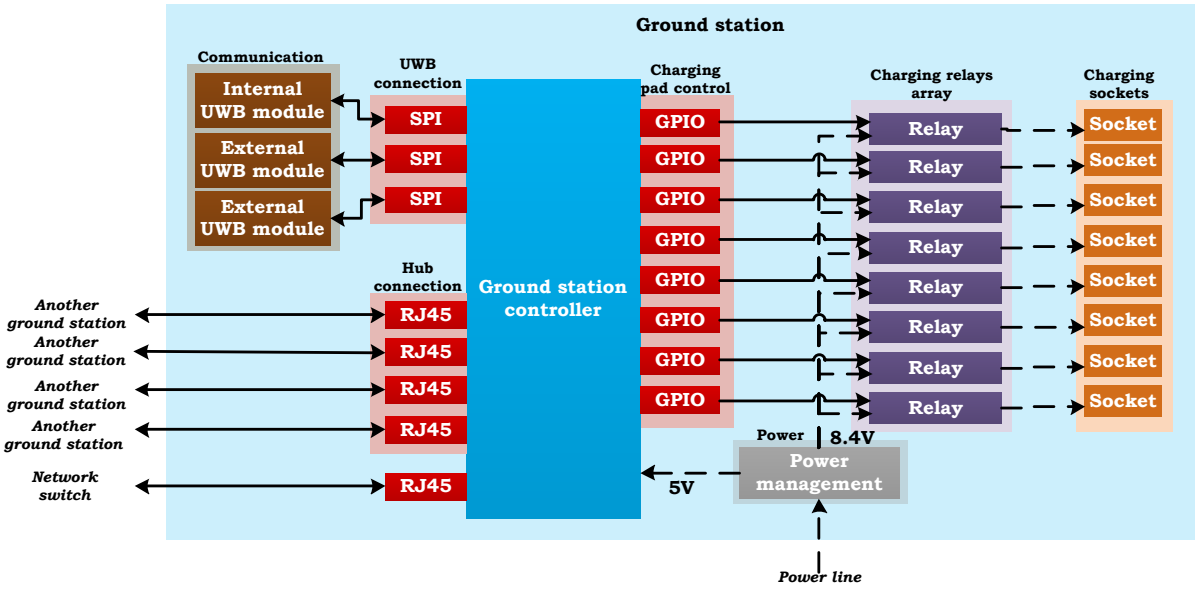


Figure 11.9: Electronics diagram of the ground stations. The interfaces with external components are also shown. Solid lines represent signals and broken lines represent power connections

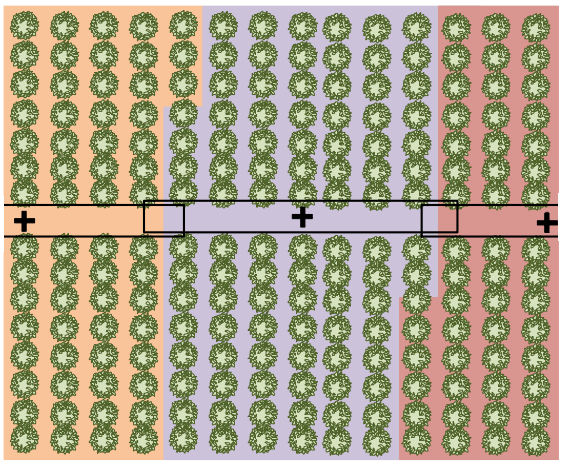

Figure 11.10: Illustration of the row assignment among the ground stations (in different colours). The locations of the ground stations are shown with black crosses. Moreover, the TCZ of each ground station and the intersections of these zones are also shown

Table 11.1: Cost for the ground segment components excluding the ground stations

| Component | Price [€] | | |
|---|---|---|---|
| Server | 1600.00[a] | ± | 500.00 |
| Switching hub | 60.00[b] | ± | 30.00 |

[a] Based on Dell PowerEdge T330 Intel Xeon E3-1240 v6 3.7GHz + 2 1TB 7.2K RPM hard drives `http://www.dell.com` [Cited 26 June 2017]

[b] `https://www.centralpoint.nl` [Cited 26 June 2017]

Table 11.2: Weight and cost break-down per ground station

| Component | Number of components | Weight [g] | Total weight [g] | Price [€] | Total price [€] |
|---|---|---|---|---|---|
| Beaglebone board | 1 | 40 ± 2 | 40 ± 2 | 43.07[a] ± 2.00 | 43.07 ± 2.00 |
| UWB tag | 1 | 0.1 ± 0 | 0.1 ± 0 | 13.50[b] ± 2.00 | 13.50 ± 2.00 |
| Relay | 8 | 4 ± 1 | 32 ± 8 | 1.57[c] ± 0.30 | 12.56 ± 2.40 |
| Other electronics + box | 1 | 200 ± 50 | 200 ± 50 | 10.00 ± 5.00 | 10.00 ± 5.00 |
| Charging pad box | 8 | 648 ± 30 | 5,184 ± 240 | 12.96[d] ± 2.00 | 103.68 ± 16.00 |
| Charging pad brace | 16 | 324 ± 15 | 5,184 ± 240 | 6.48[d] ± 1.00 | 103.68 ± 16.00 |
| Charging socket | 56 | 9 ± 1 | 504 ± 56 | 1.49[e] ± 0.50 | 83.44 ± 28.00 |
| Main strut | 1 | 1,900 ± 100 | 1,900 ± 100 | 19.20[f] ± 2.00 | 19.20 ± 2.00 |
| Total | | | 13,044 ± 696 | | 389.13 ± 73.40 |

[a] https://www.centralpoint.nl/netwerk-switches/v7/8-x-gigabit-poe-rj-45-art-pegs8-1e-num-5953521 [Cited 26 June 2017]
[b] https://www.digikey.com/product-detail/en/decawave-limited/DW1000-I-TR13/1479-1001-1-ND/4499860 [Cited 26 June 2017]
[c] https://www.sparkfun.com/products/100 [Cited 26 June 2017]
[d] https://www.distrelec.nl/en/sheet-aluminium-500-500-mm-no-brand-en-aw-5005-5x500x500mm/p/14821854 [Cited 26 June 2017]
[e] https://www.thomann.de/gb/harley_benton_parts_mono_output_jack_socket.htm [Cited 26 June 2017]
[f] https://www.distrelec.nl/en/aluminium-square-tube-length-alcoa-inc-en-aw-6060-t66-30x30x3mm-squar/p/14846282 [Cited 26 June 2017]

Information about the health (e.g. battery life, average pollination efficiency, state of motors) of each individual drone is also available. This allows for the user interface to notify the user in case there is a need for the battery to be replaced or if the ESC detects motor wearing problems. Moreover statistics about the processor and memory performance (CPU degradation can be for example detected if it requires higher voltage to be kept stable, memtest86 can be used for memory degradation measurement[7]) Additionally, there can be a map showing when was the last time each part of the greenhouse was pollinated.

Finally, an application programming interface (API) is also to be developed. The API will provide complete access to the data recorded by the system and to most of the control functionality. In that way the API will enable connecting and expanding the system with custom or third-party software.

## 11.6. Ground station weight and cost estimation

As the ground stations are to be attached to the existing greenhouse roof structure, it had to be confirmed that it can support them. Therefore, a rough initial estimate of the ground station weight was established.

A Beaglebone board weighs 40 grams[8] and it was estimated that the other electronics, together with an electronics box weigh additional 200 grams.

The box of each charging pad was approximated as a 40×40×5 cm aluminum box with wall thickness of 0.1 mm. That resulted in a weight of 20 grams. Additionally the two braces in the front and the left side were approximated in the conservative case as aluminum strips with length 30 cm, width 4 cm and thickness 1 cm, resulting in 648 grams for both. Finally, seven 6.3 mm phone sockets were also added, each weighing 9 grams[9]. This results in total charging pad weight of 1.11 kg.

The main strut is estimated as an aluminum beam with square cross-section with a side of 4 cm, length 1 m and thickness 5 mm, resulting in a weight of 1.9 kg. In total, they whole ground station weighs about 11 kg without the drones and 13 kg with the drones. The weight break-down per ground station can also be seen in Table 11.2 together with the respective cost breakdown. After a consultation with an architect[10] it was concluded that a single beam of the structure of a typical greenhouse should be able to support more than a dozen of such ground stations without a problem.

Estimated costs for the central server and the switching hub can be seen in Table 11.1. The cost margins for the server are relatively large because the cost depends on the hardware parameters which are specific for each greenhouse user.

[7] http://www.memtest86.com/ [Cited 16 June 2017]
[8] http://beagleboard.org/black [Cited 19 June 2017]
[9] https://www.amazon.co.uk/dp/B01CEZJJYQ [Cited 19 June 2017]
[10] Phone call to an expert: Vesela Petkova, Albena Design Bureau

# 12

# Technical diagrams

In this chapter, the technical diagrams showing the interaction between the subsystems are shown. The electrical component diagram can be seen in Figure 12.5. This diagram shows how the components are connected to the processor and what the interfaces are. In Figure 12.1 the electronic block diagram can be seen, in which the circuits that will be used are shown. The software diagram is presented in two parts in Figure 12.3 and Figure 12.4, and the hardware diagram is shown in Figure 12.5.
Another important diagram and an essential part of the design is the communication flow diagram. The communication flow diagram illustrates the flow of data from the environment through the system and back to the environment again. That communication flow diagram generated for our design is shown in Figure 12.6. The data handling block diagram can be seen in Figure 12.2.

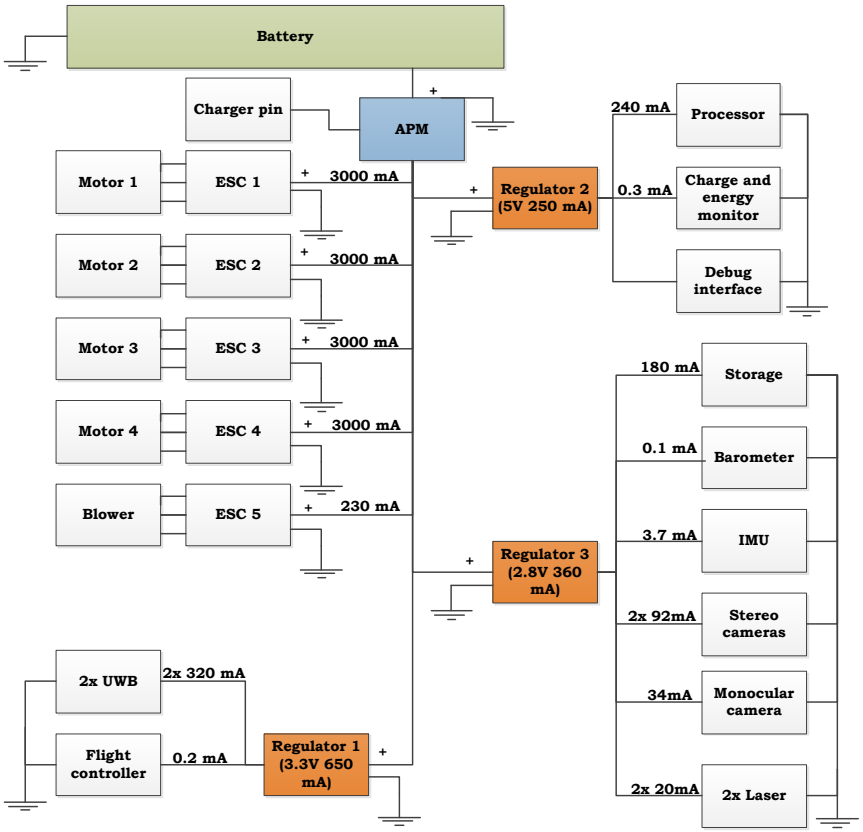


Figure 12.1: Electrical block diagram for the APIS showing the main power lines (DC current)

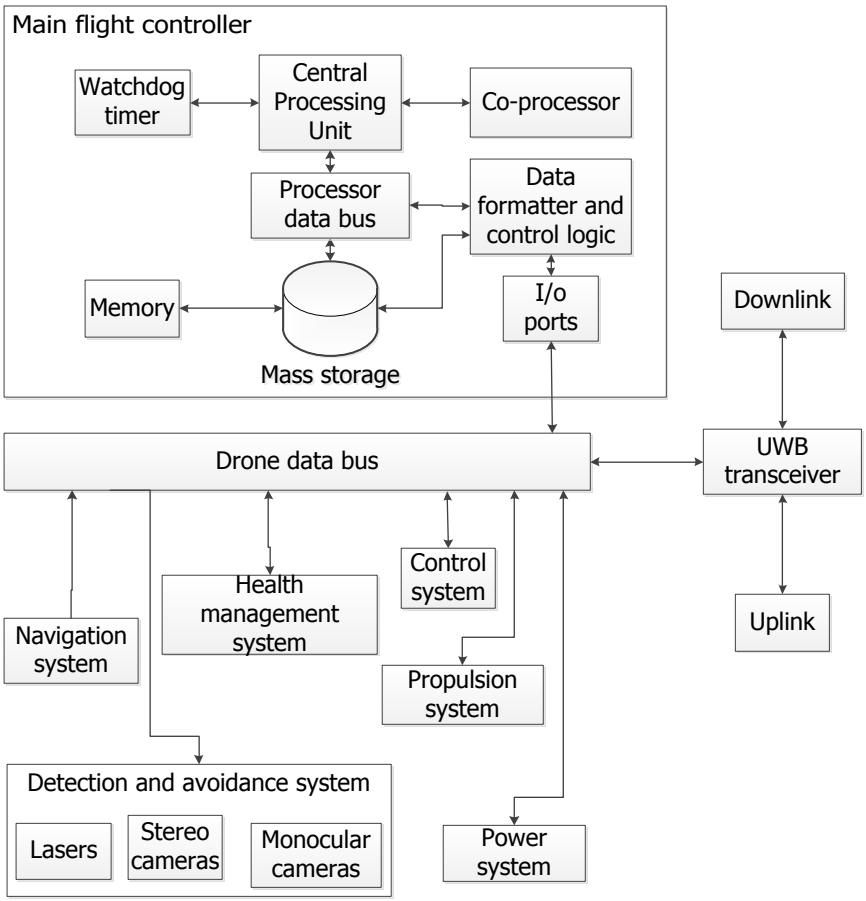


Figure 12.2: Data handling block diagram

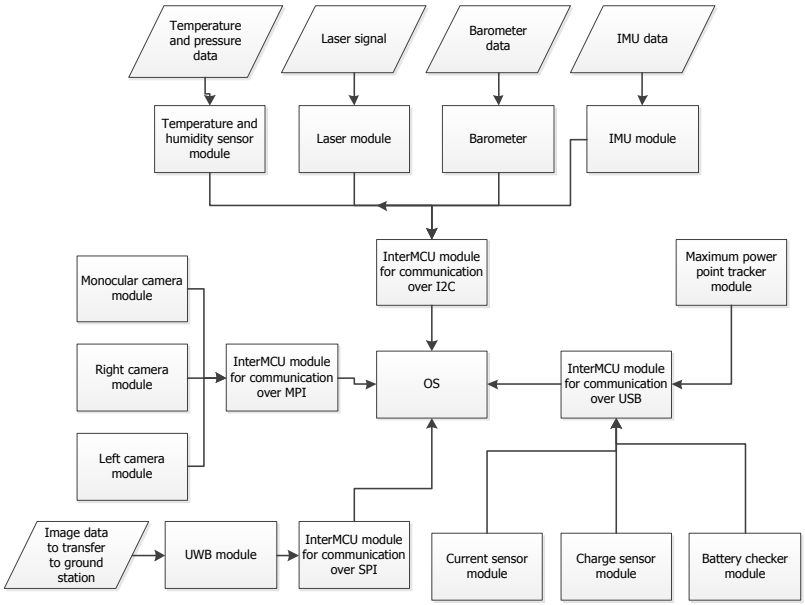


Figure 12.3: Software block diagram - part 1

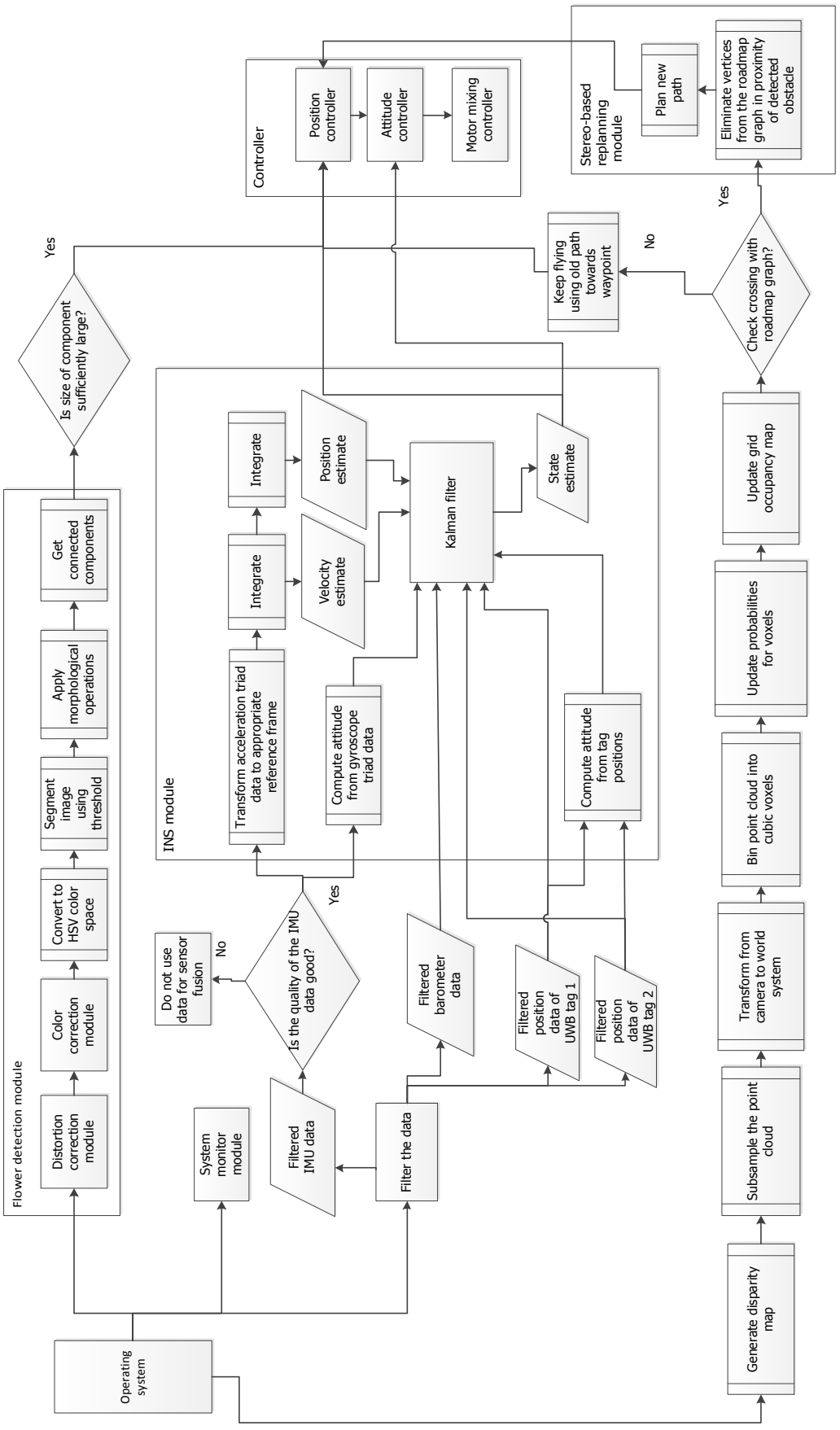


Figure 12.4: Software block diagram - part 2

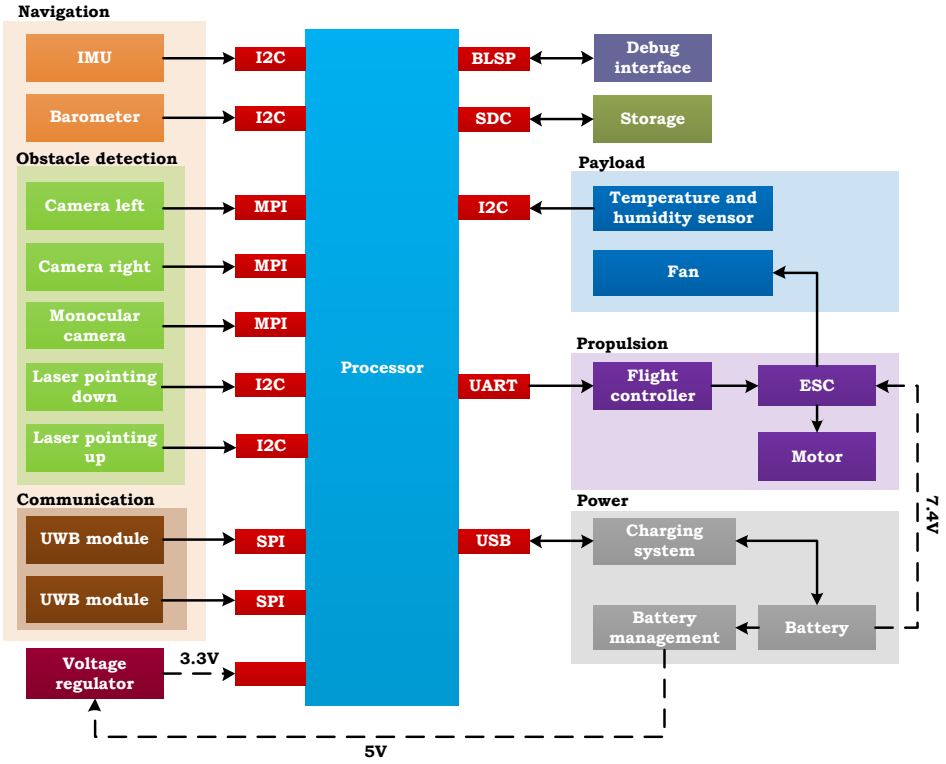


Figure 12.5: Electrical component diagram

Table 12.1: Table showing what data is communicated between the blocks of the communication flow diagram

| Number | Data description | Number | Data description |
|---|---|---|---|
| **1** | Sensor signals | **17** | State update: no path command |
| **2** | Slave device addresses | **18** | State update: start pollination phase |
| **3** | UWB signal | **19** | Blower control commands |
| **4** | Image data from monocular camera | **20** | UWB data |
| **5** | Image data from monocular camera with corrected color | **21** | Row allocation information/ designation to return to ground station |
| **6** | Image data from stereo camera | **22** | From UWB to localization module: ranging information. From localization to UWB module: location estimate |
| **7** | Processed stereo images | **23** | Location estimate |
| **8** | Disparity map | **24** | Drone health information |
| **9** | Obstacle detection signal | **25** | Crtitical health warning signal |
| **10** | Path command | **26** | Mission data |
| **11** | Sensor data | **27** | Image data |
| **12** | State estimate | **28** | Ground station information |
| **13** | Euler angle commands as well as altitude command | **29** | Command information from user |
| **14** | Corrections in Euler angles as well as altitude | **30** | Information from communciation module |
| **15** | Actuator control commands | **31** | UWB information |
| **16** | State update: guidance with path | **32** | Comands from user |

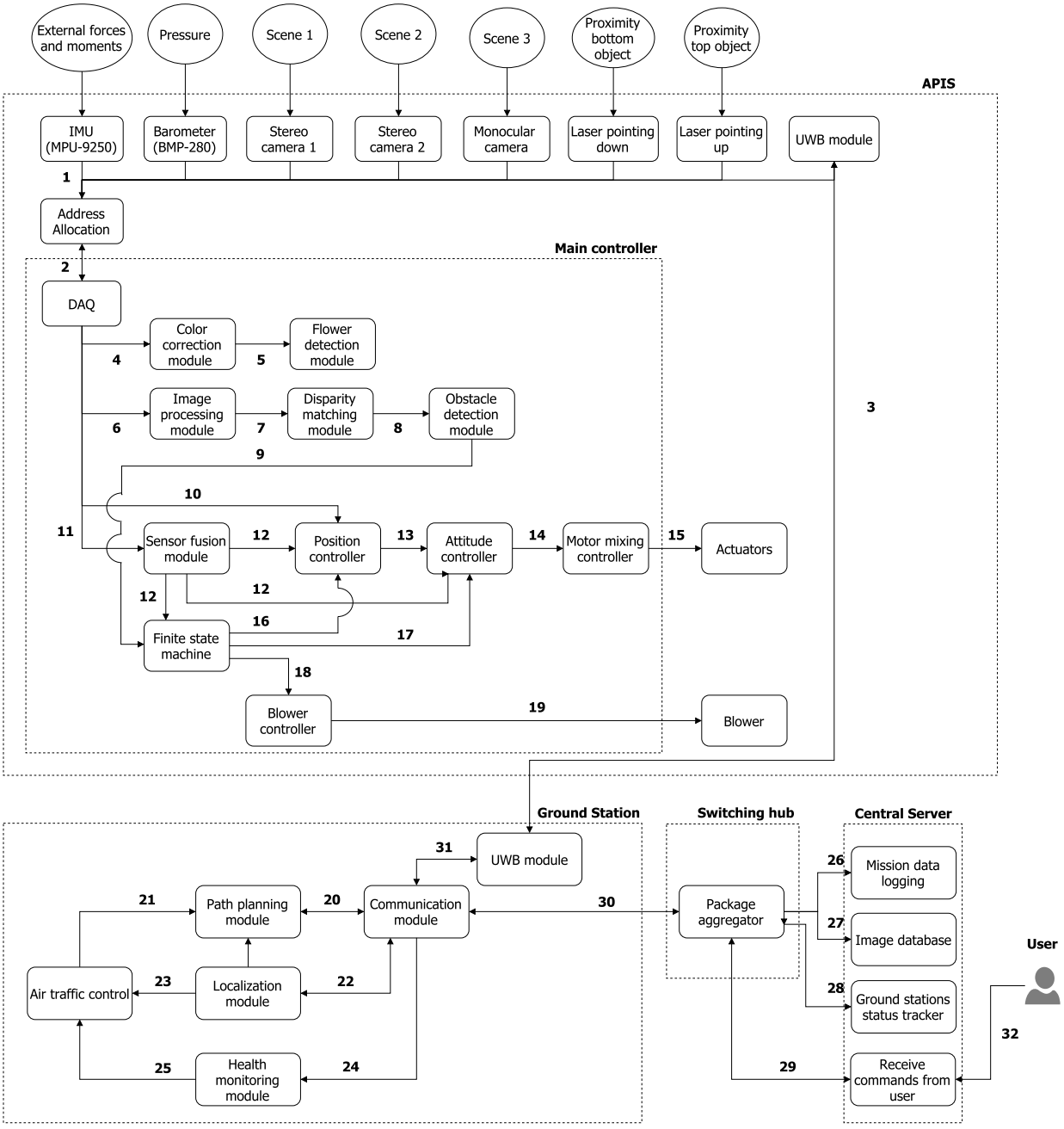


Figure 12.6: Communication flow diagram

# 13

# Final cost, mass and configuration

This chapter summarizes the technical decisions discussed in the previous sections. The main design presented here assembles all the subsystems and provides an illustration of the future product, APIS. Firstly, some general dimensions of the drone (on scale) are provided to offer a better feeling of the final product. Secondly, a first order bill of materials is tabulated together with the component price, its net weight and the source from where it can be purchased. Then, a total cost of the entire mission is generated, including that of the ground station and the system of drones. Lastly, the requirements are brushed over and they are checked for compliance. This is summarized in a compliance matrix followed by a feasibility analysis for the requirements that are not met or still left to be validated.

## 13.1. Design characteristics

APIS is a 250 g drone designed to be modular, thus flexible for different pollination methods. The current configuration presented in this paper accommodates for a blower suited for self pollination which weights 15 g. With this weight, APIS hovers at 48% of the maximum thrust, leaving plenty of throttle for agile maneuvers. According to requirement DP-MAV-14, the drone is allowed to hover at 50% of the maximum thrust, meaning that a maximum payload of 25 g can be taken on board (without the blower) or extra 10 g besides the blower.

The backbone structure was built around the battery which represents 40% of the total weight spread along the longitudinal axis. Because of that, an H-configuration was chosen in order to minimize the length of the booms. The customized battery fits in a box. In order to minimize the drag caused by the volume, the blower was designed to fit in a compact casing. As a result, a centrifugal blower was chosen to obtain the required blowing velocity. This is attached to the battery and held in place by the main case which makes sure that no moisture affects the interior of the drone.

The stereo cameras are placed in front of the case to assure visibility with the needed field of view and distance between each other. The monocular camera is placed under the blower and parallel to its exit flow. Two lasers are placed in the front on the top and the bottom of the case in order to scan the surroundings as the drone advances in the unknown environment. Last but not least, the propeller casings are there to assure the safety of the plants according to requirement *DP-SAFE-1*. Figure 13.1 illustrates how all the aforementioned features are incorporated into a single aerial vehicle with an animal-like aspect to perform the mission.

Figure 13.1: Isometric view of APIS. Rendered with CATIA V5

## 13.2. CAD technical drawings

This section provides the general outer dimensions of APIS. The CAD drawings are generated by CATIA V5 which also keeps track of the mass of each component given the material density. Figure 13.2 illustrates the top view, while the isometric, front and side views can be found in Figure 13.3.

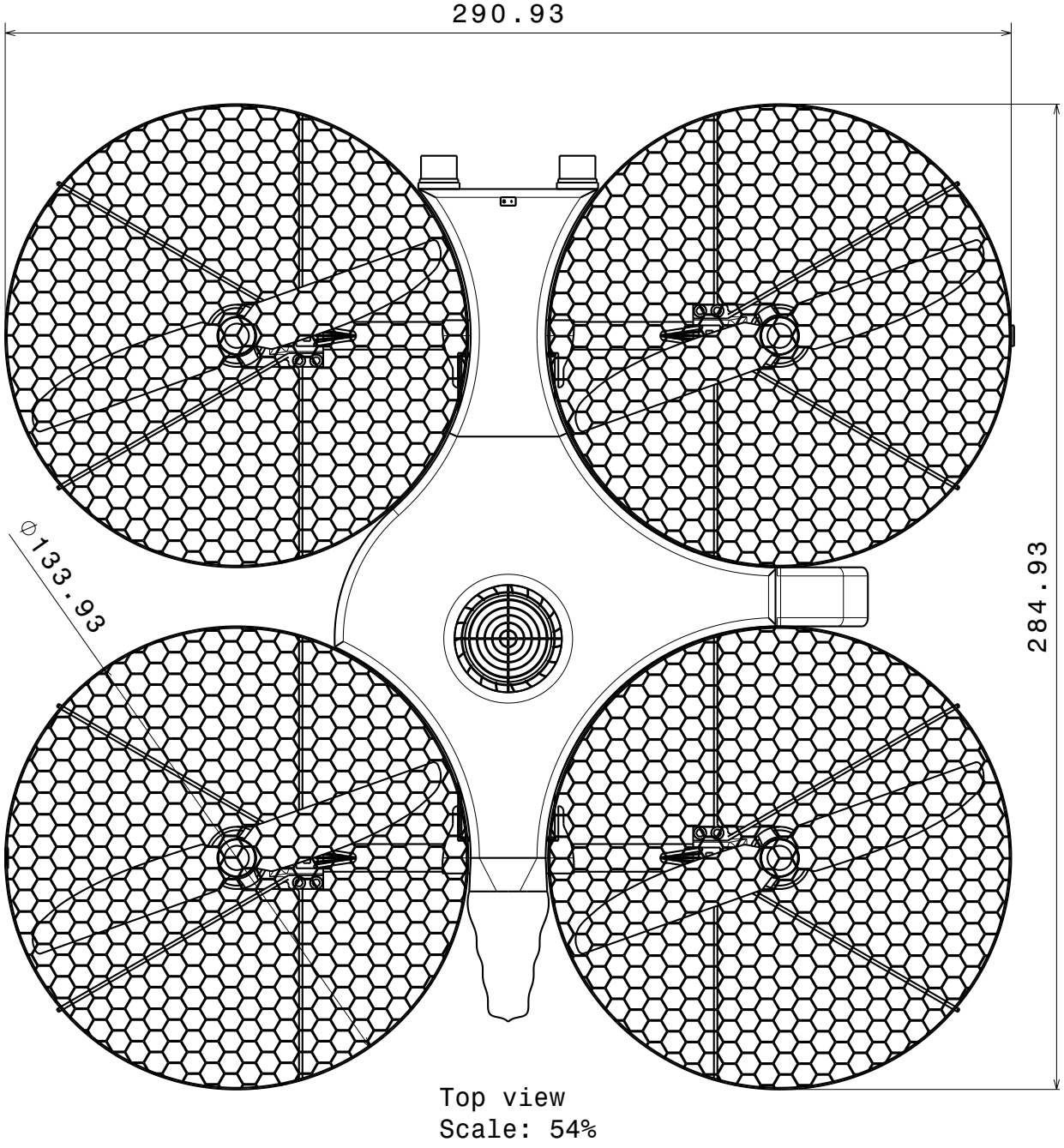


Figure 13.2: Top view of APIS. Dimensions in mm

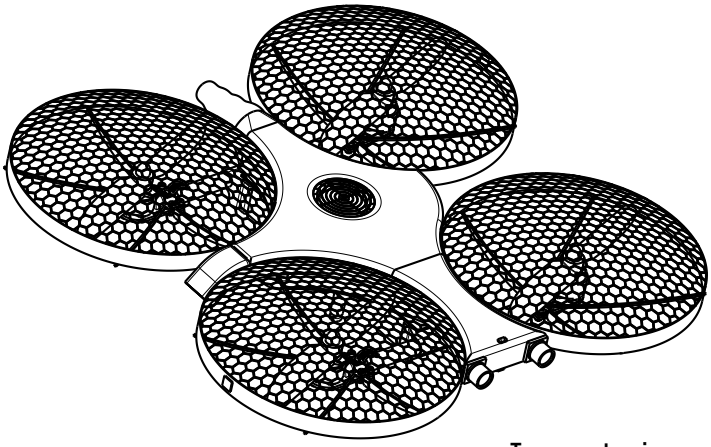

Isometric view
Scale: 27%

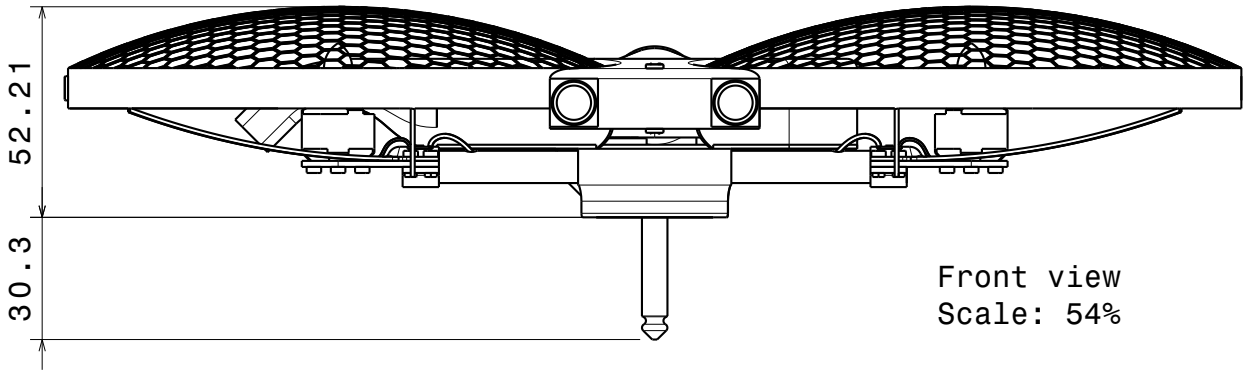


Front view
Scale: 54%

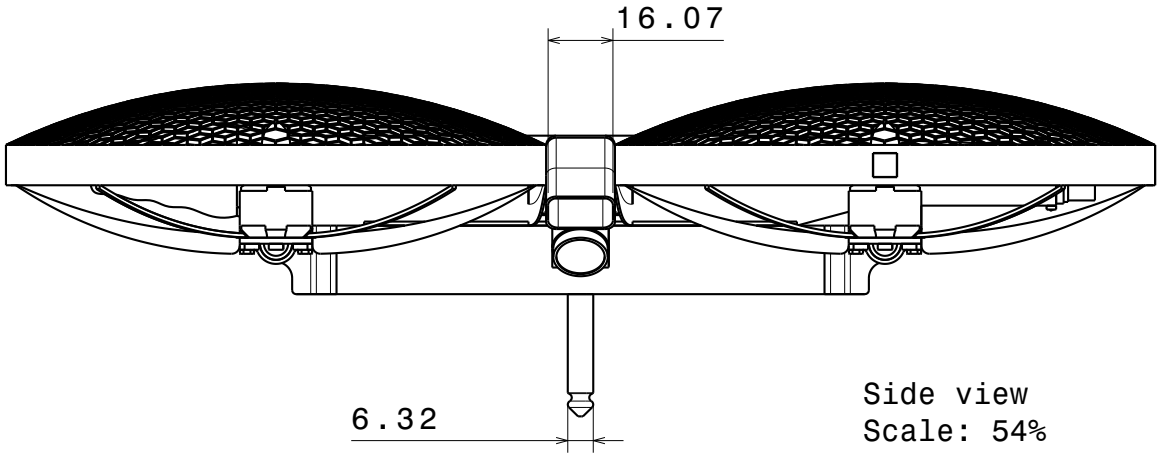


Side view
Scale: 54%

Figure 13.3: Isometric, front and side view of APIS. Dimensions in mm

## 13.3. Exploded views and BOM

This section highlights every component considered in the design. First, the blower assembly is presented in Figure 13.4 followed by the propulsion system in Figure 13.5. Lastly, Figure 13.6 illustrates the final assembly including the blower and propulsion sub-assemblies. All these exploded diagrams are followed by bills of materials (BOM) which describe each component listing the materials, masses and costs.

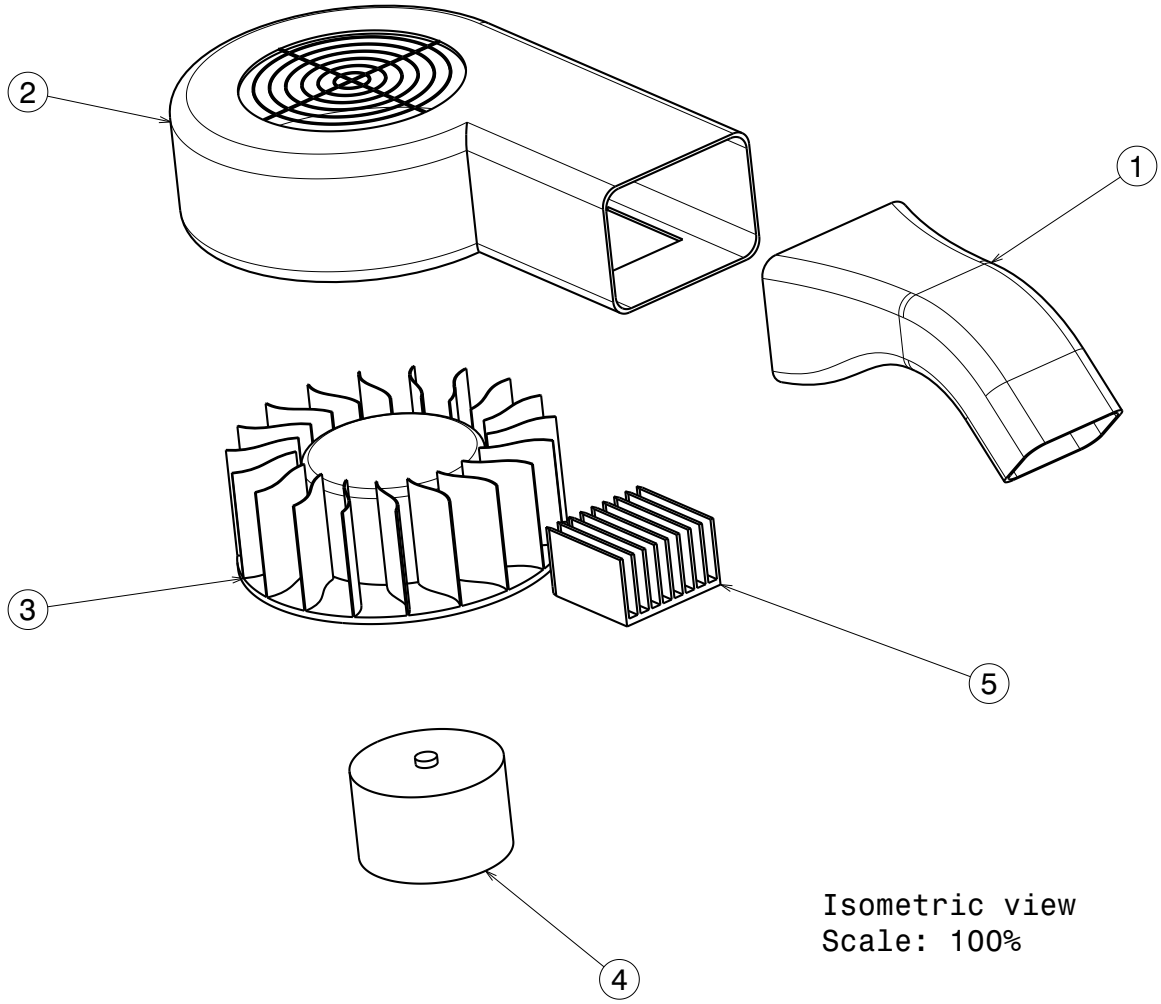


Figure 13.4: Exploded view of the blower assembly. Description of the balloon numbers is presented in Table 13.1

Table 13.1: Blower assembly (BLW01) bill of materials. Description of the balloon numbers from Figure 13.4. The listed masses and costs are per part. The totals are for the entire assembly

| Balloon no. | Part no. | Part name | Quantity | Material | Mass [g] | Cost [€] |
|---|---|---|---|---|---|---|
| 1 | BLW01TN | Tube nozzle | 1 | ABS | 1.6 ± 0.1 | 1.1 ± 0.1 |
| 2 | BLW01BC | Blower case | 1 | ABS | 3.3 ± 0.1 | 2.2 ± 0.1 |
| 3 | BLW01CP | Centrifugal propeller | 1 | ABS | 3.2 ± 0.1 | 2.1 ± 0.1 |
| 4 | BLW01BM | Brushless motor | 1 | - | 4.5 ± 0.5 | 2.5 ± 1.5[a] |
| 5 | BLW01HS | Heat sink | 1 | ALU | 2.4 ± 0.2 | 1.6 ± 0.1 |
| | | | | **Total:** | **15 ± 1.0** | **9.5 ± 2.0** |

[a] https://www.alibaba.com/product-detail/Reasonable-Price-12V-brushless-Dc-BLDC_60625423847.html [Cited 26 June 2017]

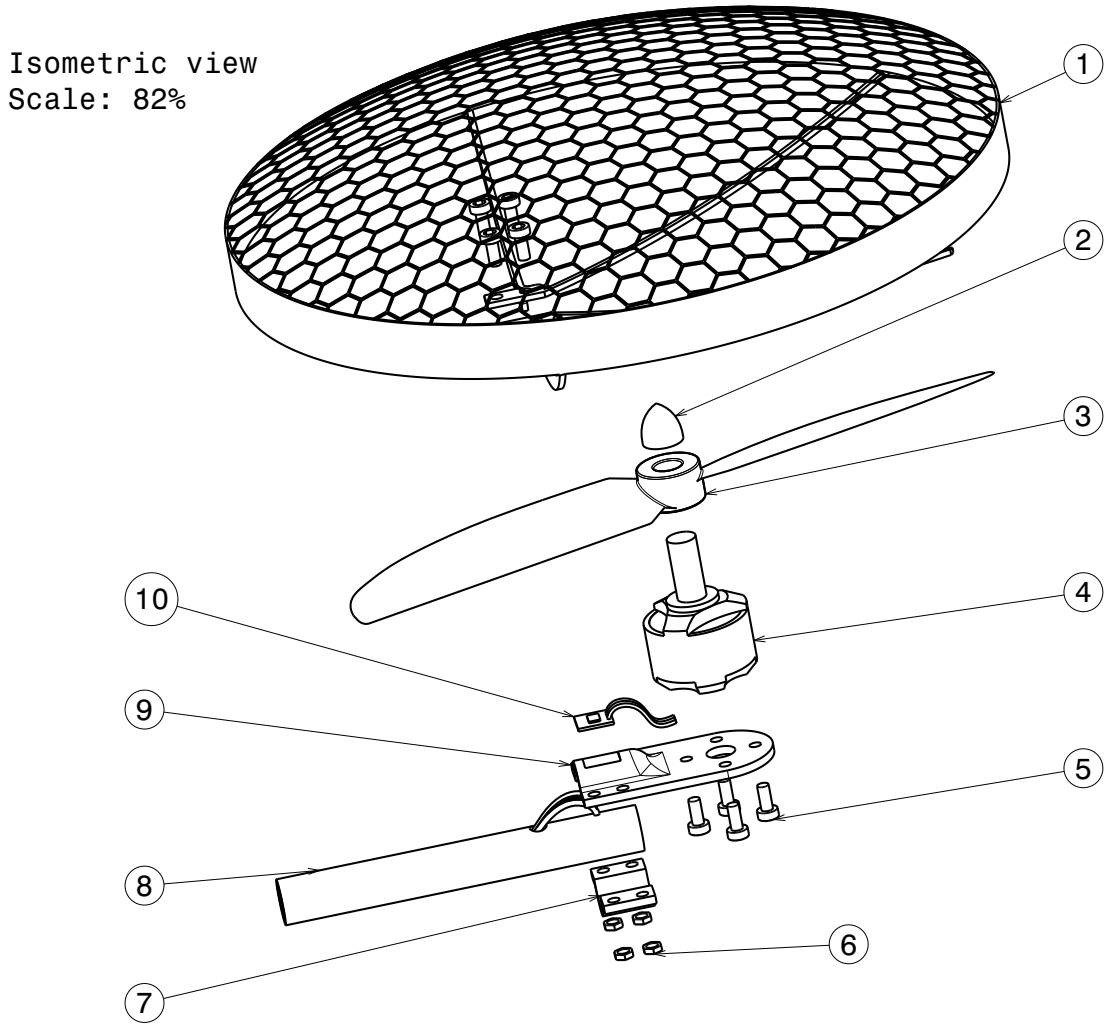


Figure 13.5: Exploded view of the propulsion assembly. Description of the balloon numbers is presented in Table 13.2

Table 13.2: Propulsion assembly (PROP01) bill of materials. Description of the balloon numbers from Figure 13.5. The listed masses and costs are per part. The totals are for the entire assembly

| Balloon no. | Part no. | Part name | Quantity | Material | Mass [g] | Cost [€] |
|---|---|---|---|---|---|---|
| 1 | PROP01PC | Propeller casing | 4 | ABS | 2.90 ± 0.10 | 1.9 ± 0.1 |
| 2 | PROP01PN | Propeller nut | 4 | ALU | 0.10 ± 0.05 | 0.1 ± 0.0 |
| 3 | PROP015P | 5" Propeller | 4 | ABS | 2.90 ± 0.10 | 1.9 ± 0.1 |
| 4 | PROP010M | Motor | 4 | - | 12.0 ± 0.20[a] | 22 ± 1.1[b] |
| 5 | PROP01B3 | M3x4.5 bolt | 24 | ALU | 0.07 ± 0.01 | 0.01 ± 0.0 |
| 6 | PROP01N3 | M3 nut | 16 | ALU | 0.01 ± 0.001 | 0.01 ± 0.0 |
| 7 | PROP01BL | Mount bracket low | 4 | ABS | 0.22 ± 0.10 | 0.2 ± 0.1 |
| 8 | PROP01HL | Hollow 8mm tube | 4 | Carbon | 2.24 ± 0.20 | 0.7 ± 0.2[c] |
| 9 | PROP01BU | Mount bracket up | 4 | ABS | 0.90 ± 0.10 | 0.6 ± 0.1 |
| 10 | PROP01SC | ESC | 4 | - | 0.10 ± 0.05 | 6.3 ± 0.5[d] |
| | | | | **Total:** | **87.3 ± 4.1** | **135.2 ± 8.8** |

[a] http://www.dys.hk/ProductShow.asp?ID=115 [Cited 26 June 2017]

[b] https://hobbyking.com/en_us/dys-1306-2300kv-bx-series-set-of-two-cw-ccw-motors.html? [Cited 26 June 2017]

[c] https://hobbyking.com/en_us/carbon-fiber-tube-hollow-8x750mm.html [Cited 26 June 2017]

[d] https://hobbyking.com/en_us/supermicro-systems-brushless-esc-3a-mi-3a.html [Cited 26 June 2017]

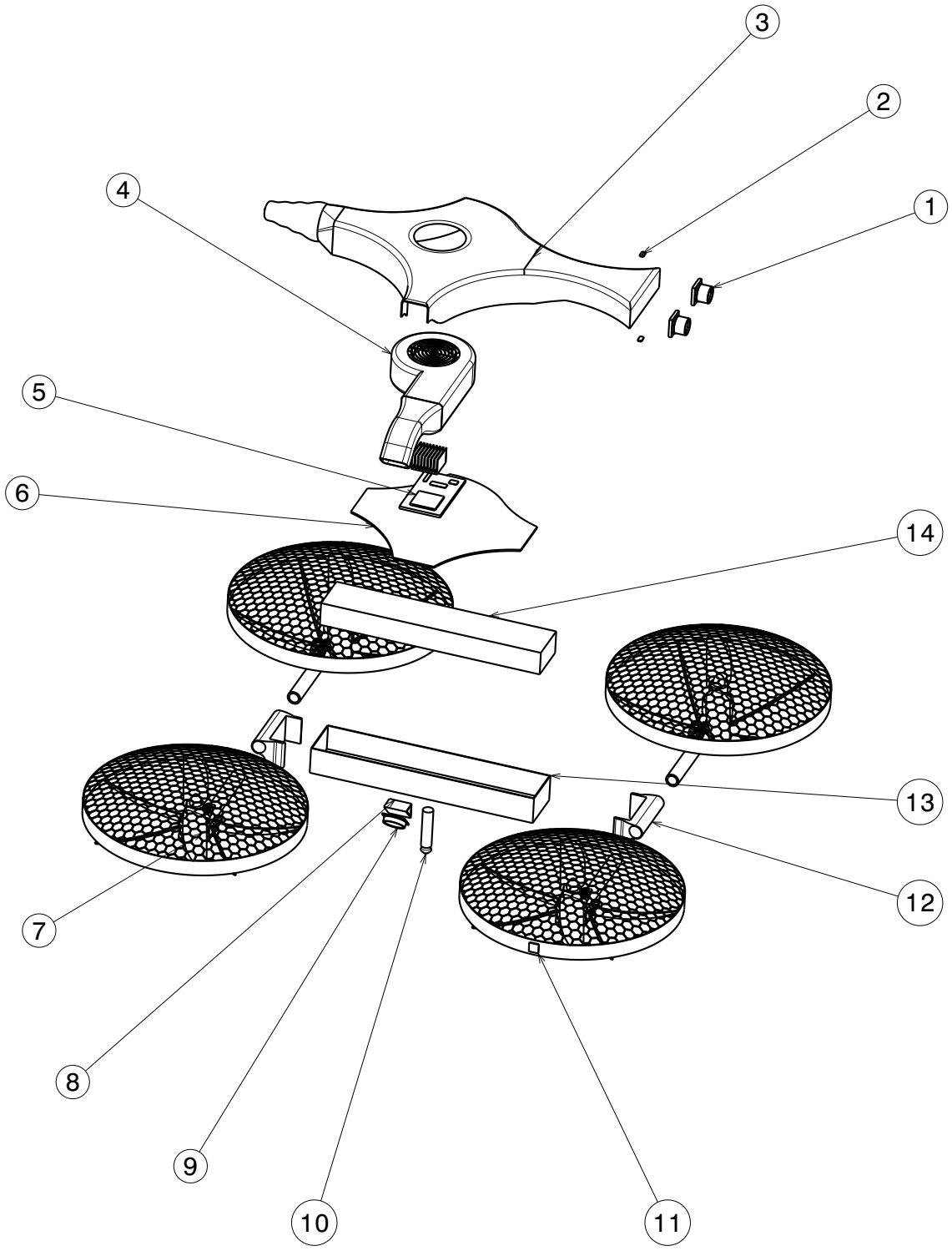


Figure 13.6: Exploded view of the APIS assembly. Description of the balloon numbers is presented in Table 13.3

Table 13.3: Main assembly (APIS) bill of materials. Description of the balloon numbers from Figure 13.6. The listed masses and costs are per part. The totals are for the entire assembly

| Balloon no. | Part no. | Part name | Quantity | Material | Mass [g] | Cost [€] |
|---|---|---|---|---|---|---|
| 1 | STR01 | Stereo camera | 2 | - | 4.0 ± 0.5 | 30.8 ± 7.6[a] |
| 2 | LSR01 | Laser | 2 | - | 0.1 ± 0.0 | 2.3 ± 0.5[b] |
| 3 | CSG01DRN | Casing | 1 | ABS | 4.6 ± 0.6 | 3.0 ± 4.1 |
| 4 | BLW01 | Blower assembly | 1 | - | 15 ± 1.0 | 9.5 ± 2.0 |
| 5 | PCB01SNP | PCB Snapdragon | 1 | - | 9.4 ± 0.5 | 80 ± 20[c] |
| 6 | PCB01SPP | PCB support | 1 | ABS | 3.2 ± 0.1 | 2.1 ± 4.1 |
| 7 | PROP01 | Propulsion assembly | 4 | - | 21.8 ± 4.1 | 33.8 ± 8.8 |
| 8 | CAM01MNT | Camera mount | 1 | ABS | 0.3 ± 0.0 | 0.2 ± 0.0 |
| 9 | CAM01MNO | Monocular camera | 1 | - | 6.0 ± 0.2 | 50.8 ± 7.1[d] |
| 10 | CHG01 | Charging pin | 1 | ALU | 0.4 ± 0.1 | 0.7 ± 0.1 |
| 11 | UWB01 | UWB | 2 | - | 0.1 ± 0.0 | 13.5 ± 1.2[e] |
| 12 | BRK01 | Bracket | 2 | ABS | 1.8 ± 0.1 | 1.2 ± 0.1 |
| 13 | CSG01BTT | Battery case | 1 | Carbon | 10.8 ± 4.1 | 3.7 ± 1.2 |
| 14 | BTT01 | Battery | 1 | - | 100.5 ± 3.0 | 14.6 ± 6.0[f] |
| | | | | **Total:** | **249.5 ± 23.3** | **394.2 ± 54.2** |

[a] http://www.optics-online.com/dsl_fifth.asp [Cited 26 June 2017]
[b] http://www.st.com/en/imaging-and-photonics-solutions/vl53l0x.html [Cited 26 June 2017]
[c] https://pcbshopper.com/ [Cited 26 June 2017]
[d] http://www.optics-online.com/dsl_fifth.asp [Cited 26 June 2017]
[e] https://www.digikey.com/product-detail/en/decawave-limited/DW1000-I-TR13/1479-1001-1-ND/4499860 [Cited 26 June 2017]
[f] https://hobbyking.com/en_us/graphene-1500mah-4s-65c-w-xt60.html?___store=en_us [Cited 26 June 2017]

Table 13.3 lists all the components needed for the drone to be assembled, including the propulsion and the blower sub-assemblies. As summarized at the end of the table, the total mass of the drone is approximately 250 g (273 g in the upper limit) and the total costs are about 400 € (450 € maximum). One can observe that even in the worst case, the design of the quad still satisfies the requirements of being maximum 300 g and costing no more than 500 €.

## 13.4. Resource allocation / budget breakdown

In order to arrive to the final values mentioned above, the team followed a systematic contingency approach that centralized the design process and tracked the main changes. This is presented in Figure 13.7 and it shows how at the beginning of the detailed design phase the uncertainties were ±50% and at the end of the design, the final weight was computed to be 250 g with an uncertainty of ±9%.

The plot was constructed by braking down the drone into main sub-systems such as propulsion (motors, ESCs and propellers), structure (all the connection bits and structural parts such as casings), blower (including the nozzle and the radiator), cameras (two stereo and one monocular), battery and electronics (PCB). A substantial table kept track of all the changes of the design in thrust, weight of components or other variables. In order to observe the actual effect and perform the necessary iterations, one change at the time was allowed and the list of modifications per each sub-system is detailed below.

**Propulsion** The starting point for the motors was taken form the preliminary design where DYS 1306 motors were used to provide a maximum of 130 g of thrust each. 16 g per motor, propeller and ESC were assumed at that stage with an uncertainty of ±2 g. On the 23rd of June it was confirmed that the same DYS 1306 would be perfectly suited for the new design and with a better estimate of the propeller by CATIA, the motor, propeller and the ESC are assumed to be weighing since that date 15 g ± 1 g due to the wiring (short cables are included in the 12 g of a motor, but the heavy connectors compensate for a needed longer length of the cables).

**Structure** Because the components were not known in the beginning, for a long time, the structural mass of the drone was assumed to be 30% of the total weight (value taken from the referenced drones on the market as explained in Chapter 9). After the other main components such as the battery or the motors were known, the structure was built around them in CATIA. With time, and after some iterative processes, the structural weight stabilized to 46 g with a margin of ± 14 g due to the simplifications in the design which omitted some bolts, clamps or adhesives.

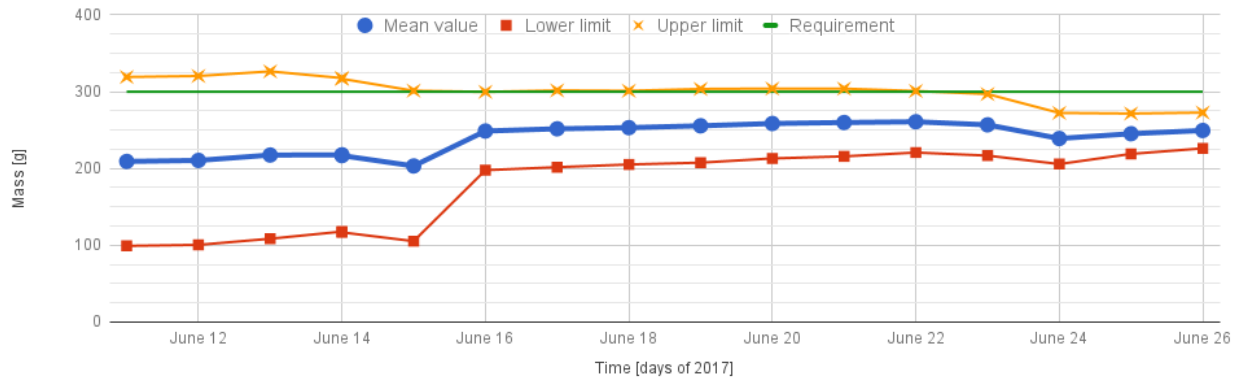


Figure 13.7: Evolution of the total mass over time, during the detail design phase. The mean value and the margins are plotted together with the weight requirement of 300 g

**Blower** Initially, a fifth DYS 1306 motor was assumed to do the job of pollination meaning that 16 g were reserved for the payload with a margin of ± 15 g. After a more detailed research of the amount of velocity needed for pollination (explained in Chapter 5), the blower was sized down to 2.5 g (thus the sudden drop on the 15th of June). This however, was a mistake as the selected micro motor was in fact not providing the 10 m/s required by the CFD analysis. Over time, a bigger motor was chosen with a high margin. On the 19th of June a radiator was added in this sub-system in order to warm up the air targetted to the flower. In the end, an industrial centrifugal blower was chosen and remodelled in CATIA for weight optimization, reaching a final mass og 15 g ± 1 g.

**Cameras** The preliminary design required only two stereo cameras for navigation and flower detection and thus, 4 g was originally allocated for this sub-system (weight taken from Delfly stereo cameras). Unfortunately, this stereo pair was not considered enough for accurate navigation and precise flower detection, therefore higher quality cameras were considered together with a third one on the side of the drone dedicated for localizing the flowers. These three cameras ended up in total at 15 g with a margin of ± 0.5 g due to the accurate manufacturer specifications.

**Battery** Initially a 1.2Ah Li-Po battery was considered at the beginning of the detailed design phase with a low weight of 56 g. This was proven in Chapter 6 that was not the case. A higher capacity was needed and a different battery technology was required for a higher amount of charging cycles. As a consequence, 100.5 g ± 3 g were set for the final weight of the battery. This can be clearly observed as a major change on 16th of June in Figure 13.7.

**Electronics** The weight of the PCB did not vary that much over the detail design phase. It was assumed at the beginning to be 8.2 g and in the end, after many iterations and modifications of the original Snapdragon Flight board explained in Chapter 7, the weight reached 12.6 g.

## 13.5. Total costs

At this point, the total number of drones needed to pollinate a typical green house (4 hectares) is fixed to 64. 58 APIS vehicles are required to perform the mission in 3 days and 6 extra are added for redundancy. 8 ground stations are required for the same green house to offer support for 8 drones each. Additionally, a server and a hub are needed to centralize the entire system, take decisions and sore relevant information. All these costs are summed up and concluded in Table 13.4. Note that the total value of 30,000 € represents the initial cost. A monthly fee of 934 € ± 384 € is required to cover the 64 short-life batteries. All these costs are the material costs and they not include shipment, manufacturing logistics, R&D or other miscellaneous costs.

Table 13.4: Initial cost of the entire pollination system (for a 4 hectares greenhouse)

| Product | Price [€] | Quantity | Subtotal [€] |
|---|---|---|---|
| APIS | 394 ±54 | 64 | 25,216 ±3,456 |
| Ground station | 389 ±73 | 8 | 3,112 ±584 |
| Hub | 60 ±30 | 1 | 60 ±30 |
| Server | 1,600 ±500 | 1 | 1,600 ±500 |
| | | **Total:** | **29,988 ±4,570** |

## 13.6. Compliance matrix

In this section, the requirements compliance matrix is presented. This table includes the requirements and an indication of whether they have been met. It serves as an indication for the value the design delivers.

Table 13.5: Overview of top level design requirements

| Label | | | Requirement | Compliance | Note |
|---|---|---|---|---|---|
| *MAV* | | | | | |
| DP | MAV | 1 | The MAV shall take-off, fly and land autonomously. | ✓ | Section 8.1 |
| DP | MAV | 2 | The MAV shall locate, approach and shake a minimum of 500 flowers a day. | ✓ | Section 2.5 |
| DP | MAV | 3 | The MAV shall return to its charging station, land and recharge. | ✓ | Section 8.1 |
| DP | MAV | 4 | Multiple MAVs shall be able to fly simultaneously in the same greenhouse. | ✓ | Section 11.4 |
| DP | MAV | 5 | The MAV shall keep track of which parts of the greenhouse were processed and when. | ✗ | - |
| DP | MAV | 6 | The MAV shall store visual images of all visited flowers in a central database. | ✓ | Section 11.5 |
| DP | MAV | 7 | The MAVs shall be in constant communication with the support system. | ✓ | Section 8.2 |
| DP | MAV | 8 | Average power consumption of a MAV shall be no more than 70W. | ✓ | Section 8.2 |
| DP | MAV | 9 | The MAV shall be able to fly uninterruptedly for 12 minutes without charging. | ✓ | Section 8.2 |
| DP | MAV | 10 | The MAVs shall be able to send telemetry data to the support system. | ✓ | Chapter 11 |
| DP | MAV | 11 | The MAVs shall have a maximum speed of 5 m/s. | ✓ | Section 3.2 |
| DP | MAV | 12 | The MAV shall keep track of the flowers it has pollinated. | ✓ | Section 11.3 |
| DP | MAV | 13 | The MAV shall not weigh more than 300 grams. | ✓ | Chapter 13 |
| DP | MAV | 14 | The MAV shall not hover at more than 50 % thrust | ✓ | Section 6.1 |
| *Support system* | | | | | |
| DP | SPP | 1 | The support system shall be able to send status data to the manufacturer. | ✓ | Section 11.3 |
| DP | SPP | 2 | The support system shall provide power to the MAVs. | ✓ | Section 11.3 |
| DP | SPP | 3 | The support system shall be able to send control signals to the MAVs. | ✓ | Section 11.3 |
| DP | SPP | 4 | The support system shall be able to gather telemetry data about the MAVs. | ✓ | Section 11.3 |
| DP | SPP | 5 | The support system shall be able to receive/gather and save pictures from the MAV. | ✓ | Chapter 11 |
| DP | SPP | 6 | The support system shall provide a defined area to the MAV to perform its function. | ✓ | Section 11.4 |
| *User interfaces* | | | | | |
| DP | UI | 1 | The system does not require special training for operation. | ✓ | Chapter 4 |
| DP | UI | 2 | The user shall be able to load the pictures from the system. | ✓ | From the server Section 11.3 |
| DP | UI | 3 | The UI shall not be compromised by the greenhouse environment. | ✓ | Web-based interface Section 11.5 |
| DP | UI | 4 | The system shall have an emergency stop button. | ✓ | Section 11.3 |
| *Crops* | | | | | |
| DP | CROP | 1 | The targeted crops shall be grown in a greenhouse. | ✓ | Tomato crops selected as crop |

| | | | | | |
|---|---|---|---|---|---|
| DP | CROP | 2 | The MAV shall target multiple crops. | ✓ | Modularity of the payload Section 13.1 |
| *Environment* | | | | | |
| DP | ENV | 1 | The MAV shall be water-proof. | ✓ | Section 13.1 |
| DP | ENV | 2 | The MAV shall be able to withstand temperatures ranging from 5 deg C to 50 deg C. | ✓ | Chapter 7 |
| DP | ENV | 3 | The MAV shall be able to withstand the chemicals used in the greenhouse. | ✓ | Chapter 7 |
| DP | ENV | 4 | The MAV shall be able to withstand the lighting conditions used in the greenhouse. | 🔧 | - |
| DP | ENV | 5 | The MAV shall be able to withstand the atmospheric conditions in the greenhouse. | 🔧 | - |
| *Market* | | | | | |
| DP | MRK | 1 | The MAV shall not be currently available in the market. | ✓ | Section 19.4 |
| DP | MRK | 2 | The system cost shall be competitive with the current service of bees. | ✗ | Proof-of-concept, not yet competitive |
| DP | MRK | 3 | Publicity strategy shall be established before the proof of concept demonstration. | ✓ | Conferences, marketing strategy Section 19.4 |
| *Resources* | | | | | |
| DP | RES | 1 | The system of MAVs shall be designed by a team of 9 students. | ✓ | |
| DP | RES | 2 | The structural design of the MAV shall be performed in CATIA V5. | ✓ | Section 13.1 |
| DP | RES | 3 | No external advisors or consultants shall be hired. | ✓ | Made contact with experts but none were hired |
| DP | RES | 4 | No equipment, materials or components shall be bought. | ✓ | Nothing was bought |
| *Legal* | | | | | |
| DP | LEG | 1 | The system shall not infringe any patent laws. | ✓ | To the best of our knowledge |
| DP | LEG | 2 | The subsystems that have contact with the plants shall comply with the Food Contact Materials of the targeted market countries. | ✓ | No contact with flower |
| DP | LEG | 3 | The MAVs shall comply with the aviation authority regulations of the targeted market countries. | ✓ | Flying inside and height does not exceed 10 m |
| *Sustainability* | | | | | |
| DP | SUST | 1 | The MAV shall have a minimum life-time of 8 months. | 🔧 | - |
| DP | SUST | 2 | The MAV shall have no emissions. | ✓ | Chapter 17 |
| DP | SUST | 3 | The materials and joining methods used shall allow for full recyclability. | ✓ | Section 17.1 |
| DP | SUST | 4 | No hazardous materials shall be used in the system. | ✓ | Section 17.1 |
| DP | SUST | 5 | No hazardous substances shall be created in case of a reaction of the system materials with any chemicals used in the greenhouse | ✓ | Section 17.1 |
| DP | SUST | 6 | The location of a MAV that got stuck shall be tracked. | ✓ | Section 8.3 |
| DP | SUST | 7 | The sound level of the MAV system shall not be more than 100 dB. | ✓ | Section 17.3.2 |
| *Safety* | | | | | |
| DP | SAFE | 1 | The MAV shall not do any damage to the plants. | 🔧 | - |
| DP | SAFE | 2 | The MAV shall be able to avoid obstacles. | ✓ | Section 8.5.2 |
| DP | SAFE | 3 | The MAV shall be able to land at the base in case of losing the communication | ✓ | Chapter 16 |

| | | | | | |
|---|---|---|---|---|---|
| DP | SAFE | 4 | The MAV shall be able to land at the base in case of overheating. | ✓ | Chapter 16 |
| DP | SAFE | 5 | The system shall be able to be operated manually. | ✓ | Section 11.5 |
| DP | SAFE | 6 | In case of critical subsystem damage, the MAV shall be able to turn off the propulsion system. | ✓ | Chapter 16 |
| DP | SAFE | 7 | The MAV shall not endanger humans upon accidental impact. | 🔧 | - |
| DP | SAFE | 8 | The MAV shall not break the structural elements of the greenhouse in case of impact. | 🔧 | - |
| *Schedule* | | | | | |
| DP | SCH | 1 | Proof of concept shall be demonstrated by December 20, 2017. | 🔧 | - |
| DP | SCH | 2 | First delivery shall be completed before July 1, 2018. | 🔧 | - |
| DP | SCH | 3 | Lead time shall be no more than 2 months. | 🔧 | - |
| DP | SCH | 4 | System installation time shall be no more than 3 days. | ✓ | Section 4.3 |
| DP | SCH | 5 | Baseline review shall be completed, documented and presented by May 9, 2017. | ✓ | See baseline report |
| DP | SCH | 6 | Mid-term review shall be completed, documented and presented by May 30, 2017. | ✓ | See midterm report |
| DP | SCH | 7 | Final review shall be completed, documented and presented by June 30, 2017. | ✓ | This report |
| DP | SCH | 8 | The design process and results shall be presented at the DSE Symposium Day on July 6, 2017. | ✓ | |
| *Cost* | | | | | |
| DP | CST | 1 | The material cost of a single MAV shall be no more than 500 euros. | ✓ | Section 13.3 |
| DP | CST | 2 | The total system costs for 10 MAVs and their supporting systems in a single greenhouse shall not exceed 50,000 | ✓ | Section 11.6 |
| DP | CST | 3 | The yearly maintenance costs for 10 MAVs and their supporting system shall not exceed 10,000 euros. | 🔧 | - |
| DP | CST | 4 | The project development costs shall be amortized by July 1, 2022. | 🔧 | - |
| *Manufacturing* | | | | | |
| DP | MAN | 1 | Working conditions shall comply with the legal regulations. | 🔧 | - |
| DP | MAN | 2 | No materials and substances which are hazardous to the environment shall be used. | ✓ | Section 17.1 |
| DP | MAN | 3 | Lean manufacturing procedures shall be implemented. | ✓ | Chapter 15 |
| DP | MAN | 4 | Sustainable approach to manufacturing strategy shall be established. | ✓ | Section 17.2 |
| *Maintenance* | | | | | |
| DP | MAIN | 1 | A system fault shall be serviced in no more than 3 days. | ✓ | Section 4.4 |
| DP | MAIN | 2 | A mobile repair kit shall be designed. | ✓ | Section 4.4 |
| DP | MAIN | 3 | A self-diagnose analysis shall be implemented in the system. | ✓ | Section 14.3 |
| DP | MAIN | 4 | A software update shall be delivered by the manufacturer only remotely. | ✓ | Section 14.3 |
| *End of life* | | | | | |
| DP | EOL | 1 | End of life support and service shall be established in less than 3 months after the first delivery. | ✓ | Section 4.4 |
| DP | EOL | 2 | The system shall be removable in less than one day by five people. | ✓ | Section 4.4 |
| DP | EOL | 3 | Removing the system shall not compromise the system's functions permanently. | ✓ | Section 4.4 |

Table 13.6: Overview of requirements to perform the mission technically

| Label | | | | | Requirement | Compliance | Note |
|---|---|---|---|---|---|---|---|
| *Structure* | | | | | | | |
| DP | MAV | 11 | STR | 1 | The structure shall be able to withstand at least 2g acceleration. | ✓ | Chapter 9 |
| DP | SUST | 1 | STR | 2 | The structure shall be able to withstand a fatigue load of $3 \cdot 10^{9}$ cycles. | 🔧 | - |
| DP | SUST | 1 | STR | 3 | The structure shall have a safety factor of 1.5. | ✓ | Section 9.3.4 |
| DP | MAV | 11 | STR | 4 | The structure shall withstand an impact with a hard surface at max. speed. | ✓ | Chapter 9 |
| DP | MAV | 2 | STR | 5 | The structure shall be able to withstand the vibrations of the payload system. | ✓ | Section 9.4.3 |
| DP | MAV | 9 | STR | 6 | The structure shall protect the propulsion system in case of impact. | ✓ | Chapter 9 |
| *Control* | | | | | | | |
| DP | MAV | 2 | CON | 1 | The MAV shall have a pointing accuracy of 7°. | 🔧 | - |
| DP | MAV | 2 | CON | 2 | The control system shall provide the stability required by the payload subsystem. | 🔧 | - |
| DP | MAV | 1 | CON | 3 | The control system shall have stabilization loops and guidance loops. | ✓ | Chapter 10 |
| DP | MAV | 1 | CON | 4 | There shall be a separation between vertical and horizontal control. | ✓ | Chapter 10 |
| DP | MAV | 1 | CON | 5 | Four modes of autonomous control shall be discerned | ✓ | Chapter 10 |
| *Communication* | | | | | | | |
| DP | LEG | 3 | COM | 1 | The communication system shall use only frequencies allocated for general use. | ✓ | Section 8.2 |
| DP | SAFE | 5 | COM | 2 | The communication system shall deliver control commands within 100 ms. | ✗ | Section 8.2 |
| DP | MAV | 7 | COM | 3 | The communication system shall compensate for Doppler effects. | ✓ | Section 8.2 |
| DP | MAV | 7 | COM | 4 | The communication system shall regain a communication channel when one is lost. | ✓ | Section 8.2 |
| DP | MAV | 10 | COM | 5 | The communication system shall provide downlink capacity to send telemetry data every 1000 ms. | ✓ | Section 8.2 |
| DP | MAV | 6 | COM | 6 | The communication system shall provide a high-throughput channel for image delivery. | ✓ | Section 8.2 |
| *Onboard computer* | | | | | | | |
| DP | MAV | 1 | CMP | 1 | The onboard computer shall have a clockspeed of no less than 1.5 GHz. | ✓ | Chapter 7 |
| DP | MAV | 8 | CMP | 2 | The onboard computer shall have a power consumption of less than 5 Watt. | ✓ | Chapter 7 |
| DP | MAV | 13 | CMP | 3 | The onboard computer mass shall be less than 20 grams. | ✓ | Section 13.3 |
| DP | MAV | 2 | CMP | 4 | The onboard computer shall have interfaces for at least 10 sensors. | ✓ | Section 7.4 |
| DP | MAV | 4 | CMP | 5 | The onboard computer shall have interfaces for at least 5 actuators. | ✓ | Section 7.4 |
| DP | MAV | 7 | CMP | 6 | The onboard computer shall have interfaces for the communication system. | ✓ | Chapter 7 |
| *Power* | | | | | | | |

| | | | | | | | |
|---|---|---|---|---|---|---|---|
| DP | MAV | 9 | POW | 1 | The degradation of the battery shall be no more than 5 percent. | ✓ | Section 6.4 |
| DP | MAV | 9 | POW | 2 | The chosen battery shall withstand no less than 250 discharge cycles. | ✓ | Section 6.4 |
| DP | MAV | 3 | POW | 3 | The depth of discharge of the battery shall be less than 90% percent. | ✓ | Section 6.4 |
| *Propulsion* | | | | | | | |
| DP | MAV | 2 | PRO | 1 | The propulsion subsystem shall allow three degrees of freedom. | ✓ | Section 6.1 |
| DP | MAV | 11 | PRO | 2 | The propulsion subsystem shall provide no more than 1 g of acceleration. | ✓ | Section 6.1 |
| DP | MAV | 11 | PRO | 3 | The propulsion subsystem shall provide no less than -0.5 g of acceleration. | ✓ | Section 6.1 |
| DP | MAV | 11 | PRO | 4 | The propulsion subsystem shall provide a rate of climb of 0.1 m/s. | ✓ | Section 6.1 |
| *Sensors* | | | | | | | |
| DP | MAV | 4 | SNS | 1 | The sensors shall have the capability to provide the required data to the control system. | ✓ | Section 7.3 |
| DP | MAV | 6 | SNS | 2 | The sensors shall assign a location to the pictures. | ✓ | Section 7.3 |
| DP | MAV | 1 | SNS | 3 | The sensors shall be calibrated automatically. | ✓ | Manual only during installation |
| *Swarming* | | | | | | | |
| DP | MAV | 4 | SWA | 1 | The MAVs shall not collide with each other. | ✓ | Section 8.1 |
| DP | MAV | 5 | SWA | 2 | The MAVs shall not pollinate the same flower. | ✓ | Section 5.3 |
| DP | MAV | 1 | SWA | 3 | The MAVs shall keep a safe distance from each other. | ✓ | Section 8.1 |

## 13.7. Feasibility analysis

Some of the requirements established could not be met, as can be seen in Table 13.5 and Table 13.6. This section elaborates on the reason why the design fails to comply with these requirements. Furthermore, while some are not met (✗), others need further work for validation (🔧). First, the requirements relating to the overall system will be addressed, after which the ones pertaining to the subsystems are discussed.

Going through the list, the first requirement that is not satisfied is *DP-MAV-5*. The MAV shall not keep track of the parts of the greenhouse it has processed, but the ground station will do this. Another requirement that is not met is *DP-MRK-2*. The system cost does not have to be competitive with the current pollination service of bees, as this system is a proof-of-concept design. Further research or testing should decrease the price of the system be able to become competitive. Some requirements still need validating. This is the case with *DP-SUST-1*, *DP-ENV-4*, *DP-ENV-5* *DP-SAFE-1*, *DP-SAFE-7*, and *DP-SAFE-8*. The three scheduling requirements that are not met (*DP-SCH-1*, *DP-SCH-2*, and *CP-SCH-3*), can only be met over time. The same for the cost (*DP-CST-3* and *DP-CST-4*) and manufacturing requirements (*DP-MAN-1*). Upon reviewing requirement *DP-SAFE-5*, it was decided that manual control would be impractical; it was envisioned that manual control would be needed for emergency situations, for example. However, the intervention of a human being would be too slow and ineffective. Instead, other measures had been devised as discussed in earlier segments, an example of which is the incorporation of the emergency button. Hence, it was deemed that manual control would no longer be needed, and thus this requirement was no longer considered

As for the subsystem requirements, the rationale for having not complied with them is delved into in the following. Requirement *DP-SUST-1-STR-2* is a child requirement of *DP-SUST-1*, which as explained earlier will need to be checked for in the future. More specifically, it is a requirement that remains to be validated via fatigue tests. As for *DP-MAV-2-CON-1*, there are several limitations to checking this requirement. One problem is that the coefficients that are needed for the mathematical model which is used for control are not readily available and need to obtained using motor tests. Another problem is that inaccuracies in modeling, especially the external disturbances will lead to discrepancies with reality. Requirement *DP-MAV-2-CON-1* is a quantification of requirement *DP-MAV-2-CON-2*. Hence, the same discussion applies as that of *DP-MAV-2-CON-1*. Finally the same rationale for requirement *DP-SAFE-5-COM-2* applies as that of its parent requirement.

# 14

# Reliability, availability, maintainability and safety

Reliability availability maintainability and safety are crucial aspects of the design. Those elements often determine the effectiveness of the system and decide about the success of the design. All the 4 elements are closely interrelated. For instance the reliability aspects determine needs for maintainability and together decide about the availability of the system.

## 14.1. Reliability

Reliability by definition is a probability of the system performing in satisfactory manner in given period of time. The total reliability of the whole system can be found by defining first reliability of the critical components and then summing the reliabilities using probability addition rules.

By following this approach all the critical components are identified and the failure sequence is analyzed on the fault tree. The failure modes are further elaborated on in Section 14.4. For reliability considerations the focus is only on dependencies between different failures. The top level failures of the drone with the most significant components distinguished are presented on the fault tree in Figure 14.1. As shown the mission can fail in two cases: when the drone is unable to pollinate the flower, or when the drone is unable to sustain the flight. For each case there are multiple failure events that can lead to those consequences.

One remarkable feature are the "or" gates present in different system levels. Those gates which combine failures of different components mean that the failure of the upper level system can be caused by multiple alternative events happening independently. This is not the most optimal case, and indicates on lack of redundancy in the design. The rationale behind such a choice is explained in more detail in Section 14.1. Nevertheless the required reliability of the drone still can be achieved by managing reliability of particular subsystems and components.

The reliability of the whole system is estimated by estimating reliability of each component shown on the fault tree in Figure 14.1.

For the electric motor the reliability is estimated using model from a military handbook [68]. The model considers 2 failure modes - due to wear of bearings and failure of the winding. The failure rate for given operating time is calculated using Equation (14.1). The coefficients $\alpha_b$ and $\alpha_w$ depend on the operating temperature. Taking conservative approach and assuming the temperature to be 40 deg, coefficients $\alpha_b$ and $\alpha_w$ are equal to 80,000 h and 500,000 h

$$\lambda_p = \frac{t^2}{\alpha_b^3} + \frac{1}{\alpha_w} \tag{14.1}$$

For operation time of 5 years the failure rate is $5.747 \cdot 10^{-6}/h$ which was obtained as shown in Equation (14.2). The same applies for the blower, where the reliability is determined mainly by the electric engine of the fan.

$$\lambda_p = \frac{(5 \cdot 365 \cdot 24 \cdot \frac{12}{27})^2}{80,000^3} + \frac{1}{500,000} = 5.747 \cdot 10^{-6}/h \tag{14.2}$$

The most critical structural part are the arms. The arms are greatly over-designed - the maximum stress in the critical case is about 3 orders of magnitude lower than the strength of the material (200 MPa for the chosen rods). The probability of failure is negligible. Assuming standard deviation of 10 MPa in the material properties and Gaussian distribution of the material strength, the probability of failure is negligibly small and can be omitted in the reliability analysis.

The reliability of the battery is estimated from the number of lifecycles provided by producer. Chosen battery according to the test data provided by the manufacturer is able to withstand 900 cycles. This number is verified with

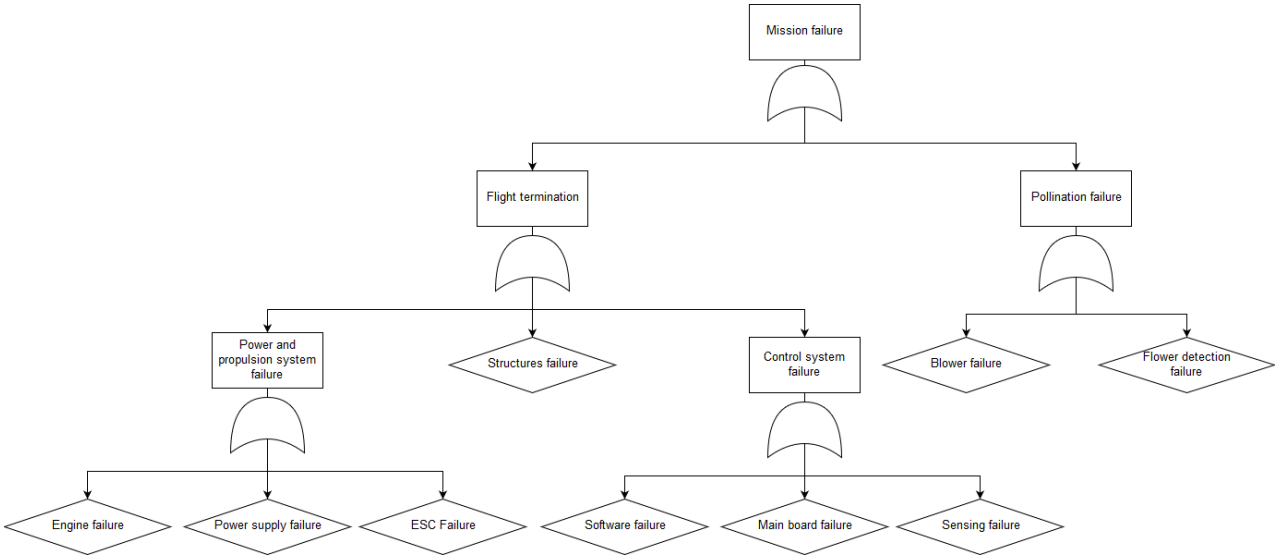


Figure 14.1: Fault tree of the top level failures

experiments for LiPo batteries done by Williard [69], which reports mean time to failure of 600 cycles. Taking more conservative approach, and assuming 600 cycles it can be calculated that the mean time between failures is 270 h (assuming that the cycle is 27 minutes in total). The failure rate is then $0.00374/h$. Failure rate of the battery will be dominating failure mode.

Failures of other components are rather difficult to estimate without appropriate data. The main board, sensors and flower detection subsystem consist of dozens of electronic components. Estimation of reliability even using simplified approach as in the *Military handbook for reliability prediction of electronic equipment* very detailed specifications are needed. The data is not commonly available and can be obtained only by testing. Instead it is much more efficient to find the failure rates by testing the subsystems. It is assumed that the mean time to failure for those components is in order of years. The reasoning behind this assumption is that the same components are often used in common electronic devices which are able to last for 3-5 years. For instance smartphones are equipped with sensors like accelerometers as well as cameras. Furthermore most of smartphones have advanced processors similar to the one on-board of the drone. Cumulatively failure rates of all those components is still significant, and can not be neglected. Nevertheless it is expected to be few orders of magnitude lower than for the battery, and due to lack of data is not further analyzed.

Reliability of the software is probably the most dynamic of all. As the software is updated the reliability instantaneously decreases. The reason is that as the new version is implemented the risk of discovering new unknown problems is much higher. The overall reliability however increases over time, as the new versions include fixes for already identified problems, and generally improve the performance of the system.

One way to increase the reliability of the systems is to incorporate redundancy concepts in the design. The consequence the achieved performance is often sub-optimal - for instance the weight is increased, or power consumption is larger than necessary. This is however the price that needs to be paid. Such approach is often taken for flight critical subsystems, for which the failure results in catastrophic consequences for the whole system.

The whole pollination system consists of multiple drones. The mission objective - which is to pollinate the flowers can be still achieved even in case of loss of 10% of the fleet. This is elaborated in more details in Section 14.2. In case of failure the drone needs to report the event to the flight planning and control system. The systems can then reassign the tasks among the functioning drones. In critical case, when there is no spare drones left the consequence is a delay in pollination. This however can be accounted for by taking safety margins for predicted mission time.

Considering the drone design, the redundancy was rather avoided. The main reason for that was optimization of the weight, power consumption and efficiency of the system.

## 14.2. Availability

Availability is the or probability that a system will be ready or available when required for use. This metric is related to maintainability and reliability. The more reliable the system, the more available it is. Similarly, a system that is easier to maintain, has a higher probability of being available for use. This system consists of 8 ground stations, each accommodating 8 drones. There are 58 drones continuously required for pollination, and the remaining 6 drones stay

available for use in case some of the drones fail. In this case the system can operate with full performance even in case 10% of the fleet fails. This approach significantly improves reliability, and therefore availability of the whole system.

Furthermore, the spare drones can be used to keep the system performance on sufficient level during the maintenance. This can be achieved if the maintenance activities are executed at up to 6 drones at the time.

## 14.3. Maintainability

Maintainability refers to the ease of how it can be maintained. The modularity of the design and the accessibility to the components that constitute it are therefore key parameters that determine how maintainable the APIS is.

Regarding the first criteria, the drone was designed such that the payload is modular. Replacing the payload by a new one is therefore a relatively easy task. Furthermore, the batteries are the component that need to be replaced the most often. Easy access to the battery compartment was ensured. Indeed, the main casing of the drone can be easily unclipped and after removing the blower that rests on top of the battery casing, the battery can be replaced. Another component that can be easily accessed are the motors. Indeed, the protective casing can be easily removed, and the motors can be accessed. The propellers are simply clipped on the motors with a nut and if they need to be replaced, they are easily accessible.

Even though the design of the drone was done such that the components can be easily accessed in case of maintenance needs, some components are not that easy to be replace. Indeed, the cameras used for the stereo vision and the monoscopic vision are a combination of a selected lens and a selected sensor. If they are damaged, the user cannot simply purchase them as off the shelf products. The same goes for the processor and the main board. The snapdragon is not currently easily purchasable. Maintenance of these parts will therefore prove to be complicated.

It must however be said that most of the other parts are on the other hand easily accessible. Indeed, the motors used can be ordered online and the same goes for the propellers. The blower is also an off the shelf product and is therefore easily maintainable.

## 14.4. Safety: operating hazard analysis

To account for safety in the design, the operating hazard analysis is performed. The analysis in principle identifies possible threats, investigates possible consequences and causes and verifies whether the implemented design solutions are sufficient to cope with the hazards. All the hazards are initiated by failure of one of the systems. There are multiple combinations of failure sequences of different components and systems which lead to various consequences.

First all the critical failures of different components are identified, and listed in the Table 14.1. For each failure a possible catastrophic effect is defined, and a mitigation strategy is developed. The failure mode and effect analysis table is a foundation for more detailed operational hazard analysis, which is described in following paragraphs.

Table 14.1: System failure mode and possible countermeasures

| System | Item | Failure mode | Effect | Countermeasure |
|---|---|---|---|---|
| **Control** | Software | Errors, overflow | Uncontrolled flight, unpredicted behaviour | Emergency system |
| | Sensing system (obstacle avoidance, UWB, cameras) | Short circuit | Loss of navigation, unpredicted behaviour | Autonomous safe landing system, emergency system |
| | PCB board | Overheating | Loss of control | Active cooling (heat sink) |
| **Propulsion** | Motor and ESC | Wear of bearings, short circuit | Loss of lift, loss of control | Fail-safe landing control algorithm |
| **Structures** | Booms and fittings | Fatigue | Loss of lift, loss of control | Fail-safe landing control algorithm |

There are 3 critical hazards identified that are analyzed: harm to the greenhouse workers, damaging the plants and damaging the greenhouse equipment.

**Rotors** Spinning rotors can injure people in the greenhouse, as well as damage the plants. There are few different scenarios that can lead to this situation. It can happen as a consequence of failure of the control system, when the drone starts flying in an uncontrolled manner. Another alternative is a failure of the obstacle avoidance system. In case of injuring people there is also additional human factor - for instance lack of caution. To minimize the consequences of this

hazard the rotors are shielded with special guards. Those guards shield the propeller on perimeter in such way that it is impossible to access the propeller tip from the side. Additionally the guards provide with a mesh above the rotor. The mesh is fine enough to prevent sucking in the leafs from above. Each guard is supported by 4 spars from the bottom. The spars also play a safety role and prevent access to the propellers for bigger objects.

**Impact** The second critical hazard is that the drone hits into a greenhouse equipment, plant, or a greenhouse worker. The list of possible causes is similar as for the propeller hazard. Due to a failure of the control system which can be caused by the failure of software, sensors, or obstacle avoidance system the drone might begin to fly in an uncontrolled way, which might lead to crash.

**Emergency system** As a countermeasure an emergency system will be incorporated into the traffic control system. In case of a catastrophic emergency (especially potential worker injury) the system will be activated and all the drones will be immediately grounded (lower the altitude in a controlled way). The system can be activated by the greenhouse staff by pushing the buttons which will be placed in different accessible locations in the greenhouse. The system will be implemented in a fail-safe way. During the operations drones will be continuously receiving signal from the ground stations communicating that the safety system is inactivated, and allowing for flight. In case the emergency system is activated the signal stops, initiating the flight termination procedure of the drones. The large disadvantage of this approach is that the flight is terminated even in case of a false alarm - e.g. when the drone temporarily looses communication with the ground station, it automatically executes the emergency landing procedure. As the emergency landing is executed immediately the drones might damage the plants underneath, or get damaged themselves by landing in inconvenient places. It is a price however that needs to be paid for maximum reliability of the system.

**Fall** Another alternative hazard is that the drone loses lift and falls, which results in an impact and possible damage or injury. Possible causes include loss of the engine or failure of the structure. The loss of the engine can be caused by failure of a different propulsion system sub-components including ESC, failure of the engine or wear out of the bearings. To minimize the risk in case of such failure the fail-safe landing control algorithm is activated. The algorithm is able to recover the control of the altitude in case of failure of one of the engines. Although with only 3 engines it is impossible to balance the moment and the vehicle starts to spin around its central axis, the altitude can be controlled by remaining propellers and the impact can be reduced.

**Fire** The last hazard considered is catching the fire. The risk is especially severe, and it has the most serious consequences. There are several alternative failures that can lead to setting up fire. One possibility is due to a short circuit of one of the electronic components. The most critical part however is the battery. Lithium polymer batteries can catch fire very abruptly when punctured.

For this case the hazard mitigation strategy focuses on eliminating the causes. All the electronic parts both in control as well as in propulsion system can fail due to short circuit. The risk is minimized by securing those parts from moisture. This is done by insulating and coating exposed connections. The only exposed part is the charging pin. In order to minimize the risk of short-circuiting the contacts on the pin, it will be switched off when the charging is finished. This means that during flight the pin will be electronically insulated from the main electronic system and there is no possibility of short circuiting it.

Furthermore all the crucial electronic components are secured from a mechanical damage. The most critical part - the main PCB board is enclosed in a casing which provides additional protection from the environment. The battery is accommodated within the main structure box, which shields the battery from the surroundings. The wires connecting the motors with the main board are led inside the booms, which minimizes risk of cutting it. The stereo camera is placed in such way that in case of frontal impact it is protected by the propeller guards, which will absorb most of the impact energy.

# 15

# Production plan

After the design phase is finished, the production phase can start. Before this, a production plan should be created in order to know in what order components have to be made, the production processes used and how the components are assembled together. When creating a detailed production plan, the costs, inventory investment and changes in work-force levels can be minimized[1]. The design consist of two main components that need to be produced, the drones and the ground stations. First, the production plan for the drones will be explained and after that the production plan of the ground station will be explained.

## 15.1. Production plan for the drones

First the manufacturing processes of the materials used in the drones will be addressed. After that, the production of the parts will be elaborated on and, finally, the attachments between the components will be explained.

The design of the drones has been split up into the following main categories for production: the main structure, the propulsion system, the electronics, the blower and the casing. The different components of each of the subsystems can be seen in Table 15.1.

Table 15.1: Categories used for the production phase

| **Categories** | **Main structure** | **Propulsion system** | **Electronics** | **Blower** | **Casing** |
|---|---|---|---|---|---|
| **Components** | Carbon fibre arms<br>Clamps<br>Carbon fibre box | Motor<br>Propeller<br>Motor mount<br>ESCs<br>Propeller casing | Battery<br>Charging pin<br>Stereo cameras<br>Fish eye camera<br>Lasers<br>Wires<br>PCB | Blower<br>Blower mount | Casing main structure |

The production of these subsystems will be elaborated on in the production flow diagram. This will include the order in which the components have to be produced. However, not all components have to be manufactured by ourselves. The carbon fibre arms, motors, propellers and the electronics, except for the PCB can be bought online. For every component that remains, the manufacturing process will be explained. Since most of the components are made out of carbon fibre and ABS plastic, first the different processes that can be used for these materials will be discussed.

### 15.1.1. Manufacturing processes

For manufacturing the carbon fibre parts there are two processes that can be considered, open molding and close molding. Open molding is mostly used for large parts and small production series, such as the production of boat hulls. Since the drone has a maximum length of about 30 cm, the product is assumed to be small. Also the production series is considered large because for one system 64 drones are needed. Therefore close molding will be used. This process, also called vacuum infusion, is based on pushing the resin into the laminate by applying a difference in pressure. When doing

[1] http://www.smetoolkit.org/smetoolkit/en/content/en/907/Preparing-Your-Production-Plan [Cited 21 June 2017]

this correctly, the resin will be spread equally over the laminate. For this process a mould is needed. Furthermore, this process minimizes the chemical emission, making it the most environmentally friendly out of the considered processes[2].

Plastic components are manufactured by using 3D printers or injection moulding. The 3D printers are used for small production series and are cheaper to use. This is because no moulds are needed while making use of less tooling and setup costs. However, when the production series increases injection moulding can be more cost beneficial. Therefore, for creating prototypes and in the first stages of the business, 3D printing will be used and when the demand for the drones comes above a certain threshold, injection moulding will be used[3].

For choosing the 3D printing process that is best for this product, the accuracy, the materials and the environment will be taken into account. All 3D printers are based on adding material layer by layer until the component has been made. There are six different types of 3D printers, stereolithography, digital light processing, fused deposition modeling, selective laser sintering, electronic beam melting and laminated object manufacturing[4]. The first two types are using photopolymers and are mostly used for prototyping, because the costs are relatively low and because they do not take a lot of time. A drawback of these is the low accuracy they can acquire. Fused deposition modeling is based on production-grade thermoplastics, which gives high mechanical, thermal and chemical quality. This process is also environmental friendly. The fourth process uses lasers to produce parts and the materials that can be used are nylon, glass, ceramics and metals. Electronic beam melting is used for making metal parts. The last 3D printing method is mostly used for parts made out of paper. Due to the fact that the material used is plastic, all the processes based on making metal parts can not be used. Furthermore, a final product has to be created, therefore, a high accuracy is needed. Also when looking at the environmental friendly aspect, only one 3D printer performs best. Therefore, the process that will be used for manufacturing the low production series plastic parts is fused deposition modeling.

Injection molding is a whole different process, which is based on injecting a liquid material. The process followed can be seen in Figure 15.1[5]. First the mold is placed into the machine and is clamped such that the mould can not open when the injection of the heated material takes place. Then the plastic granules are put into the hopper and they will go to the barrel. After that, the plastic granules are transported with a screw to the heating area and the plastic will be melted until it is liquid. Then the liquid plastic is injected in the mould and cooled.

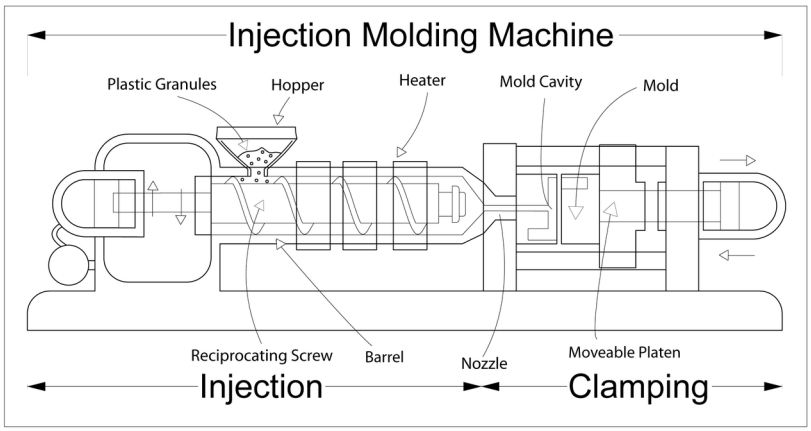


Figure 15.1: Injection molding machine

## 15.1.2. Manufacturing the parts

This section will describe the manufacturing processes used for each of the parts. It is assumed that the a high product series is required, thus injection moulding will be used for manufacturing the parts out of ABS plastic.

- **Clamps**: The clamps are made out of ABS plastic, which means that injection molding will be used. Before making the clamps, the dimensions of the carbon tube have to be checked. Since a tight fit is needed, the dimensions should have a high level of accuracy. A margin has to be taken into account for the carbon tubes since it is impossible to create identical products. This margin is given by the manufacturer of the carbon tubes. The upper

[2] http://www.compositesworld.com/knowledgecenter/closed-molding/Closed-Mold-Process/Vacuum-Infusion-Process [Cited 22 June 2017]

[3] https://www.xometry.com/blog/3d-printing-vs-injection-molding-breakeven [Cited 22 June 2017]

[4] http://3dprintingfromscratch.com/common/types-of-3d-printers-or-3d-printing-technologies-overview/ [Cited 22 June 2017]

[5] http://easchangesystems.com/wp-content/uploads/2015/08/Injection_molding_machine.png [Cited 22 June 2017]

margin will be chosen for the hole in the clamp, such that all the carbon tubes will fit. The mold needed for the injection molding process will be made out of aluminum and will be manufactured using a milling machine. An automated computer numerical control (CNC) milling machine will be used. After the mold has been created the clamps can be manufactured.

- **Carbon fibre box**: The carbon fibre box will be made by using vacuum infusion. For this, first a mold has to be created, which will be made out of wood. After that the carbon fibre box can be made. When the carbon fibre box is done, a hole is drilled in the bottom of the box for the charging pin. For this a high speed and a low feed rate drilling machine will be used to assure high quality of the hole [70].
- **Motor mount**: The motor mount is created out of ABS plastic and in order to make them the same process as the clamps will be used. However, less precision is required, because there are no tight fits needed.
- **Propeller casing**: The propeller casing will also be made out of ABS plastic. Since the cover is based on a honeycomb structure and has a very small thickness a proper release agent is needed to make sure the casing will not be damaged when released from the mold.
- **PCB**: To be able to design the PCB, the schematics need to be created in order to fit all the components. This will be the most time consuming part of production, because the schematics have to be designed from scratch. When this has been done the customized PCB can be ordered.
- **Blower and blower mount**: The blower that will be used in the design can be bought online[6]. However, a custom made nozzle has to be attached to it in order to let the exhaust be closer to the plants. This part will be manufactured from ABS plastic. High precision is needed, due to the aerodynamic requirements, which means the mold has to be created with a high level of accuracy.
- **Casing main structure**: The casing of the main structure will also be made out of ABS plastic. For this part no high precision is needed, because the casing will not be a critical part of the design. After the part has been made, the casing has to be painted in order to give the drone a nice look.

### 15.1.3. Attachments

After all the individual parts are obtained the drone will be assembled and all components must be attached. Different techniques will be used to attach the components together. Since the majority of the components are made from plastic, a lot of them can be attached by using glue:

- Stereo cameras to payload box
- Fisheye camera to payload box
- Lasers to payload box
- Blower to PCB support plate
- Nozzle to blower
- Arm clamps to payload box
- ESCs to motor mounts

The battery will be placed in the payload box supported by dampers and attached with hook-and-loop-fasteners. On top of the battery, the PCB support plate is attached through hook-and-loop-fasteners as well. The PCB itself is attached on the plate by screws. Furthermore the carbon fibre arms of the drone are assembled to the main structure by sliding them in the clamps, subsequently they are fastened by implementing a small hole and screw in the clamp. The propellers and motor are assembled using a nut which is screwed on top of the propeller. The motor-to-motor mount, the propeller casing-to-motor mount and the motor-to-main structure mount connections will be done using bolts. Finally the casing that will cover the whole drone will be attached via a click-on system, thus no attachment material is needed for this. In Figure 15.2 a visual representation of the complete production plan for the MAVs is given.

## 15.2. Production plan for the ground system

Not only the drones, but also the ground stations need a solid production plan. The ground station can be seen in Section 11.2. A ground station consists of the following components:

- Main structure
- Landing pads
- Sockets
- Socket supports
- Electronics box

Two main materials are used to manufacture the ground stations, which are aluminum and plastic. Additionally, a bit of copper is used for the charging sockets. For the parts that are made from plastic, the same manufacturing method

[6] `http://www.delta-fan.com/Download/Spec/BFB0512VHD-F00.pdf` [Cited 22 June 2017]

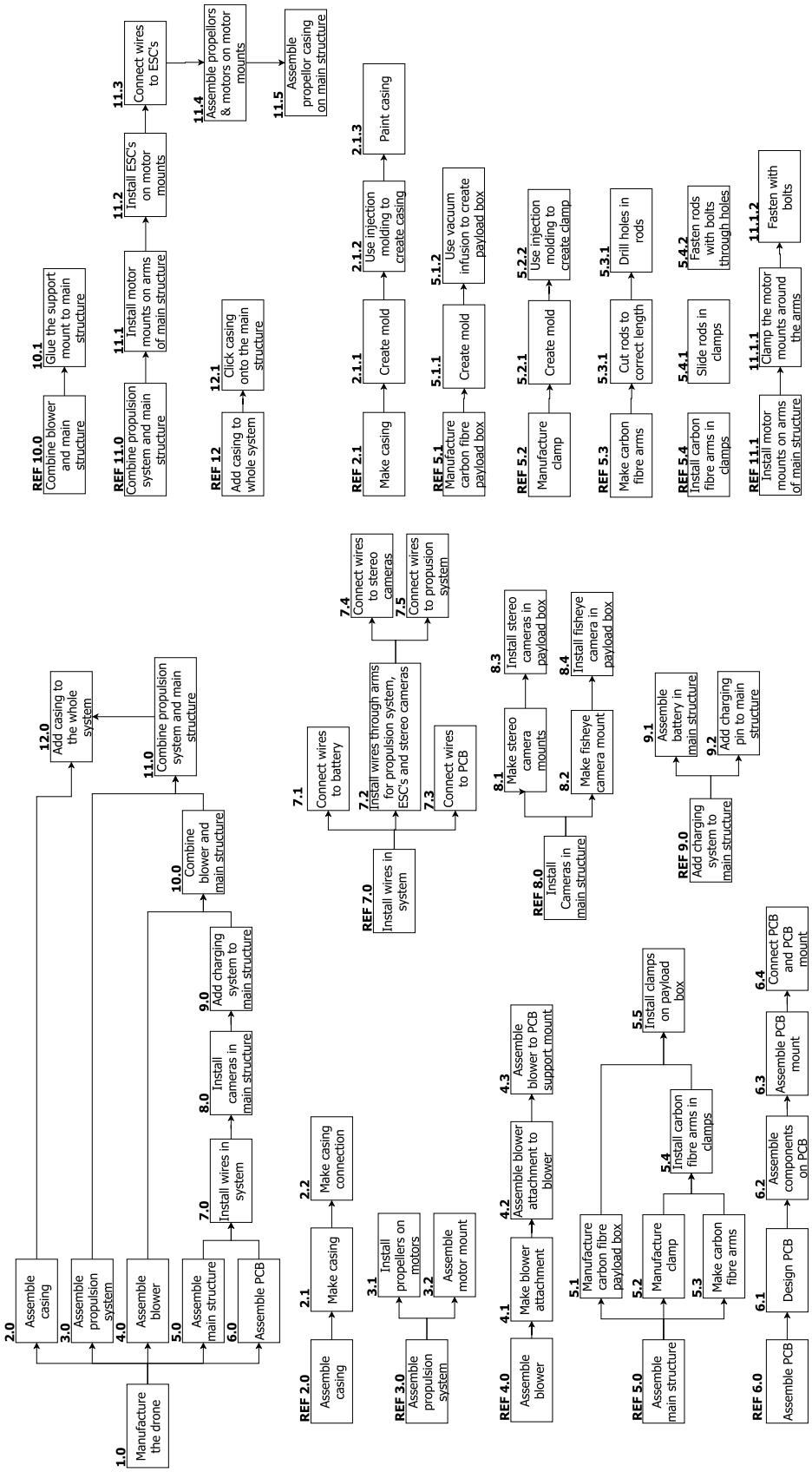


Figure 15.2: Production flow diagram for the MAV

is used as for the plastic parts of the drones, injection molding. Only the socket supports and the electronics box will be made out of plastic. The sockets will be glued in the socket supports and the socket supports will be glued on the charging pads. Furthermore, the electronics box will be bolted to the main tube.

What can be seen in Section 11.2 is that there is a main structure where the landing pads are attached to. It consists of hollow aluminum tubes where electronic wires need to go through. These tubes can be bought online and cut to the right size by using a saw. The upper "V" will be welded to the main tube. The landing pads will also be made out of aluminum and can be made by milling it to the right size. Because of the fact that a lot of landing pads need to be made with the same size, a CNC milling machine will be used. By using this, only one CNC program has to be made which can be used for all pads. The landing pads will have vertical attachments which can be bolted to the main tube. Finally the visual recognition stickers for the drones will be placed on the structure. The flow diagram of the whole progress can be seen in Figure 15.3

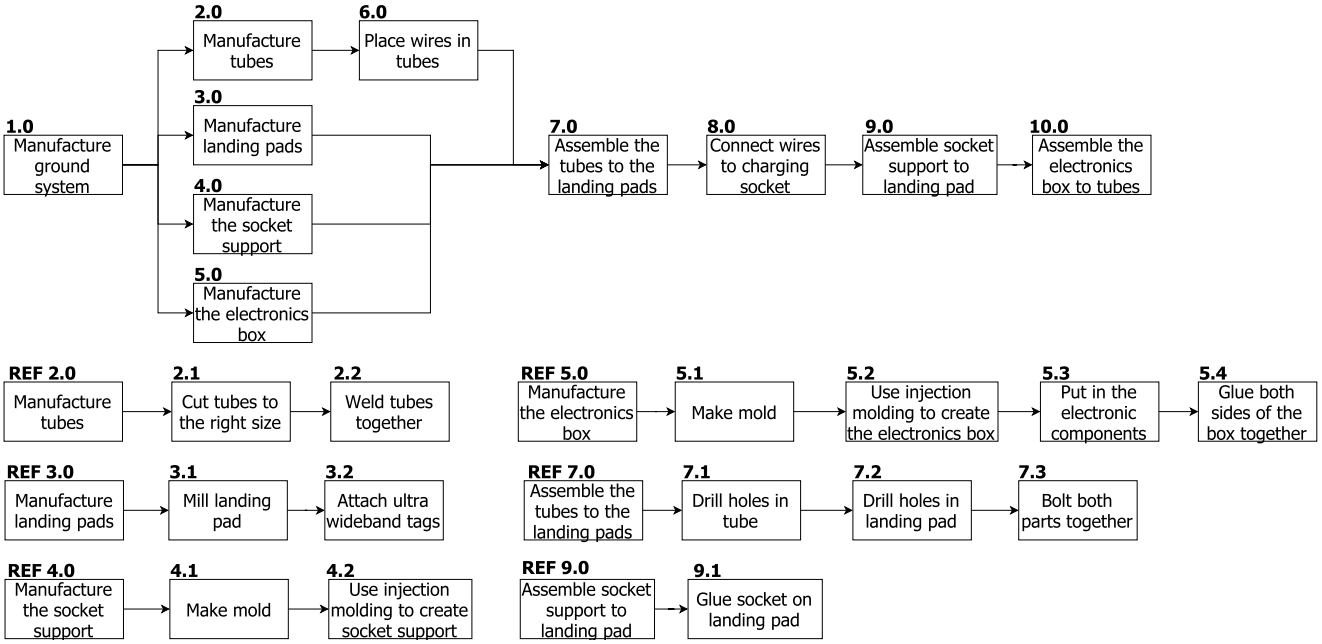


Figure 15.3: Production flow diagram for the ground system

# 16

# Risk and mitigation

The risk management process is performed in three phases. First all the technical risks are identified for given subsystem. This is done by analyzing different subsystem components under working conditions. In next step, the risks are listed and assessed. The assessment focuses on two components of the risks, namely on probability of the event and on severity of the consequences. There are 5 levels of probability defined, and listed in Table 16.1. The levels are defined based on the guidelines developed by NASA Engineering and Safety Center [71]. Each level has certain probability range, which enables to qualify events (possible failures) in a more systematic way. Similarly there are 5 different levels of severity defined in Table 16.2. Each level has a description (in the 3rd column) which allows to qualify particular consequence in a definitive way.

Table 16.1: Levels of probability of failure defined for use in the risk matrix

| **Probability scale** | **Probability** | **Probability range** |
|---|---|---|
| 5 | Very high | P>0.1 |
| 4 | High | 0.1>P >0.01 |
| 3 | Moderate | 0.01 >P >0.001 |
| 2 | Low | 0.001>P >$10^{-6}$ |
| 1 | Very low | $10^{-6}$>P |

Table 16.2: Levels of severity defined for use in the risk matrix

| **Severity scale** | **Severity** | **Description** |
|---|---|---|
| 5 | Catastrophic | Mission failure |
| 4 | Critical | Mission success questionable |
| 3 | Significant | Decrease in performance |
| 2 | Marginal | Degradation of secondary mission, small decrease in performance |
| 1 | Negligible | Nonoperational impact |

In the last step risks are prioritized and mitigated. The mitigation actions focus on decreasing probability of the event or reducing the consequences. Some of the risks might be accepted without any mitigation. This is usually the case when either the risk is relatively low, or the mitigation action would result in an in-feasible solution (for instance the part is relatively cheap and can be easily replaced in case of failure). The described approach was implemented on all the subsystems. The results are listed in tables below for each of the subsystems. For each of risks a probability (P) and severity (S) were estimated, and mitigation action was defined. Each risk was reevaluated after mitigation and assigned new mitigated probability (MP), and mitigated severity (MS).

From each of the subsystems, three largest risks were chosen and placed in the risk matrix, as shown on Figure 16.1. Those risks - after mitigation - are then placed in the mitigated risk matrix shown in Figure 16.2. Comparing two matrices the results of mitigation are apparent. Primarily most of the risks were in orange and red zone, which correspond respectively to high and extreme risk. After mitigation there are no risks in the red zone, which means that all the critical risks were eliminated. Most of the risks were mitigated by decreasing probability of occurrence. Furthermore, most of the high risks (items at the orange field) are eliminated as well, and only two items are left in this range.

Table 16.3: Risk matrix for the blower subsystem

| ID | Risk | Cause | P | Effect | S | Mitigation action | MP | MS |
|---|---|---|---|---|---|---|---|---|
| BL1 | Blower is unable to provide flow with exhaust velocity of 10 | Underestimated pressure losses | 3 | Ineffective pollination | 4 | Safety factor of 1.5 on the system performance | 1 | 3 |
| BL2 | Blower provides flow of more than 20 | Design not optimized, flow phenomena in the system predicted inaccurately | 2 | Overdesigned system: higher weight and power consumption; damage of the flowers | 4 | Design optimization; implementing jet control system, calibration during the tests | 2 | 2 |
| BL3 | Suck in objects to the system | Exposed inlet | 3 | Object can damage parts of the system: damage the fan, duct, heat sink; object can be accelerated with exhaust jet and make damage to a plant or a person | 5 | Add mesh at the fan inlet to prevent entrance of large particles | 1 | 5 |
| BL4 | Overheating the plant | Excessive heat generated by the fan, motor and heat sink | 2 | Damage of the flower | 3 | Analysis of the heat transfer in the system | 1 | 3 |
| BL5 | Blower jet dissipation | Interference with the rotor wake | 3 | Ineffective pollination | 4 | Place the blower exhaust outside the wake | 2 | 4 |
| BL6 | Force exerted on the flower by the blower is too low | Mass flow is insufficient, distance is too large | 3 | Ineffective pollination | 4 | Safety factor of 1.5 on the exhaust velocity, control distance to the flower | 2 | 4 |

Table 16.4: Risk matrix for the charging subsystem and the ground segment

| ID | Risk | Cause | P | Effect | S | Mitigation action | MP | MS |
|---|---|---|---|---|---|---|---|---|
| GS1 | The charging pin is short-circuited | Water condensation on the pin | 4 | Burning of (part of) the drone and ground station electronics | 5 | Impose operation conditions of humidity of less than 80%; add a temperature sensor to the charging pin* | 2 | 4 |
| GS2 | A drone is severely damaged upon vertical impact | The charging pin impinging the drone electronics and structure | 2 | The drone cannot operate and needs to be repaired or replaced | 4 | Make the pin detachable upon application of a strong force | 2 | 2 |
| GS3 | The ground segment cannot be installed | Greenhouse structure or space limitations | 2 | The system cannot be installed | 5 | Provide on floor ground station installation option as well | 1 | 5 |
| GS4 | A ground station malfunctions | Software or hardware failure, or cable disconnection | 2 | There is no entity controlling the drones assigned to this ground station | 4 | The central server reassigns the drones to a neighboring station that guide them to the failed ground station and gives them landing instructions | 2 | 2 |
| GS5 | The central server or the switching hub malfunctions | Software or hardware failure, or cable disconnection | 2 | There is no coordination between the ground stations | 4 | The ground stations instruct all drones to go back and land. | 2 | 2 |
| GS6 | A power outage occurs | Electrical grid issues | 1 | No communication or navigation for the drones possible so they cannot return to the ground stations | 5 | Install backup power batteries that provide sufficient power for the drones to return to the ground stations | 1 | 2 |
| GS7 | Access to a charging pad is obstructed | Greenhouse worker leaving equipment near the pad | 3 | A drone will not have access to charging | 4 | The drone can take turns with the other drones to charge; the system notifies the user | 3 | 1 |
| GS8 | Remote hackers attack the system | Vulnerabilities in the software implementation | 2 | The system, the plants, and the greenhouse infrastructure might be destroyed | 5 | Hire cybersecurity consultants to ensure the security level of the system; Restrict root access only for direct connection inside the greenhouse | 1 | 5 |

* Humidity level of 80% allows for the charging pin to be 4° cooler than the surrounding air before condensation occurs [72, 73]. For higher humidity levels this temperature margin grows smaller. A difference of more than 4° is expected to be very unlikely to occur. Nevertheless, in case that is observed, the temperature sensor of the pin will detect it as potential dew condition and charging will not be allowed to start.

Table 16.5: Risk matrix for the battery subsystem

| ID | Risk | Cause | P | Effect | S | Mitigation | MP | MS |
|---|---|---|---|---|---|---|---|---|
| BAT1 | Battery catching fire | Overheating due to excessive usage or shortcircuit | 4 | APIS or tomatoes get burnt | 5 | Monitor voltage and temperature | 2 | 5 |
| BAT2 | Not having enough energy on-board | Increased energy consumption due to subsystem wear-off | 4 | Shorter missions and not pollinating in time | 2 | Monitoring of energy consumption per mission and foresee the degradation | 3 | 2 |
| BAT3 | Shorter life cycle than expected | High DoD/C-rate or manufacturer inaccurate | 4 | Higher maintainability | 3 | Never exceed 4C at charging and request test battery | 3 | 3 |
| BAT4 | Higher mass than what is advertised | Manufacturing defects | 3 | Decreased mission duration or cycle life | 3 | Request test battery and get rid of casing if needed | 2 | 3 |
| BAT5 | Bigger battery size than advertised | Manufacturing defects | 3 | Integration issues on the structure | 3 | Increase the size of box | 3 | 2 |
| BAT6 | Battery not being customizable | Graphene technology might differ internally from common Lipoly | 3 | Battery cannot be integrated | 5 | Change to another choice of battery | 3 | 3 |

Table 16.6: Risks associated with the propulsion subsystem

| ID | Risk | Cause | P | Effect | S | Mitigation | MP | MS |
|---|---|---|---|---|---|---|---|---|
| PRO1 | 1 motor failing | Overheating / defective motors / short circuit | 3 | Manual pick-up and return to ground station | 5 | Software patch for extra power drainage / testing previous to implementation / fuses | 1 | 5 |
| PRO2 | Motors under-performing | Environment being detrimental and corroding motors | 3 | Higher maintenance | 2 | Apply coatings for the coils or buying a higher quality motor | 1 | 2 |
| PRO3 | Overheating | Excess of current and bad heat dissipation | 3 | Higher maintenance and reduced lifetime | 2 | Adding aluminium as the frame to dissipate heat | 2 | 4 |
| PRO4 | Underbalanced propellers | Physical impact or axis misalignment | 4 | Worse efficiency and vibrations on electronics | 3 | More regular maintenance | 3 | 3 |
| PRO5 | Casing blocking the propellers | Bending of the case | 4 | Higher power consumption and lifetime reduction | 5 | Software patch to check rpm's with power | 3 | 5 |

Table 16.7: Risk matrix for the structure

| ID | Risk | Cause | P | Effect | S | Mitigation | MP | MS |
|---|---|---|---|---|---|---|---|---|
| STR1 | Failure of arms due to impact | Impact due to collision with rails | 2 | Propellers disintegrated from structures, wires break. New arms and wires must be incorporated in the system. | 4 | Add propeller casing. This will make sure that when the drone falls on the arms, the propeller casing will first touch the object, break and take the shock. The propeller casing is easy to replace. | 1 | 4 |
| STR2 | Failure of propeller | Impact due to collision | 4 | Propeller is broken. Propeller must be replaced. | 3 | Add propeller casing. | 1 | 3 |
| STR3 | Structure disintegrates due to glue failure. | Glue failure due to high humidity level in greenhouse | 3 | Structure is disassembled. | 4 | Properly test adhesive used in design for humidity properties (or investigate data sheets). | 1 | 4 |
| STR4 | Failure of arms due to vibrations | Eigen frequency of structure near motor frequency | 4 | Propellers disintegrated from structures, wires break. New arms and wires must be incorporated in the system. | 4 | Ensure that the eigen frequency of the drone is at least two times higher than the frequency of the motors. | 1 | 4 |
| STR5 | Failure of the payload box | Impact due to collision with ground or rails | 2 | Payload box must be replaced. MAV must completely be reassembled, Battery, PCB and blower can be damaged. | 5 | Add casing around the payload box, such that the casing will break first. This is much easier to replace and can take the shock. | 1 | 5 |
| STR6 | Failure of MAV | Impact due to collision with ground or rails | 4 | Arms break off and damaged electronic parts or battery. | 2 | Add casing to protect the whole structure. | 2 | 2 |
| STR7 | Entanglement in wires or plants | Objects get stuck in the spacings in the structure (between the rotors) | 3 | Drone will get stuck, must be set free manually. | 3 | Make sure that there are no places where the wires can get stuck. When stuck within the plants add a warning system such that the owner knows that the drone is stuck. | 2 | 2 |
| STR8 | Failure of blower due to impact | Impact due to collision with ground or rails | 2 | Not able to perform pollination anymore | 4 | Add casing to the drone. | 1 | 4 |

Table 16.8: Risk matrix for navigation

| Tag | Risk | Cause | P | Effect | S | Mitigation action | MP | MS |
|---|---|---|---|---|---|---|---|---|
| NAVR1 | UWB signal lost | Flying too far away from the ground tags | 2 | No location information, no health information | 5 | Redundancy in localization | 1 | 5 |
| NAVR2 | Flying towards a wire | Drift in position | 3 | Drone could crash into wire | 4 | Make controller more robust; Add an extra tag | 2 | 4 |
| NAVR3 | Flying height too low | Cup was not properly detected; improper registering of location of the cup | 2 | Fly in between the plants instead of on top of the row ; | 4 | Change cup into more visually detectable obstacle Have all drones that see the cup communicate the location of the cup to the ground station | 1 | 4 |
| NAVR4 | Drone flying in same row | On-board HW/SW did not perform as expected | 1 | Crash into drone and damage surroundings | 5 | Consider communication in between drones | 1 | 5 |
| NAVR5 | Object moving faster than what can be detected | Camera has fps that is too low | | Possibility of crashing into the obstacles. | | Change the camera to one that has a larger fps | | |
| NAVR6 | Flowers are not detected | Lighting conditions, Flower color has changed | 2 | The flowers that are not detected will not be pollinated | 5 | Change the algorithm used to a more efficient one that ; works in various lighting conditions and that does not only use the colour of the pixels | 1 | 5 |
| NAVR7 | Overloading of the UWB | Too many signals sent over one band | 2 | Time for drone to receive and send data to the ground station is very large | 3 | Increase time in between two calibration handshakes | 1 | 2 |
| NAVR8 | Not enough space for more pictures | Not enough memory | 1 | Pictures will not be saved or some might be overwritten | 3 | Hover and transmit images via UWB then delete the transmitted images for extra space | 1 | 2 |
| NAVR9 | Not being able to detect the cup | Cup not being in fov of drone | 2 | Drone will start flying at the row at the wrong height | 3 | Track drone heading when it is being descended | 1 | 3 |
| NAVR10 | Not enough space to move sideways from ground station during takeoff | The ground station was designed for a certain greenhouse dimension which if smaller could make take-off complex | 3 | Crash into nearby obstacle - such as a plant | 4 | Adjust flight path: trial by error try upwards | 1 | 4 |

Table 16.9: Risk matrix for electronics subsystem

| ID | Risk | Cause | P | Effect | S | Mitigation | MP | MS |
|---|---|---|---|---|---|---|---|---|
| EL1 | Processor not able to process all the things at the same time | The clock rate is not high enough | 3 | Not able to do obstacle detection, control, power regulation etc. at the same time | 5 | Use a processor that has a clock rate that can handle all the components | 1 | 5 |
| EL2 | Not enough input ports for all the components | The CPU is not able to handle the amount of components needed | 3 | Important components can not be added | 4 | Make sure that the processor has enough ports for all the components | 1 | 4 |
| EL3 | Failure of CPU | Programmed wrong | 4 | The drone is not able to operate | 5 | Use an off the shelf CPU, that has already been proven in drone flight | 2 | 5 |
| EL4 | Failure of the IMU | Damaged or installed wrong | 3 | Not able to know the orientation of the drone | 3 | Use an off the shelf IMU, that has already been proven in drone flight | 1 | 3 |
| EL5 | Failure of the barometer | Damaged or installed wrong | 3 | Not able to know the height of the drone | 3 | Make sure that there is another subsystem that can measure the height | 1 | 3 |
| EL6 | Failure of the stereo-cameras | Damaged | 2 | Not able to detect obstacles | 3 | Add another system for obstacle avoidance to have more redundancy | 2 | 2 |
| EL7 | Lasers stop working | Damaged | 2 | Not able to detect obstacles | 4 | Add another system for obstacle avoidance to have more redundancy | 2 | 3 |
| EL8 | Failure of UWB | Damaged | 2 | Not knowing the position of the drone | 4 | Use two UWB modules | 2 | 2 |

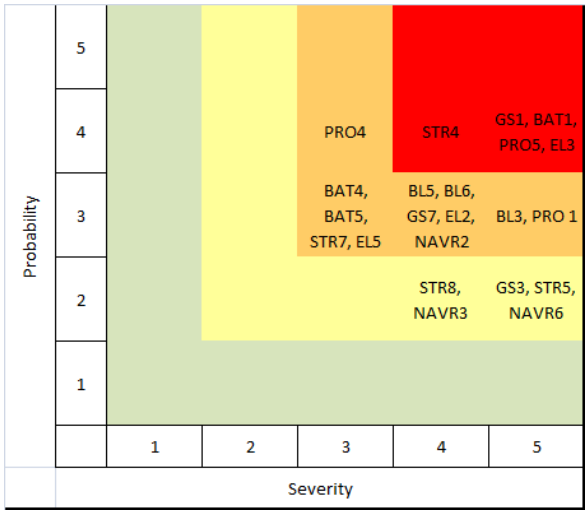


Figure 16.1: Risk matrix with sample risks from all the subsystems

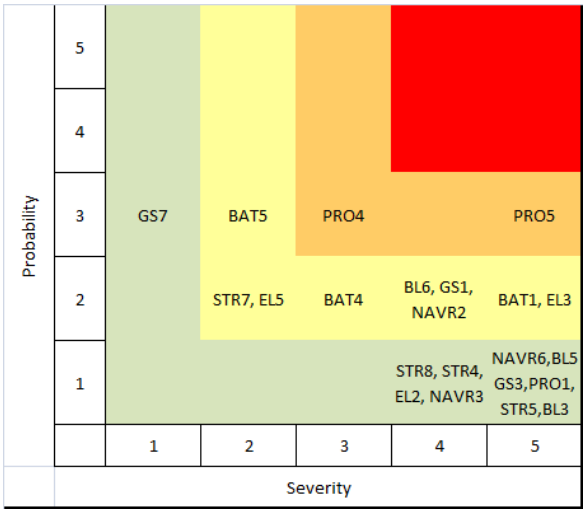


Figure 16.2: Mitigated risk matrix with sample risks from all the subsystems

# 17

# Sustainable development strategy

All products have a certain impact on the world. This impact has social, environmental and economical implications. If the impact in these three areas combined is minimized, sustainable development succeeds. In this chapter, the way sustainable development is taken into account in this design and the impact of this design on the environment are discussed. These aspects are evaluated according to the Lifecycle design strategies (LiDS) wheel (Figure 17.1), which presents seven phases in the lifetime of the product and shows metrics to evaluate the sustainability in these phases [74]. These phases are shown in Sections 17.1 to 17.4. Furthermore, the contribution of the system to sustainable development is evaluated in Section 17.5, which is largely inspired by the midterm report [9].

The analysis shown below is a qualitative one and gives no concrete numbers on how sustainable the product is. A detailed lifecycle analysis can be performed using dedicated tools, such as Ecoinvent[1].

## 17.1. Material aspects in the design

The first two spokes of the wheel have to do with the material aspects in the design. The structural elements of the drone are made of carbon fibre and ABS plastic. The APIS also contains a Lithium-polymer graphene battery, five electric motors and electronics.

ABS plastic is a thermoplastic polymer that has a wide range of uses. In the electronics and automotive industry it is often employed, as well as in the well-known Lego bricks. It can be mass produced and in production, the harmful emissions are below workplace limits [75]. When 3D-printed or injection moulded, the amount of material used during production can be greatly reduced. However, one concern should be identified. In confined spaces using 3d printers , ultra fine particle levels can reach dangerous levels. Lastly, although most ABS plastics are oil-based, effort is done to make the switch to sustainable sources[2].

The payload box and the motor arms are made of carbon fibre reinforced plastic. The quality aspects of this material are fairly low. The production of carbon fibre is energy intensive, 14 times more than conventional steel [76]. Furthermore, although recycling carbon fibre is possible, it is more cumbersome compared to conventional methods[3]. Lastly, the production waste in the production of carbon fibre is high compared to alternatives[4]. Production techniques should be optimized to minimize this waste. The main advantages of the use of carbon fibre lie in the use phase of the vehicle. For example, it is corrosion resistant and chemically stable, although the epoxy resin can be sensitive to UV light[5]. ABS plastic has similar properties[6].

Another material that scores low on the 'quality scale' is the lithium polymer battery. This component contains some heavy metals, that require a lot of energy to extract and making it from recyclable material is not yet feasible. Nonetheless, recycling the material is done, although it is energy-intensive. According to literature [77], the levels of copper, cobalt and nickel are classified hazardous for humans by U.S. regulations. Another aspect that is important to note is the flammability of the material. The brushless motors are generally made of materials with metals of a high quality and value. The motors are therefore often recyclable or made of recycled metals [78].

[1] http://www.ecoinvent.org/home.html [Cited 23 June 2017]

[2] https://www.environmentalleader.com/2016/06/will-legos-150-million-sustainable-plastics-challenge-make-biobased-the-norm/ [Cited 22 June 2017]

[3] https://recyclenation.com/2015/10/is-carbon-fiber-better-for-environment-than-steel/ [Cited 22 June 2017]

[4] https://www.theguardian.com/sustainable-business/2017/mar/22/carbon-fibre-wonder-material-dirty-secret [Cited 22 June 2017]

[5] http://www.christinedemerchant.com/carboncharacteristics.html [Cited 23 June 2017]

[6] http://www.fibox.com/137/Plastic%20materials:%20PC,%20ABS,%20GRP_ENG3.html [Cited 23 June 2017]

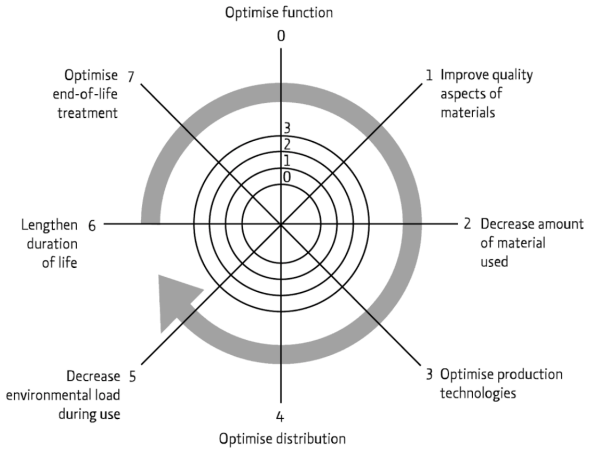


Figure 17.1: Elements in the LiDS wheel

Finally, the printed circuit boards in the drones are of material with a high environmental impact. Due to their complexity, recycling is difficult and energy intensive [79]. The complexity also means that a large range of materials is used: plastics, ceramics and several different metals. Metals such as chromium, lead and mercury can be harmful to people [80].

## 17.2. Production and distribution

The next step in the life cycle is the production and distribution of the product. Combining and integrating all these different components results in a flyable vehicle. The production of this vehicle can be made environmentally efficient. Fewer production steps, low energy consumption in production and a reduction in production waste are good for environment and good for profit. In distribution, clean packaging and energy efficient transport should be employed. In Chapter 15, an elaborate production plan is made. From this chapter, injection moulding, vacuum infusion and milling are three main production processes. Injection moulding is a widespread production process. It involves heating a polymer resin and injecting it into a mould. The energy use of this process was investigated in [81]. Energy consumption of this industry is fairly high. The entire U.S. injection moulding industry uses a similar amount of energy as the electricity production of several developed countries, including the Netherlands. Composite materials are produced by vacuum infusion. Compared to traditional methods, this process results in less resin waste and, as it is a closed system, no harmful gas emissions. Milling of aluminum produces a fair amount of production waste at first sight. This metal waste however, can be recycled well. In a larger scope, one could imagine that an automated process impacts more on the environment, while a manual process has more social impact.

In distribution, an energy and economically efficient method could be envisioned. As greenhouses are often built in dense clusters around the world (the Westland region in the Netherlands or the Almeria region in Spain for example), production could happen close to these regions to limit the transport impact and increase service for the client.

## 17.3. Operational phase

During the use phase of the product, the most obvious environmental impact of the product can be identified. In the generation of electricity, there are still emissions in the environment. An elaborate analysis on this is shown in Section 17.3.1. Another sustainability aspect in the design is the noise that the vehicles emit, as investigated in Section 17.3.2. In Section 17.3.3, other characteristics in the use phase are considered.

### 17.3.1. Power consumption

The APIS system needs to use a certain amount of electricity to be able to perform its function. This electricity comes at a certain cost. The farmer needs to buy the electricity at a certain price and in the generation of electricity there is an environmental impact. This impact can be well measured by the $CO_2$ emissions needed for electricity generation. The European Environment Agency provides a clear overview of the so-called emission intensity (grams $CO_2$ per kWh) of the electricity mix in 2015. This data is used to estimate the environmental impact of the system during its use. In Table 17.1, the total $CO_2$ emissions of the typical system are presented. The energy mix in the Netherlands can be

considered quite environmentally unfriendly. A low percentage of electricity production is renewable and a large portion is produced by polluting coal fire plants [82]. As the Netherlands signed the Paris accords, it will strive to use more renewable energy.

Table 17.1: Emissions in a typical greenhouse in different countries

| Country | Emission intensity [g/kWh] | CO2 emissions [kg/year] |
|---|---|---|
| Netherlands | 451.4 | 294.01 |
| Spain | 304 | 198.00 |
| EU | 275.9 | 179.70 |

Table 17.2: Change in energy use and CO2 emissions

| Situation | Energy use [kWh/year/m$^2$] | CO2 emission [kg/year/m$^2$] |
|---|---|---|
| Current situation | 104.17 | 61.92 |
| With APIS | 0.0163 | 0.0074 |
| Change [%] | 0.016 | 0.012 |

To give these numbers some perspective, it is relevant to compare these with the electricity use and $CO_2$ emissions of the Dutch greenhouse sector. According to [83], the yearly energy use of a typical Dutch greenhouse is 375 MJ·m$^{-2}$ or 104.2 kWh·m$^{-2}$. The energy use of the APIS system, pollinating a greenhouse of 200 by 200 meters every three days is estimated to be a marginal 0.0163 kWh·m$^{-2}$ a year. This means a total increase of 0.016 %. In short, adding the system does not largely contribute to the energy use of the greenhouse. These results are tabulated in Table 17.2.

### 17.3.2. Noise characteristics

Noise is another sustainability aspect that can be identified during the use phase. If the system of drones produces too much noise, it can have annoying, or even harmful consequences for humans working in the greenhouse. Moreover, most countries' working conditions legislation stipulates maximum noise levels allowed in the environment where workers without special protection gear operate.

Noise (and sound for that matter) is usually measured in Sound Pressure Level (SPL), denoted by $L_p$:

$$L_p = \log_{10}\left(\frac{p}{p_0}\right)\text{dB}, \tag{17.1}$$

where $p_0$ is the reference sound pressure, usually taken to be 20 $\mu$Pa. In reality, people do not perceive sounds the same way across the frequency spectrum. For example, a low frequency sound will be perceived less loud than a high frequency sound with the same pressure level. Therefore, in order to address the actual human perception of the noise levels, weights are used to adjust the sound pressure level for different frequencies. The most popular of which, and typically used in regulations and research, is the *A-weighting* defined in the international standard IEC 61672:2003 [84]. A-weighted sound levels are denoted by dB(A).

The Dutch legislation is used as a baseline for the allowed noise that the APIS system design has to comply with. In particular, the Working Conditions Decree in its revision from September 2016 was consulted [85]. The maximum noise level stipulated there that is exempt of special requirements regarding medical examinations or protective equipment is 80 dB(A), defined with $p_0 = 20\mu$Pa.

Modelling the noise of quad-rotors with numerical means is still something that is generally considered unreliable [86]. Therefore, instead, experimental studies were consulted. The literature consistently reports noise level values of less than 80 dB(A) measured at distances representative to the ones potential human workers in the greenhouse would have [86–88]. For the same reason, the only way to establish accurate noise values for the APIS drones is by performing field test in an actual greenhouse.

One could assume that as there are a number of drones in the confined space inside the greenhouse, the noise levels would be much higher. Nevertheless, thanks to the plants inside, the noise levels as would be experienced by a human worker on the ground are not expected to be higher than the values for a single drone. Numerous studies have been conducted into the attenuation capabilities of plants [89, 90]. In particular, it has been shown that multiple periodic rows of plants are quite effective for noise reduction due to a periodicity in the density of the area they cover [91]. Therefore, it is expected that the tomato plants in the greenhouse will absorb a large part of the noise, particularly in the high frequencies, which are also the ones more strongly perceived by humans.

Moreover, several techniques for reduction of propeller noise can be implemented. For example, Lu et al. have demonstrated that shrouds around the propeller have a favorable effect on the noise emission levels [92]. The APIS drones are equipped with shrouds around the propellers, so it is expected that they will benefit from this phenomenon. Additionally, further noise reduction can be achieved by tripping the flow over the propeller. This is believed to reduce the laminar boundary layer noise and to ensure that no laminar separation bubbles exist. Leslie et al. report reduction of up to 6-7 dB(A) for small MAV propellers by using such techniques [93]. Therefore, it can be concluded that the

greenhouse environment, together with propeller noise reduction techniques will most probably result in noise levels below the 80 dB(A) stipulated in regulations.

### 17.3.3. Other considerations in use phase

Lengthen duration of the use phase is tightly related to reliability and maintainability as discussed in Chapter 14. A product that is easy to maintain and that is reliable has longer technical life-span and therefore a lower environmental impact. The battery is a key element in the drone. It is the subsystem with the highest weight and a low number of cycles. In Section 6.4, the battery selection is explained and the choice of battery is done, mainly based on its number of cycles. It is now estimated that the battery has a lifetime of about 400 hours and that, using the APIS intensively, the battery needs to be replaced every month. Naturally, this operation is not very sustainable. Therefore, great effort should be made to collect and dispose the lithium polymer batteries safely and in a sustainable way. Also, a great plus for the APIS is the modular design. The modular payload provides opportunity to work with other types of plants too. This gives the possibility to lengthen the lifetime of the system.

## 17.4. End of life

A sustainable end-of-life treatment can be looked at from two ways. Either the entire, or parts of the product should be reused, or materials in the product should be efficiently recycled. The first goal should be to disassemble the product at end of life and aim for reuse of parts. If the APIS has a broken payload box for example, the motor arms could still be good to use in another vehicle. If reuse of parts is not possible, different materials should be separated and recycled. As discussed above, although most product can or are even required to be recycled, this process can be energy intensive and thus unsustainable. Good awareness should be created and collection policy should be put in place to ensure good recycling or refurbishing of the products. Broken products could be sent back to the manufacturer, disassembled and different parts can be recycled. Special care should be taken in the disposal of the LiPo batteries. Large battery recycling schemes have been employed in several countries and a large portion of the material can be recycled [94]. Looking at LiDS wheel in Figure 17.1, all the spokes from beginning to end have been evaluated. Only the last one, about optimizing the function has not been evaluated. This is about answering the question if the chosen product is the most sustainable way of performing the mission. This will be considered in the next section.

## 17.5. Contribution of system to sustainability

The way the product or system contributes to sustainability is presented below. This contribution is split up in three areas. First the social contribution of the system, secondly the environmental contribution and finally the economical contribution.

The social contribution to sustainability can both have a positive impact or a negative impact. One example of social impact is to the workers in the greenhouse. They could be affected by the noise or the drones flying around, although the noise levels are below restrictions. Compared to the current pollination solution, bees flying around, the noise could be more, but the risk of being stung or hit by a bee is almost completely mitigated. Another impact to society has more ethical grounds. Currently, agriculture is drastically changing by using genetically modified crops to boost yield. A large controversy is surrounding this topic as people do not like to eat food that is artificially enhanced[7]. A similar controversy could arise when pollinating robots are flying around and taking over an essential natural process. Furthermore, legal aspects should also be considered. Could controversy about this topic result in stricter laws that limit the use of artificial pollinators? On the other hand, in some countries the use of a natural, but invasive pollinator is forbidden. For example, in New Zealand and Australia, the use of invasive bumblebees species is prohibited[8]. A mechanical pollinating system lets crops grow in greenhouses in these areas and provide home-grown vegetables to the population. The last social contribution that is discussed could have social impact in the long term. According to vanilla farmer Henk de Kroon, the way vanilla is currently cultivated is not sustainable. This plant is has to be pollinated by hand at one single moment by a group of people. The crop is mainly cultivated in Madagascar, where men, women and children work for a very low wage in very bad conditions. If, after further research, a pollinator drone is made accurate enough to do this process, a pollinator drone could aid in this process. This could improve the living conditions of these people.

One environmental contribution of this system lies on the intersection between social and economical implications. One could imagine that, if the system becomes efficient enough, it could replace with natural pollinator insects. The need to protect these insects (bees, bumblebees) is then limited and environmental impact (loss of insects) is then enormous. In any case, all measures should be taken to preserve natural pollination by bees. Looking at the mission need statement,

[7] `http://www.iflscience.com/environment/myths-and-controversies-gmos-0/` [Cited 23 June 2017]

[8] `http://www.environment.gov.au/biodiversity/invasive-species/insects-and-other-invertebrates/invasive-bees` [Cited 23 June 2017]

the system would only be put in place when the natural mechanisms are insufficient, endangered or ineffective. Another environmental impact has to do with the greenhouse environment. The drones will fly around not only pollinating, but also taking pictures and gathering other environmental data. This data can then be used to optimize the use of resources in the greenhouses and limit the waste of energy. Furthermore, the positive environmental impact can be seen in the preservation of certain crops.

The system also offers multiple economical advantages. Firstly, the pollination service that is required is ensured. This limits the risk for the farmer and provides economic benefits for him. Secondly, a mechanical system could decrease the use of expensive manual labor for the farmer. To refer to the example mentioned above, a test project to cultivate vanilla in the Netherlands is already put up[9]. According to Henk de Kroon, large-scale development is hampered by the high labor cost in the Netherlands. An mechanical pollination system would provide a reliable and cheap pollination service and make large-scale development possible. Coupled to this point is the third advantage. In food industry currently, there is a trend towards increasing the traceability of crops [95]. Having an active monitoring system can improve this aspect and add extra economic value. Finally, it is expected that the system enhances pollination, thus boosts yield and increases profits.

[9] https://www.wur.nl/nl/Dossiers/dossier/Vanille-uit-de-Nederlandse-kas-Nedervanille.htm [Cited 23 June 2017]

# 18

# Sensitivity analysis

A sensitivity analysis is carried out to check if the requirements are still met with the largest uncertainties. To do so the key parameters that drive the requirements are first defined. This includes UWB precision, mass and battery capacity. When possible, the uncertainties of those parameters are found through Monte Carlo simulations. The 95% confidence interval has been given.

## 18.1. Battery capacity

A Monte Carlo simulation will be carried out to determine the range of certainty of the battery capacity. The latter depends on a variety of parameters that each have their own uncertainty. All these parameters will be distributed uniformly on the range [value - uncertainty, value + uncertainty]. Generating 1000000 samples, the capacity can be calculated and 95% and 99% confidence intervals can be provided by using Equation (18.1) and Equation (18.2). These depend on the mean (aM) and the standard deviation (bM) of the entire sample size.

$$95\ \%\ \text{confidence interval} = \left[\frac{aM - 1.96 * bM}{\sqrt{N}}, \frac{aM + 1.96 * bM}{\sqrt{N}}\right] \tag{18.1}$$

$$99\ \%\ \text{confidence interval} = \left[\frac{aM - 2.57 * bM}{\sqrt{N}}, \frac{aM + 2.57 * bM}{\sqrt{N}}\right] \tag{18.2}$$

A distinction has to be made between the capacity required for the mission and the capacity the chosen battery has. In fact, the chosen battery of APIS is 1500 mAh. On the other hand, depending on the duration and power consumption during the mission, different capacities of the battery will be consumed. These two values altogether give the depth of discharge for the mission. The latter is of remarkable importance given its notable impact on the lifetime. Such is the importance, that the requirements (DP-MAV-3-POW-3) include a maximum depth of discharge of 90%, however for the nominal mission a DoD of 78.5% is used, Chapter 6. Arguably, the questions is whether in a regular basis the DoD will be under this maximum requirement. It depends on the watt hours required which in turn depends on the energy in the mission. As it was explained in Chapter 6, the total energy is a function of the energy consumption of the various phases. In a typical nominal mission there are 7 phases: take-off, cruise, detection, pollination, turning, cruise back and landing. The times given to each of these phases have uncertainties and so do the power consumption. These can be found in Table 18.1. Multiplying these two gives the energy consumption for the phase. The energy listed in Table 18.1 is however not the total energy, but part of the energy of the considered phase that was found differently (through a Python model for instance) as more factors came into play. It therefore carries its own uncertainty. A more elaborate discussion can be found in Chapter 6. The final column of this table shows the total uncertainty in the energy calculations for each phase.

Calculating the battery capacity 1,000,000 times, the standard deviation and the mean can be found. They were found to be 189.8 and 1231 respectively. It must be noted that they change each time all the samples are recalculated as the seed that generates the random numbers is different each time. The 95% confidence interval that was constructed was : [1164.2;1165.5], as well as a 99% one : [1164.0;1165.7]. This means that given the uncertainties listed in Table 18.1, even though they would occur, it can be said 99% confidently that the required capacity of the battery will be between [1164.0;1165.7]. For a nominal mission, the capacity the battery was sized for was 1,177 mAh, consequently, as shown from the Montecarlo simulation, the battery is slightly overdesigned. Unfortunately, this is not optimal, however this small margin can be argued to be desired for small unforeseen energy consumption, such as internal resistance in the battery. Finally, a comment can be made regarding the maximum value that was obtained: 1,336.9 mAh. Following

Table 18.1: Uncertainties for the times spent and power consumed in each phase

| Phase | Times [s] | Power variations [W] | Energy variations [J] | Total energy variations [J] |
|---|---|---|---|---|
| Take-off | 3 ±2 | 3.546 | 132.48 ± 20.66 | (3 ±2) · 3.546 + (132.48 ± 20.66) |
| Cruise | 50 ±10 | 3.546 | 2210 ± 344.5 | (50 ± 10)· 3.546 + (2210 ± 344.5) |
| Non-pollinating | 36.5 ±10 | 5.341 | 1614 ± 251.7 | (36.5 ± 10)· 5.341 + (1614 ± 251.7) |
| Pollination | 478 ±10 | 5.341 | 21128.2 ± 3296.61 | (478 ± 10)· 5.341 + (21128.2 ± 3296.61) |
| Turning | 2 ±1.8 | 47.7 | N.A. | (2 ±1.8)· 47.7 |
| Cruise back | 50 ±10 | 3.546 | 2024 ± 344.5 | (50 ± 10) · 3.546 + (2210 ± 344.5) |
| Landing | 10 ±5 | 3.546 | 442.47 ± 69.02 | (10 ± 5)· 3.546 + (442.47 ± 69.02) |

from the requirement DP-MAV-3-POW-3, a maximum depth of discharge of 90% is needed to promote a healthy and lengthily lifetime for the battery. Thus, for a nominal capacity of 1,177 mAh, a maximum capacity of 1,307 mAh could be consumed during the mission without much damage to the battery. The maximum value for the Montecarlo shows that one mission in 1,000,000 will drain an excess of 70 mAh. This is obviously undesired, but will definitely not be a catastrophic risk, especially because the physical maximum the battery is 1,500 mAh.

## 18.2. UWB position and attitude determination

The sensitivity analysis for the UWB position estimate was performed in a manner similar to the one for the battery outlined above. In particular, a Monte Carlo simulation with 1000 runs was implemented. The lower number of samples is due to the fact that a single evaluation of the UWB position analysis code is more computationally expensive than for the battery.

The parameter bearing most uncertainty in the module is the standard deviation of the ranging errors. As explained in Section 8.3, the nominal value, as reported by the manufacturer, is 3.5 cm. In order to assess the effects of variability of this value on the position estimation accuracy, the positioning analysis tool was run for standard deviation values on a uniform distribution [2.0 cm; 5.0 cm]. For each evaluation, the maximum positioning error was recorded and the 95% and 99% confidence intervals were obtained. The 95% confidence interval was found to be [1.96 cm; 4.46 cm], and the 99% confidence interval to be [1.86 cm; 4.60 cm]. This ranges are considered small enough, as the task, requiring highest precision is landing, which has a tolerance of about 2 cm but is largely assisted with visual cues.

The attitude determination depends on the position estimation accuracy and the number of measurements averaged for a single sample. The second is design choice, trading update frequency with attitude accuracy, as detailed in Section 8.4. Hence, it will not be considered as variable for the sensitivity analysis and will be have the fixed value of 10. The sensitivity to the position estimation accuracy, however, was investigated, as there is significant uncertainty in its value. The manufacturer of the UWB module[1] reports position errors of 10 cm. Nevertheless, shown above, using the method outlined in Section 8.3 results in maximum error in the 99% confidence interval of 4.60 cm. Therefore, in order account for these different values, the interval [4 cm; 15 cm] was set.

In total 10,000,000 evaluations were run for on-board module points uniformly distributed in spheres with radii as given above. The resulting distribution converges to a half-normal probability density distribution. Its 95% confidence interval was found to be [0.13°; 5.37°], and the 99% confidence interval to be [0.027°; 7.53°]. The upper extremes of these intervals are considered small enough for the navigation applications considered. Nevertheless, higher accuracy can easily be achieved by increasing the number of measurements averaged per sample.

## 18.3. Total mass

The total mass of the drone was estimated to be 249.5 ± 23.3g. The effect of these variations can results in some changes on the entire mission performance. Parameters such as the flying time, the depth of discharge of the battery and the number of drones are all affected.

First, without varying the current depth of discharge, the flying time is reduced to 9 min and some seconds, if the total weight is increased to the upper limit of 249.5 g plus the margin of 23.3 g, adding up to 272.8g. If the same number of drones are kept in the package, the mission cannot be performed in the required time. This is because exactly 58 drones are required to pollinate the greenhouse in 3 days for a mission time of 10.5 min, however for a mission of only 9 min, a total of 67 drones would be required. Even considering the extra 6 drones which would be provided in the package, 3 drones would still be required. If the number of drones per package is increased to meet the 67 drones requirement,

[1] `https://www.decawave.com/sites/default/files/resources/DW1000-Datasheet-V2.12.pdf` [Cited 24 June 2017]

the total cost goes up by 1520 € given that one extra ground station would have to be provided to accommodate all the drones.

Now if the scenario of a varying depth of discharge is considered, the flying time can be kept constant. If the mass of the drone increases to 272.8g, the depth of discharge increased from 78.5% to 89.3%. This means that the mission would still fit in the requirements, but with a severe impact of the battery lifetime. Furthermore, given the extra consumption of energy, the charging time will also increase from 15 min to 17.3 min. The latter also impacts the number of drones required, although not as much as in the previous case. The exact number of drones would increase from 58 to 61, luckily this value would still be covered by the extra drones provided in the package.

If the total mass of the drone is actually smaller, the flying time can be increased. This has an effect on the lifecycles of the motors as they would be spinning more. Indeed, if the mass of the drone is reduced to 226.2g, the flying time can be increased from 10.5 min to 12.5 min. For that increase in flying time, the lifecycle of the motors drops to 18 years.

# 19

# Post-DSE phase

The DSE is the pinnacle of the Bachelor of Aerospace Engineering program at TU Delft. As such it carries the symbolic significance of "an end" or "a conclusion". Nevertheless, the current chapter is an attempt to envision what would happen with the pollinator drone project if the effort continued past the DSE Symposium event.

First, the long-term vision for the pollinator drone technology will be presented in Section 19.1. Then the organizational development for the group is outlined in Section 19.2. It considers two possible tracks: an academic and a commercial one, allowing for continue reevaluations of whether to switch from the first to the second. In this long-term planning it was observed that the most critical phase is the one supposed to happen immediately after the end of the project, namely the prototype building and testing phase. Precisely because of its relative importance, it considered in detail in Section 19.3. Then, two important aspects for the potential future commercialization are discussed. First, the funding and marketing strategy is discussed in Section 19.4. Then, the difficulties encountered when estimating the return on the investment are outlined in Section 19.5.

## 19.1. Long-term technology vision

Currently there are alternatives to drone pollination for self-pollinating crops. The most prevalent one being the commercial bees that are readily available on the market. Indeed, at the moment bees are significantly cheaper than a system for drone pollination. However, there are some instances where bees cannot be obtained due to restrictions imposed by legislation or regulations[1], or are affected by a disease. In these cases means of mechanical pollination are used. Sometimes manual pollination is performed. The cost of manual pollination is usually higher than a drone system. Therefore, in such cases, the APIS system can immediately have market value. In other cases, however, there are other automated mechanical pollination means implemented[2]. The cost of these might be comparable or lower than the one of APIS, making for a difficult market entry. Nevertheless, APIS provides something that none of the other currently available pollination methods offers. That is the imaging capability. Flower imaging for helath monitoring and yield prediction is expected to become vital for the next generation of smart horticulture and APIS has this functionality already implemented.

The APIS pollinator drone was conceived as a proof of concept for drone pollination. Its goal is to demonstrate that it is possible to perform mechanical pollination with drones using only currently available technology. Even more, it was designed with the vision to serve as a test bed for future technology developments. As a result, the true value of APIS lies in enabling long-term developments in the field.

There are various alternatives for self-pollinating flowers, as mentioned before. But not as many for cross-pollinating. This is where another market potential for drones is believed to exist. Nevertheless, the technology development must start here, with drones for self-pollination as a first step. The APIS drones were designed with this in mind, manifested in the modularity of the payload section and the ease with which the blower can be swapped for a device for cross-pollination. As the accuracy of the sensors, image processing and control algorithms increases and the electronics shrink even further, it is expected that pollinator drones will eventually be able to pollinate via physical contact with the flowers. Moreover, it is very probable that in the (near) future the MAV community will succeed in meeting the expectations of the general public and indeed produce pollinator drones with the size of bee, something now possible only with a lot of constraints and limitations as shown by Harvard's RoboBees [96].

[1] http://www.hydroponics.com.au/issue-88-bumblebees-for-pollination-of-greenhouse-tomato-crops-in-australia [Cited 30 June 2017]

[2] http://www.weeklytimesnow.com.au/agribusiness/horticulture/automated-pollination-machine-on-trial-in-australia/news-story/5fa92217c5f562f5912f634fc4357121 [Cited 30 June 2017]

In future, we expect that pollinator drones will be able to pollinate any crop, anywhere, at any time. Again, as a first investigation effort, the current treatment was limited to tomato plants. Nevertheless, the long-term goal is, of course, to target a larger variety of crops. Moreover, even though the APIS system was designed to work in greenhouses, there is even larger demand for pollination outdoors. As mentioned before, there are other efficient means for indoor pollination, the best example being commercially available bee colonies. Considering outdoor pollination, however, the options are much more limited. Therefore, this constitutes another significant market opportunity.

The potential of the imaging and monitoring capabilities of APIS is also not to be neglected. There are already a number of successful business cases of agricultural applications of drone imagery. Some examples being Aurea Imaging, Pix4D and Bird.ai. Nevertheless, currently the focus of these applications is on the bulk of crops. However, as outlined in Horizon 2020 [97], the future of agriculture lies in giving personal attention to every plant, providing care for its own specific needs. APIS can provide not only that, but also go even one level deeper: a one-to-one interaction with every single individual flower. This ability is facilitated by the fact that a pollinator drone has to visit every single flower. For example, during a discussion with Giuliano Vitali from University of Bologna it became evident that there is a need for mapping and 3D reconstruction of individual orchard trees. That is currently impossible as agricultural drones generally fly only above the fields, and therefore cannot image flowers on the sides or on the bottom of a tree. This, however, is something that a pollinator drone can easily do as a secondary mission.

The current state of the APIS design allows for pollination and imaging of tomato flowers in the controlled environment of a greenhouse. However, using this as a starting step, the future developments are expected to allow for much more versatile platforms with a significantly larger variety in the applications. Pollinator drones will eventually become a market reality and APIS will be always remembered as the pioneer of this field.

## 19.2. Long-term organizational vision

The long term vision of the post-DSE activities is very difficult to predict as it depends on a number of internal factors, e.g. human resources, finance, knowledge, as well as on external forces like competition, market pull and the economy. Nevertheless, two main possibilities were envisioned: continuation as an academic endeavor or transformation into a commercial entity. However, before such a decision can be made, there is the most critical phase for the prospective team to pass. Namely, that is the prototype building and testing phase. The whole process described in this section is illustrated in the project design and development logic flowchart in Figure 19.1.

During the prototype building and testing phase the team has to go through the iterative process of updating the design, producing and integrating parts for the drones and the ground stations, and testing parts, components, drones and ground stations. The need for this is stipulated by the cyclic nature of solving implementation challenges. In the process, it is expected that the group could also acquire even further depth of understanding of the technology and principles behind the design, allowing them to improve and optimize the system even further. It is expected that at the end of this phase, a fully working demonstration mission could be performed. As that is an academic project, journal article publication and conference presentations are also expected. Due to the importance of this initial phase, it is given special attention in Section 19.3.

Once the prototype building and testing phase is concluded, decision has to be made of whether to continue with further academic projects or to try to commercialize the developed technology. The main criterion behind this decision is expected to be the market opportunities for such a technology. In other words, the market readiness. If the time is not deemed suitable for starting the commercialization procedure, further research into the technologies that might be able to bring APIS to the market can be investigated.

In case future research is considered, there is a main cycle of coming up with research ideas, searching for funding opportunities for these ideas and writing research proposals. For the case of MAVs, there is the additional opportunity of using a relevant competition as a platform for developing and testing some of the technology needed for the progress of APIS. Once funding for research is secured, another cycle is entered. The research cycle essentially includes planning research activities, securing the necessary resources, investigating these activities, obtaining results and then using these to adjust the planning until the point of completion. Just as most academic projects, it is expected that a publication and conference presentations will be made. In the case of a competition-driven project, participating in the competition also happens in this stage. The formal conclusion of the project follows. The experience and technology expertise established during the phase of further research serve as the basis for a new market readiness evaluation.

In case the group decides that the current moment constitutes a good market entry opportunity, a start-up company can be formed. For such a company one of the main pending issues is to find seed funding necessary to sustain their early efforts before they can start gaining revenue. The seed funding may come from university or government funds, personal or private investments, venture funds or crowdfunding. That is also the point where, slow, but important, team expansion also happens. The main goal of the start-up company will be to establish various product ideas, build prototypes and test

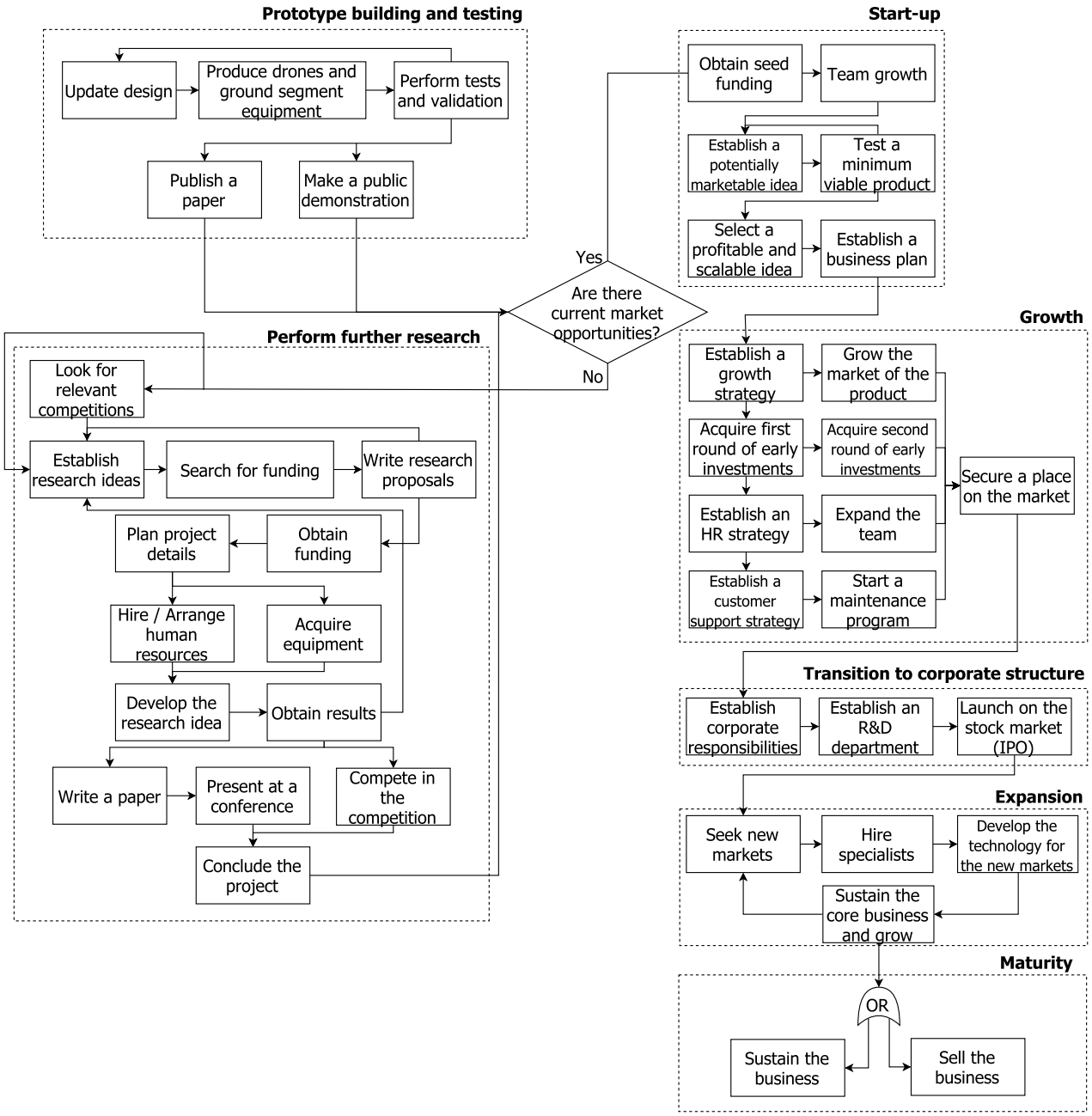


Figure 19.1: Project design and development logic

them with clients until a profitable and scalable idea is found. This is paralleled by Blank's definition of a start-up: "a temporary organization designed to search for a repeatable and scalable business model" [98]. Once that happens, they can write their vision for the future development of this idea into a business plan.

The finalizing of the business plan marks the point in which the start-up enters its growth phase. First, growth strategy has to be carefully drafted up. This is the phase where good start-ups often fail, either because they cannot scale fast enough or because they cannot keep with the market pull for scale. In order to deal with these sensitive issues, a growth strategy centered on the core technology and market has to be developed. Growth also means that there will be a tremendous need for new top tier employees. Therefore, an excellent Human Resources (HR) strategy is also needed. As APIS starts selling their product, there will be also the need for customer support and product maintenance. Having a good start with these is fundamental to retain the early adopters. Acquiring the finding necessary to grow is the pivotal point for this phase and all other activities are expected to often revolve around that. Therefore two early investment rounds have also been planned. At the end of the growth phase, it is expected that APIS will have an established market

position and brand recognition among potential future clients.

Once the company is properly established it can begin a transition to a corporate structure. That is expected to begin with redistribution of the roles and responsibilities within the team. Before this phase, the group organization structure would have been flexible to a great extent. From this point onward, however, a more rigid and well-defined positions and responsibilities are needed to prepare APIS future expansion into new markets. Such roles include executive positions with company-wide oversight such as Chief Executive Officer (CEO), Chief Technical Officer (CTO), Chief Operations Officer (COO), as well as more domain-specific positions such as Vice President (VP) of Product Development, VP of Customer Support, VP of Finance, etc. Such a corporate structure also generally requires a dedicated Research and Development (R&D) unit that is responsible for developing technology on request from the product development teams, as well as working on innovation projects that might be used as part of future products. That is also the point that is fundamental for the company to sustain the core business as it goes through this transition. Cost cutting and productivity increasing are expected to be one of the first important goals for the new executive staff. To deal with these, lean manufacturing techniques are proposed to be implemented. The transition to corporate structure is concluded with an Initial Public Offering (IPO) on the stock market.

With the IPO, the company will have acquired the necessary finance to start its expansion in new markets. An iterative process is expected to be observed, flowing from seeking new market opportunities, establishing developments teams that target these, developing the technology and starting sales. The new experience and expertise acquired in-house are to be retained by facilitating an elaborate knowledge management environment. At the same time, it would be vital for the company to sustain the core business already developed and to grow the new markets established.

At some point it is expected that the company will witness a drop in the expansion rate and market opportunities. That will presumable come due to market saturation. At this point the founders and the main shareholders would have to make the decision of whether to continue with sustaining the business, focusing on cutting costs and increasing productivity and profits, or to sell it to a third party that would be willing to take charge of it during this phase.

## 19.3. Prototype building and testing phase

One way of looking at the end of the DSE is as the end of the design phase of a bigger project. The current report can be considered the document that summarizes all the details necessary for conducting a critical design review. The Final review, as conceived in the DSE framework, is in a sense precisely that. Moreover, the Symposium that concludes this project can be considered as the Design Presentation of a bigger undertaking.

If the APIS development project indeed continues beyond the design into a manufacturing and testing phase, further activities, fundamentally different than the one undertaken by the group members so far, have to be planned. Hereby the steps needed to be taken for building the prototype of the system and testing it are outlined. Only the main activities are presented with the focus being kept on four main aspects: team organization, drones and ground segment production, testing and reporting.

The team organization requires a new structure due to the fundamentally different nature of the work in this phase. For this reason, a number of specialized roles need to be assigned to the group members. These include, among others, hardware production, software development, electronics assembly, testing, as well as communication positions.

As a demonstration of the system would require building multiple drones and possibly more than one ground stations, funding for the materials, components and production costs has to be secured before the beginning of the manufacturing phase. Moreover, a greenhouse willing to act as a partner for the demonstration case has to be found. An example for such a partner could be Wageningen university, in particular their research greenhouses.

In the case of success with the proof-of-concept, the group will investigate means to commercialize or value the technology and methods developed. This is to be done in partnership with the TU Delft Valorisation Centre. In cooperation with them the team will decide whether there is value in filing for patents or establishing a spin-off business unit.

There are two main components of the APIS pollination system: the drones and the ground segment. Both of these require specific hardware and software. While the hardware production is expected to be to a large extent linear, the software development efforts will most likely be of iterative and incremental nature. In that sense, they are expected to often include some of the testing activities in one or more points of their development iterations.

Testing is the pinnacle of the building and testing phase. During testing the true capabilities of the APIS system can be demonstrated. Moreover, by fine-tuning a number of parameters in the software, the design can be further optimized. More importantly, there are a number of subsystem parameters that can only be acquired from empirical studies, most of which have not been performed as of now. Therefore, testing and production will happen in parallel to a limited extent. Nevertheless, in this basic preliminary planning these connections are not elaborated.

The reporting of this latter phase includes also the publicity efforts of the team. It is expected that throughout the prototype building and testing phase a number of internal technical reports will have to be written. A continuous publicity

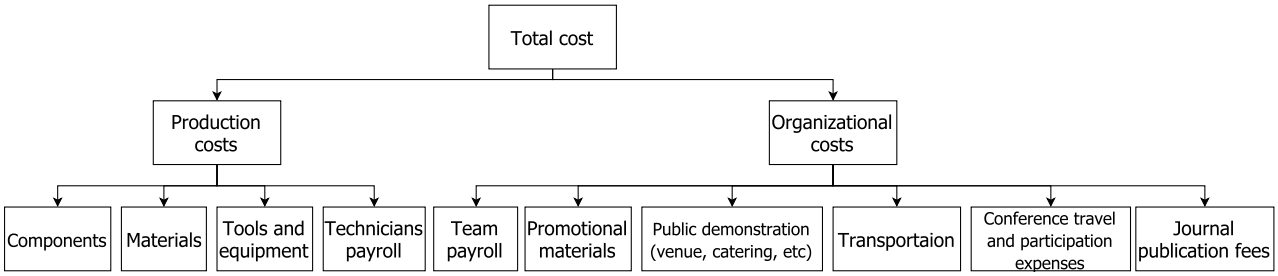


Figure 19.2: Cost breakdown structure for the prototype building and testing phase

campaign is also envisioned to be a major point of the reporting of the project. Maintaining social media profiles, as well as participation in relevant forums are examples of such publicity activities.

Moreover, during the DSE, a number of industry contacts were established. Keeping these informed about the state of the project is planned to happen regularly during the production and testing phases. The results of the project are expected to be also published in the form of a journal article and presented at several conferences. The preparations for that are planned to happen well in advance, given the typical lead times of applying to such events. Finally, a public demonstration will be held for the stakeholders from the university, industry, partners and contacts established during DSE, as well as the media.

The main activities for the prototype building and testing phase are outlined in the Gantt chart in Figure 19.3. It can also be considered as a Work Breakdown Structure for the immediate tasks after the end of DSE. The Cost Breakdown Structure for the

## 19.4. Marketing strategy

Establishing a marketing strategy comprises of three main segments. First, an environmental scan has to be performed, after which a SWOT analysis is conducted. This paves the way for the last segment which is deriving a market plan. The first two segments fall under the banner of market analysis and were dealt with in Chapter 2. The third segment will be thus elaborated in the following.

Devising a market plan starts with agreeing on the vision for the organization/company. The vision contains a main goal the organization wishes to achieve within a certain timeframe. For the case of our organization, this could be national goal or a subnational goal. If this goal is met, then the organization will benefit immensely, and this could be the stepping stone towards an successful market expansion. Stated formally, the vision of the organization is as follows:

> *The organization shall commit itself to the goal of becoming the leading supplier of pollinator drones in the Netherlands during a period of 10 years.*

With a clear vision in mind, it is now the time to analyze the competition. This step involves recognizing the competitors' strengths and weaknesses, and reflecting on these insights to improve the company's performance. There are a number of incumbents and challengers on the market for selling drones. All those have unique advantages due to their product positioning on the consumer drone market. Examples of important drone-producing companies are Parrot®, DJI®, 3D robotics®, Yuneec®, and JJRC®, to name a few. However, since the product developed is a proof-of-concept, there is not an existent product, to the awareness of the authors, on the market to compete with ours in terms of pollinating functionality. It is precisely this functionality that will be adopted as an anchor for our product positioning.

After the competitive analysis comes identifying the target segments whose needs will be fulfilled by our product. Before proceeding any further, it should be expressed pronouncedly that APIS is first and foremost intended as a product that would mitigate the crisis of a dwindling bee population. For horticulture, this is a milestone. Thus, the production of APIS benefits all species consuming fruits and vegetables. However, it can be said that the demographic that would be most interested in our product would be farmers and horticulturists as they are the ones who deal with fruit, vegetable, and flower growing. Especially in Europe, and specifically the Netherlands, a lot of funding is going into smart farming and precision farming [3].

When discussing the unique value propositions of our product, key elements should be mentioned: autonomy, ease of use, payload modularity, good price, recyclable material, and most importantly, imaging and pollinating functionalities. All in all, this set of values will benefit the target segments in that as consumers they will have an easy-to-use product

[3] `http://www.hortidaily.com/article/32439/Netherlands-Two-million-euros-for-precision-farming` [Cited 23 June 2017]

that is affordable and will autonomously pollinate and monitor their plants.

As for the pricing of the product, this will be done by first assessing the value of our product in comparison to other products on the market. Since this product will be the first of its kind, this will need to be developed when similar products appear on the market. The initial selling price for APIS can be very close to overall cost. Upon gaining value and reputability on the market, the price may be alterred.

It is now the turn for establishing concrete business objectives for the company. One such goal could be the production and selling the first 100 drones within a timeframe of 2 years namely to customers in the Netherlands. One strategy to achieve that would be through a partnership with DutchGreenhouses™ as it represents a partnership of the main greenhouse companies in the Netherlands[4]. Thus, it is through this partnership that will make reaching out to customers easier. Moreover, these partnerships with other organizations will allow the company to make a good market entrance. As an example, a partnership with a known drone company such as DJI™ can be a good way to ensure the expertise of that company in the production of drones can be leveraged. Another example of a good partnership would be with Pix4d, whose expertise in software for generation of 2D and 3D maps can be benefited from.

Making use of the media to help achieve this business objective, or in other words, marketing collateral, will be made use of. This could be in the form of establishing a website, documenting customer testimonials, and making advertisements. Besides marketing collateral, other initiatives the company undertakes to promote its product could be creating events to showcase the features and capabilities of the produced pollinator drones, or participating in product evaluations and reviews. Moreover, promotional offers should be considered that would attract the customers to get the product. The APIS can be available for free trial for a period of 2 weeks for example. Moreover, offers through services for example can turn the leads into customers.

One final aspect to consider as part of the marketing plan is the distribution plan. The product can be sold directly via the company's established website, or indirectly by distributing the product to partners which carry out the selling.

## 19.5. Return on investment

The return on investment (ROI) is a very important metric for the assessment of the efficacy of the marketing plan developed. This metric is an indication of the value received when compared to the capital invested. The analysis needed to obtain the ROI includes establishing a number of aspects such as achievable market share, market price and volume of the product as well as development, production, and direct operational costs of the product.

Conducting such an analysis for APIS goes amiss on several levels. First, our product could belong to several markets: either the pollinator drone market, the imaging drones market, or more broadly, the market of pollinators (the bee market, as an example). Of these, the first is nonexistent yet. As a result, it is not possible to carry out a ROI for our product in this market. As for the latter two, our product does not completely fit in either. Though APIS is an imaging system, it also has the additional aspect of also being a pollination system, and this is an indispensable part of the positioning of APIS on the market. Hence, performing a ROI for APIS on this market might not entirely reflect the standing of APIS on its intended market.

Another dimension of the problem arises in estimating the costs: parametric cost estimation may not be possible to establish. Our product is a proof of concept; thus, there is no reference data with which to make the estimation. However, use can be made of analogous cost estimation, whereby cost data for MAVs or more generally UAVs can be adapted for our application. A parametric model for UAVs is dealt with in [99] in which cost estimation relationships (CERs) are presented for UAVs. However, even in this source, the authors make a disclaimer about the CER they established between the cost and the endurance, stating that it was not possible to validate it due to the limited data that was present at the time of writing the article. Thus, even analogous cost estimation appears to be infeasible at this stage.

However, it is foreseen that performing such an analysis will need to be done in the near future. A need for a pollinator drone market might arise. This is clear from the market analysis that was performed in Chapter 2 which proves that the traditional ways of pollination are becoming increasingly expensive.

[4] `https://dutchgreenhouses.com/about` [Cited 23 June 2017]

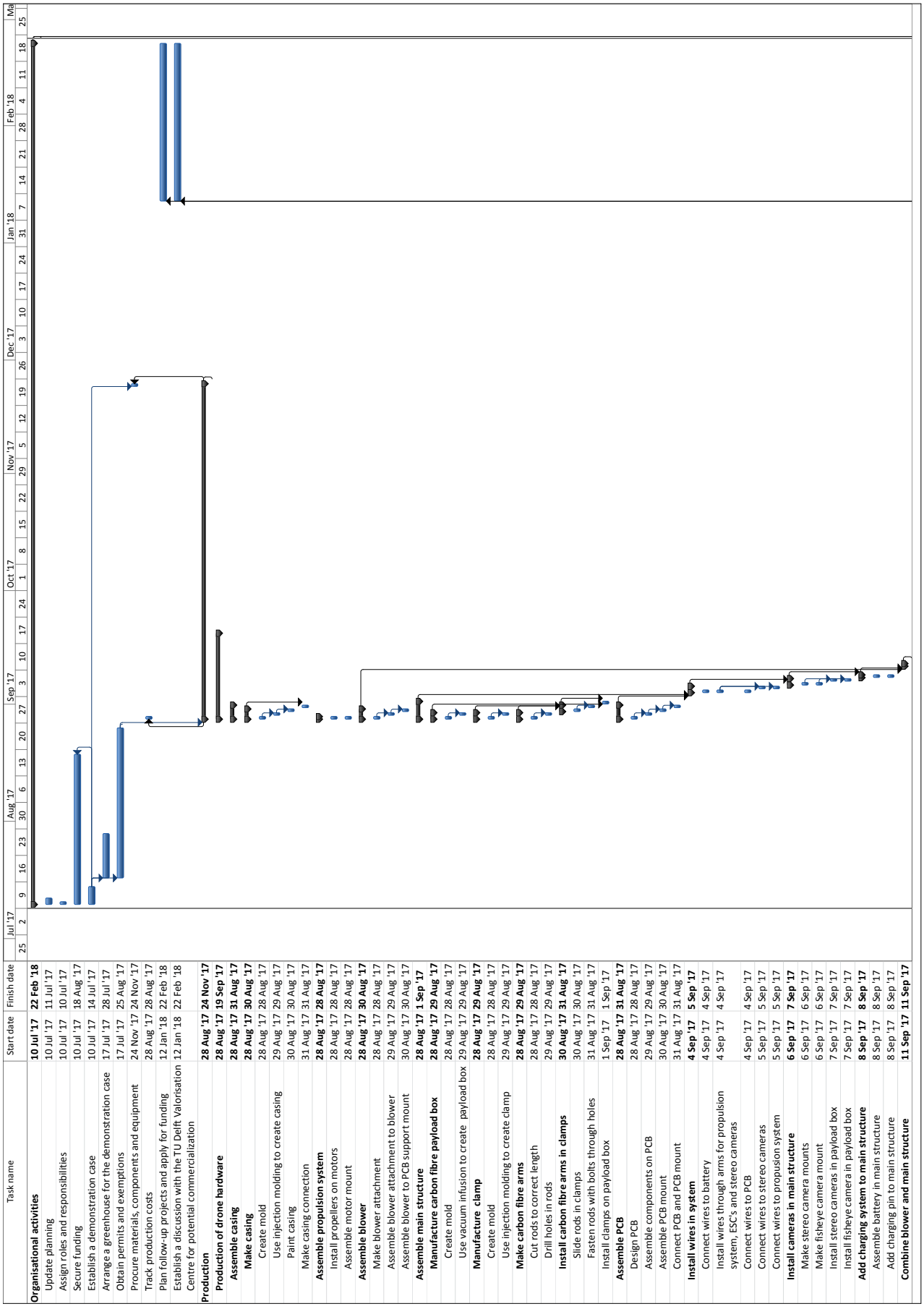


Figure 19.3: Gantt chart for the prototype building and testing phase

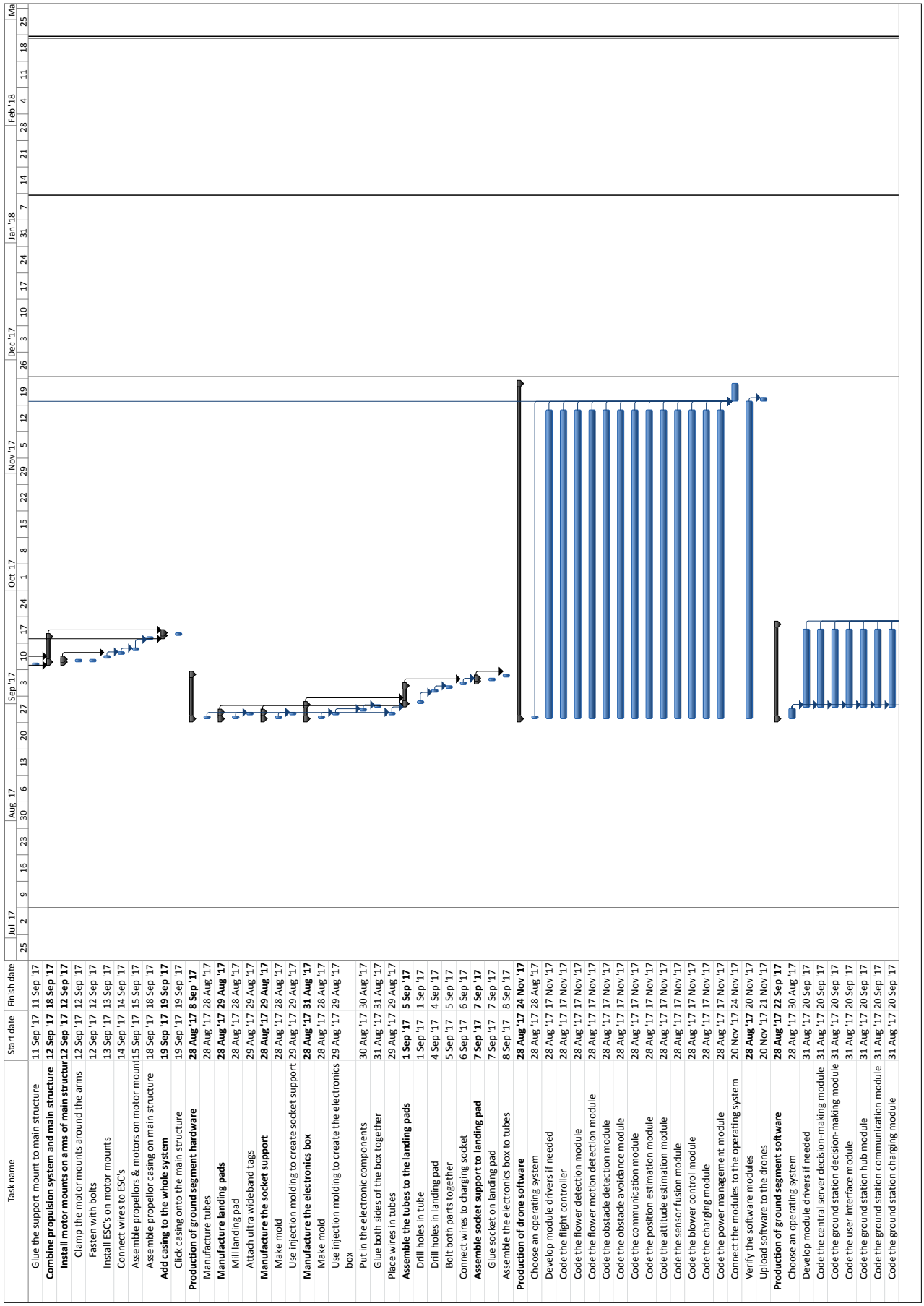


Figure 19.3: Gantt chart for the prototype building and testing phase (Continued)

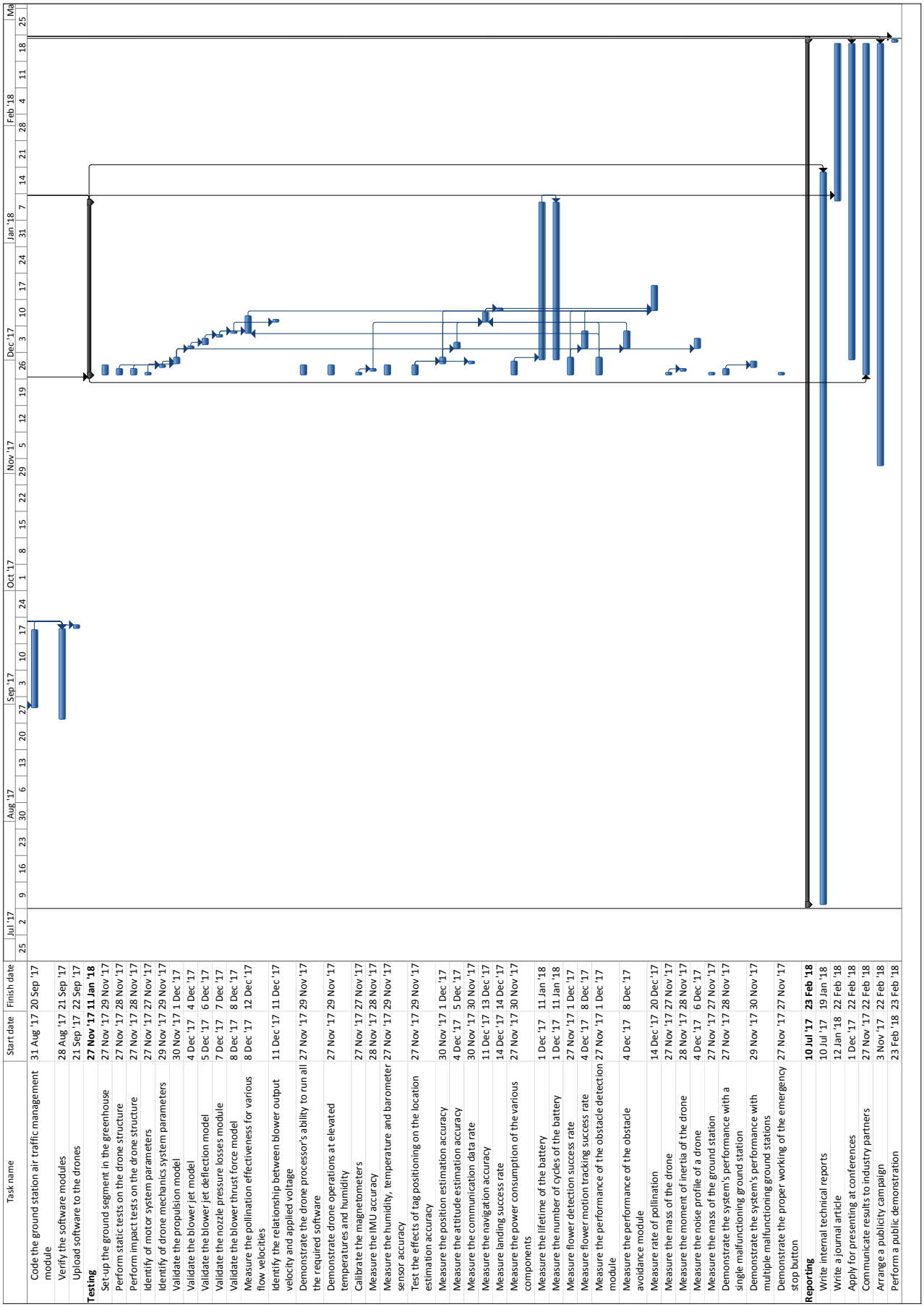


Figure 19.3: Gantt chart for the prototype building and testing phase (Continued)

# 20

# Recommendations and future opportunities

Due to the limitations of the DSE there remain a number of future developments that can still be performed. This chapter will describe the steps that have to be taken after this design phase in order to optimize the design.

## 20.1. Recommendations

To start with, the cameras can be used to collect more data. The benefits of doing this are tantamount, as having more data yields performing yield analytics, and also automatically collecting data for control experiments. That is, the detection of the fruit/vegetable will automate the collection of data pertaining to the crops which will facilitate making studies on effect of certain control conditions in the greenhouse, such as the study on the effect of irrigation depth on yield that was performed in [100]. In either case, it becomes clear that taking images of tomatoes as they grow will be important. One possibility to do that is to use the side camera for detecting and taking images of the tomatoes. There exists an algorithm which is presented in [101] and can be used.
Moreover, for added robustness in the detection of flowers, a pre-trained classifier can be used such as a support vector machine. The training can be done on a large set of tomato flower images and by extracting suitable texture features. This classifier will serve to reduce the false detection rate.

In the current design configuration, it was decided to let the MAV charge by landing the pin attached to the MAV inside one of the sockets present in the ground station. For future designs it is recommended to switch the pin and socket around. This is because the pin that currently sticks out of the drone will create some problems. For example, when the drone will fall due to depletion of energy it can fall directly on the pin which might pierce the battery.

At this point of the final design the casing of the drone has not yet been optimized. For now, the casing has been added to give protection to the electronics, battery and payload. It has not been taken into account that things can get stuck within the casing. For example, wires can get between the propeller casing and the casing of the payload. In order to prevent this, the casing should have no sharp corners and no cavities where wires may invade the structure.

Another thing that can be improved in the future is the methods to design a good control system for the MAVs. To be able to obtain the motor coefficients required for the model used in the design, motor test data is required, which was not available now. In the future, this information would allow obtaining coefficients corresponding to our drone which are needed for the model, after which the tunes can be gained using the Ziegler-Nichols method or the Tyreus-Luyben method.

Until now, the blower has been designed by using a CFD analysis. However, the actual system has only been slightly tested on tomato flowers. Therefore, the next step that has to be taken is to validate the CFD model with a more rigorous methodology. After that, the actual pollination method has to be validated by doing more and better tests on tomato plants using the exact APIS' blower. In the end the drone including the blower should be tested. When this system has been proven the blower can be replaced by another payload, which will allow for other means of shaking the flower or for cross-pollination. This could be a shaker or a stick with gel on it.

In addition to this, it is recommended that extensive lifetime tests are performed on the battery. Especially given that the electrodes are based on a novel material such as graphene, to properly ensure quality all along the mission development, tests on relevant environments are advised.

Some optimization can also be performed on the ground station. With improved control, better precision landing can be established. As a result, the landing pads can be made smaller. Moreover, air traffic control can improved. It could be made more versatile and dynamic to allow for multiple drones to take-off and land at the same time.

In addition to this, the assigned duration for the MAV to properly point the blower to the cluster of flowers should be tested more extensively. It is suspected that 4 seconds might be an overdesign, thus tests to reliably find a more appropriate duration can help to further boost APIS efficiency.

## 20.2. Expected future technological developments

At the current pace that technology is advancing, a wide range of opportunities opens. These opportunities are hereby listed and will set a ground onto which APIS can become more efficient, affordable and safe.

During the design of this MAV, the battery has proven to be a subsystem of limited capabilities when it comes to charging rates, lifetime or weight. Nonetheless, in the coming future, technologies to push the storage of electrical energy more efficiently, for longer and with faster charging times are on the verge of appearing. In fact, the lithium-metal technology developed at MIT already has its own start-up (SolidEnergySystems) and is a matter of time that it becomes widely available. In fact, this technology enables almost twice the energy density of the current Li-Po. Following this trend, this battery would increase the flying time up to 25 min, for which only 30 drones and 4 ground stations are projected to be needed.

The UWB navigation is a relatively new technology. That is why it is expected that the accuracy of the ranging estimates and the data link throughput will further increase in the coming years. As was noted before, the UWB localization with broadcasting technology, as proposed here, bears very close resemblance to the problem of state estimation with GNSS. Therefore, the applicability to UWB localization of technologies commonly applied for GNSS, such as carrier phase shift measurements can be further investigated. Moreover, to the best of the group's knowledge, no previous use of UWB for attitude determination has been made. This poses challenges specific to the attitude determination, in particular the possible ranging estimation error correlation. As this is a promising research direction, such further studies are expected to be performed, leading to much more accurate and reliable navigation and localization techniques.

A well-known law that has guided computer development over the past years, is the Moore's law. This states that the number of transistors in an integrated circuit doubles every two years. Although the pace is expected to slow down, development in this field is still going at an incredible speed. [1]. Over the coming years, research in small customer electronics will spur miniaturization and computing performance. Micro air vehicle development will also benefit from this. Navigation, obstacle detection and image processing, in fact, everything that needs to be computed or processed, can be done faster, more reliable and more accurate.

With the advance on miniaturization and optical technology, several more sensors could fit into APIS in the near future. The use of infrared and near-infrared vision to monitor chlorophyll levels on crops is already a purchasable reality[2]. However, their weight is prohibitive for MAV, thus it is expected that in the coming years, these sensors can also be a part of APIS when the weight is reduced. Together with such a sensor, a $CO_2/O2$ measure could be mounted on board too, allowing for more accurate model of the state of the greenhouse.

[1] https://www.nytimes.com/2015/09/27/technology/smaller-faster-cheaper-over-the-future-of-computer-chips.html[Cited 28 June 2017]

[2] https://www.micasense.com/rededge/[Accessed 25 June 2017]

# 21

# Conclusion

In this final report, the selected concept from the midterm phase has been designed in depth. The ultimate goal of the design was to make a proof-of-concept for a pollinating autonomous system. This goal was refined to pollinating a tomato greenhouse of 4 hectares in 3 days. The outcome of this design is a micro air vehicle named APIS, which stands for Autonomous Pollination and Imaging System. The system is composed of a set of 64 autonomous APIS and 8 ground stations at a final cost of €30,000 .

Each APIS is based on a 28.3x27.8 cm H-configuration with four propellers of 5" (approximately 12 cm). Driven by 4 DC-motors, they are able to deliver a combined 520 g of thrust. This thrust is enough to efficiently lift the 249.5 g MAV. The APIS are equipped with a front-facing pair of stereo cameras (1616x1216 pix) for obstacle detection. A pair of laser rangers top and bottom of the MAV complement this task. To detect the flowers, a fish eye high-res (2592x1944 pix) camera is mounted onto the side of the MAV. Right below of it, an air nozzle connected to an inertial fan produces an airflow with an exit velocity of 10 m/s to pollinate. The inertial fan is mounted on top of the MAV and it also cools down the electronics while blowing. To find its absolute location and heading, the MAV is equipped with a multi-function barometer and two ultra wide band tags. The UWB tags also serve as data transfer channels for location and imaging downloading. To complement this, a flight controller (ATMega 328) seats on new generation processor Qualcomm Snapdragon 801. In fact, the Snapdragon 801 also runs stereo matching, image detection and all the communication through the UWB. Also, it comes with a 32 GB flash memory and 2 GB of RAM for this purpose. The entire MAV is powered from a state-of-the-art 2S1P 1500 mAh graphene Li-Po battery. In addition, the battery is charged through a pin connection based on mobile phone technology is located below of the MAV and runs at a depth of discharge of 78.5%. Each APIS has a total material cost of 394.20€.

The charging takes place on the groundstations, which are equipped with hexagonal slots where the charging pin slides in. These groundstations can accommodate 8 drones and are placed hanging from the greenhouse frames 0.5 meters above the top of the crop. Each groundstation also serves the purpose of UWB anchor and MAV master. The groundstation comes with a Beaglebone board which takes care of the task division and UWB communication. Additionally, a common server and hub are added to coordinate all the groundstations and store data for the user interface. The greenhouse is pollinated every three days for 12 hours. For this, the MAV will fly for 10.5 min and charge for 15 min. In fact, the MAVs will be assigned rows and will pollinate symmetric lengths on both sides of the row before returning to charge. It was also found that after a period of 1 month, the batteries will have to be replaced.

Despite the fact that quadcopters are not an original idea of this group, the proposed concept bears several novel ideas. The general framework of drone-greenhouse symbiosis and interaction can be considered central for the development of this project. Autonomous charging through a rigid pin is another example. Furthermore, the UWB protocol proposed and UWB absolute heading estimation are techniques that promise high update rate position and attitude estimations. Pollinating tomatoes by inducing an airflow from a distance in the way presented here is also a novelty. Besides that, hanging groundstations to make easier use of the greenhouse and using the blower to also cool the electronics were also new ideas which improved this design.

During the design of APIS, more practical implications were also analyzed. The reliability, availability, maintainability and safety of the design were considered. Moreover, the risks associated with each subsystem and the full-scale MAV were found and a mitigation action was proposed. Some of these, impacted the sustainability of the design in a negative way. Consequently, to account for this, a sustainability development strategy was composed. Following this strategy, power consumption, noise or end-of-life procedures were duly engineered. Following it, sensitivity analysis were performed for key subsystems such as the battery and localization. Furthermore, with the eyes on a bright future, a post-DSE schedule is given to follow for a potential product development. Lastly, a set of recommendations is given based on the current design and the expected future technological developments.

# Bibliography


[1] Velthuis, H. H. and Van Doorn, A., "A century of advances in bumblebee domestication and the economic and environmental aspects of its commercialization for pollination," *Apidologie*, Vol. 37, No. 4, 2006, pp. 421.

[2] James, R. and Pitts-Singer, T. L., *Bee pollination in agricultural ecosystems*, Oxford University Press, 2008.

[3] Monsanto, "US Beekeeping industry," 2016.

[4] Potts, S. G., Biesmeijer, J. C., Kremen, C., Neumann, P., Schweiger, O., and Kunin, W. E., "Global pollinator declines: trends, impacts and drivers," *Trends in ecology & evolution*, Vol. 25, No. 6, 2010, pp. 345–353.

[5] Aizen, M. A., Garibaldi, L. A., Cunningham, S. A., and Klein, A. M., "Long-term global trends in crop yield and production reveal no current pollination shortage but increasing pollinator dependency," *Current Biology*, Vol. 18, No. 20, 2008, pp. 1572–1575.

[6] Gallai, N., Salles, J.-M., Settele, J., and Vaissière, B. E., "Economic valuation of the vulnerability of world agriculture confronted with pollinator decline," *Ecological economics*, Vol. 68, No. 3, 2009, pp. 810–821.

[7] Rabobank, "Glasgroenteteelt, Rabobank Cijfers & Trends," 2016.

[8] Fiix, "Reactive Maintenance," 2017.

[9] DSE Team S9, "Midterm report: Greenhouse pollinator drone," Tech. rep., Delft University of Technology, 2017.

[10] Short, T. and Bauerle, W., "influence of pollinating techniques on tomato yields and quality," *Ohio Agr Res Develop Center Res Sum*, 1972.

[11] Hanna, H., "Air blowers are less effective pollinators of greenhouse tomatoes than electric vibrators but cost less to operate," *HortTechnology*, Vol. 14, No. 1, 2004, pp. 104–107.

[12] Schlichting, H., "Laminare strahlausbreitung," *ZAMM-Journal of Applied Mathematics and Mechanics/Zeitschrift für Angewandte Mathematik und Mechanik*, Vol. 13, No. 4, 1933, pp. 260–263, In German.

[13] Bickley, W., "LXXIII. The plane jet," *The London, Edinburgh, and Dublin Philosophical Magazine and Journal of Science*, Vol. 23, No. 156, 1937, pp. 727–731.

[14] Landau, L. D. and Lifshitz, E. M., "Fluid mechanics," 1987.

[15] Squire, H., "The round laminar jet," *The Quarterly Journal of Mechanics and Applied Mathematics*, Vol. 4, No. 3, 1951, pp. 321–329.

[16] White, F. M. and Corfield, I., *Viscous fluid flow*, Vol. 3, McGraw-Hill New York, 2006.

[17] Pope, S., *Turbulent Flows*, Cambridge University Press, 2000.

[18] Abramovich, G. N., Girshovich, T., Krasheninnikov, S. I., Sekundov, A., and Smirnova, I., "The theory of turbulent jets," *Moscow Izdatel Nauka*, 1984.

[19] Bruschi, G., Nishioka, T., Tsang, K., and Wang, R., "Drag coefficient of a cylinder," 2003.

[20] Chapman, R. F., *The insects: structure and function*, Cambridge university press, 1998.

[21] Zheng, Z. and Zhang, N., "Frequency effects on lift and drag for flow past an oscillating cylinder," *Journal of Fluids and Structures*, Vol. 24, No. 3, 2008, pp. 382–399.

[22] Blevins, R., *Flow-induced vibration*, Van Nostrand Reinhold Co., 1977.

[23] Zhang, X., Guo, Q., Xu, Y., Li, P., Chen, C., and Wu, S., "Mechanical Testing of Tomato Plant Stem in Relation to Structural Composition," *Agricultural Research*, Vol. 5, No. 3, 2016, pp. 236–245.

[24] Escobar, J. A., "Computational Study of the Wake of a Quadcopter Propeller in Hover," 2017.

[25] Landgrebe, A. J., "The wake geometry of a hovering helicopter rotor and its influence on rotor performance," *Journal of the American Helicopter Society*, Vol. 17, No. 4, 1972, pp. 3–15.

[26] Inc., D. E., "DC Blower Datasheet," 2005, http://www.delta-fan.com/Download/Spec/BFB0512VHD-F00.pdf, accessed on 12.06.2017.

[27] Torres, G. E. and Mueller, T. J., "Low aspect ratio aerodynamics at low Reynolds numbers," *AIAA journal*, Vol. 42, No. 5, 2004, pp. 865–873.

[28] Ortiz, X., Rival, D., and Wood, D., "Forces and moments on flat plates of small aspect ratio with application to pv wind loads and small wind turbine blades," *Energies*, Vol. 8, No. 4, 2015, pp. 2438–2453.

[29] Kunz, P. J., *Aerodynamics and design for ultra-low Reynolds number flight*, Ph.D. thesis, Stanford University, 2003.

[30] Pawlowski, A., Guzman, J. L., Rodríguez, F., Berenguel, M., Sánchez, J., and Dormido, S., "Simulation of greenhouse climate monitoring and control with wireless sensor network and event-based control," *Sensors*, Vol. 9, No. 1, 2009, pp. 232–252.

[31] Roldán, J. J., Joossen, G., Sanz, D., del Cerro, J., and Barrientos, A., "Mini-UAV based sensory system for measuring environmental variables in greenhouses," *Sensors*, Vol. 15, No. 2, 2015, pp. 3334–3350.

[32] Svalastog, M. S., *Indoor Positioning-Technologies, Services and Architectures*, Master's thesis, 2007.

[33] Hatami, A. and Pahlavan, K., "Performance comparison of RSS and TOA indoor geolocation based on UWB measurement of channel characteristics," *Personal, Indoor and Mobile Radio Communications, 2006 IEEE 17th International Symposium on*, IEEE, 2006, pp. 1–6.

[34] Alarifi, A., Al-Salman, A., Alsaleh, M., Alnafessah, A., Al-Hadhrami, S., Al-Ammar, M. A., and Al-Khalifa, H. S., "Ultra wideband indoor positioning technologies: Analysis and recent advances," *Sensors*, Vol. 16, No. 5, 2016, pp. 707.

[35] Welch, G. and Bishop, G., "An introduction to the Kalman filter," 1995.

[36] Karapistoli, E., Pavlidou, F.-N., Gragopoulos, I., and Tsetsinas, I., "An overview of the IEEE 802.15. 4a standard," *IEEE Communications Magazine*, Vol. 48, No. 1, 2010.

[37] Misra, P. and Enge, P., *Global Positioning System: Signals, Measurements, and Performance*, Ganga-Jamuna Press, 2011.

[38] Montenbruck, O. and Gill, E., *Satellite Orbits: Models, Methods, and Applications*, Physics and astronomy online library, Springer Berlin Heidelberg, 2000.

[39] McElhinny, M. and McFadden, P. L., *The magnetic field of the earth: paleomagnetism, the core, and the deep mantle*, Vol. 63, Academic Press, 1998.

[40] Lightsey, E. G., Cohen, C. E., Feess, W. A., and Parkinson, B. W., "Analysis of spacecraft attitude measurements using onboard GPS," *Advances in the Astronautical Sciences*, Vol. 86, 1994, pp. 521–532.

[41] Floreano, D., Zufferey, J.-C., Srinivasan, M. V., and Ellington, C., *Flying insects and robots*, Springer, 2010.

[42] Lee, T.-J., Yi, D.-H., Cho, D.-I., et al., "A Monocular Vision Sensor-Based Obstacle Detection Algorithm for Autonomous Robots," *Sensors*, Vol. 16, No. 3, 2016, pp. 311.

[43] Sagar, J. and Visser, A., "Obstacle avoidance by combining background subtraction, optical flow and proximity estimation," *IMAV 2014:*

*International Micro Air Vehicle Conference and Competition 2014, Delft, The Netherlands, August 12-15, 2014*, Delft University of Technology, 2014.

[44] Achtelik, M. W., Lynen, S., Weiss, S., Kneip, L., Chli, M., and Siegwart, R., "Visual-inertial SLAM for a small helicopter in large outdoor environments," *Intelligent Robots and Systems (IROS), 2012 IEEE/RSJ International Conference on*, IEEE, 2012, pp. 2651–2652.

[45] Tijmons, S., de Croon, G. C., Remes, B. D., De Wagter, C., and Mulder, M., "Obstacle avoidance strategy using onboard stereo vision on a flapping wing mav," *IEEE Transactions on Robotics*, 2017.

[46] Serrata, A. A. J., Yang, S., and Li, R., "An intelligible implementation of FastSLAM2. 0 on a low-power embedded architecture," *EURASIP Journal on Embedded Systems*, Vol. 2017, No. 1, 2017, pp. 27.

[47] Scharstein, D., Szeliski, R., and Zabih, R., "A taxonomy and evaluation of dense two-frame stereo correspondence algorithms," *Stereo and Multi-Baseline Vision, 2001.(SMBV 2001). Proceedings. IEEE Workshop on*, IEEE, 2001, pp. 131–140.

[48] Oleynikova, H., Honegger, D., and Pollefeys, M., "Reactive avoidance using embedded stereo vision for MAV flight," *Robotics and Automation (ICRA), 2015 IEEE International Conference on*, IEEE, 2015, pp. 50–56.

[49] McGuire, K., de Croon, G., De Wagter, C., Tuyls, K., and Kappen, H., "Efficient Optical flow and Stereo Vision for Velocity Estimation and Obstacle Avoidance on an Autonomous Pocket Drone," *IEEE Robotics and Automation Letters*, Vol. 2, No. 2, 2017, pp. 1070–1076.

[50] LaValle, S. M., "Rapidly-exploring random trees: A new tool for path planning," 1998.

[51] Yao, J., Lin, C., Xie, X., Wang, A. J., and Hung, C.-C., "Path planning for virtual human motion using improved A* star algorithm," *Information Technology: New Generations (ITNG), 2010 Seventh International Conference on*, IEEE, 2010, pp. 1154–1158.

[52] Hrabar, S., "3D path planning and stereo-based obstacle avoidance for rotorcraft UAVs," *Intelligent Robots and Systems, 2008. IROS 2008. IEEE/RSJ International Conference on*, IEEE, 2008, pp. 807–814.

[53] Oppenheim, D., Edan, Y., and Shani, G., "Detecting Tomato Flowers in Greenhouses Using Computer Vision," *World Academy of Science, Engineering and Technology, International Journal of Computer, Electrical, Automation, Control and Information Engineering*, Vol. 11, No. 1, 2017, pp. 104–109.

[54] Fleyeh, H., "Color detection and segmentation for road and traffic signs," *Cybernetics and Intelligent Systems, 2004 IEEE Conference on*, Vol. 2, IEEE, 2004, pp. 809–814.

[55] Bascle, B., Bernier, O., and Lemaire, V., "Illumination-invariant color image correction," *Lecture notes in computer science*, Vol. 4153, 2006, pp. 359.

[56] Yilmaz, A., Javed, O., and Shah, M., "Object tracking: A survey," *Acm computing surveys (CSUR)*, Vol. 38, No. 4, 2006, pp. 13.

[57] Barry, A. J., Oleynikova, H., Honegger, D., Pollefeys, M., and Tedrake, R., "Fast Onboard Stereo Vision for UAVs," 2015.

[58] Fernandez, A., "Basic structural dynamics in multicopters," Tech. rep., Autoquad, 2014.

[59] Kuchnicki, S., "Simple Vibration Problems with MATLAB," December 2009.

[60] Darlow, M. and Zorzi, E., "Mechanical design handbook for elastomers," 1986.

[61] Phang, S. K., Li, K., Chen, B. M., and Lee, T. H., "Systematic Design Methodology and Construction of Micro Aerial Quadrotor Vehicles," *Handbook of Unmanned Aerial Vehicles*, Springer, 2015, pp. 181–206.

[62] Balas, C., "Modelling and linear control of a quadrotor," *Cranfield University*, 2007.

[63] Hoffmann, G., Rajnarayan, D. G., Waslander, S. L., Dostal, D., Jang, J. S., and Tomlin, C. J., "The Stanford testbed of autonomous rotorcraft for multi agent control (STARMAC)," *Digital Avionics Systems Conference, 2004. DASC 04. The 23rd*, Vol. 2, IEEE, 2004, pp. 12–E.

[64] Valavanis, K. P. and Vachtsevanos, G. J., *Handbook of unmanned aerial vehicles*, Springer Publishing Company, Incorporated, 2014.

[65] Raptis, I. A., Valavanis, K. P., and Moreno, W. A., "A novel nonlinear backstepping controller design for helicopters using the rotation matrix," *IEEE Transactions on Control Systems Technology*, Vol. 19, No. 2, 2011, pp. 465–473.

[66] David, Drexel University for Primary Industries, "Quad-Sim," `https://nl.mathworks.com/matlabcentral/fileexchange/48053-quad-sim`, 2016, Online; accessed 15 June 2017.

[67] Qualcomm Technologies, Inc., "PMM8920 Power Management Module Device Specification," 2016.

[68] of America: Department of Defense, U. S., *Military Handbook: Reliability Prediction of Electronic Equipment: MIL-HDBK-217F: 2 December 1991*, Department of defense, 1991.

[69] Williard, N., He, W., Osterman, M., and Pecht, M., "Reliability and failure analysis of Lithium Ion batteries for electronic systems," *Electronic Packaging Technology and High Density Packaging (ICEPT-HDP), 2012 13th International Conference on*, IEEE, 2012, pp. 1051–1055.

[70] Bouman, G. and van Hoorn, M., "Design and Production of composite laminates," Tech. rep., Delft University of Technology, 2016.

[71] Malone, M. and Moses, K., "Development of Risk Assessment Matrix for NASA Engineering and Safety Center (NESC)," *Project Management Challenge*, 2005.

[72] Wallace, J. and Hobbs, P., *Atmospheric Science: An Introductory Survey*, International Geophysics, Elsevier Science, 2006.

[73] Lawrence, M. G., "The relationship between relative humidity and the dewpoint temperature in moist air: A simple conversion and applications," *Bulletin of the American Meteorological Society*, Vol. 86, No. 2, 2005, pp. 225–233.

[74] Mulder, K., *Sustainable development for engineers: A handbook and resource guide*, Greenleaf Publishing, 2006.

[75] Unwin, J., Coldwell, M. R., Keen, C., and McAlinden, J. J., "Airborne emissions of carcinogens and respiratory sensitizers during thermal processing of plastics," *Annals of Occupational Hygiene*, Vol. 57, No. 3, 2012, pp. 399–406.

[76] Das, S., "Life cycle assessment of carbon fiber-reinforced polymer composites," *The International Journal of Life Cycle Assessment*, Vol. 16, No. 3, 2011, pp. 268–282.

[77] Kang, D. H. P., Chen, M., and Ogunseitan, O. A., "Potential environmental and human health impacts of rechargeable lithium batteries in electronic waste," *Environmental science & technology*, Vol. 47, No. 10, 2013, pp. 5495–5503.

[78] Commission of the European Communities, "Commission Regulation implementing Directive 2005/32/EC of the European Parliament and of the Council with regard to ecodesign requirements for electric motors," Tech. rep., European Union, 2009.

[79] Xiang, D., Mou, P., Wang, J., Duan, G., and Zhang, H. C., "Printed circuit board recycling process and its environmental impact assessment," *The International Journal of Advanced Manufacturing Technology*, Vol. 34, No. 9, 2007, pp. 1030–1036.

[80] Li, J., Shrivastava, P., Gao, Z., and Zhang, H.-C., "Printed circuit board recycling: a state-of-the-art survey," *IEEE transactions on electronics packaging manufacturing*, Vol. 27, No. 1, 2004, pp. 33–42.

[81] Thiriez, A. and Gutowski, T., "An environmental analysis of injection molding," *Electronics and the Environment, 2006. Proceedings of the 2006 IEEE International Symposium on*, IEEE, 2006, pp. 195–200.

[82] International Energy Agency, "Energy Policies of IEA Countries: The Netherlands," Tech. rep., International Energy Agency, 2014.

[83] Van der Velden, N. and Smit, P., *Energiemonitor van de Nederlandse glastuinbouw 2015*, Wageningen Economic Research, 2016.

[84] IEC, "61672: 2003: Electroacoustics–Sound Level Meters," 2003, Standard, IEC.

[85] Government of the Netherlands, "The Working Conditions Decree," 2006, Text amended up to September 1, 2016. Translation in English

provided by the Netherlands Focal Point for Safety and Health at Work.

[86] Kloet, N., Watkins, S., and Clothier, R., "Acoustic signature measurement of small multi-rotor unmanned aircraft systems," *International Journal of Micro Air Vehicles*, Vol. 9, No. 1, 2017, pp. 3–14.

[87] Sinibaldi, G. and Marino, L., "Experimental analysis on the noise of propellers for small UAV," *Applied Acoustics*, Vol. 74, No. 1, 2013, pp. 79–88.

[88] Intaratep, N., Alexander, W. N., Devenport, W. J., Grace, S. M., and Dropkin, A., "Experimental Study of Quadcopter Acoustics and Performance at Static Thrust Conditions," *22nd AIAA/CEAS Aeroacoustics Conference*, 2016, p. 2873.

[89] Aylor, D., "Noise reduction by vegetation and ground," *The Journal of the Acoustical Society of America*, Vol. 51, No. 1B, 1972, pp. 197–205.

[90] Bullen, R. and Fricke, F., "Sound propagation through vegetation," *Journal of sound and Vibration*, Vol. 80, No. 1, 1982, pp. 11–23.

[91] Martínez-Sala, R., Rubio, C., García-Raffi, L. M., Sánchez-Pérez, J. V., Sánchez-Pérez, E. A., and Llinares, J., "Control of noise by trees arranged like sonic crystals," *Journal of sound and vibration*, Vol. 291, No. 1, 2006, pp. 100–106.

[92] Lu, Z., Debiasi, M., and Khoo, B. C., "Acoustic characteristics of a multi-rotor MAV and its noise reduction technology," *INTER-NOISE and NOISE-CON Congress and Conference Proceedings*, Vol. 253, Institute of Noise Control Engineering, 2016, pp. 393–403.

[93] Leslie, A., Wong, K. C., and Auld, D., "Broadband noise reduction on a mini-UAV propeller," *14th AIAA/CEAS Aeroacoustics Conference (29th AIAA Aeroacoustics Conference)*, 2008, p. 3069.

[94] Bernardes, A., Espinosa, D. C. R., and Tenório, J. S., "Recycling of batteries: a review of current processes and technologies," *Journal of Power Sources*, Vol. 130, No. 1, 2004, pp. 291–298.

[95] Opara, L. U., "Traceability in agriculture and food supply chain: a review of basic concepts, technological implications, and future prospects," *Journal of Food Agriculture and Environment*, Vol. 1, 2003, pp. 101–106.

[96] Wood, R., Nagpal, R., and Wei, G.-Y., "Flight of the Robobees," *Scientific American*, Vol. 308, No. 3, 2013, pp. 60–65.

[97] European Commission, "Horizon 2020: Work Programme 2016–2017. 9. Food security, sustainable agriculture and forestry, marine and maritime and inland water research and the bioeconomy," 2017.

[98] Blank, S. and Dorf, B., *The Startup Owner's Manual: The Step-by-step Guide for Building a Great Company*, K&S Ranch, Incorporated, 2012.

[99] Valerdi, R., Merrill, J., and Maloney, P., "Cost metrics for unmanned aerial vehicles," *AIAA 16th Lighter-Than-Air Systems Technology Conference and Balloon Systems Conference*, 2005.

[100] Monte, J. A., Carvalho, D. F. d., Medici, L. O., da Silva, L. D., and Pimentel, C., "Growth analysis and yield of tomato crop under different irrigation depths," *Revista Brasileira de Engenharia Agrícola e Ambiental*, Vol. 17, No. 9, 2013, pp. 926–931.

[101] Schillaci, G., Pennisi, A., Franco, F., and Longo, D., "Detecting tomato crops in greenhouses using a vision based method," *International conference on safety, health and welfare in agriculture and agro*, 2012.